

**X-Ray Fluorescence Emission Following K Capture and  
*1s* Photoionization of Mn and Fe in Various Chemical  
Environments**

DISSERTATION

zur Erlangung des Doktorgrades  
des Fachbereichs Physik  
der Universität Hamburg

vorgelegt von

**Pieter Glatzel**  
aus Mainz

Hamburg 2001

Gutachter der Dissertation: Prof. Dr. B. Sonntag  
Prof. Dr. S. P. Cramer

Gutachter der Disputation: Prof. Dr. B. Sonntag  
Prof. Dr. R. L. Johnson

Datum der Disputation: 14. Dezember 2001

Sprecher des Fachbereichs  
Physik und Vorsitzender  
des Promotionsausschusses: Prof. Dr. F.-W. Büßer

## Zusammenfassung

### Röntgenfluoreszenzemission nach K-Elektroneneinfang und $1s$ Photoionisation von Mn und Fe in verschiedenen chemischen Umgebungen

Die K-Fluoreszenzemission von Mn und Fe in verschiedenen chemischen Umgebungen wurde im Rahmen dieser Arbeit untersucht. Ein Kristallspektrometer mit vier bis acht Analysatorkristallen wurde konstruiert und die spektralen und fokalen Eigenschaften wurden studiert. Zwei Mechanismen zur Erzeugung eines  $1s$  Loches,  $1s$  Photoionisation und radioaktiver Zerfall durch Elektroneneinfang aus der K-Schale (K-Einfang), wurden genutzt, um die Störung der Valenzelektronen aufgrund der Innerschalenanregung zu untersuchen. Mehrfachanregungen in den Zwischen- und Endzuständen wurden im Hinblick auf einen Vergleich zwischen den beiden Anregungsmechanismen diskutiert. Es zeigte sich, dass die K-Fluoreszenz nach Photoionisation durch Mehrfachanregungen beeinflusst ist. Die Valenzelektronen relaxieren nicht adiabatisch nach  $1s$  Photoionisation, sondern energetisch höher liegende Zustände werden bevölkert. Die K-Einfangsspektren zeigen deutlich geringere Störung der Valenzschale und geben somit Information über einen Zustand der Valenzelektronen, der ungefähr dem Grundzustand entspricht. Bezüglich des Einflusses der chemischen Umgebung zeigte sich, dass die  $K\alpha_1$  Linienbreite und die  $K\beta_{1,3}$  Schwerpunktsenergie von der effektiven Zahl der Valenzelektronen mit ungepaartem Spin abhängen. Ligandenfeldmultipletrechnungen einschließlich Konfigurationswechselwirkung wurden durchgeführt, um die K Emissionsspektren mit einem Innerschalenloch im Endzustand zu simulieren. Die chemische Abhängigkeit kann mit der Austauschwechselwirkung zwischen dem Innerschalenloch und dem ungepaarten Spin in der Valenzschale erklärt werden. Untersuchungen an Ni bestätigen diese Interpretation. Die Spektren aufgrund von Übergängen der Valenzelektronen in die  $1s$  Schale des Metallatoms ( $K\beta$  Satellitenlinien) wurden mittels Dichtefunktionsrechnungen interpretiert. Eine grobe quantitative Übereinstimmung mit dem Experiment ergab sich für eine molekulare Mn-Nitridoverbindung bereits aus einem einfachen Einelektronenbild. Dipolübergänge dominieren die  $K\beta$  Satellitenspektren.



## Abstract

An investigation of the Mn and Fe K fluorescence emission in various chemical environments was carried out in the framework of this thesis. A crystal array spectrometer employing four to eight analyzer crystals was built and its spectral and focal properties were examined. Two modes of  $1s$  vacancy creation - photoionization and radioactive electron capture decay from the K shell (K capture) - were used to study the valence shell perturbation due to  $1s$  core hole creation. Multiple excitations in the intermediate and final states are discussed with respect to a comparison of the two modes of excitation. It was found that the K fluorescence after photoionization is influenced by shake transitions, *i.e.* the valence electrons relax non-adiabatically after the core hole creation. The K capture spectra, in contrast, show considerably less perturbation of the valence shell and therefore provide information about the valence electron configuration that approximately corresponds to the ground state configuration. Concerning the influence of the chemical environment on the K fluorescence it was found that the  $K\alpha_1$  linewidth and the  $K\beta_{1,3}$  center of gravity energy show a dependence on the valence shell net spin. Ligand field multiplet calculations including configuration interaction on the basis of ligand-to-metal charge transfer were carried out to model the spectra that have a core hole in the final state. The exchange interaction between the core hole and the spin-unpaired valence electrons can explain the observed chemical dependence. Studies on Ni support this interpretation. The spectra that result from transitions of the valence electrons to the metal  $1s$  shell ( $K\beta$  satellite lines) were interpreted using density functional theories. A rough quantitative agreement between theory and experiment could be achieved within a one-electron, sudden approximation picture for a molecular Mn-nitrido complex. The  $K\beta$  satellite spectra are dominated by dipole transitions.



# Contents

<b>1</b>	<b>Introduction</b>	<b>1</b>
1.1	Inner-Shell X-ray Spectroscopies . . . . .	1
1.2	Theories . . . . .	3
1.3	Modes of Excitation . . . . .	5
<b>2</b>	<b>Instrumentation</b>	<b>8</b>
2.1	Crystal Spectrometer . . . . .	8
2.1.1	Energy Calibration . . . . .	9
2.1.2	Instrumental Energy Broadening . . . . .	10
2.1.3	Ray-Tracing Calculations . . . . .	17
2.2	Detectors . . . . .	21
2.3	Experimental Set Up Using Synchrotron Radiation . . . . .	23
2.4	Data Evaluation and Error Analysis . . . . .	25
<b>3</b>	<b>Theory</b>	<b>27</b>
3.1	The Ligand Field Multiplet Model . . . . .	28
3.1.1	N-Electron Atom . . . . .	28
	Self-Consistent Field Method . . . . .	28
	Corrections to the SCF Method . . . . .	30
	Theory of $K\beta$ Emission in Atoms . . . . .	32
	Theory of $K\alpha$ Emission in Atoms . . . . .	34
3.1.2	N-Electron Atom in a Ligand Field . . . . .	37
3.1.3	Ligand-to-Metal Charge Transfer . . . . .	43
3.1.4	Limitations of Ligand Field Multiplet Theory . . . . .	47
3.2	Density Functional Theory . . . . .	48
<b>4</b>	<b>Double Excitation</b>	<b>52</b>
4.1	Multiple Excitations upon $1s$ Vacancy Creation . . . . .	53
4.2	Radiative Auger Emission . . . . .	56

<b>5</b>	<b>Influence of the Core Hole on K Fluorescence Emission</b>	<b>59</b>
5.1	K $\beta$ Lines . . . . .	59
5.1.1	Experimental Observation . . . . .	59
5.1.2	Relaxation after <i>1s</i> Vacancy Creation . . . . .	61
5.1.3	The <i>1s</i> Intermediate State . . . . .	62
5.1.4	Final State Lifetime Broadening . . . . .	64
5.1.5	Calculated K $\beta$ Spectra . . . . .	66
5.1.6	Uncertainty Introduced by Empirical Parameters . . . . .	71
5.1.7	Concluding Remarks . . . . .	72
5.2	K $\alpha$ Lines . . . . .	74
5.2.1	Motivation: Chemical Dependence of K $\alpha_1$ Linewidth . . . . .	74
5.2.2	( <i>2p,3d</i> ) Exchange Interaction in a Poly-Nuclear System . . . . .	77
5.2.3	Analysis of the K $\alpha_1$ Linewidth in <sup>55</sup> Fe and Mn Compounds . . . . .	78
5.2.4	Multiplet Calculations . . . . .	81
5.2.5	Concluding Remarks . . . . .	86
5.3	K $\beta$ Satellite Emission . . . . .	86
<b>6</b>	<b>K<math>\beta</math> Satellite Spectra</b>	<b>90</b>
6.1	K $\beta$ Satellite Spectra in Fe <sub>2</sub> O <sub>3</sub> . . . . .	90
6.2	Angular Dependence of K $\beta$ Satellite Lines in [Mn(N)(CN) <sub>5</sub> ] <sup>3-</sup> . . . . .	93
<b>7</b>	<b>Chemical Dependence of K<math>\beta</math> Emission</b>	<b>100</b>
7.1	K $\beta$ Main Lines in <sup>54</sup> Mn Compounds after K Capture . . . . .	100
7.2	K $\beta$ Main Lines in <sup>55</sup> Fe Compounds after K Capture . . . . .	105
7.3	K $\beta$ Lines in Ni Compounds and Fe Proteins . . . . .	108
7.3.1	Heme Center in Myoglobin . . . . .	108
7.3.2	Ni Compounds . . . . .	109
<b>8</b>	<b>Summary and Outlook</b>	<b>114</b>
<b>A</b>	<b>Two-Dimensional Gas Proportional Counter</b>	<b>116</b>
<b>B</b>	<b>(<i>2p,3d</i>) Exchange Interaction in a Poly-Nuclear System</b>	<b>118</b>

# 1 Introduction

The valence electron configuration of  $3d$  transition metals in a chemical environment is an important topic of study in materials science and biochemistry. Transition metal compounds can have interesting material properties such as superconductivity [106], high Curie temperature [91] and high (giant, colossal) magneto resistivity [101, 109]. In biophysics they often play a crucial role in the active center of metalloproteins [111], *e.g.* Fe in hemoglobin, Ni in hydrogenases and Mn in photosystem II. The various spectroscopic techniques that are used to study the electronic structure differ in their applicability and the information that can be gained. Techniques that use photons to probe the sample cover a large range of the electromagnetic spectrum starting at microwave frequencies in electron spin resonance (ESR) to hard x-rays with photon energies above 14 keV to excite nuclear resonances (*e.g.* Mössbauer spectroscopy). Photon energies between 400 and 10000 eV can create a hole in a transition metal K or L shell and are therefore used for ‘inner-shell’ or ‘core-hole’ x-ray spectroscopy. This thesis discusses ( $1s$ ) K fluorescence spectroscopy as a tool to study transition metals in inorganic compounds and proteins. But before this technique is elaborated in detail it is set in context with other inner-shell x-ray spectroscopies that are widely used.

## 1.1 Inner-Shell X-ray Spectroscopies

One approach to study the metal  $3d$  electron configuration in inner-shell spectroscopy is to take advantage of the dipole allowed  $2p$  to  $3d$  electron transition. L-edge absorption spectroscopy can be realized using many different techniques (transmission, electron yield, fluorescence yield) and it has been used in many applications to study transition metals in different chemical environments [42, 37]. The L-edge energies of  $3d$  transition metals range from 400 eV (Sc) to 1100 eV (Zn). This energy range is referred to as the ‘soft x-ray’ region. Though successfully applied in many studies, L-edge spectroscopy involves experimental difficulties that sometimes yield questionable results. As an example, the attenuation length ( $1/e$  path length) of 700 eV photons in MnO is approximately  $0.11 \mu\text{m}$  [105] which is surface sensitive in terms of possible chemically alteration of the sample. In case of proteins it is sometimes disputed whether the redox state of the protein is changed when the sampled is exposed to ultra-high vacuum (UHV). Furthermore, ionizing x-rays can permanently alter the chemical state of the transition metal atom in the protein. This ‘radiation damage’ is caused by free radicals and hydrated electrons that are created in the sample [96]. The experimental problems are alleviated or even solved if one uses higher photon energies ( $\geq 5$  keV, ‘hard x-rays’) with larger attenuation lengths. Hard x-ray spectroscopy does not require UHV and is more bulk sensitive. The attenuation length of 10 keV photons in MnO is  $\approx 15 \mu\text{m}$  [105]. This facilitates sample handling and makes sample integrity more likely. Radiation damages are considerably reduced because the energy deposited per sample unit volume decreases with increasing photon energy at identical incident photon flux densities.

The electronic transitions that are investigated in hard x-ray spectroscopy of  $3d$  transition metals in most cases involve the metal K-shell. K-edge absorption spectroscopy can be considered a standard spectroscopic tool [79]. In particular, the extended x-ray absorption fine structure (EXAFS) is widely used to determine short-range geometry parameters [113]. However, the pre-edge and near-edge structure (XANES) is shaped by numerous effects (quadrupole and dipole resonances, single and multiple scattering from neighboring atoms)

and theoretical interpretation is a challenge. The short  $1s$  core hole lifetime broadens the spectral features and it becomes difficult to favor one theoretical result over another because the experiment yields little structure to test the theory. Furthermore, many problems in materials science and biophysics address the local electronic structure of the metal atom, *i.e.* the orbitals localized at the metal atom that have mainly metal  $3d$  character. In XANES spectroscopy,  $1s$  to  $3d$  quadrupole transitions (pre-edge features) are weak and often appear on a high background due to dipole allowed transitions at higher energies and it is therefore difficult to isolate the  $1s$  to  $3d$  resonances.

It has been long known that both K emission and K absorption exhibit a chemical sensitivity (for a review see [94] and references therein). The strongest K fluorescence lines result from  $2p$  to  $1s$  transitions ( $K\alpha$  lines). About 8 times weaker are the  $3p$  to  $1s$  transitions and again 50-100 times weaker are transitions from higher orbitals to the  $1s$  orbital. Both latter fluorescence emissions are denoted  $K\beta$  lines. This is shown in Figure 1 in a simplified term scheme and experimental spectra for MnO are shown in Figure 2. In order to be able to separate spectral features within the  $K\alpha$  and  $K\beta$  groups and detect spectral changes due to the chemical environment it is necessary to employ crystal analyzers ( $E/\Delta E > 5000$ ) as opposed to solid state detectors (*e.g.* Ge or NaI,  $E/\Delta E < 40$ ) as energy dispersive element in the experimental set up. In this work one Bragg reflection in the beam path between sample and detector is used. The set up will be referred to as ‘high resolution hard x-ray spectroscopy’ in this thesis in order to distinguish it from experiments that use solid state detectors for energy resolution (*e.g.* in fluorescence detected absorption spectroscopy). This term is, of course, at odds with efforts that produce sub-meV resolution at keV incident energies that are commonly referred to as ‘high resolution’, as well. In our nomenclature, these monochromators deserve to be called ‘very high resolution’.

The denotation of the  $K\beta$  spectral features used in Figures 1 and 2 has its origin in the spectroscopy of high  $Z$  materials, such as Rhodium and Uranium, where the  $3p$  spin-orbit splitting is large enough to yield two distinct  $3p_{1/2}$  ( $K\beta_3$ ) and  $3p_{3/2}$  ( $K\beta_1$ ) final states (for an overview see references [94, 2]).  $K\beta_2$  was assigned to transitions from  $4p$  orbitals and  $K\beta_5$  to  $3d$  orbitals. The nomenclature was transferred to transition metals and there, with a deeper understanding of the dominating interactions, partly lost its actual physical meaning. The importance of the ( $3p, 3d$ ) exchange splitting for the  $K\beta$  main lines in  $3d$  metals was first pointed out by Tsutsumi [132]. The K fluorescence final states are discussed in detail in Chapter 3. Throughout this thesis I will denote  $3p$  to  $1s$  transitions as  $K\beta$  main lines and transitions at higher fluorescence energies  $K\beta$  satellites. The  $K\beta'''$  structure at highest fluorescence energies is due to double ionizations as will be explained in Chapter 4.

K fluorescence lines with a core hole in the final state give an indirect probe of the valence shell configuration. The hole ( $2p$  or  $3p$ ) in the final state of the radiative transition interacts with the valence shell electrons. This interaction is expressed by the two-electron operator in the atomic Hamiltonian. The strength of the interaction can be determined by calculating the electron-electron direct and exchange contribution. Since the integrals depend on the overlap of the corresponding wavefunctions, the electron-electron Coulomb interaction is greatest for valence electrons that are localized at the metal atom. Thus, the factors that mainly influence the K fluorescence are changes in the chemical environment that alter the electron configuration at the metal site. This distinguishes inner-shell x-ray spectroscopy from many other techniques (ESR, FTIR) that probe a larger volume around the metal atom and this has to be borne in mind when results from different spectroscopic techniques

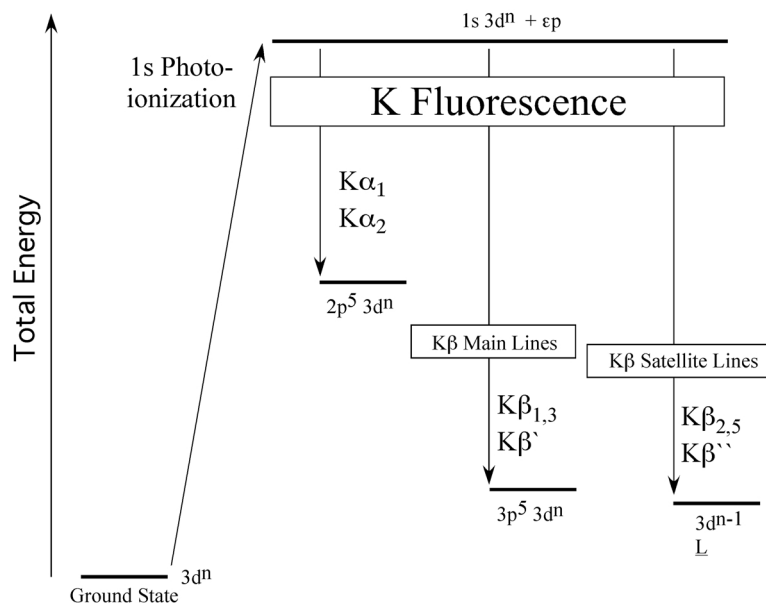


Figure 1: *Simplified energy scheme for K fluorescence emission. In this scheme the 1s intermediate or fluorescence initial state is reached in a photoionization process. Alternatively, the 1s vacancy can be created in a K electron capture decay of a radioactive isotope. The different radiative decay channels of the 1s vacancy give rise to the K fluorescence spectrum. The continuum electron is neglected in the final states.  $\underline{L}$  denotes a hole in a ligand orbital.*

are compared. An example will be given in Section 7.3.1.

One drawback of high resolution K emission spectroscopy compared to K absorption spectroscopy as a tool for chemical analysis is that crystal emission analyzers have a small solid angle. However, larger crystal analyzers with smaller bending radii and high-flux x-ray sources at synchrotrons now enable one to record high resolution fluorescence spectra even on dilute samples such as proteins. A crystal array analyzer was built in the framework of this thesis. The instrument is discussed in Chapter 2. At this point it is mentioned that the K fluorescence yield in Mn (30 %) is nearly by a factor 100 larger than the  $L_{II,III}$  yield (0.5%) [82]. This is important when fluorescence detected L-edge absorption spectroscopy is compared to K high-resolution fluorescence spectroscopy. The three spectroscopic techniques (L absorption, K absorption, K emission) mentioned above all have their advantages and disadvantages and they complement each other. This work contributes to the understanding of K fluorescence emission from  $3d$  transition metals in a ligand environment. Considerable work has already been done by several authors; however, high-resolution hard x-ray fluorescence spectroscopy still is rarely applied in chemical analysis and a deeper understanding may promote the use of this spectroscopic technique.

## 1.2 Theories

The analysis of inner-shell spectra of a free transition metal atom or ion is a complex many-body problem that cannot be solved analytically, and numerical simulations are limited by computer capacities. Thus, approximations have to be made and it remains a topic of

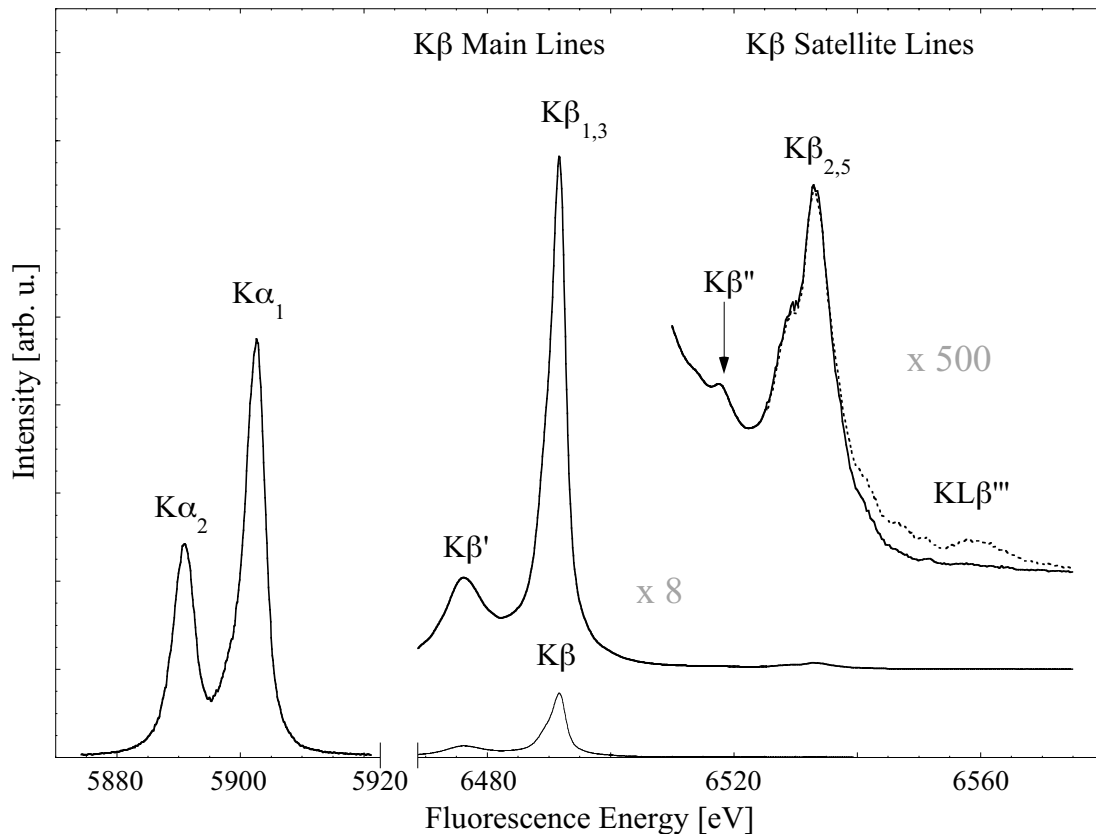


Figure 2: *K* emission lines in *MnO*. The final state configurations are given in Figure 1. The  $K\beta'''$  structure is due to doubly ionized final states. The magnifications for the  $K\beta$  main and satellite lines are given.

controversy which effects can be neglected and which cannot. The matter becomes more complicated when the atom is embedded in a ligand environment. There one can roughly distinguish between molecular complexes that do not exhibit any translational symmetry and complexes within a lattice structure. Many authors treat even the latter by means of a cluster model (*e.g.*  $MX_6$  in octahedral symmetry) and either neglect band formation at all or introduce it empirically. The choice of theory depends on the electron transition that is observed experimentally. K-edge absorption spectra can be well reproduced within a multiple scattering formalism based on real space Green functions ('FEFF code', [4]). This code can as well reproduce variation of the  $L_3/L_2$  ratio across the  $3d$  transition metal series [110]. However, it fails to reproduce much of the structure within the  $L_3$  and  $L_2$  lines. The ligand field multiplet approach to analyze inner-shell x-ray spectra of transition metal compounds already suggested in 1959 by Tsutsumi [132] and further developed by Sugano, Thole and others [124, 128] has been applied successfully to L-edges [42] and K emission spectra [81]. The multiplet interpretation for the overall structure of the K fluorescence spectra is supported by results obtained using photoelectron spectroscopy ( $3p$  and  $2p$  XPS) on free metal atoms [52, 63, 141]. In order to account for weak structures and smaller deviations between theory and experiment it is not clear whether a more elaborate atomic approach including relativistic effects [9] or configuration interaction [137] already suffices or whether solid state effects have to be taken into account [50, 134, 103]. Deutsch *et al.*

include quantum electrodynamics to explain their spectra following double photoionization [46]. Some authors invoked density functional theory for qualitative arguments to explain experimental observations [74]. In this thesis ligand field multiplet theory is applied to interpret  $K\alpha$  and  $K\beta$  main lines and molecular orbital theory for the  $K\beta$  satellites. In the latter case, the molecular orbitals were obtained using Kohn-Sham density functional theory. These two theoretical approaches, ligand field multiplet theory including ligand-to-metal charge transfer and density functional theory, are outlined in Chapter 3.

It is emphasized that in this work I try to reproduce in theoretical calculations the trends that are observed in experimental spectra for a metal in varying chemical environments or following different modes of excitations. The goal is not to achieve perfect agreement between theory and experiment for one spectrum but to explain spectral changes following changes in the ligand environment, the mode of excitation (see below) or the orientation of a single crystalline sample within one theoretical framework. This approach, of course, assumes that the approximations made in the theory are equally good for the different cases that are compared. For this approach to work the theory needs to be the overall correct approach to the problem and the approximation must not strongly affect the feature that shows the spectral change. This problem will be addressed when the results are discussed.

Another point has to be mentioned in this introduction. In the language of a chemist the term ‘oxidation state’ of an atom in a chemical environment has vital importance. The metal atom oxidation state is, in most cases, derived using a few general guidelines that can be found in standard textbooks on chemistry. A change of the ligand environment often implies a change of the oxidation state of the metal atom. The steps of biochemical reaction (redox) cycles are classified in terms of the oxidation states of the participating atoms. The use of the term ‘oxidation state’ is justified in many contexts and for many spectroscopies. However, it creates some confusion when it is used to derive the number of electrons in the valence shell of an atom and its spin state, *i.e.* the net number of unpaired electrons located at the atom. Even though this concept works rather well for ionic compounds it can be very misleading for molecular complexes that usually exhibit strongly covalent bonds and the electron density for an occupied valence orbital is spread across several atoms. Core hole fluorescence spectroscopy tests the immediate surrounding of the excited atom. The electron and spin density located at the excited atom do not correspond to the numbers derived from the ‘formal’ oxidation state. Density functional theory can yield a number that is closer to the actual value. I will try in Chapter 5.2 to build a bridge between ligand field multiplet theory and density functional theory using the calculated electron and spin densities of the metal atom.

### 1.3 Modes of Excitation

K fluorescence spectra will be shown where the  $1s$  hole is created in two different ways (modes of excitation). In photoionization (PI) a photon excites a  $1s$  electron into the continuum. Alternatively, one can take advantage of a radioactive decay. Orbital electron capture is a process closely related to nuclear  $\beta$  decay that competes with positron emission [80, 142]. An orbital electron is captured by the nucleus yielding a neutron that remains in the nucleus and an escaping electron neutrino. The atomic number of the daughter nucleus is decreased by one while the atomic mass number is unchanged:  $Z^A + e^- \rightarrow (Z-1)^A + \nu_e$ . The capture rate depends on the probability of finding the electron inside the nucleus and is therefore largest

for  $1s$  electrons (K capture (KC) decay). The half-lives of  $^{55}\text{Fe}$  and  $^{54}\text{Mn}$  are 2.76 years and 312.2 days, respectively. The nuclear recoil energy can be calculated from momentum conservation and assuming a zero neutrino mass one obtains:

$$E_R = \frac{E_\nu^2}{2Mc^2} \quad (1)$$

where  $E_\nu$  is the kinetic energy of the escaping neutrino and equals the total disintegration energy  $Q$ . The nuclear decay paths for  $^{55}\text{Fe}$  and  $^{54}\text{Mn}$  are shown in Figure 3.  $^{55}\text{Fe}$  decays into the nuclear ground state of  $^{55}\text{Mn}$ . The  $Q$  value of the electron capture decay of  $^{55}\text{Fe}$  is 231.6 keV [89] and the recoil energy of the nucleus is 0.523 eV.  $^{54}\text{Mn}$  decays into an excited nuclear state of  $^{54}\text{Cr}$ . The  $Q$  value is 1377.1 keV [89] and the recoil energy of the nucleus is 18.85 eV.

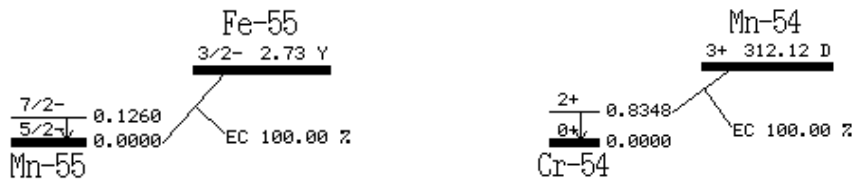


Figure 3: *Electron capture (EC) decay paths with branching ratios for  $^{55}\text{Fe}$  and  $^{54}\text{Mn}$ . The nuclear spin, parity and half-life of the mother isotopes are given. Furthermore, the energies of the lowest nuclear excited states of the daughter nuclei are shown (in MeV).*

In order to estimate whether the distortion of the lattice caused by the nuclear recoil has an influence on the K fluorescence spectra I calculate the distance traveled by the nucleus within the lifetime of the  $1s$  core hole ( $\sim 5 \cdot 10^{-16}$  s [83]) in a simple picture assuming a free atom. One obtains 0.007 Å for  $^{55}\text{Fe}$  and 0.041 Å for  $^{54}\text{Mn}$  which is in the range of vibrational amplitudes in solids at room temperature [27]. The energies of the vibrational modes in transition metal compounds are between 50 and several hundred meV [92]. Typical interatomic distances in molecules and solids are  $\approx 2$  Å. For  $^{55}\text{Fe}$ , the distortion of the lattice due to the recoil energy is less than 0.5% and can be neglected in the context of this thesis. In case of the  $^{54}\text{Mn}$  spectra it is possible that a high vibrational mode influences the spectra. In a ligand field model this distortion alters the ligand field splittings (10Dq, Ds, Dt). However, the analysis of the  $^{54}\text{Mn}$  spectra in this work is very basic due to poor statistics in the experimental spectra and the conclusions are expected not to be influenced by possible lattice distortions. A further investigation of the vibrational distortion after K capture in  $^{54}\text{Mn}$  is therefore not pursued at this point.

Figure 4 illustrates for radioactive  $^{55}\text{Fe}$  and stable  $^{55}\text{Mn}$  that the same formal atomic configurations are reached after K capture in  $^{55}\text{Fe}$  and  $1s$  photoionization in  $^{55}\text{Mn}$ , respectively. This suggests a comparison of the x-ray fluorescence following the two modes of excitation as will be done in Chapter 5. At this point it shall only be noted that changes in the nucleus (isotope effect, nuclear excitation) can influence the K fluorescence emission besides the mode of excitation and the chemical environment. As an example, Borchert *et al.* used K capture decay in  $^{131,132}\text{Cs}$  to observe shifts of the Xe K x-rays due to the nuclear finite-size effect and the magnetic hyperfine structure [23]. They pointed out that the expected shifts are on the order of  $10^{-2}$  to  $10^{-3}$  of the natural linewidth of the  $1s$  excited state. In the case

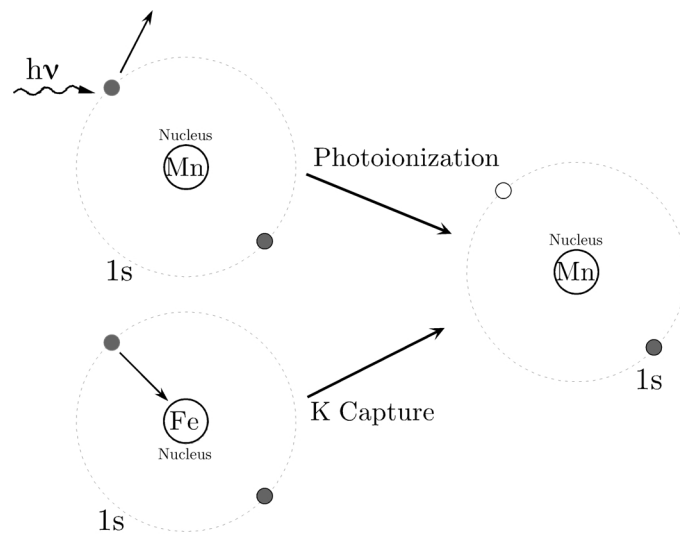


Figure 4: *K capture in  $^{55}\text{Fe}$  and  $1s$  photoionization in  $\text{Mn}$ . Both processes result in an ion that has a  $\text{Mn}$  ( $Z=25$ ) nucleus and a hole in the  $1s$  shell.*

of  $^{55}\text{Fe}$  this would result in a 1-10 meV shift which is far below the resolution of the crystal spectrometer employed in the studies presented here.

## 2 Instrumentation

The experimental work of this thesis requires an excitation x-ray source if no radioactive sample is measured and an analyzer crystal spectrometer with a photon detector. This Chapter deals mainly with the fluorescence spectrometer and briefly describes the synchrotron beam-lines that provided the incident x-ray beam. No resonantly excited spectra are shown in this thesis and the energy bandwidth of the incident x-rays therefore does not influence the fluorescence emission. The important characteristics of the incident beam in this context are the total flux at the sample and the beam spot size on the sample surface. The energy of the incident beam becomes important in the context of double excitations. This is discussed in Chapter 4.

### 2.1 Crystal Spectrometer

High resolution spectra from fluorescence events that involve a transition metal K-shell can be recorded using a crystal analyzer that is arranged with sample and detector in a Rowland geometry. In a Johann type instrument, the crystal planes lie parallel to the crystal surface and the crystal is bent to a radius  $R$  [71]. The geometry is shown in Figure 5. I will use the following convention to denote the axes: lower case ‘xyz’ refer to the dimensions relative to the Rowland plane of one crystal as shown in Figure 5. Upper case ‘XYZ’ refer to the axes in the multi-crystal array spectrometer as shown in Figure 7 where there are four xyz-systems, one for each crystal.

The spectral and focal properties of a Johann type spectrometer have been discussed in detail by several authors [20, 87, 84] and I will therefore limit the discussion here to basic remarks concerning the crystal spectrometer with one analyzer crystal. Biological samples usually have low metal concentrations that require a large acceptance analyzer. A crystal array analyzer that employs 8 crystals capturing a total solid angle of 0.07 sr has been developed previously [15]. This instrument is operated using a simplified  $\theta/2\theta$  scanning procedure. The multi-crystal spectrometer and the scanning procedure require some discussion concerning energy broadening and focussing properties.

The synchrotron based work presented in this thesis was carried out using the previously built instrument. It was also used for some of the K capture studies. As part of this thesis research, I built a second instrument dedicated to the K capture work. The K capture experiment imposes fewer constraints on the instrumental layout. The second crystal array analyzer was therefore designed to meet the requirements of the K capture experiment with the result of lower costs and simpler operation. The discussion of the focal and spectral properties in this Section apply to both spectrometers.

The analyzer crystals were purchased from the company Crismatec [38]. They are made from a 0.15 mm thick single crystal wafer that is cut along the desired Miller plane. The wafer is glued onto a spherically bent glass substrate with a radius of curvature of  $R=860$  mm. Crystals with a diameter  $2r$  of 89 mm (Ge(1,1,1), Si(2,2,0), Si(5,5,1)) and 44.5 mm (Ge(3,1,0)) were used. The captured solid angle of one crystal in Johann geometry therefore is  $\approx 6.7 \cdot 10^{-4}$  and  $\approx 1.7 \cdot 10^{-4}$  of the total  $4\pi$  sr, respectively.

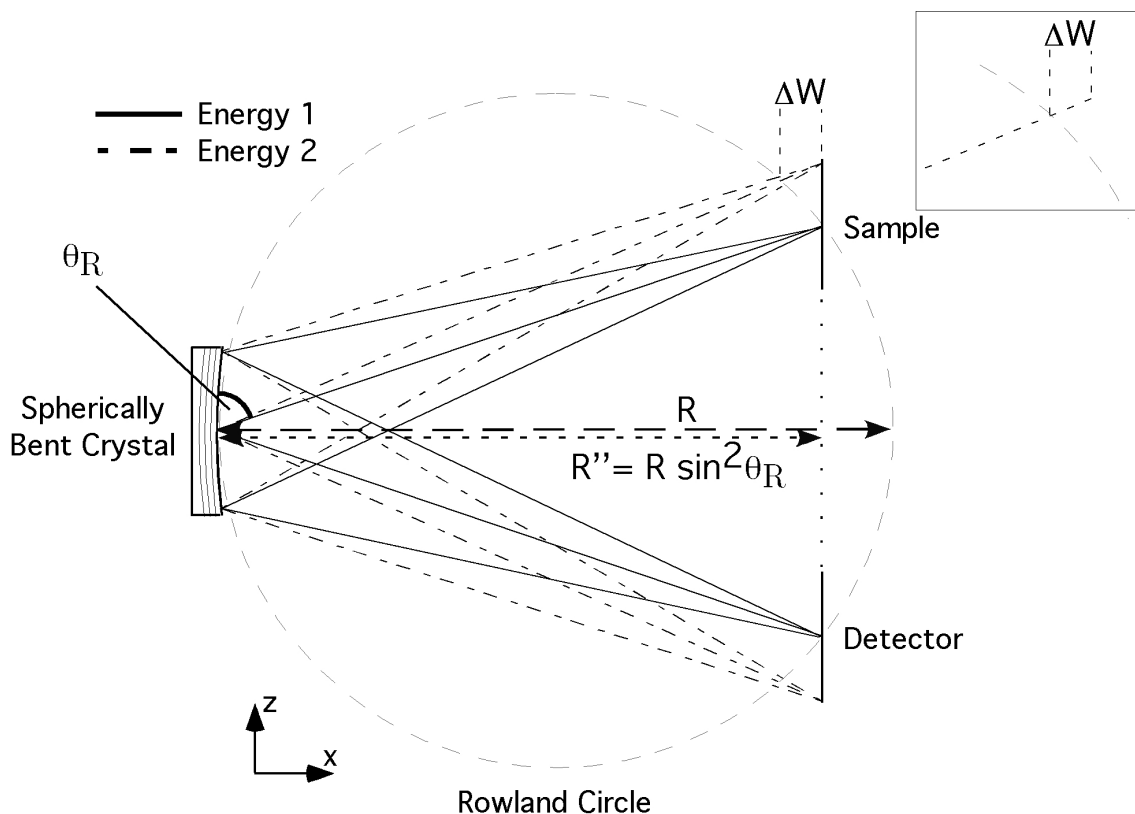


Figure 5: *Johann geometry with Rowland circle. The crystal planes are parallel to the crystal surface which is bent to a radius  $R$ . The radius of the Rowland circle is  $R/2$ . An energy scan is achieved by moving sample and detector away from the focussing circle (vertical lines). The  $y$ -axis points into the plane of the drawing.*

The wavelength of a reflection from parallel crystal planes can be obtained from Bragg's law:

$$2d \sin \theta = n\lambda \quad (2)$$

with the Bragg angle  $\theta$ , the integer  $n$  and the d-spacing  $d = a/\sqrt{(h^2 + k^2 + l^2)}$  where  $a$  is the lattice parameter and  $h, k, l$  are the Miller indices. Bragg's law assumes a unity index of refraction and is therefore only approximate. A more accurate value for the energy can be obtained with dynamical theory [144, 70, 11]. Using the program XOP [51] for Si(4,4,0) at  $84.2^\circ$  (6490 eV, Mn  $K\beta$ ) and Ge(3,3,3) at  $73.2^\circ$  (5947 eV, Cr  $K\beta$ ) a deviation for the reflected energy between Bragg's law and dynamical theory of 77 meV and 178 meV, respectively, was calculated. The error introduced by using equation 2 to calculate the energies is much smaller than the error for the absolute energy calibration of the spectrometer (see Table 1). I will therefore simply use Bragg's law to determine the fluorescence energies.

### 2.1.1 Energy Calibration

Absolute energy calibration was achieved by measuring the Bragg angle using optical tools. The error for the Bragg angle mainly results from inaccuracies when determining the  $z$ -positions of the center of the crystals and the source volume of the spectrometer defined by

either the center of the synchrotron beam spot on the sample or of the radioactive source. I estimate this error to 1 mm which translates into different errors for the fluorescence energies depending on the Bragg angle and the fluorescence energy (see equation 7). The absolute errors for the energy calibrations are summarized in Table 1. No absolute energy calibration using a tabulated reference fluorescence line was performed for the spectra presented in this thesis. This was not necessary since only statements about line shapes and relative energy shifts are made. Because of the latter great care was taken to maintain the relative energy calibration. For this, the relative position calibration between the source volume of the spectrometer and the center of the crystals had to be kept constant because it determines the Bragg angle. I will discuss how this was achieved during the synchrotron experiments at the end of this Chapter where the synchrotron beamlines are described.

In order to switch from synchrotron to K capture measurements first the synchrotron beam spot on the sample was determined using optical tools and the radioactive sample was then inserted into the same position. I estimate a combined error for the accuracy of the vertical positioning of the sample and the determination of the vertical position of the synchrotron beam on the sample to  $\pm 0.2$  mm. I directly compare fluorescence energies between K capture and photoionization experiments only for Mn  $K\beta$  main line spectra. The relative error here is  $\pm 0.07$  eV. An identical procedure was carried out when different radioactive samples were measured where the optical tool was aligned on the source volume of the spectrometer. The error for the vertical positioning here is  $\pm 0.1$  mm. For Mn the  $K\beta$  main lines this translates into  $\pm 0.04$  eV and for the Cr  $K\beta$  main lines into  $\pm 0.09$  eV.

### 2.1.2 Instrumental Energy Broadening

One can distinguish between intrinsic ( $\Delta E_{int}$ ) and geometrical ( $\Delta E_{geo}$ ) contributions to the instrumental broadening of the crystal spectrometer [15]. The angular or Darwin width ( $\Delta E_{dyn}$ ) of a perfect crystal can be calculated with the dynamical theory. The energy resolution  $\Delta E_{dyn}/E$  is approximately constant for a given Bragg reflection [11]. For a Si(4,4,0) and a Ge(3,3,3) reflection  $\Delta E_{dyn}$  equals 69 meV and 122 meV at incident energies of 6490 eV and 5947 eV, respectively [51]. The bending of the single crystal wafer results in figure errors and d-spacing variations that degrade the energy resolution. This together with the Darwin width forms the intrinsic instrumental broadening  $\Delta E_{int}$ . Hämäläinen *et al.* estimated for a Si(4,4,0) Bragg reflection at  $84.2^\circ$  in Johann geometry  $\Delta E_{int} \leq 0.3$  eV [62]. This number will vary for different Bragg reflections and angles and it, of course, depends on the quality of the crystal.  $\Delta E_{int}$  cannot be changed and it sets the lower limit for the instrumental energy broadening. It will be shown below that the geometrical contributions  $\Delta E_{geo}$  strongly depend on the experimental conditions and for most of our applications they will dominate the overall instrumental energy broadening.

The required instrumental energy resolution depends on the spectra that are to be measured. The  $K\alpha$  and  $K\beta$  main line spectra presented in this thesis have a lifetime broadening of greater than 1.5 eV (see reference [83] and Chapter 5). The spectra are composed of a wealth of final states due to multiplet, spin-orbit, crystal field and configuration interaction effects. These splittings together with the lifetime broadening result in an intrinsic FWHM of the  $K\beta_{1,3}$  or  $K\alpha_1$  peaks of 2-4 eV. This value is considerably larger than  $\Delta E_{int}$ . It is therefore not necessary to choose experimental conditions that yield the best possible instrumental energy resolution, but one can sacrifice some energy resolution in favor of more convenient

experimental operation. The design of the spectrometer used for this work is a compromise between energy resolution and other experimental considerations such as sample handling, scanning procedure and solid angle. The instrumental broadening as well as spectral and focal properties of the multi crystal array spectrometer will be discussed in the following starting with a point source in Johann geometry using one crystal. Examples will be given for Mn and Cr  $K\beta$  spectra because they were taken with the, respectively, largest and smallest Bragg angles representing the best and worst case in terms of energy resolution (see Table 1).

### Point Source in Johann Geometry

For a discussion of the geometrical contributions to the instrumental energy broadening it is helpful to write down the first derivative of equation 2:

$$\left| \frac{\Delta E}{E} \right| = \Delta\theta \cot\theta \quad (3)$$

A first order contribution to a change  $\Delta\theta$  in the Bragg angle corresponds to a first order contribution in the energy resolution  $\Delta E$ . The cotangent term increases the broadening for smaller Bragg angles.

There are two geometrical contributions to the energy broadening of a one-crystal spectrometer in Johann geometry for a point source on the Rowland or focal circle that can be written for Bragg angles close to  $90^\circ$  [94, 84, 87]:

$$\Delta E_J = \frac{1}{2} E \left( \frac{r}{R} \right)^2 \cot^2 \theta \quad (4)$$

$$\Delta E_S = \frac{1}{2} E \left( \frac{r}{R} \right)^2 \cot^4 \theta \quad (5)$$

where  $E$  is the incident energy,  $r$  is half the diameter of the crystal,  $R$  the bending radius of the crystal and  $\theta$  is the Bragg angle.  $\Delta E_J$  is due to the fact that the radius of curvature of the crystal surface (and thus the Bragg planes) is identical to the diameter  $R$  of the Rowland circle (see Figure 5). This results in different Bragg angles across the crystal for x-rays in the Rowland plane. The broadening would be eliminated in a Johansson geometry where the curvature of the Bragg planes still has the radius  $R$  but the curvature of the crystal surface has the radius of the Rowland circle  $R/2$ , *i.e.* the Bragg planes are no longer parallel to the crystal surface. It is however much more elaborate and therefore costly to fabricate such a crystal and the broadening  $\Delta E_J$  is not the dominant contribution to the overall energy broadening.  $\Delta E_S$  is due to the fact that the crystal extends out of the Rowland or focussing plane. This effect is very small because it scales with the fourth power of  $\cot\theta$ .

### Energy Broadening due to Simplified Scanning Procedure

Figure 5 illustrates the energy scanning procedure that was used to record the spectra. Instead of keeping sample and detector on the Rowland circle, both are moved by the same distance opposite to each other in  $z$ -direction out of the Rowland circle. An equivalent motion is to move the crystal by  $\Delta z$  and the detector by  $2\Delta z$  in the same direction while keeping the sample stationary. The Rowland condition is therefore only fulfilled for one energy that

will be denoted  $E_R$  in the following. The energy broadening for a point source positioned out of the Rowland circle is given for  $\theta$  close to  $90^\circ$  as:

$$\Delta E_W = E \frac{r \sin \theta \Delta W}{R^2 \sin \theta + R \Delta W} \cot \theta, \quad \Delta W = R * \frac{\sin^2 \theta_R - \sin^2 \theta}{\sin \theta} \quad (6)$$

where  $\Delta W$  is the distance between the sample and the Rowland circle as given in Figure 5. Here,  $\theta$  is the Bragg angle for the energy  $E$  while  $\theta_R$  is the Bragg angle for which the spectrometer resolution is optimized, *i.e.* for the reflection on the Rowland circle.

The simplified scanning procedure greatly facilitates the experimental setup as well as operation and reduces the probability of errors in the positioning of the components (sample, crystal(s), detector) relative to each other. Particularly in the synchrotron experiment where the source volume of the spectrometer cannot be moved freely because it is defined by the synchrotron beam, this procedure helps to stabilize the relative energy calibration. The same scanning procedure can be used when several crystals are employed. In this case, it would be very elaborate to keep sample and detector on the two intersection points between the different Rowland circles that describe the focal points of the spectrometer (see Figure 7) during an energy scan. It would be possible by rotating the crystals around the Z-direction and simultaneously moving them along the X-direction in case the source volume cannot be moved. Furthermore, all crystals together with the detector would need to be moved along the Z-direction. For four crystals one would require ten synchronized motions which is not a very desirable mode of operation.

Equations 4, 5 and 6 give the total energy spread, *i.e.* the difference between the minimum and maximum energy. In order to compare the calculated results to the full width at half maximum (FWHM) of a  $K\alpha$  or  $K\beta$  spectrum it is necessary to obtain an approximate intensity distribution for one crystal. This can be done by assuming a linear relation between the illuminated crystal surface and the intensity. Since  $z$  is the energy dispersive direction I integrate a differential surface  $dS$  of the crystal in  $y$  direction and determine its dependence on  $z$ . The spherical curvature of the crystal can be neglected for this rough estimate. The FWHM of the calculated intensity curve suggests a scaling of the crystal radius  $r$  by a factor 0.88.

Figure 6 shows the contributions to the instrumental energy broadening for a point source in the energy ranges of a Mn and a Cr  $K\beta$  spectrum. The spectrometer is assumed to be optimized at the  $K\beta_{1,3}$  peak energy (6490 eV for Mn, 5947 eV for Cr). The Bragg angles  $\theta_R$  are  $84.2^\circ$  and  $73.2^\circ$  for the Mn and Cr  $K\beta_{1,3}$  peaks, respectively, where a Si(4,4,0) Bragg reflection is used for Mn  $K\beta$  and a Ge(3,3,3) Bragg reflection for Cr  $K\beta$ .  $\Delta E_S$  is negligible and therefore not shown. In both cases it is evident that the off-Rowland contribution  $\Delta E_W$  is dominant for high fluorescence energies. The combined broadening is given as  $\sqrt{\Delta E_J^2 + \Delta E_W^2}$  where the two contributions are assumed to have a Gaussian shape. The broadening can be neglected for the Mn  $K\beta$  main line region (below 6500 eV) compared to the  $1s$  core hole lifetime (1.16 eV) but increases considerably for higher energies. However, even in the satellite region at about 6535 eV (Mn  $K\beta_{2,5}$ ) no significant broadening is expected from the contributions included in Figure 6. It is therefore possible to record spectra outside the Rowland condition with moderate loss in energy resolution for Bragg angles greater than  $80^\circ$  and a small sample size. The influence of the sample dimensions will be discussed below.

The instrumental resolution decreases considerably with smaller Bragg angles as in the case of Cr. Within the  $K\beta$  main line region (5920 eV-5960 eV) the calculated broadening still

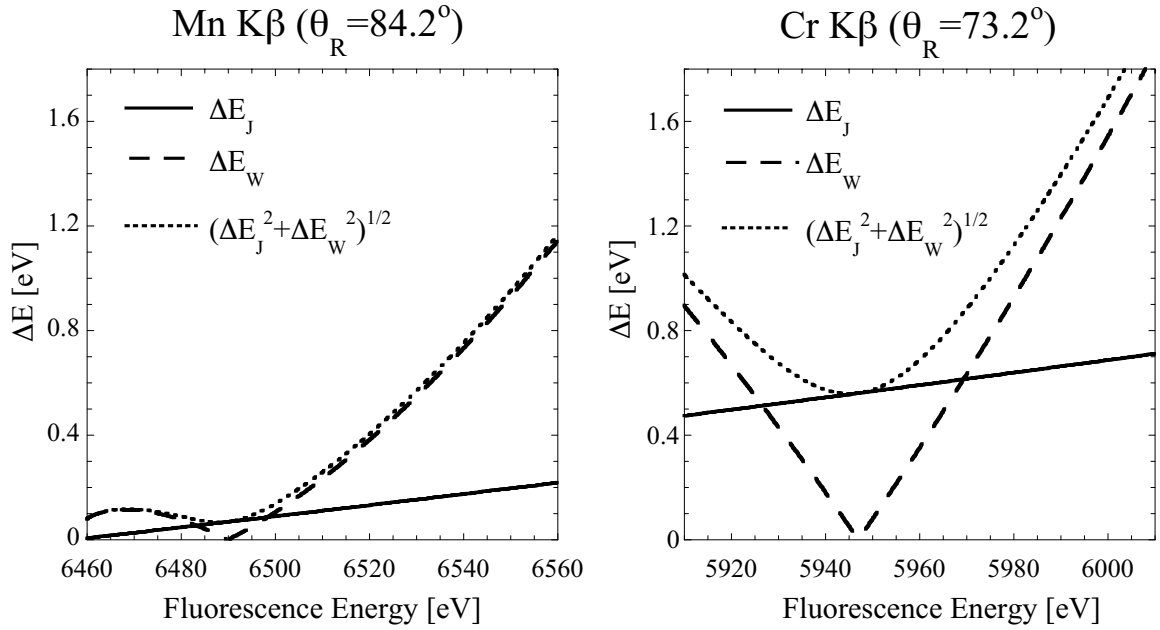


Figure 6: Geometrical contributions to the instrumental energy broadening for a point source. The energy ranges of the Mn and Cr K $\beta$  emission are shown.

lies below the  $1s$  lifetime broadening (1.08 eV for Cr). Depending on the intrinsic width of the K $\beta$  satellite lines a significant effect can be expected for the Cr high energy region.

### Energy Broadening due to Finite Sample Size

A finite sample size further contributes to the energy broadening. A sample with dimensions  $\delta x, \delta y$  and  $\delta z$  will extend in all three directions out of the Rowland circle. The resulting energy broadening will be largest for the component in  $z$ -direction because it is the energy dispersive direction of the spectrometer. This can be readily seen from equation 3 since  $\delta z$  and  $\Delta\theta$  have a linear relation for  $\theta$  close to  $90^\circ$ :  $\Delta\theta = \delta z/R$  and therefore:

$$\Delta E_z = E \frac{\delta z}{R} \cot \theta \quad (7)$$

Equation 7 can be used for a sample extending over  $\delta z$  as well as for a displacement of a point source by  $\delta z$ . Approximate equations for  $\delta x$  and  $\delta y$  can be given as well:

$$\Delta E_y = \frac{1}{8} E \left( \frac{\delta y}{R} \right)^2 \quad (8)$$

$$\Delta E_x = E \frac{\delta x}{R} \cot^2 \theta \quad (9)$$

$\Delta E_y$  extends out of the Rowland plane and can be neglected for a detector acceptance smaller than 15 mm in  $y$ -direction. The equation for  $\Delta E_x$  applies for a sample extending over  $\delta x$  as well as for a displacement of a point source in  $x$ -direction by  $\delta x$ .

## Energy Broadening in Multi-Crystal Spectrometer

The overall geometrical energy broadening can be given by [15]:

$$\Delta E_{geo} = \sqrt{(\Delta E_x + \Delta E_W)^2 + (\Delta E_y + \Delta E_S)^2 + (\Delta E_z + \Delta E_J)^2} \quad (10)$$

The contributions  $\Delta E_z$  and  $\Delta E_x$  are increased in a multi crystal array analyzer as will be shown below. Here, the Rowland circles for each crystal intersect in two points where the sample and the detector are positioned for the optimal energy  $E_R$ . All crystals are mounted on an optical table that can be scanned in Z-direction. (As mentioned before, I use lower case (xyz) to refer to the dimensions of each crystal and upper case (XYZ) to refer to the dimensions of the multi-crystal spectrometer). The arrangement is shown in Figure 7 for four crystals. Each crystal is mounted in a holder with three degrees of freedom. The crystal mount and the three motions are shown in Figure 8. The spectrometer components are aligned by first bringing source volume, *i.e.* synchrotron beam spot on the sample or radioactive source, and detector on a vertical line and then adjusting the crystals to the correct distance from this vertical line ( $R''$  in Figure 5). After the Bragg angle has been determined using optical tools, the crystals are adjusted to have a common focus on the detector. Equation 7 then holds for a height difference  $\delta Z$  between the centers of the crystals relative to each other. A different alignment procedure where the crystals are aligned to give a fluorescence line ( $K\alpha$  or  $K\beta$ ) at the exact same energy improves the energy resolution at the cost of a broader focus. A  $\theta/2\theta$  scan is performed in the synchrotron experiment where the source volume is stationary by moving all crystals together by the same distance  $\Delta Z$  and the detector by  $2\Delta Z$ . In the K capture experiment it is possible to use a position sensitive detector and simply scan the sample in Z-direction while keeping crystals and detector stationary.

Depending on the orientation and position of the sample relative to the different Rowland circles the broadening will be different for each crystal and the overall broadening is expected to be larger for several crystals than for one crystal. This can be understood by assuming a flat sample that extends only in y- and z-direction relative to the Rowland plane for one crystal.  $\Delta E_y$  is very small and the main contribution in this case comes from  $\Delta E_z$ . If one keeps the sample orientation constant and looks at a different crystal and its Rowland circle one obtains a contribution from  $\Delta E_x$  because relative to this Rowland circle the sample extends into x-direction, namely the projection of the sample area onto the new Rowland plane of the next crystal.  $\Delta E_x$  yields a larger broadening than  $\Delta E_y$  and the overall broadening will increase. I will calculate the energy broadening by using equation 10 assuming the worst case, *i.e.* for the crystal that yields the largest energy contribution.

The instrumental energy bandwidth can be determined experimentally using an incident beam with known energy bandwidth. One possibility would be to use the elastically scattered synchrotron beam if the monochromator energy bandwidth is known. However, the energy resolution of the monochromators at the beamlines that we visited was not well enough characterized to determine the energy bandwidth of the crystal spectrometer. Another possibility is to use a fluorescence line that only has one contribution, *i.e.* can be assigned to just one final state that is not split. It will be shown in Chapter 6.2 that the  $K\beta''$  or ‘cross-over’ peak at 6524.8 eV in the complex  $[\text{Rh}(\text{en})_3][\text{Mn}(\text{N})(\text{CN})_5]\cdot\text{H}_2\text{O}$  only has one contribution according to Kohn-Sham density functional calculations. The calculations do not include  $3d$  spin-orbit and  $(1s,3d)$  exchange interaction. However, both interactions are

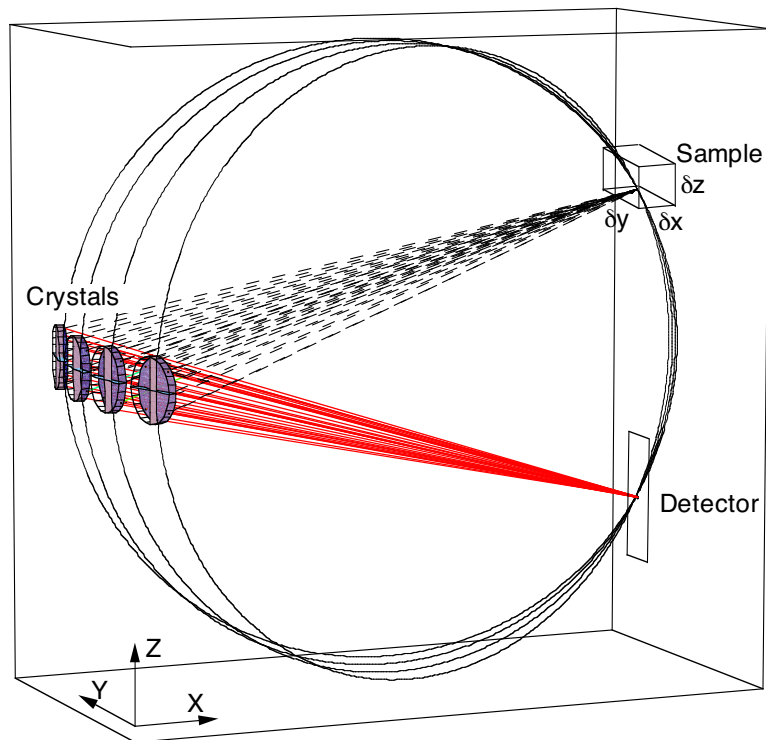


Figure 7: Crystal array spectrometer with four analyzer crystals. The Rowland circle is shown for each crystal. Sample and detector are centered in the intersection points of the four Rowland circles.

small ( $\approx 0.05$  eV) and can therefore be neglected for the rough estimate of the instrumental broadening attempted here. I will therefore use this transition to investigate the energy broadening in the following.

Spectra were taken (a) with two and (b) with eight crystals. The crystals are arranged asymmetrically as shown in Figure 9 and the spectrometer was optimized at the  $K\beta_{1,3}$  peak energy (see Table 1). Only crystals 7 and 8 were used in case (a). I used a Voigt profile, *i.e.* a convolution of a Gaussian with a Lorentzian line shape, to fit the cross-over peak in order to estimate the instrumental broadening. The experimental spectra with the fitted curves are shown in Figure 10. Since I do not know the final state lifetime I performed two fits with different Lorentzians. First, I used a Lorentzian of 1.16 eV FWHM for the  $1s$  lifetime neglecting the final state lifetime. For cases (a) and (b) the fit then yields a  $1.17 \pm 0.05$  eV and  $1.50 \pm 0.04$  eV FWHM Gaussian broadening, respectively. Using a 1.5 eV FWHM Lorentzian, *i.e.* including a 0.34 eV final state lifetime broadening, I obtain  $0.96 \pm 0.06$  eV and  $1.30 \pm 0.05$  eV. However, the standard deviation of the least square fit decreases with the broader Lorentzian and the first values are probably closer to the actual instrumental broadening.

Including eight instead of two crystals in the spectrometer results in an increase of the instrumental energy bandwidth by approximately 0.3 eV. For case (a) with two analyzer crystals equation 10 gives  $\Delta E_{geo} = 1.01$  eV for a  $\delta y = 1$  mm and  $\delta z = 0.5$  mm sample which was the approximate size of the single crystalline samples. With eight crystals only  $\Delta E_x$  and  $\Delta E_y$  become larger if I assume perfectly aligned crystals, *i.e.* all crystal centers have

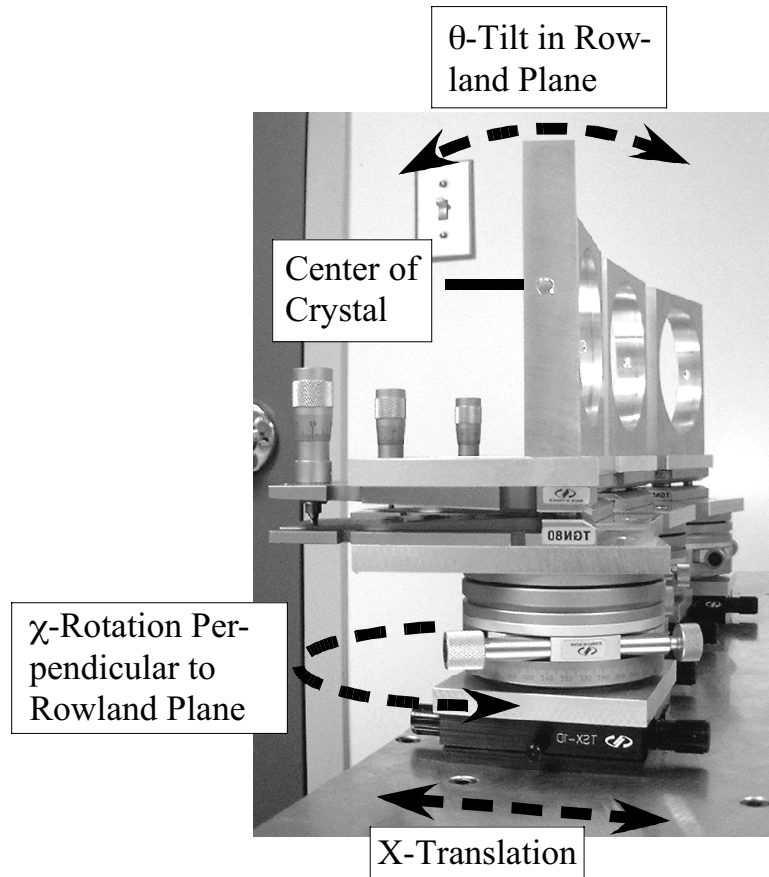


Figure 8: *Crystal mount with three degrees of freedom. The translation in X-direction is not in the Rowland plane of the crystal but in the X-direction of the multi-crystal array spectrometer as shown in Figure 7. The components shown here are not motorized and are used for the K capture experiment. The degrees of freedom are the same in the synchrotron set up but different components are utilized that can be motorized to allow for alignment from outside the experimental hutch.*

the exact same Z-position with a common focus on the detector, and the calculated overall geometrical broadening then is 1.07 eV, *i.e.* an increase of 0.06 eV. The full observed increase in instrumental broadening of 0.3 eV can be explained by assuming slightly different heights of the crystals ( $\delta Z=1$  mm  $\rightarrow \Delta E_{geo}=1.33$  eV) together with a non-perfect alignment of the Rowland circles relative to each other resulting in a displacement  $\delta x$  (I neglect  $\Delta E_y$ ). The initial alignment of the spectrometer for the run when the spectra shown in Figure 10 were taken was performed such that all crystals had a common focus on the detector. Different heights Z of the crystals then result in the described broadening. It was mentioned before that alternatively one can align the crystals to yield fluorescence lines at the exact same energies. Most likely, this will considerably reduce the additional broadening when more than one crystal is used. Currently we follow the second alignment procedure. In an improved setup one could include an individual z-adjustment for each crystal. In an iterative procedure align all crystals can then be aligned to have a common focus at the same Bragg angle.

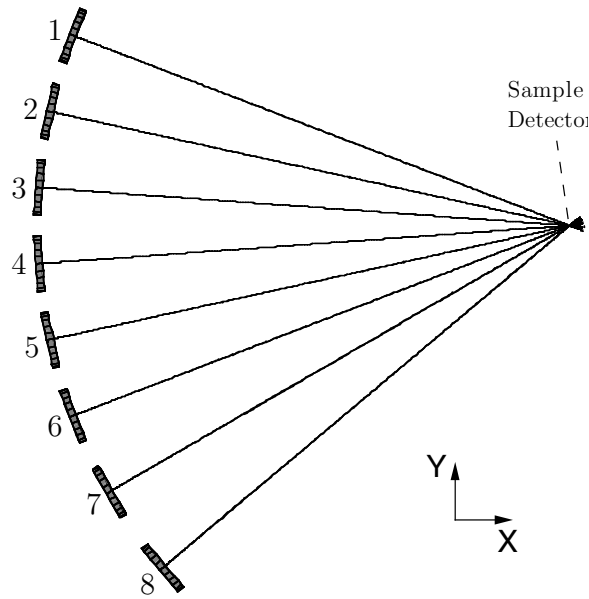


Figure 9: *Asymmetric arrangement of 8 crystals. In the synchrotron experiment the beam enters the spectrometer in positive Y-direction and the sample is tilted in the (X,Y) plane. The Z-axis points out of the drawing plane.*

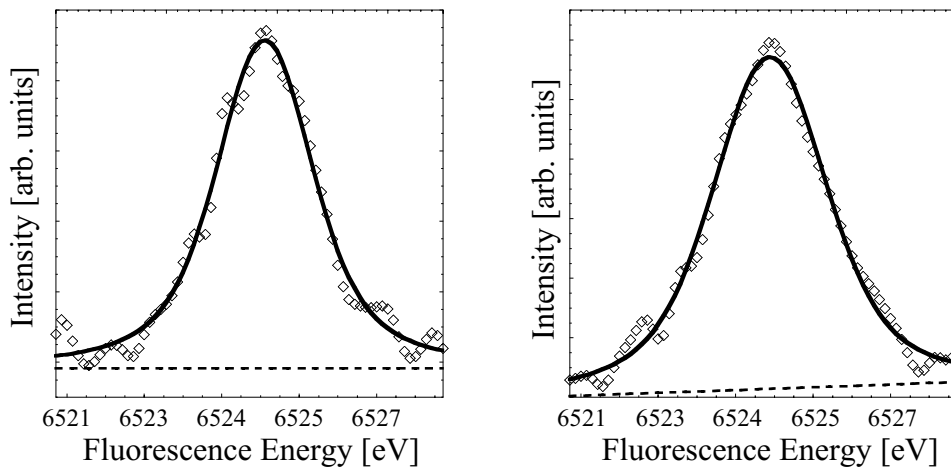


Figure 10: *The Mn  $K\beta''$  or cross-over peak in  $[Rh(en)_3][Mn(N)(CN)_5]\cdot H_2O$  with Voigt fits. The fits shown use a 1.16 eV Lorentzian. The spectrum on the left was taken with crystals 7 and 8 (see Figure 9) while the spectrum on the right was taken with eight crystals.*

### 2.1.3 Ray-Tracing Calculations

In order to estimate the focus size as well as the energy distribution on the detector I performed ray-tracing calculations using the *Optica* package in the program *Mathematica*. The calculations assume a perfect crystal and neglect dynamical lattice effects, *i.e.* solely determine the geometrical contribution. The crystals are aligned to have a common focus on the

detector center. No intensity distribution was determined and the energy broadening resulting from the ray-tracing calculations is the difference between the minimum and maximum energy determined from the Bragg angles which I will refer to as ‘total energy spread’. A direct comparison with the FWHM of a  $K\beta$  spectrum is thus not possible but the calculations give a good idea of the influence of the geometry on spot size and energy broadening.

Since the ray-tracing gives exact results for the geometrical energy broadening in a given set up it can be used to verify whether equation 10 is a good approximation to the functional dependence between sample position or size and energy broadening. For this I determined the ratio between the total energy spread given in the ray-tracing results and the calculated values from equation 10 for varying sample dimensions and positions. It is found that this ratio only varies by 2% for the Mn  $K\beta$  ( $\theta_R=84.2^\circ$ ) range confirming the equations for the different contributions to the geometrical broadening. For the Cr  $K\beta$  range the ratio varies by 10%. The Bragg angle here is  $73.2^\circ$  and therefore far from backscattering. The approximations that led to the equations for the instrumental broadening assumed  $\theta_R \approx 90^\circ$  and therefore become inaccurate but still give a good estimate for the energy broadening.

Figure 11 shows the ray-tracing results for the Mn  $K\beta$  scan range using 8 crystals arranged asymmetrically as shown in Figure 9. The ray-tracing was performed using eight cones of rays illuminating the outermost radius of each crystal with 8 rays per cone from 9 positions on the sample. The sample size is  $\delta Y=5$  mm and  $\delta Z=1$  mm. These were the dimensions for the K capture experiments. For the synchrotron experiments at SSRL (see below) the incident beam was collimated by a four-blade aperture to  $\delta X=2$  mm and  $\delta Z=1$  mm hitting the sample under  $65^\circ$  relative to the normal on the sample surface. This results in a slightly larger (by  $\approx 0.1$  eV) geometrical broadening compared to the K capture setup. However, the focus of the synchrotron beam yields a non-homogeneous, approximately Gaussian shaped intensity distribution on the sample which will slightly decrease the broadening compared to the K capture experiment where the intensity is uniformly distributed across the sample area. The overall instrumental broadening will therefore be similar in both experiments and due to the lifetime broadening the slightly different experimental conditions will not be observable in the spectra. The statements made in the following concerning the spectral and focal properties apply to the K capture as well as the synchrotron experiments.

The area of the contour plots in Figure 11 shows the focus in the (Y,Z) plane, *i.e.* the detector plane. The shading indicates the energy distribution. Sample center and detector are aligned in the focal spot of the 8 Rowland circles in (a) at 6490.0 eV fluorescence energy ( $\theta_R = 84.2^\circ$ ). The total focus size is  $\delta Y=7.1$  mm and  $\delta Z=1.8$  mm, *i.e.* the original sample size is only slightly broadened. The  $K\beta$  satellite region lies at about 6535 eV ( $\theta = 81.2^\circ$ ) which corresponds to a sample displacement of 45 mm in the positive z-direction relative to the position on the Rowland circle and accordingly a negative displacement for the detector. The ray-tracing results are shown in (b) for the same optimal spectrometer energy  $E_R$  of 6490.0 eV as in (a). The spot size hardly changes in Y-direction while it is broadened to 4.1 mm in Z-direction. The total energy spread is 3.0 eV and the energy shading indicates that the slope is mainly along the Z-direction. This suggests that defining a smaller acceptance area on the detector could increase the instrumental energy resolution. The drawback, of course, would be a loss in intensity.

Figure 11 (c) shows the image for the same sample size and Bragg angle (and therefore fluorescence energy) as in (b) but with the Rowland condition optimized at  $E_R=6535.0$  eV ( $\theta_R = 81.2^\circ$ ). The spot size is  $\delta Y=9.93$  mm and  $\delta Z=2.52$  mm, *i.e.* broader in Y but narrower

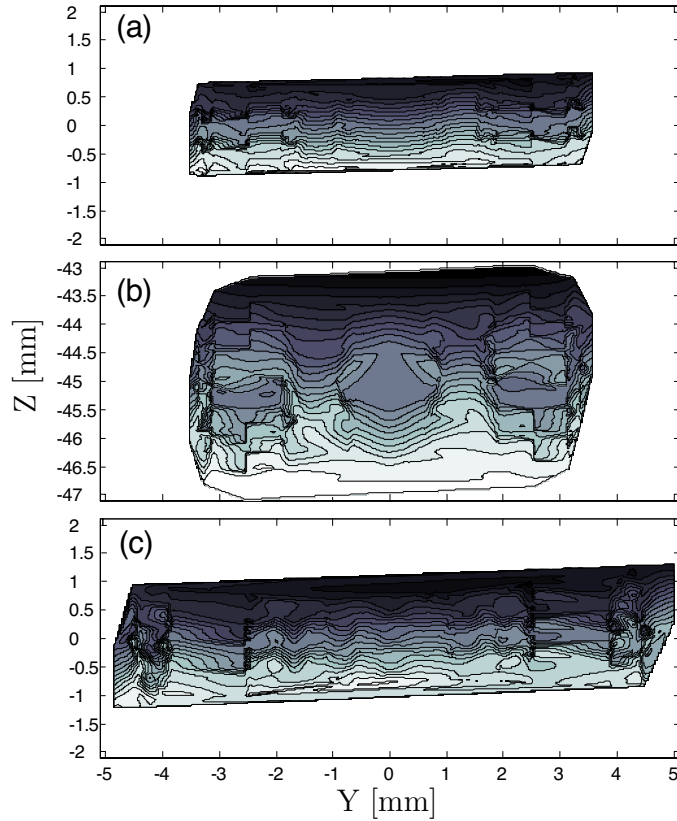


Figure 11: *Contour plots of the focus on the detector using 8 crystals in the Mn  $K\beta$  range obtained in the ray-tracing calculations. The shading indicates the energy distribution. Sample and detector are on the Rowland circle in (a) and the energy is 6490.0 eV ( $\theta_R = 84.2^\circ$ ). The plots (b) and (c) show the focus for 6535.0 eV fluorescence energy ( $\theta = 81.2^\circ$ ) with the spectrometer optimized (b) at 6490.0 eV ( $\theta_R = 84.2^\circ$ ) and (c) at 6535.0 eV ( $\theta_R = 81.2^\circ$ ). The axes give the dimensions relative to the focal point (the intersection points of the eight Rowland circles) in Y- and Z-direction.*

in Z direction compared to (b). With a  $\delta Z=3$  mm slit in front of the detector one therefore expects higher count rates in the  $K\beta$  satellite region when the spectrometer is optimized for 6535.0 eV (c) instead of 6490.0 eV as in (b). K capture measurements using a  $^{55}\text{Fe}_2\text{O}_3$  sample with the same dimensions as used in the ray-tracing calculations and a  $\delta Z=3$  mm and  $\delta Y=15$  mm slit in front of the detector for the cases (b) and (c) show an increase of the count rate from  $\approx 0.15$  counts/sec. to  $\approx 0.2$  counts/sec. in the  $K\beta_{2,5}$  peak (the linewidth does not change) corroborating the ray-tracing results. The total energy spread for case (c) is 2.2 eV, *i.e.* 0.8 eV smaller than for case (b). Equation 10 gives 1.8 eV and 1.3 eV for (b) and (c), respectively, and the ratio between the ray-tracing and the calculated results is 1.7 in both cases.

The experimental  $K\beta$  spectra presented in this thesis were taken with the spectrometer optimized at the  $K\beta_{1,3}$  peak energy for the entire  $K\beta$  energy range. Considering the results

for cases (b) and (c) it is necessary to justify why the spectrometer was not optimized for the  $K\beta$  satellite region. The main reason was to save time during the synchrotron experiments. A change of the set up to another optimal energy would cost an eight hour shift at the synchrotron. We therefore decided that the loss in energy resolution has to be accepted. As an example, the FWHM of the  $K\beta_{2,5}$  peak in  $\text{Fe}_2\text{O}_3$  is 4.6 eV and no difference in the experimental energy broadening could be observed with the spectrometer optimized at 6490.0 eV and at 6535.0 eV. For the K capture experiments it was one objective to compare the results with the synchrotron experiment in order to investigate whether there is a dependence on the mode of excitation. It was therefore necessary to create identical experimental conditions for the synchrotron as well as the K capture experiment and the experiment was never optimized for the  $K\beta$  satellite region except for the one study on  $^{55}\text{Fe}_2\text{O}_3$  mentioned above.

Table 1: *Calculated energy broadening using equation 10 for the fluorescence spectra presented in this work. All energies are given in eV and  $\theta_R$  is given in degrees. The energy for which the spectrometer was optimized is denoted  $E_R$ . The  $K\beta$  range is separated into main and satellite region (second rows). A sample size of  $\delta Y=5$  mm and  $\delta Z=1$ mm was assumed. The  $\text{Si}(6,2,0)$  crystals have half the diameter of the other crystals. The absolute error is given for a vertical positioning error of  $\delta Z = 1$  mm (not to be confused with the vertical sample size).*

	Number of Crystals	Bragg Reflection	$\theta_R$	$E_R$	Fluorescence Energy	$\Delta E_{geo}$	Absolute Error $\Delta E_z(\delta Z = 1.0 \text{ mm})$
Mn $K\alpha$	4	Ge(3,3,3)	75.0	5896	5896	2.2	1.8
Cr $K\beta$	4	Ge(3,3,3)	73.2	5947	5947 5985	2.5 3.8	2.0
Mn $K\beta$	8	Si(4,4,0)	84.2	6490	6490 6535	0.8 2.0	0.8
Fe $K\beta$	6	Ge(6,2,0)	79.1	7058	7058 7106	1.5 2.2	1.6
Ni $K\beta$	5	Si(5,5,1)	80.5	8265	8265 8325	1.8 3.5	1.6

We used a 3 x 15 mm<sup>2</sup> lead slit in front of the detector unless a position-sensitive detector was used (see below). The slit reduces the background in the synchrotron experiment. However, no absolute statement concerning the  $K\beta$  main line versus satellite line intensity ratio can be made because the focus exceeds the slit dimensions in the  $K\beta$  satellite region. Table 1

summarizes the broadenings and absolute energy errors calculated using equation 10 for all fluorescence spectra presented here.

## 2.2 Detectors

The synchrotron work and part of the K capture work were done using a liquid nitrogen cooled Ge detector. The manufacturer gives a best achievable FWHM of the  $^{55}\text{Fe}$   $K\alpha$  line of 149 eV [67]. The energy resolution of the Ge detector is used to improve the signal to background ratio by windowing out unwanted x-ray events. In the synchrotron experiment these are mainly due to scattered x-rays from the synchrotron beam hitting the sample. The K capture experiment is a low count rate experiment and it is desirable to window out all events due to radioactive traces in the material used in the experiment and cosmic rays. This background together with electronic noise sets the lower limit for the required radioactivity of the sample. With a 300 eV window set around 5947 eV and the detector shielded from the outside x-rays by lead I measured a dark count rate of  $8 \times 10^{-3}$  counts/seconds without any sample placed in the source volume of the spectrometer. No change of the dark count rate was observed with a 10 mCi  $^{55}\text{Fe}$  source placed in the source volume. The 6.5 and 6.0 keV radiation that is emitted following the radioactive decay can be fully blocked by thin layers of lead.  $^{54}\text{Mn}$  emits 834.8 keV  $\gamma$ -rays due to the decay of the nuclear excited state [90]. Even with 10 cm of lead between sample and detector the dark count rate increased by a factor of 2-5 with similar window settings when a 0.5 mCi  $^{54}\text{Mn}$  sample was placed in the source volume of the spectrometer. The high dark count rate is probably due to Compton scattering inside the sample and therefore x-rays whose energies lie within the selected energy window. The count rate in the  $K\beta_{1,3}$  peak of a 10 mCi  $^{55}\text{Fe}$  source was 10 counts/seconds using eight crystals. The radioactivities of the  $^{54}\text{Mn}$  and  $^{55}\text{Fe}$  samples were between 0.2 and 0.5 mCi (MnO) at the time when the spectra were taken. The respective approximate count rates were between 0.1 and 0.5 counts/seconds in the  $K\beta_{1,3}$  peak using four crystals. Due to bad signal to background ratio ( $\approx 15:1$  in the  $K\beta_{1,3}$  peak) resulting from frequent dark counts it was not possible to measure the  $K\beta$  satellite region of the  $^{54}\text{Mn}$  samples. All radioactive samples were prepared by Sandra Fiskum at Pacific North West National Laboratory (PNNL).

Part of the K capture work was performed using a two-dimensional gas proportional counter that was developed in the group of Graham Smith at Brookhaven National Laboratory [22, 120, 121]. The implementation of the detector in the K capture experiment is described in appendix A. The 10 cm \* 2 cm detector area is defined by two perpendicular arrangements of cathode wires. Parallel to one cathode plane is an anode plane. The electronic noise is minimized by the coincidence requirement for the two cathodes and the anode plane. The anode signal can be used to achieve a moderate energy resolution of 20%. The position resolution at  $90^\circ$  incident angle is  $\approx 0.2$  mm [120]. This value increases for incident angles smaller than  $90^\circ$ . However, no data was available for the position resolution at different incident angles. For angles smaller than  $80^\circ$  the degrading position resolution is expected to decrease the instrumental energy resolution. As an example,  $\delta Z = 0.2$  mm translates into 0.15 eV for the Mn  $K\beta_{1,3}$  line ( $\theta_R = 84.2^\circ$ ) and to 0.42 eV for the Cr  $K\beta_{1,3}$  line ( $\theta_R = 73.2^\circ$ ). If the position resolution of the position sensitive detector decreases to 0.3 mm for the small Bragg angle for Cr, the instrumental energy bandwidth is increased to 0.63 eV which is more than half of the  $1s$  lifetime broadening. The detector was operated with a research grade

80% Ar/20% CO<sub>2</sub> mixture. The x-ray conversion efficiency of Ar is about 20% for 6 keV photons (see reference [22] for details). The position sensitive detector was used to record the Mn K $\alpha$  spectra shown in Chapter 5.

Using a position sensitive detector it is possible to simply move the sample up and down for an energy scan while crystals and detector remain stationary. Figure 13 shows the contour plot of Mn K $\alpha$  lines emitted from a 10 mCi metallic <sup>55</sup>Fe source. The two line plots show the spectra resulting from an integration in Y (K $\alpha$  spectrum) and Z (horizontal focus size) direction.

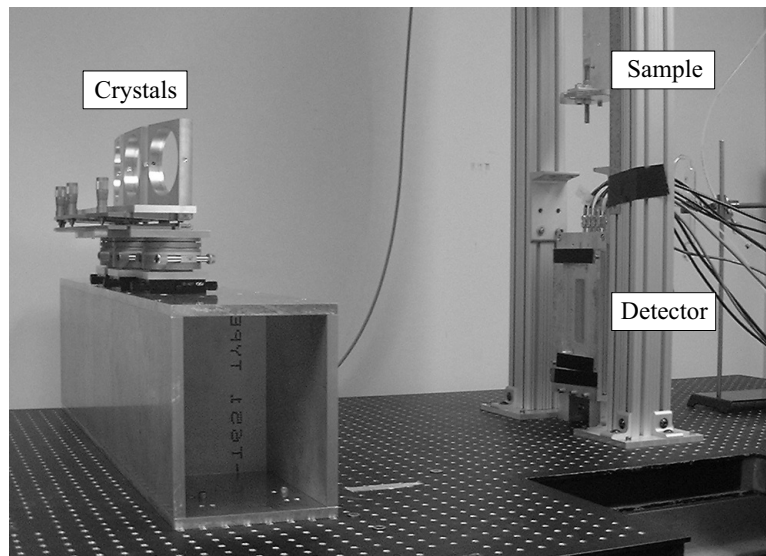


Figure 12: *Experimental set up for the K capture studies with the position sensitive detector and the sample mount that can be scanned vertically. During data acquisition a helium-filled bag encloses the entire beam path.*

The set up employing the two-dimensional detector offers an advantage over the Ge detector concerning the relative energy calibration. Since a change of the chemical environment can be observed in a shift of the fluorescence energy this is a crucial aspect in the experimental procedure. Using the two-dimensional detector the energy calibration is determined by the relative alignment between crystals and detector. Both are not changed once the spectrometer is calibrated. For a  $\theta/2\theta$  scan just the sample is moved vertically. The relative energy calibration therefore does not change. In the other set up that was optimized for the synchrotron experiment the crystals are moved together with the detector during scanning. To ensure constant relative energy calibration the different samples have to be placed at exactly the same positions. The error in this sample alignment translates into an error in the relative energy calibration as explained before. Figure 12 shows the experimental set up that was designed for the K capture work. A He-filled bag is inserted between sample/detector and crystals during data acquisition to reduce absorption in air. The bag is made out of 76  $\mu\text{m}$  thick plastic foil. Four layers of the plastic bag absorb approximately 10% at 6.5 keV.

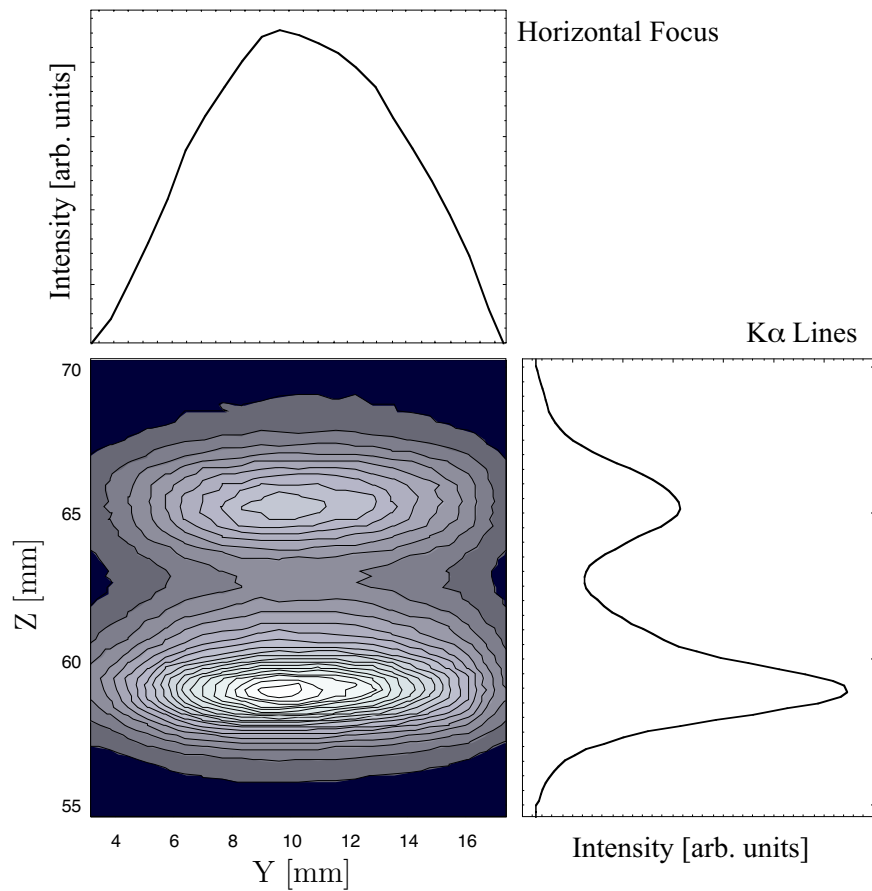


Figure 13: *Contour plot of the Mn  $K\alpha$  lines. The two-dimensional image was acquired using the position sensitive detector. The shading shows the intensity. The two line plots show the integrated intensities in the Y and Z direction. For details see Table 1.*

## 2.3 Experimental Set Up Using Synchrotron Radiation

The experiments using synchrotron radiation were performed at the Stanford Synchrotron Radiation Laboratory (SSRL) and the Advanced Photon Source (APS). The wiggler beam-line 10-2 at SSRL is equipped with a water-cooled Si(1,1,1) double crystal monochromator and a bent cylinder focussing mirror [123]. The experimental set up downstream of the focussing mirror is shown in Figure 14. The incident beam is monitored using a nitrogen or helium filled ion chamber in front of the spectrometer source volume. The total flux hitting the sample is on the order of  $10^{11}$  photons per second at 9 keV. A four-blade aperture slit upstream of the sample and the ion chamber defines the beam size on the sample. The beam intensity distribution on the sample is defined by a convolution of the slit size and

the beam intensity profile. Slight vertical movements of the synchrotron beam alters the energy calibration of the spectrometer. In order to maintain the position calibration between the beam spot on the sample and the center of the crystals, the entire experimental set up consisting of the crystals, the detector, the sample stage and the aperture slit with the ion chamber were mounted on an optical table that could be moved vertically (Figure 14). Before each scan a vertical optimization using the optical table was performed such that the ion chamber detected maximum beam intensity. Since the position of the center of the aperture slit is fixed relative to the center of the crystals, this procedure ensures a constant energy calibration of the spectrometer.

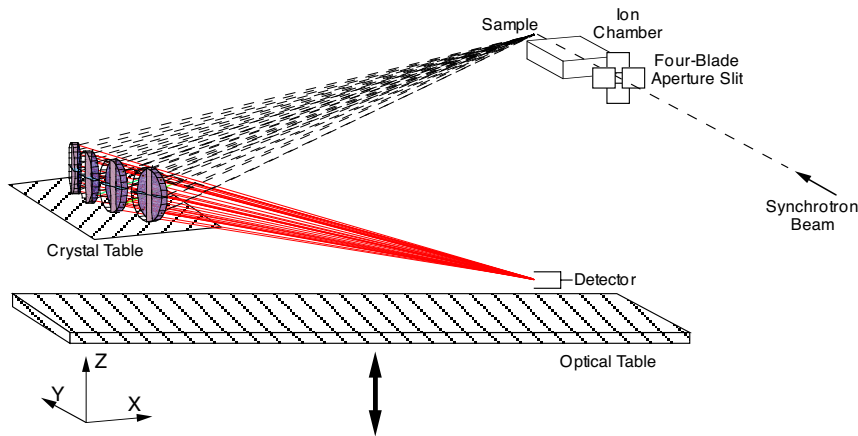


Figure 14: *Experimental set up at a synchrotron facility. At SSRL, all components shown are mounted on an optical table that can be adjusted vertically relative to the incident x-ray beam. At the APS, the vertical beam position can be adjusted relative to the experimental setup and the additional vertical motion using the optical table is not necessary.*

The BioCAT undulator beamline 18ID at the APS employs a liquid nitrogen cooled double crystal Si(1,1,1) monochromator where the second crystal provides sagittal focussing. An elliptically bent mirror is used for harmonic suppression and meridial focussing [28]. The beam can be focussed below 0.1 mm \* 0.1 mm, however, for the spectra shown in this thesis a focus of 0.5 mm vertical and 1 mm horizontal FWHM was used. The consequences on the instrumental broadening of the fluorescence spectrometer due to the smaller source size (Table 1 is for 1 mm \* 5 mm source size) are discussed when the spectra taken at the APS are shown. Using the fundamental of the undulator radiation the total flux was on the order of  $10^{13}$  photons per second at 9 keV as measured in the ion chamber. The beamline provides a beam position monitor and a feedback system to lock the absolute beam position. Vertical adjustment of the spectrometer to maintain the energy calibration was therefore not necessary.

A considerable improvement concerning the scanning procedure was achieved in collaboration with the BioCAT beamline support. We can now perform ‘continuous’ scans instead of step scans. While in a step scan crystals and detector are driven to a  $\theta/2\theta$  position and then the counts are acquired, driving and data acquisition are performed simultaneously in a

continuous scan. The detector is moved with twice the velocity of the crystals while the count rate on the detector is acquired ‘on the fly’. For a count time of 0.5 seconds per data point the continuous scan mode reduces the dead time per scan up to a factor of six.

In all experiments the incident energy was chosen well above the corresponding K-edge energy in order to avoid post-collision (PCI) effects [65]. Sample integrity was ensured by repeatedly measuring a fluorescence line and checking for changes in the spectral features. If radiation damage was observed, particularly in the protein samples, different positions on the sample were chosen and the duration of illumination on each sample spot was kept below the limit where changes due to radiation damage occurred in the spectra. For this, the sample is mounted on a sample stage that can be moved in Z-direction as well as parallel to the sample surface in the XY-plane. With respect to sample radiation damage it is mentioned that at SSRL as well as APS the option exists to insert Al filters to reduce the incident flux. Furthermore, a beam shutter that blocks the synchrotron beam can be inserted when no data are acquired during motor motions. Filters are used for radiation sensitive, concentrated model compounds. Furthermore, the incident beam is attenuated in order to minimize saturation of the detector electronics. We keep the total count rate below  $\approx 30000$  counts/seconds with  $0.25 \mu\text{s}$  shaping time. All photoionization spectra shown in this work have  $K\beta_{1,3}$  peak count rates of 20000-30000 counts/seconds.

## 2.4 Data Evaluation and Error Analysis

The raw experimental spectra recorded at the synchrotrons were corrected for variations in the incoming photon flux as measured in the nitrogen or helium filled ion chamber. In case of the K capture experiments, no correction for the decrease in intensity due to the lifetime of the isotope was necessary because the time per scan ( $< 12$  hrs.) was much shorter than the lifetime of the isotope (decrease of radioactivity due to lifetime less than  $1/500$  over scan range). A constant background was subtracted from all K capture but not from the photoionization spectra. For most  $K\beta$  satellite spectra that are shown the tail of the  $K\beta_{1,3}$  line was subtracted. The statistical errors taking background subtraction into account are shown for the spectra unless the line or symbol used in the graphs is approximately the size of or smaller than the error bar.

Experimental errors can occur for the measured intensities as well as for the energy scale. In case of the synchrotron experiment, variations in the purity of the ion chamber gas or voltage instabilities between the high-voltage plates can cause errors in the measured flux intensity. These errors can be minimized by averaging over several scans. The germanium detector is moved across the surface of the He-filled plastic bag and inhomogeneities in the material can cause systematic variations in the intensities. However, these variations are expected to be less than 1% and thus will not influence the analysis of the spectra as performed in this thesis. The counting efficiency of the Ge detector or the gas proportional counter does not vary over time to my knowledge. The spectra recorded with the two-dimensional gas proportional counter were corrected for the radiation response across the detector surface.

Errors for the absolute and relative energy calibration due to the vertical synchrotron and sample positioning were addressed before. In order to ensure that no drift occurred due to hardware problems (mainly step losses in the stepper motors) the  $K\beta$  emission from the same sample was measured repeatedly over the course of the experiments. In case of the

K capture experiment the emission from the same sample was recorded before and after a series of samples. No hardware problems were detected for the spectra shown in this work. Another source of error that was not addressed yet is the measured distance  $R''$  between the center of the crystals and the imaginary vertical line connecting the source volume and the detector surface (see Figure 5). This value enters the formula to calculate the energy from the height  $z$  defined as half the distance between sample and detector:

$$E[\text{eV}] = C \frac{1}{\sin(\arctan(\frac{R''}{z}))} = C \frac{z \sqrt{1 + (\frac{R''}{z})^2}}{R}, \quad C = \frac{12398.52}{2 \frac{a[\text{\AA}]}{\sqrt{h^2+k^2+l^2}}} \quad (11)$$

where  $a$  is the lattice constant ( $a_{Si}=5.4309 \text{ \AA}$ ,  $a_{Ge}=5.6574 \text{ \AA}$ ) and  $h,k,l$  are the Miller indices of the Bragg plane. A possible error in  $a$  is neglected. A deviation  $\Delta R''$  from the real value will result in an error for the energy that varies with the height  $z$  as can be seen from the first derivative with respect to  $R''$ :

$$\Delta E_{R''} = C \frac{z}{R''^2 \sqrt{1 + (\frac{R''}{z})^2}} \Delta R'' \quad (12)$$

As a consequence, the measured differences in energy between spectral features are connected with an error. A plot of  $\Delta E_{R''}$  is shown in Figure 15 for the  $z$ -ranges of the Mn and Cr  $K\beta$  spectra. The absolute error is considerably larger for Cr, however, the change of the error across the range of  $z$  is approximately 0.2 eV for both cases assuming  $\Delta R''=1 \text{ mm}$ . This is the error we have to keep in mind when analyzing measured energy splittings.

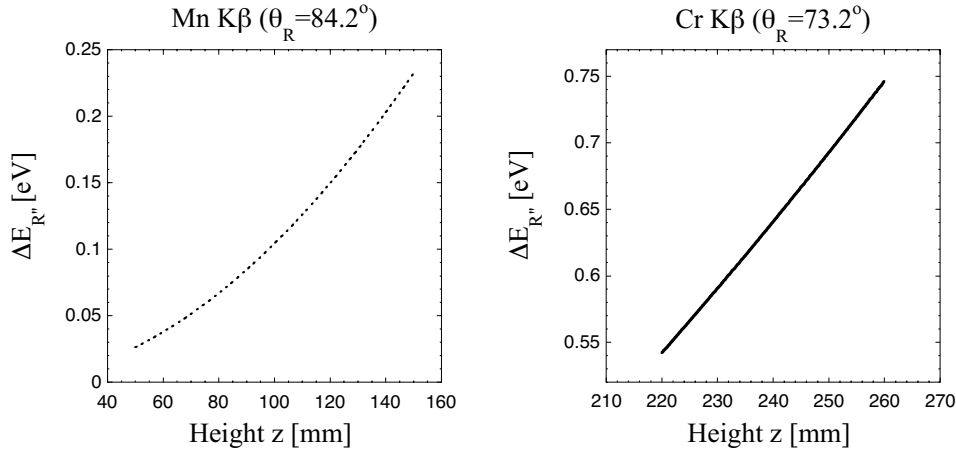


Figure 15: Error  $\Delta E_{R''}$  versus height  $z$  given as half the distance between sample and detector assuming  $\Delta R''=1 \text{ mm}$ . The  $z$ -ranges for the Mn and Cr  $K\beta$  lines are shown.

### 3 Theory

The study of the electronic structure in molecules and solids requires the interplay between theory and experiment. Two theoretical approaches are widely used to model the electronic structure of transition metals in a ligand environment: Ligand field multiplet theory and density functional theory in the formalism developed by Kohn and Sham [64, 78]. They will be outlined in this Chapter and the differences between the two models will be described. Both approaches, as they are described and applied in this work, do not explicitly include band structures that are formed due to the translational symmetry in an extended lattice. (The charge transfer model has the option to include a ligand band which is not used here). This assumption can be justified for core-to-core transitions, first, because the band formation is very weak for core orbitals in transition metals [7, 5]. Inner shell or core orbitals have mainly atomic character and are localized around the nucleus. Hence, the interaction with core orbitals of adjacent atoms that are energetically close is very weak. A second argument for the neglect of band formation is the fact that the valence electrons only indirectly influence core hole spectra via the direct electron-electron Coulomb and the exchange interaction. The width of the valence band does not directly show in the spectra. Delocalization of the valence electrons due to band formation weakens the Coulomb interaction and can be accounted for empirically by reducing the Coulomb interaction (*e.g.* scaling of Slater integrals). Care has to be taken when valence electrons are directly involved in the radiative transition as it is the case in the  $K\beta$  satellite lines. Only  $K\beta$  satellite spectra will be treated theoretically in this work for molecular complexes where either no translational symmetry applies or where the unit cell is big enough to neglect band formation [7].

Focussing on the local environment of the metal atom or ion, I will start as general as possible in order to outline the approximations made in the two models. First, one has to decide whether relativistic effects need to be included when writing down the Hamiltonian of an electronic system. A common approach is to add correction terms to the non-relativistic Schrödinger equation that account for relativistic effects instead of solving the Dirac equation for the system [26]. The correction term usually depends on the transition that is observed in the experiment and the information one aims to extract from the spectra. A full relativistic model is necessary for exact calculations of binding energies [26]. The chemical dependence of the K fluorescence will be studied by analyzing relative shifts of fluorescence energies as well as the spectral shape that is mainly determined by the electron-electron Coulomb and spin-orbit interactions. We are not interested in determining absolute values for binding energies. The Darwin term as well as relativistic corrections to the kinetic energy can therefore be neglected and only the spin-orbit correction term is added to the Schrödinger equation. The electron spin furthermore enters the theory in the form of spin-orbitals.

In a complete, though non-relativistic, theoretical description of the electronic structure in molecules and solids the Coulomb interaction of all electrons and nuclei have to be included in the Hamiltonian of the system besides the kinetic energies of the electrons and nuclei.

$$H = -\frac{1}{2} \sum_{I=1}^{N_Z} \frac{\hbar^2}{M_I} \nabla_{R_I}^2 - \frac{1}{2} \sum_{j=1}^{N_{e^-}} \frac{\hbar^2}{m} \nabla_{r_j}^2$$

$$- \sum_{I,j=1}^{N_Z, N_e} \frac{Z_I e}{(4\pi\epsilon_0)R_{Ij}} + \sum_{i<j=1}^{N_e} \frac{e^2}{(4\pi\epsilon_0)r_{ij}} + \sum_{I<J=1}^{N_Z} \frac{Z_I Z_J}{(4\pi\epsilon_0)R_{IJ}}$$

Since the Schrödinger equation using this Hamiltonian cannot be solved, neither analytically nor numerically, the problem has to be simplified. The nuclear and electronic motion are separated in the Born-Oppenheimer approximation [26]. We will assume the nuclei to be fixed at their positions since we are not concerned with vibrational levels and focus on the electronic Hamiltonian. Using atomic units, the electronic Hamiltonian to be solved then is:

$$H = -\frac{1}{2} \sum_{j=1}^{N_e} \nabla_{r_j}^2 - \sum_{I,j=1}^{N_Z, N_e} \frac{Z_I}{r_{Ij}} + \sum_{i<j=1}^{N_e} \frac{1}{r_{ij}} + \sum_{I<J=1}^{N_Z} \frac{Z_I Z_J}{R_{IJ}} \quad (13)$$

Ligand field multiplet theory tackles the problem by starting with the atom and then including symmetry and hybridization effects on the atomic orbitals. Following the arguments given above this approach is most suitable for core hole spectroscopy. Kohn-Sham density functional theory attempts to solve the poly-nuclear Hamiltonian for the electron density. It aims to describe ground state properties of molecules such as spin states and magnetic moments. However, the results can be used, as well, to understand core hole spectra. The two models are outlined in the following. Upper case N will be used to denote the total number of electrons considered in the Hamiltonian and lower case n to denote the number of valence electrons on the metal ion.

### 3.1 The Ligand Field Multiplet Model

The ligand field multiplet theory attempts to model core-hole spectra. The basis of the calculations is atomic multiplet theory. The local geometry is accounted for by branching from the spherical symmetry of the free ion to the symmetry of the metal center with the ligands. Hybridization of the valence orbitals is treated in a ligand-to-metal charge transfer scheme. The theory is semiempirical since input parameters are necessary for the description of an N-electron atom in a ligand environment. The parameters in a calculation that includes one ligand-to-metal charge transfer configuration are the ligand field splitting(s), the ligand-metal hopping terms, the core-hole-d-electron Coulomb potential and the charge transfer energy. The different steps of the calculations are described in detail in the following. A Mn n=5 system, i.e. five valence electrons, will serve as example to illustrate the computational steps. All ligand field multiplet calculations shown in this work, except Figure 48, were performed by the author of this thesis.

#### 3.1.1 N-Electron Atom

##### Self-Consistent Field Method

The theory starts with the description of an N-electron atom:

$$H = \sum_{i=1}^N \left( -\frac{1}{2} \nabla_{r_i}^2 - \frac{Z}{r_i} \right) + \sum_{i<j=1}^N \frac{1}{r_{ij}} \quad (14)$$

where atomic units are used. The electron spin is included by using spin-orbitals. The ansatz  $\Phi$  to solve the Schrödinger equation with the Hamiltonian 14 is written as a product of one-electron wavefunctions and the Pauli exclusion principle is satisfied by describing  $\Phi$  as a Slater determinant. The Schrödinger equation is then solved in the self-consistent field (SCF) approximation as developed by Hartree and Fock [36, 26]. The Hartree-Fock method is an independent particle model and the non-relativistic Hamiltonian for the one-electron wavefunction  $\phi_\mu(\vec{r}_i)$  is written as

$$h_i = \sum_{i=1}^N \left( -\frac{1}{2} \nabla_{r_i}^2 + V_{HF}(r_i) \right) \quad (15)$$

and the total Hartree-Fock Hamilton operator is:

$$H_{HF} = \sum_i h_i \quad (16)$$

$V_{HF}$  is the Hartree-Fock potential. It contains the electron-nucleus attraction as well as the direct and exchange potentials:

$$V_{HF} = -\frac{Z}{r_i} + \sum_{\mu} V_{\mu}^d(\vec{r}_i) - \sum_{\mu} V_{\mu}^{ex}(q_i) \quad (17)$$

where  $q_i$  includes the spin-coordinate besides the spatial coordinates  $\vec{r}_i$ . The index  $\mu$  includes all quantum numbers describing the orbital and the sum extends over all N occupied one-electron spin-orbitals.  $V_{\mu}^{ex}$  and  $V_{\mu}^d$  describe the electron-electron interaction and are therefore two-electron operators defined by the operations on an orbital  $\phi_\lambda$ :

$$V_{\mu}^d(\vec{r}_i) \phi_\lambda(\vec{r}_i) = \left[ \int \phi_{\mu}^*(\vec{r}_j) \frac{1}{r_{ij}} \phi_{\mu}(\vec{r}_j) d\vec{r}_j \right] \phi_\lambda(\vec{r}_i) \quad (18)$$

$$V_{\mu}^{ex}(q_i) \phi_\lambda(q_i) = \left[ \int \phi_{\mu}^*(q_j) \frac{1}{r_{ij}} \phi_\lambda(q_j) dq_j \right] \phi_\mu(q_i) \quad (19)$$

The symbol  $\int q_j$  implies an integration over the spatial coordinate  $\vec{r}_j$  and a summation over the spin-coordinate of electron j.  $V^{ex}$  arises from the electron spin and the Pauli exclusion principle and the exchange integral assumes finite values only for electrons with parallel spins. In atomic physics it is said that the Hartree-Fock method partly includes electron correlation because of the exchange operator [26, 36]. However, other theoretical models such as Kohn-Sham density functional theory distinguish between exchange and correlation potentials [77]. A definition for electron correlation that excludes exchange interaction will be given below when the corrections to the self-consistent field method are discussed.

$V_{HF}$  is a central field potential for closed shells. This is no longer true for open shells. It is however possible to obtain an approximate Hartree-Fock central field potential by averaging over spin directions and angles [26]. The one-electron solutions of equation 15 then have spherical symmetry and the familiar quantum numbers n,l and m can be used to describe the orbitals. This works well for free atoms and ions even though in some cases deviations from spherical symmetry have to be taken into account in order to explain satellite structures observed in experimental spectra. It is obvious that considerable modifications are necessary when the N-electron system is introduced in a non-spherical environment as will be described in Section 3.1.2.

## Corrections to the SCF Method

Two corrections to the central field approximation will be considered: spin-orbit interaction and electron correlation. The electron correlation effects can be defined as the difference between the exact energy of the Hamiltonian given in equation 14 and the solution in the Hartree-Fock limit, ignoring that  $V^{ex}$  already includes some electron correlation [26]. They are due to the part of the Coulomb interaction that cannot be described as a central potential and to the fact that the Hartree-Fock method is a variational method, *i.e.* the energy eigenvalues give an upper limit to the exact solutions of the Schrödinger equation using the Hamiltonian 14. Furthermore, the  $N$  occupied one-electron wavefunctions do not form a complete set of basis functions [7, 36]. A complete set would be formed of an infinite number of orbitals of which the lowest  $N$  orbitals are occupied in the ground state.

One way to account for electron correlation is to use a linear combination of Slater determinants made up of one-electron wavefunctions that are solutions of the central field approximation. This approach is usually referred to as configuration interaction (CI). CI will be very important throughout this thesis and therefore shall be outlined using two configurations in the following within the formalism used in references [36] and [8].

The wavefunctions  $\phi_i$  are solutions of the Hamiltonian  $h_i$ . They are combined in the Slater determinant wavefunction  $\Phi_1$  to describe the  $N$ -electron system. In order to improve this description of the  $N$ -electron system we consider a second Slater determinant wavefunction  $\Phi_2$  where two electrons occupy other quantum states than in  $\Phi_1$ . The new wavefunction to describe the  $N$ -electron system shall be denoted  $\Psi$ :

$$\Psi = \begin{pmatrix} \Phi_1 \\ \Phi_2 \end{pmatrix} \quad (20)$$

The energy matrix for the Schrödinger equation  $H\Psi = E\Psi$  then reads:

$$H_{CI} = \begin{pmatrix} H_{11} & H_{12} \\ H_{21} & H_{22} \end{pmatrix}, \quad H_{ij} = \langle \Phi_i | H | \Phi_j \rangle \quad (21)$$

The  $H_{ij}$  are matrices because the  $\Phi_i$  are Slater determinants.  $H_{CI}$  is symmetric and therefore  $H_{12} = H_{21}^T$ . The  $H_{ii}$  are diagonal because the  $\phi_i$  are solutions of the Schrödinger equation for single configuration wavefunctions using  $H$ . Diagonalization of the matrix gives the two new energy eigenvalues of the system. The two eigenfunctions belonging to the eigenvalues are the new wavefunctions that describe the system. They are linear combinations of the SCF wavefunctions  $\Phi_i$ . Any additional SCF configuration that is included results in an additional CI wavefunction.

The non-diagonal elements of the Hamiltonian matrix and the energy difference  $E_{11}-E_{22}$  determine the strength of the mixing between the two configurations. Generally, strong CI can be expected when the magnitude of the non-diagonal matrix elements is large compared with the energy difference between the two SCF solutions [36]. In order to obtain non-zero mixing, the wavefunctions must not differ in more than two orbitals because the Hamiltonian involves only one- and two-electron operators. If only two configurations are included, as in the example above, only states  $\Phi_2$  where two electrons change their orbitals (doubly excited determinants) mix with the lowest energy HF wavefunction  $\Phi_1$  because all non-diagonal Hamiltonian matrix elements between  $\Phi_1$  and singly excited states vanish (Brillouin's theorem) [7]. When CI is used in the ligand-to-metal charge transfer scheme only one electron

changes its orbital and no mixing between the two configurations would occur if the atomic Hamiltonian were used. In order to mix the two configurations, an additional term has to be added to the Hamiltonian to describe the ligand to metal electron hopping (see Chapter 3.1.3). This is equivalent to using empirical parameters for the non-diagonal matrix elements in equation 21. Furthermore, for the two configurations to mix they need to be of equal parity because the Hamilton operator has even parity. As a consequence, both states can be reached from the ground state via the dipole operator when the system interacts with a photon.

In general, CI effects can be divided into weak and strong CI depending on the overlap between the interacting electrons [137]. The former can be approximated by appropriate scaling of the direct and exchange Slater integrals while the latter requires explicit inclusion of the strongly interacting configurations. The foregoing outline of CI accounts for strong configuration interaction. Strong CI can have considerable consequences for calculated spectra. In a dipole allowed transition to an orbital  $\Phi_1$  that strongly couples to another orbital  $\Phi_2$  it is possible to obtain two lines in the spectrum instead of one line without CI. Furthermore, weak and strong CI can cause a shift of the calculated transition energies. The two different ways to deal with CI have the important difference that scaling of the Slater integrals does not yield additional peaks in the calculated spectrum in contrast to a full inclusion of additional configurations like in equation 21.

It shall be noted that this general definition of ‘configuration interaction’ includes mixing of configurations that have identical principal and orbital quantum numbers but different angular momenta. This kind of configuration interaction will be referred to as ‘symmetry mixing’. An example will be given below.

In the independent particle model the relativistic correction for the spin-orbit interaction can be written as [26]:

$$H_{LS} = \sum_i \xi(r_i) \vec{l}_i \cdot \vec{s}_i \quad (22)$$

$$\xi(r_i) = \frac{1}{2m^2c^2} \frac{1}{r_i} \frac{dV(r_i)}{dr_i} \quad (23)$$

i.e. the correction is calculated for every one-electron wavefunction in a central potential  $V(r_i)$ . The total angular momentum

$$\vec{J} = \sum_i^N (\vec{l}_i + \vec{s}_i) \quad (24)$$

is a constant of motion and therefore, together with the parity, gives a good quantum number to describe the system (neglecting hyperfine interaction). The magnitude of the spin-orbit correction strongly depends on the orbital that is occupied by the electron. Examples are given below in Table 2.

Electron correlation as defined at the beginning of this Section and spin-orbit interaction can be treated using perturbation theory and, depending on their relative strengths, the N-electron system can be described in the LS or jj coupling scheme (apart from other coupling schemes) [26, 36]. To a good approximation,  $3d$  transition metal configurations with open  $3d$  and  $3p$  shells can be described using LS coupling [94]. The ligand field multiplet calculations

presented in this thesis describe the states using the total angular momentum and neither coupling scheme is applied.

### Theory of $K\beta$ Emission in Atoms

Throughout this thesis the interaction of an electron system with a photon will be treated in the dipole approximation. Using the selection rules in LS coupling it is possible to discuss a  $K\beta$  spectrum in a  $3d^5\ ^6S$  configuration qualitatively. The  $1s$  photoionization  $1s^2 3d^5 \rightarrow 1s 3d^5 \epsilon p$  yields  $^5,7S$  intermediate states. I assume the  $K\beta$  decay to be a two-step process and no interaction between the intermediate states is considered. It is helpful for the analysis of the spectra to separate the decays from the  $^7S$  and  $^5S$  intermediate states. The dipole selection rules yield  $^5P$  and  $^7P$  as the final state LS terms. The  $^7P$  symmetry can only be formed by a  $^6S\ 3d$  parent term while the  $^5P$  term can be formed by  $^6S$ ,  $^4P$  and  $^4D$  parent terms and therefore symmetry mixing might be important. The  $^7S$  intermediate term can only decay into the  $^7P$  final state while the  $^5S$  intermediate term decays into all interacting  $^5P$  final states (Figure 16).

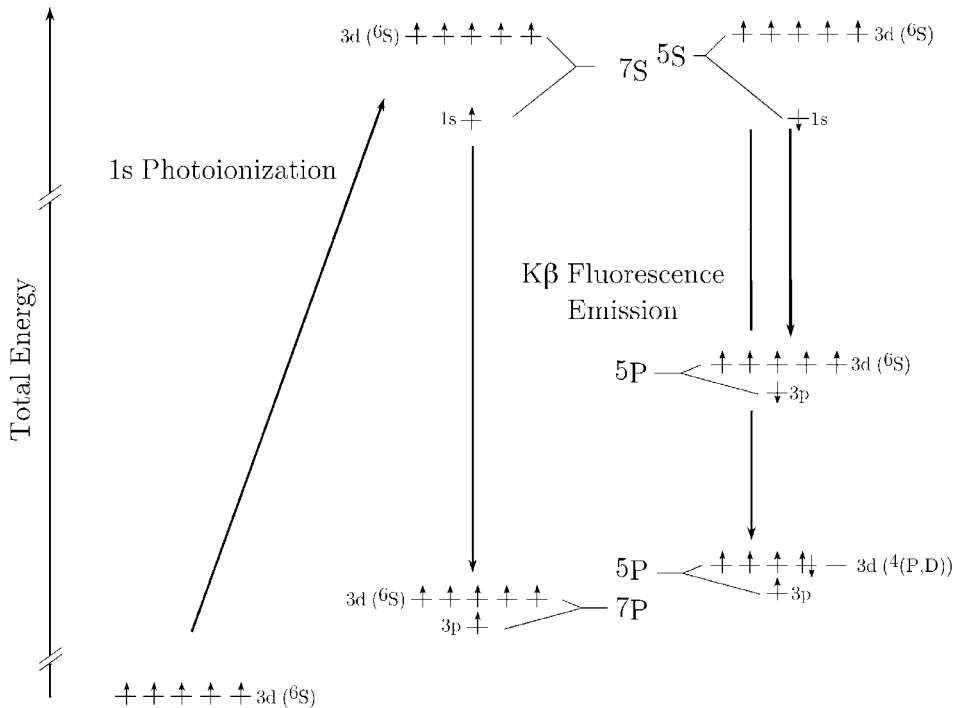


Figure 16: *Term scheme for  $K\beta$  emission in  $Mn\ 3d^5$  based on atomic multiplet theory. Only one  $3p^5 3d^5\ (^4L)\ ^5P$  term is included and only the unpaired  $3p$  electron is shown for clarity.*

The non-diagonal matrix elements responsible for symmetry mixing in the core hole excited state depend on the two-electron Coulomb integrals for the non-equivalent electrons. These integrals are large for  $(3p, 3d)$  interaction but small for  $(1s, 3d)$  interaction (see Table 5 in Chapter 5). The described configuration mixing can be viewed as a spin flip in the  $3d$  shell due to the interaction of the  $3d$  shell with a core hole. This spin flip is much less likely when a  $1s$  hole is created and therefore symmetry mixing is expected to be very small in the  $K\beta$  intermediate state. The scheme in Figure 16 shows that two electrons have to change in order to make the symmetry mixing non-zero in the  $3p$  to  $1s$   $K\beta$  decay. The spin flip final

state ( $(^4P,D) ^5P$ ) can only be reached from the  $^5S$  state when the spin of the ‘hole’ ( $1s$  or  $3p$ ) changes together with one spin in the  $3d$  shell. The same process from the  $^7S$  intermediate state would lead to a triplet final state which cannot be reached within the dipole selection rules in LS-coupling.

The ordering of the different final states can be understood considering the electron spins (Figure 16). The Slater exchange integrals are zero for electrons with opposite spin orientations and positive otherwise. Furthermore, they enter the equations to calculate the average energy of a configuration with negative coefficients [36]. Configurations with parallel spins are therefore lower in energy than configurations with paired spins. The fluorescence decay gives the energy difference between intermediate and final states and therefore gives higher energies for terms with parallel spins. The  $(^6S)^7P$  and  $(^4(P,D))^5P$  terms are split by the  $(3d,3d)$  direct interaction and the  $(^6S)^5P$  term is at lowest fluorescence energies due the  $(3p,3d)$  exchange interaction. This term is sometimes referred to as the ‘low-spin component’ of the  $K\beta$  or  $3p$  XPS final states [137].

The different effects that shape a  $K\beta$  spectrum are illustrated in Figure 17. The center of gravity energy, i.e. the sum of the energies of all final states weighed by their intensities, for the final states is arbitrarily set to 50 eV in all calculations shown in this Chapter. The energy axis is denoted ‘Relative Final State Binding Energy’ and is plotted from left to right in descending order. This facilitates comparison with Figure 16, where the ‘total energy’ axis follows the magnitude of the binding energy, as well as comparison with the experimental spectra in the following Chapters where higher fluorescence energy corresponds to lower final state binding energy as can be seen in Figure 16. In Figure 17 (a) all Slater integrals and spin-orbit interactions have been set to zero. All other interactions that further will be included do not change the center of gravity energy in the spectra. In (b) the  $(3p,3d)$  integrals have been set to their calculated values and the strong  $(3p,3d)$  exchange interaction splits the  $^7P$  and  $^5P$  final states that are populated according to their statistical weights. Multiplet theory gives for the splitting  $\Delta E(^7P, ^5P) = \frac{12}{15}G_{3p3d}^1 + \frac{36}{70}G_{3p3d}^3 = 17.1$  eV [119]. To account for weak intraatomic configuration interaction the exchange splitting can be scaled down to 70%, i.e. 12.0 eV. The two final states are the main components of the experimentally observed  $K\beta_{1,3}$  line at high energies and the  $K\beta'$  structure at lower fluorescence energies.

Symmetry mixing is included in (c). The  $3p^5 3d^5 (^4P,D) ^5P$  states draw intensity from the  $3p^5 3d^5 (^6S) ^5P$  state. The intensity of the  $^5P$  final state symmetry is then distributed over several eV. The calculations show that the  $3p^5 3d^5 (^4D) ^5P$  peak is considerably stronger than the  $3p^5 3d^5 (^4P) ^5P$  final state. The  $3p^5 3d^5 (^6S) ^5P$  final state is shifted to higher energies because the center of gravity of the entire multiplet remains unchanged. This demonstrates that the  $K\beta_{1,3}$ - $K\beta'$  splitting though mainly caused by the  $(3p,3d)$  exchange splitting is further enhanced by symmetry mixing. Following the discussion of CI above it is not entirely correct to denote the symmetry mixed states by just one LS term. The correct form would be a linear combination of the interacting LS terms. Here the strongest contribution is used to denote the state.

Figure 17 (d) finally shows the effect of the  $3p$  spin-orbit interaction. If experimentally unresolved, the spin-orbit terms broaden the peaks in the spectra but do not affect the relative intensities and hardly the splitting between the peaks. The  $3d$  spin-orbit splitting does not visibly affect the spectra.

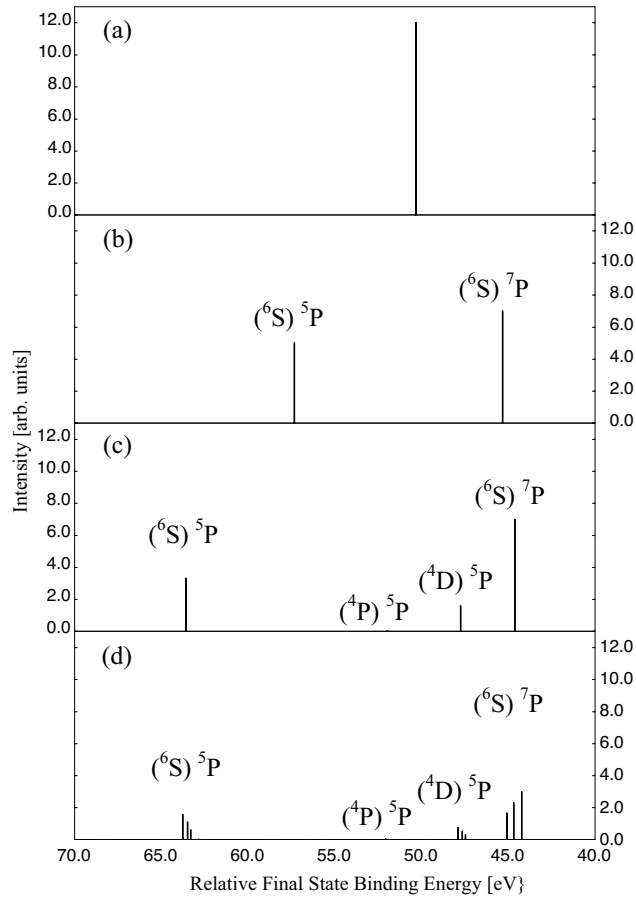


Figure 17:  $K\beta$  final states in  $Mn 3d^5$  based on atomic multiplet theory. In (a) all Slater integrals and spin-orbit interactions have been set to zero. In (b) the  $(3p,3d)$  integrals have been set to their calculated values. Symmetry mixing is included in (c) and (d) shows the effect of  $3p$  spin-orbit interaction.

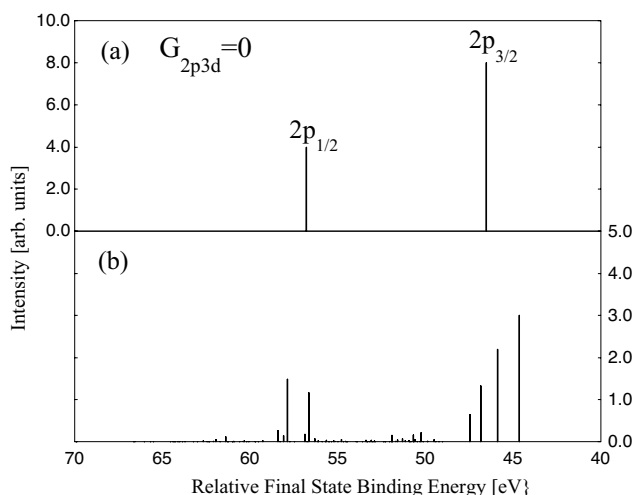
### Theory of $K\alpha$ Emission in Atoms

$K\alpha$  and  $K\beta$  emission have the same fluorescence initial states with a  $1s$  vacancy but in  $K\alpha$  emission this vacancy is filled by a  $2p$  electron. In the Hartree-Fock self-consistent field description the two possible decays differ in the spin-orbit and Slater parameters of the final states. Table 2 compares the values for a  $Mn 2p^5 3d^5$  and  $3p^5 3d^5$  configuration. The spin-orbit splitting is almost ten times larger for a  $2p$  hole in the final state while the exchange splitting is about three times larger for a  $3p$  hole. As a consequence, the overall spectral shape of  $K\beta$  emission is dominated by the  $(3p,3d)$  exchange interaction while the  $K\alpha$  spectra are shaped by the  $2p$  spin-orbit splitting. The final states of a  $K\alpha$  transition can be roughly described in j-j coupling because of the strong  $2p$  spin-orbit interaction. A detailed analysis of the  $2p$  XPS final states in atomic Mn is given in [141].

The calculated  $K\alpha$  final states for  $Mn 3d^5$  are shown in Figure 18 for two cases. In (a) the Slater exchange integrals  $G_{2p3d}^{1,3}$  integrals are set to zero. The spectrum simply reflects the  $2p$  spin-orbit splitting and the two states are populated according to their statistical weight. The  $(2p,3d)$  direct Coulomb interaction ( $F_{2p3d}^2$ ) does not cause any splitting of the final states because the  $3d$  orbital angular momentum is zero in the lowest state of a  $3d^5$  configuration.

Table 2: Slater integrals and spin-orbit parameters (in eV) for a Mn  $2p^5 3d^5$  and  $3p^5 3d^5$  configuration.

$2p^5 3d^5$	$3p^5 3d^5$
$\zeta_d=0.06$	$\zeta_d=0.05$
$\zeta_p=6.85$	$\zeta_p=0.80$
$F_{dd}^2=12.21$	$F_{dd}^2=11.47$
$F_{dd}^4=7.65$	$F_{dd}^4=7.18$
$F_{pd}^2=6.99$	$F_{pd}^2=12.40$
$G_{pd}^1=5.18$	$G_{pd}^1=15.40$
$G_{pd}^3=2.95$	$G_{pd}^3=9.38$

Figure 18:  $K\alpha$  final states in Mn  $3d^5$  based on atomic multiplet theory. (a) The  $(2p,3d)$  exchange integral is set to zero and the stick spectrum just shows the  $2p$  spin-orbit splitting. All Slater integrals and symmetry mixing are included in (b).

$F_{2p3d}^2$  causes some symmetry mixing but the intensities of the symmetry mixed final states are too weak to be visible in the Figure. All Slater integrals are set to their calculated values in (b). The two lines are split by the Slater exchange integrals and further states are populated due to symmetry mixing. Generally, in systems with zero orbital angular momentum in the ground state we have  $J=S$  for the  $3d$  electrons and the  $K\alpha_1$  line is solely split by the  $(2p,3d)$  exchange interaction. However, the magnitude of the splitting can depend on the  $(2p,3d)$  direct interaction if symmetry mixing is included, *i.e.* states with  $3d$  angular momenta larger than zero. The direct integral enters the non-diagonal matrix elements and therefore influences the intensity of symmetry mixed states. We have seen for the  $K\beta$  emission that a redistribution of intensity can lead to a shift in energy of final states because the center of

gravity of the multiplet stays constant. Figure 19 shows the calculated  $K\alpha$  final states for Mn  $3d^5$  ( ${}^6S$ ), *i.e.*  $L=0$ , without and with  $F_{2p3d}^2$ . The weak symmetry mixed states between  $K\alpha_1$  and  $K\alpha_2$  considerably redistribute and a slight contraction of the  $K\alpha_1$  splitting can be seen. However, the effects on the strong final states that form  $K\alpha_1$  are weak and the width of the  $K\alpha_1$  line in  $L=0$  systems is mainly determined by the  $(2p,3d)$  exchange interaction.

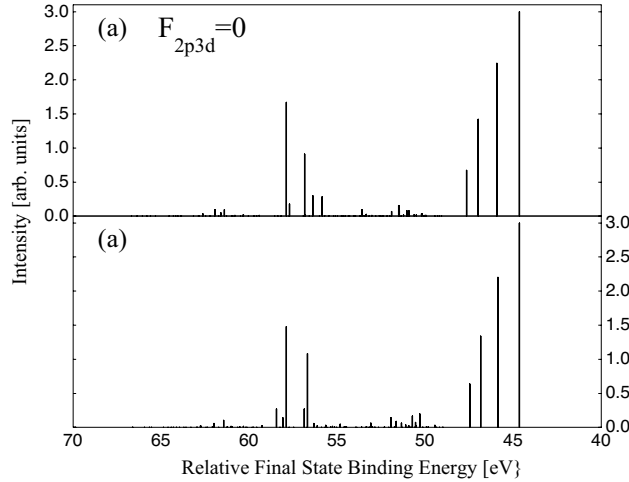


Figure 19:  $K\alpha$  final states in Mn  $3d^5$  based on atomic multiplet theory; (a)  $(2p,3d)$  direct Slater integral is set to zero, (b) all Slater integrals are set to their calculated values.

For  $L \neq 0$  systems,  $F_{2p3d}^2$  contributes to the splitting. This is shown in Figure 20 for a  $3d^4$  system with a  ${}^5D$  ground state. Including the  $(2p,3d)$  direct Coulomb interaction induces a splitting of approximately the same magnitude as the  $(2p,3d)$  exchange interaction. Furthermore, the Figure shows that including all Slater integrals does not yield a spectrum that is a superposition of the spectra (b) and (c) where either the direct or the exchange interaction are set to zero. Both integrals enter the non-diagonal electrostatic matrix elements and the symmetry mixing transfers intensity between final states.

Neglecting spin-orbit interaction, the splitting due to the  $(2p,3d)$  direct interaction can be understood by looking at different couplings of the orbital angular momenta in the  $2p$  hole and the  $3d$  electrons. Differently coupled angular momenta mean different relative orientations of the electron densities in the  $3d$  and  $2p$  shells resulting in stronger or weaker Coulomb interaction between the two shells. The direct Coulomb integral  $F_{2p3d}^2$  enters the equation for the total energy with coefficients that vary with the coupling [36, 119]. If the  $3d$  angular electron distribution has S symmetry, the averaged  $(2p,3d)$  direct Coulomb interaction is the same for all orientations of P symmetry in the  $2p$  shell. In this case, no orbital angular momentum induced splitting occurs.

There is an important phenomenon in  $3d$  transition metal compounds which is sometimes referred to as ‘quenching’ of the orbital electron momentum. In some cases, this can be readily understood group theoretically when the spherical symmetry of the free ion is reduced to the symmetry of the metal atom in a ligand environment. This is addressed below when ligand field theory is discussed. Generally, a lower symmetry can remove some or all of the orbital degeneracy of  $3d$  orbitals and thus the orbital angular momentum [54]. This observation is directly related to paramagnetism in solids. Measurements of the effective magnetic moment  $\mu_{eff}$  (via the magnetic susceptibility  $\chi$ ) in  $3d$  transition metal compounds

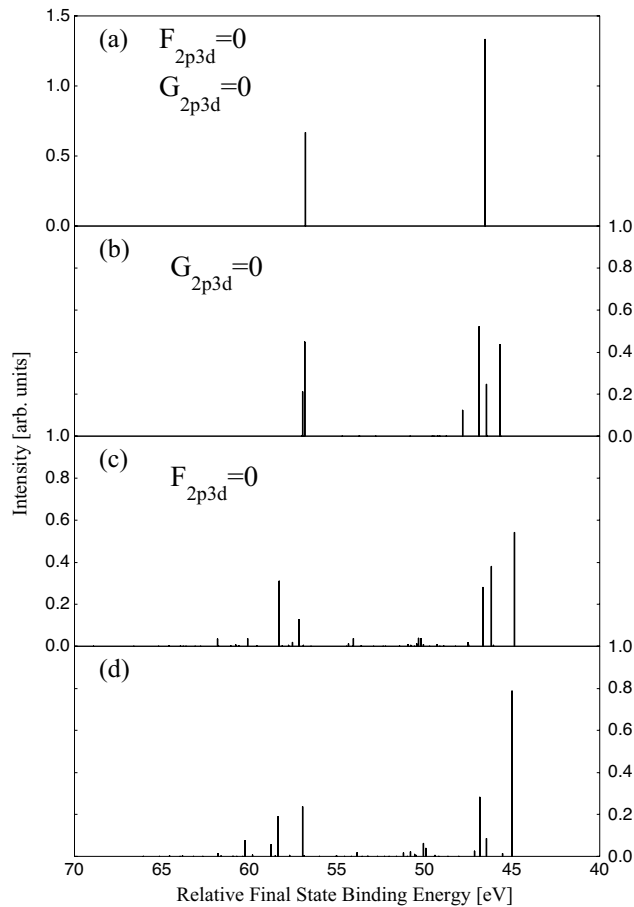


Figure 20:  $K\alpha$  final states in  $Mn 3d^4$  based on atomic multiplet theory; (a) All  $(2p,3d)$  Slater integrals are set to zero, (b) the  $(2p,3d)$  direct Slater integrals are set to their calculated values, (c) the  $(2p,3d)$  exchange Slater direct integrals are set to their calculated values, (d) all Slater integrals are set to their calculated values.

do not agree with calculations that assume a total angular momentum  $J$  as derived from the spin and orbital angular momentum coupling in the free ion (see *e.g.* [54, 5]). Much better agreement is achieved by setting  $J = S$ , *i.e.* assuming a zero orbital angular momentum. A theoretical treatment of paramagnetism was provided by van Vleck who found that the room temperature magnetic susceptibility to a good approximation is a function of the net spin of the metal valence shell (see *e.g.* [61]). In a simple picture this can be understood by the finding that averaging over all angular orbital momenta in the crystal field split  $3d$  levels yields approximately zero orbital angular momentum. This is noted here because we have seen that the  $K\alpha_1$  line is solely split by the  $(2p,3d)$  exchange interaction for zero angular momentum. It therefore reflects the spin state of the metal ion in a ligand environment.

### 3.1.2 N-Electron Atom in a Ligand Field

In a simple picture, the change of the potential that acts on the metal electrons in a ligand environment can be described by additional point charges located around the metal atom. This approach was first introduced by Becquerel and Bethe in 1929 [12, 18]. The metal

together with the ligand can then no longer be described in spherical symmetry. In most cases the new symmetry can be assigned to one of the 32 point groups. The change in symmetry comes with a loss of the 5-fold  $3d$  degeneracy and a ligand induced splitting between the metal valence orbitals occurs (ligand field splitting). In order to accurately calculate the splitting one would need to represent the ligand electrons by a charge distribution  $\rho(\vec{r})$  as is done in density functional theory [29]. The calculations presented here are a semiempirical approach and the ligand field parameters are not calculated *ab initio*. The ligand field is dealt with by reducing the  $O_3$  symmetry of the free atom or ion to the lower symmetry of the poly-nuclear complex under consideration using empirical values for the ligand field splitting. Usually only the first coordination sphere is included. Furthermore, the influence of the ligand field on the metal core electrons is neglected. This introduces an error in the calculated absolute energies because of possible chemical shifts and, for very low symmetries, the degeneracy of the  $p$  orbitals can be lifted. We are not interested in calculating absolute energies and only compounds with approximately cubic symmetry will be considered in this work where the  $p$  orbitals are not split by the ligand field.

As an example we consider an octahedron  $MX_6$ , i.e. a metal surrounded by 6 identical ligands on the  $(x,y,z)$  axes with equal metal-ligand distances. The point group of this complex is  $O_h$ . The irreducible representations (irreps) in  $O$  symmetry are  $A_1, A_2, E, T_1, T_2$ . Inversion symmetry ( $O_h$ ) doubles the number of irreducible representations adding the indices (g)erade or (u)ngerade to the representation symbol. Group theory states that wave functions suitable to describe the electronic states of the system must possess the same transformation properties under the symmetry operations of the group as does an irreducible representation of the group. Investigation of the  $d$  orbitals shows that  $d_{z^2}$  and  $d_{x^2-y^2}$  are transformed into each other and form a basis for an irreducible representation. The irreducible representation must be 2-dimensional and gerade and therefore identifies with  $E_g$ . Similarly,  $d_{xy}, d_{xz}$  and  $d_{yz}$  form a basis for the irrep  $T_{2g}$ . The five-fold degeneracy of the  $d$ -orbitals in  $O_3$  symmetry is split and the new orbitals are denoted  $e_g$  and  $t_{2g}$ . The energy difference between the two orbitals is the ligand field splitting and is commonly denoted  $10Dq$ .

The quenching of the orbital angular momentum was mentioned before. No orbital angular momentum is connected with A and E terms in cubic symmetry as can be seen from evaluating the direct product [10]. The angular momentum operator  $\vec{L}$  belongs to the irrep  $T_{1g}$  in  $O_h$  [54]. To obtain the expectation values for  $\vec{L}$  we have to evaluate the integrals  $\langle \Psi_\Gamma | \vec{L} | \Psi_\Gamma \rangle$  where  $\Psi_\Gamma$  represents the wave function describing the atom in the ligand field with the irrep  $\Gamma$ . In order to find out whether the integral is zero or finite we can evaluate the direct products  $\Gamma \times T_{1g} \times \Gamma$ . If the direct product does not contain  $A_{1g}$ , the integral is zero [54]. This is the case for  $\Gamma=A_1, A_2$  and E terms.

The bases of the irreps  $E_g$  and  $T_{2g}$  must not necessarily be the atomic  $d$  orbitals but can be any set of linearly independent orbitals with the correct transformation properties (see Table 14 in appendix B). This means that the atomic  $d$  orbitals can hybridize with the ligand orbitals to form molecular orbitals. The hybridizing orbitals must have the same symmetry with respect to the poly-nuclear complex. It is therefore convenient to describe the ligand orbitals as metal  $d$  orbitals and ensure the correct symmetry for hybridization. Since electron-electron interaction between the metal and ligand orbitals is neglected in the calculations, the ligand electron is assigned a very high principal quantum, e.g.  $99d$ , in order to ensure a negligible overlap between the ligand and the metal wavefunctions. Details of how hybridization is dealt with in the present theory will be given in Section 3.1.3.

The following formalism is based on works by Kotani and de Groot (see [81, 42] and references therein). The formulae will be written in second quantization with the creation and annihilation operators  $a$  and  $a^\dagger$  as well as the number operator  $n = a^\dagger a$  [35]. The orbital on which the operator acts is written as subscript to the operator. The ground state Hamiltonian for the metal ion in second quantization is written as follows:

$$H_M = \sum_{\Gamma, \sigma} \epsilon_{d\Gamma} a_{d\Gamma\sigma}^\dagger a_{d\Gamma\sigma} \quad (25)$$

$$+ \frac{1}{2} \sum_{\nu_1, \nu_2, \nu_3, \nu_4} g_{dd}(\nu_1, \nu_2, \nu_3, \nu_4) a_{d\nu_1}^\dagger a_{d\nu_2} a_{d\nu_3}^\dagger a_{d\nu_4} \quad (26)$$

$$+ \zeta_d \sum_{\nu_1, \nu_2} (\vec{l} \cdot \vec{s})_{\nu_1 \nu_2} a_{d\nu_1}^\dagger a_{d\nu_2} \quad (27)$$

$$+ U_{dd} \sum_{(\Gamma, \sigma) \neq (\Gamma', \sigma')} a_{d\Gamma\sigma}^\dagger a_{d\Gamma\sigma} a_{d\Gamma'\sigma'}^\dagger a_{d\Gamma'\sigma'} \quad (28)$$

The  $d$  orbitals split by the ligand field are denoted  $d\Gamma$  following the common notation  $\Gamma$  for irreps and are  $e_g$  and  $t_{2g}$  in  $O_h$  symmetry. The spin state is denoted by  $\sigma$ . Spin and orbital are combined in the indices  $\nu_i$ . The terms 26 and 28 contain the Slater direct and exchange operators  $g$ . For diagonal matrix elements we have  $(\nu_1, \nu_2) = (\nu_3, \nu_4)$ . The Hamiltonian includes symmetry mixing and the non-diagonal matrix elements contain four different electron wavefunctions, *i.e.*  $(\nu_1, \nu_2) \neq (\nu_3, \nu_4)$ . The term 26 therefore includes diagonal and non-diagonal matrix elements.

$U_{dd}$  identifies with the Slater integral  $F_{dd}^0$ . It does not contribute to the multiplet splitting and was therefore written separately from the other two-electron terms. Its value is not calculated *ab initio* but is one of the empirical input parameters in the computational procedure. It becomes important when more than two configurations are included because it affects the relative energy position of the interacting configurations. For the calculations shown in this work no more than two configurations are included. This is usually done for late transition metal compounds (*e.g.* Ni compounds) where charge transfer effects become more important [133, 40].

The x-ray intermediate state has a core hole and the following terms have to be added to the ground state Hamiltonian:

$$H_{M_c} = \sum_{\mu} \epsilon_c a_{c\mu}^\dagger a_{c\mu} \quad (29)$$

$$+ \sum_{\nu_1, \nu_2, \mu_1, \mu_2} g_{cd}(\nu_1, \nu_2, \mu_1, \mu_2) a_{d\nu_1}^\dagger a_{d\nu_2} a_{c\mu_1}^\dagger a_{c\mu_2} \quad (30)$$

$$+ \zeta_c \sum_{\mu_1, \mu_2} (\vec{l} \cdot \vec{s})_{\mu_1 \mu_2} a_{c\mu_1}^\dagger a_{c\mu_2} \quad (31)$$

$$- U_{cd} \sum_{\Gamma, \sigma, \mu} a_{d\Gamma\sigma}^\dagger a_{d\Gamma\sigma} (1 - a_{c\mu}^\dagger a_{c\mu}) \quad (32)$$

The orbital that contains a core hole is denoted  $c$ . No irrep is connected with the core hole because the influence of the ligand field is neglected for core orbitals. The index  $\mu$  combines the spin and orbital state of the core level. The two-electron interaction between the core hole and the valence electrons is given in term 30. A core-hole-d-electron Coulomb attraction

potential  $U_{cd}$  accounts for the change in effective nuclear charge caused by the creation of an inner shell vacancy. It is, like  $U_{dd}$ , not calculated *ab initio* but taken as a result from other measurements.

It is possible to write down symmetry branching rules for the transformation from a group to one of its subgroups. Table 3 lists the branching rules in terms of the orbital angular momentum for the transformation from  $SO_3$  to  $O$  symmetry. The ligand field only causes a splitting for angular momenta 2 and higher.

Table 3: *The  $SO_3 \rightarrow O$  Branching rules for integer angular momenta*

Spherical	Octahedral
S	$A_1$
P	$T_1$
D	$E+T_2$
F	$A_2+T_1+T_2$
G	$A_1+T_1+T_2+E$
H	$T_1+T_1+T_2+E$
I	$A_1+A_2+T_1+T_1+T_2+E$

The ground state for a  $t_{2g}^3 e_g^2$  configuration therefore has  ${}^6A_1$  symmetry following the branching from the atomic  $3d^5 {}^6S$  configuration. That a high-spin (sextet) configuration is the lowest energy term (Hund's rule) can be readily understood in terms of the ( $3d, 3d$ ) exchange interaction that lowers the energy and is maximal for a sextet when all spins are parallel. However, in a strong crystal field the splitting between the  $e_g$  and  $t_{2g}$  orbitals becomes large enough to make a  $t_{2g}^5$  configuration energetically more favorable where four spins are paired and do not contribute to the exchange interaction. This is shown in Figure 21. The atomic equivalent would be a  $3d^5 {}^2I$  configuration. Table 3 shows that I splits into 6 levels in cubic symmetry. Tanabe and Sugano calculated the energy positions of a transition metal with 5 valence electrons and found that the ground state in a strong crystal field has  ${}^2T_2$  symmetry [124].

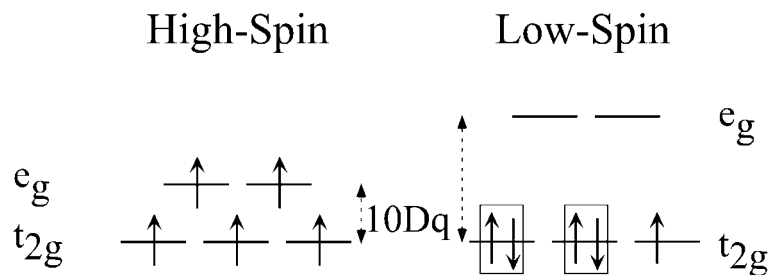


Figure 21: *High-spin and low-spin valence shell configuration for a  $n=5$  system in an octahedral environment.*

In order to determine dipole allowed final states in the new symmetry one can apply the direct product of group theory. The coordinates (x,y,z) as the part of the dipole operator that is affected by the symmetry change transform as  $T_1$  in O symmetry. Using the direct product (see *e.g* [54]) one can write down the dipole allowed transitions for all irreps in O symmetry. For the dipole matrix elements:

$$\langle IS|T_1|FS\rangle \quad (33)$$

between initial (IS) and final state (FS) one obtains the relations shown in Table 4.

Table 4: *Irreps of initial and final states in dipole approximation for cubic symmetries.*

IS	FS			
A <sub>1</sub>	T <sub>1</sub>			
A <sub>2</sub>	T <sub>2</sub>			
T <sub>1</sub>	A <sub>1</sub>	T <sub>1</sub>	T <sub>2</sub>	E
T <sub>2</sub>	A <sub>2</sub>	T <sub>1</sub>	T <sub>2</sub>	E
E	T <sub>1</sub>	T <sub>2</sub>		

If we neglect spin-orbit interaction and further assume that the exchange interaction between the  $1s$  shell and the  $t_{2g}$  and  $e_g$  electrons is equal we have two  $1s$  intermediate states with  ${}^7A_1$  and  ${}^5A_1$  symmetry in an  $n=5$  system. Table 4 gives 2 possible final states,  ${}^7T_1$  and  ${}^5T_1$  neglecting symmetry mixing.

Including the electron spin in the group theoretical considerations introduces a difficulty because of possible half-integer values of the total angular momentum  $J$ . The system is no longer symmetric with respect to a rotation by  $2\pi$  but by  $4\pi$ . This can be solved by treating the system in the framework of double groups. A summary can be found in the books by Ballhausen [10] and Sugano [124]. Tables for point groups and branching rules can be found in references [6] and [29].

Figure 22 illustrates the influence of the ligand field on the  $K\beta$  final states. The  $3d$  and  $3p$  spin-orbit splittings are not included in all spectra. The first spectrum (a) is the same as in Figure 17 (c) because the ligand field splitting  $10Dq$  was set to zero. In the second spectrum (b)  $10Dq$  equals 0.8 eV and 1.5 eV in the third spectrum (c). I chose these values with respect to Chapter 5 where I discuss  $K\beta$  emission in  $Fe_2O_3$  and  $MnO$ . The ligand field does not affect the septet final state because the orbital angular momentum in the  $3d$  shell is less than 2 and therefore no splitting occurs (see Table 3). The quintet states are symmetry mixed and one term in the linear combination has  $L=2$  ( ${}^4D$ ) in the atomic picture (see Figure 17). Depending on the strength of the  $L=2$  admixture in the final state the ligand field splitting will affect the final state. Figure 17 shows that additional peaks appear between the two strong quintet states and the intensity of the former ( ${}^4D$ )  ${}^5P$  state slightly decreases.

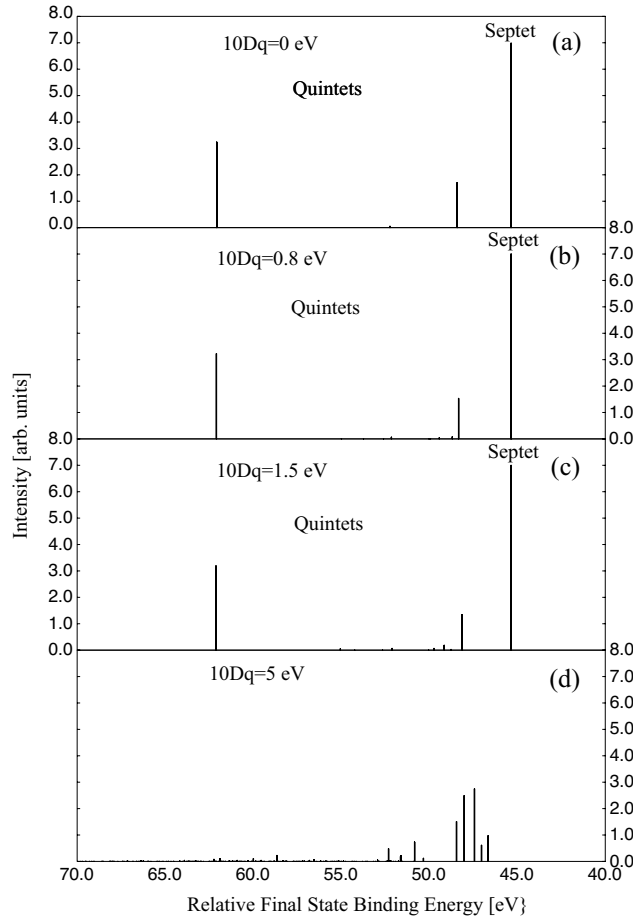


Figure 22:  $K\beta$  final states in  $Mn\ 3d^5$  based on ligand field multiplet theory with all spin-orbit splittings set to zero. The first spectrum (a) is identical to the atomic spectrum. Spectra (b) and (c) show spectra for typical  $10Dq$  values found in high-spin compounds. Spectrum (d) shows the  $K\beta$  final states for a low-spin configuration.

Inclusion of the ligand field therefore draws intensity from the  $K\beta_{1,3}$  low energy shoulder. However, the effect is rather small between realistic values of  $10Dq$  (Figure 22 (b) and (c)). The effect will further be obscured by spin-orbit interaction, the initial and final state lifetime broadening as well as ligand-to-metal charge transfer effects.  $K\beta$  spectroscopy in an  $n=5$  system is therefore hardly sensitive to the ligand field as long as the field is weak enough to maintain a valence shell high-spin configuration.

A dramatic ligand field effect can be observed when  $10Dq$  becomes large enough to force a low-spin valence shell configuration as shown in Figure 22 (d). The valence shell configuration changes from  $t_{2g}^3 e_g^2$  ( $S=5/2$ ) to  $t_{2g}^5$  ( $S=1/2$ ). For this to occur, twice the ligand field splitting has to be larger than the exchange energy of two spin-parallel pairs of  $3d$  electrons. In the calculations it is assumed that the  $1s$  intermediate state has  ${}^1,{}^3T_2$  symmetries. Table 4 shows that four final states are possible for a  $T_2$  fluorescence initial state instead of one for an  $A_1$  initial state. The  $K\beta_{1,3}$  line becomes therefore broader because of the additional splitting. The spectrum is not separated into two different spin multiplicities anymore but the singlet and triplet final states overlap. The  $(3p, 3d)$  exchange splitting decreases because the valence shell now only has one unpaired spin. Invoking the atomic picture again, for a

$3d^5$   $2I$  configuration the exchange splitting is calculated to be 3.4 eV compared to 17.1 eV for a high spin configuration. Hence, the  $K\beta'$  peak in a high-spin configuration becomes a low energy shoulder of the  $K\beta_{1,3}$  line in a low-spin configuration.

### 3.1.3 Ligand-to-Metal Charge Transfer

So far the metal ligands have only been considered in terms of the local geometry and the ligand field splitting. Two additional terms in the Hamiltonian can be included for a more quantitative treatment of the ligand environment:

$$H_{CT} = \sum_{\Gamma,\sigma} \epsilon_{\Gamma} a_{\Gamma\sigma}^{\dagger} a_{\Gamma\sigma} \quad (34)$$

$$+ \sum_{\Gamma,\sigma} V(\Gamma) (a_{d\Gamma\sigma}^{\dagger} a_{\Gamma\sigma} + a_{\Gamma\sigma}^{\dagger} a_{d\Gamma\sigma}) \quad (35)$$

The first term adds the energy of the ligand orbitals. The summation in  $\Gamma$  runs over the same irreps as for the metal valence orbitals since all those ligand electrons are taken into account that hybridize with the metal orbitals. As mentioned earlier, in the calculations the ligand orbitals are assumed to be metal  $d$  orbitals with a very high principal quantum number. The second term represents the ligand-to-metal hopping. An electron is created at the metal site and annihilated at the ligand and vice versa. Two hopping terms exist in octahedral surrounding.  $V(E_g)$  mixes metal and ligand wave functions with  $E_g$  symmetry, namely  $d_{z^2}$  and  $d_{x^2-y^2}$  in case of the metal. These orbitals are directed along the axes unlike the  $t_{2g}$  orbitals that stretch between the axes and one expects stronger mixing for  $E_g$  symmetry because the ligands are located on the axes in octahedral symmetry. Indeed, band structure calculations give  $V(E_g)$  to be about twice as large as  $V(T_{2g})$  [93]. The hopping terms are empirical parameters in the calculations. They replace the non-diagonal matrix elements in equation 21.

For a discussion of the charge-transfer effects it is helpful to analyze a simplified case with only two configurations,  $|3d^5\rangle$  and  $|3d^6\bar{L}\rangle$ , and to disregard the  $\Gamma$  dependence in  $\epsilon_{\Gamma}$  and  $\epsilon_{d\Gamma}$ , *i.e.* neglect the ligand field splitting. The charge transfer energy  $\Delta$  is defined as  $\Delta = E(d^{n+1}\bar{L}) - E(d^n)$ .  $E$  is the energy of the lowest term in each configuration in the charge transfer models. However, for computational reasons in this thesis  $\Delta$  denotes the difference between the center of gravity energies of the two configurations. For simplicity all spin-orbit and two-electron Coulomb interactions are neglected for the following illustration and we just consider a two by two energy matrix for the two configurations. The ground state energy matrix then is:

$$H_{CT} = \begin{pmatrix} E_0 & V_{eff} \\ V_{eff} & E_0 + \Delta \end{pmatrix}, \quad V_{eff} = \sqrt{2V(E_g)^2 + (8-n)V(T_{2g})^2} \quad (36)$$

The core-hole-d-electron Coulomb potential  $U_{cd}$  changes the energy of the  $3d$  electrons. The charge transfer configuration has one more  $3d$  electron and the energy matrix of the excited state therefore reads:

$$H_{CT} = \begin{pmatrix} E_0^c & V_{eff} \\ V_{eff} & E_0^c + \Delta - U_{cd} \end{pmatrix} \quad (37)$$

The relative ordering of the two configurations therefore changes upon creation of a core hole. In most cases,  $U_{cd}$  is greater than  $\Delta$  and the order of the two configurations is inverted

in the final state. This is shown in the right part of Figure 23. Two wavefunctions that are solutions of the 2x2 Hamiltonian can be formed from the two configurations  $|3d^5\rangle$  and  $|3d^6\underline{L}\rangle$ . The one with lower energy will be denoted ‘bonding combination’. It forms the ground state of the system:

$$|g\rangle = \cos \alpha |3d^n\rangle - \sin \alpha |3d^{n+1}\underline{L}\rangle \quad (38)$$

The combination at higher energy is the ‘anti-bonding combination’. We can neglect the anti-bonding combination for the ground state because it is not populated. For the final state we have to consider both combinations:

$$|f\rangle_- = \cos \beta |3d^n\rangle - \sin \beta |3d^{n+1}\underline{L}\rangle, \quad \text{bonding} \quad (39)$$

$$|f\rangle_+ = \sin \beta |3d^n\rangle + \cos \beta |3d^{n+1}\underline{L}\rangle, \quad \text{anti - bonding} \quad (40)$$

The angles  $\alpha$  and  $\beta$  that define the population ratio of the two configurations for the bonding and anti-bonding combination depend on the energy difference between the  $|3d^5\rangle$  and  $|3d^6\underline{L}\rangle$  configurations as well as the mixing term  $V_{eff}$ :

$$\tan \alpha = \frac{1}{V_{eff}} \left( \sqrt{\left(\frac{\Delta}{2}\right)^2 + V_{eff}^2} - \frac{\Delta}{2} \right) \quad (41)$$

$$\tan \beta = \frac{1}{V_{eff}} \left( \sqrt{\left(\frac{\Delta - U_{cd}}{2}\right)^2 + V_{eff}^2} - \frac{\Delta - U_{cd}}{2} \right) \quad (42)$$

Figure 23 shows the percentage of  $|3d^n\rangle$  in the bonding combination of the initial and final state for  $n=5$  versus the charge transfer energy with a fixed core-hole-d potential  $U_{cd}$  and hopping terms  $V(E_g)=2.0$  eV and  $V(T_{2g})=1.0$  eV for  $E_g$  and  $T_{2g}$  symmetry, respectively. For smaller  $\Delta$  the charge transfer configuration  $|3d^6\underline{L}\rangle$  becomes more populated and dominates for negative  $\Delta$ .  $U_{cd}$  lowers the energy of the charge transfer configuration in the final state and therefore decreases the percentage of  $|3d^n\rangle$ .

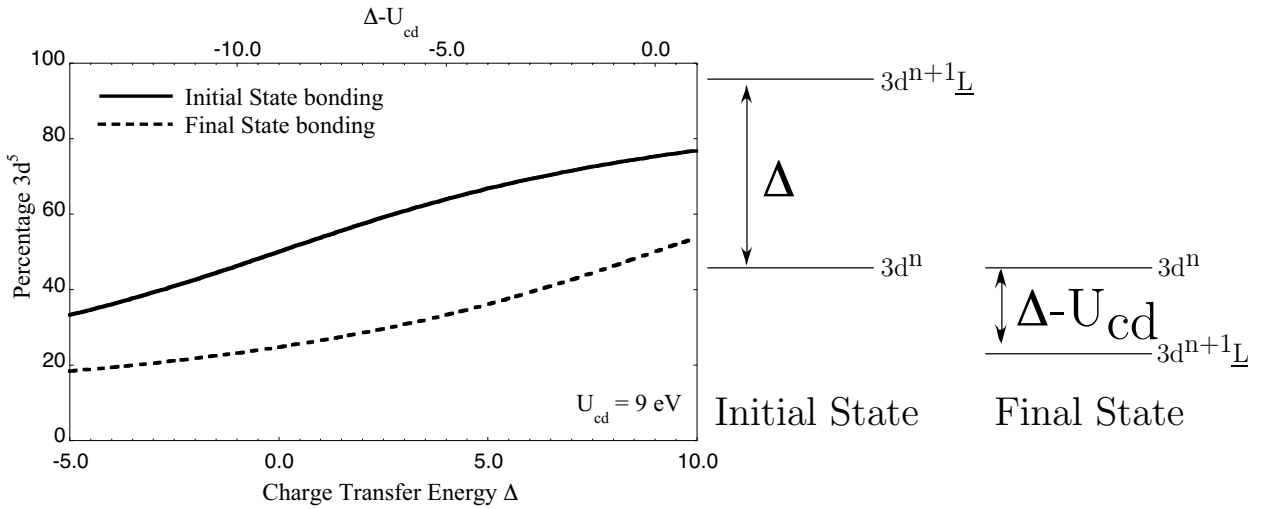


Figure 23: Percentage of  $|3d^5\rangle$  in the charge transfer bonding combinations of an initial and final state versus  $\Delta$  using  $U_{cd}=9$  eV. The ordering of the configurations is shown on the right.

Diagonalization of equation 37 yields the energies of the two combinations in the final state with a core hole. Experimentally, the difference between the energies is of particular interest and is given by:

$$\Delta(E^+, E^-) = \sqrt{(\Delta - U_{cd})^2 + 4V_{eff}^2} \quad (43)$$

Of course, two split peaks can only be observed if both combinations are populated in the final state. The intensity ratio is given by:

$$\frac{I_+}{I_-} = \frac{|\langle +|g\rangle|^2}{|\langle -|g\rangle|^2} = \tan^2(\beta - \alpha) \quad (44)$$

Intensity resulting from the populated final state anti-bonding combination can only be observed as a satellite in the experimental spectra if the population of the two configuration changes, i.e.  $\alpha \neq \beta$ , and the satellite intensity is stronger the greater the change in the energy difference between the two configurations in the initial and in the final state. The intensities  $I_{+,-}$  are proportional to the square of the overlap integrals  $\langle \pm|g\rangle$ . This evokes a comparison to shake transitions where the transition probability is related to the overlap integrals between the orbitals. Indeed, as will be pointed out below, a reordering of the configurations upon core hole creation and subsequent population of the anti-bonding combination in the charge transfer picture is similar to a shake transition. For  $U_{cd}=9$  eV the satellite intensity has a maximum at  $\Delta=\frac{U_{cd}}{2}=4.5$  eV and reaches 31.5% of the main peak intensity (Figure 24). The maximum shifts to  $\Delta=3.5$  eV for  $U_{cd}=7$  eV and now only reaches 21.9% of the main peak intensity. For small changes ( $<1$  eV) in the ordering of the configurations the satellite intensity becomes insignificant in most experiments. The energy difference between the bonding and the anti-bonding combination is shown in Figure 24 lower panel. The peak splitting depends on the separation between the interacting configurations in the final state as well as the hopping terms. It is minimal for  $\Delta=U_{cd}$ , i.e. the two configurations are degenerate, and its magnitude in the minimum solely depends on  $V_{eff}$ .

It should be noted that unlike in the atomic calculations where no term was added to the Hamiltonian to include symmetry mixing, in the charge transfer calculations term 35 explicitly describes the mixing of the two configurations. This is necessary because only one electron changes its orbital if two configurations are included and the non-diagonal Hamiltonian matrix elements without the additional term would be zero. Furthermore, the hopping terms are empirical parameters in the charge transfer calculations and give the theorist a handle to adjust the strength of the hybridization.

To evaluate the influence of ligand-to-metal charge transfer or hybridization on the  $K\beta$  emission one has to properly treat the  $1s$  intermediate state as well as the  $3p$  final state. This will be done in Chapter 5. Here we just assume the  $1s$  intermediate state to be the bonding combination and complete the series of calculations to illustrate the spectral changes connected with every additional term in the Hamiltonian. Figure 25 (a) again shows the  $K\beta$  final states without hybridization and  $10Dq=1.5$  eV. In (b) the hopping terms were set to 2.0 and 1.0 eV for  $V(E_g)$  and  $V(T_{2g})$ , respectively. The splitting between the two configurations is -2 eV in the intermediate and final state, i.e. the charge transfer configuration  $3d^6\bar{L}$  lies 2 eV below the  $3d^5$  configuration. It is thus assumed  $U_{1s3d}=U_{3p3d}$ . This approximation will be discussed in Chapter 5.

The spectra show that the septet state is hardly affected by the charge transfer. A careful look at the energy position and intensity reveals that it is slightly shifted (by 0.05 eV) to lower

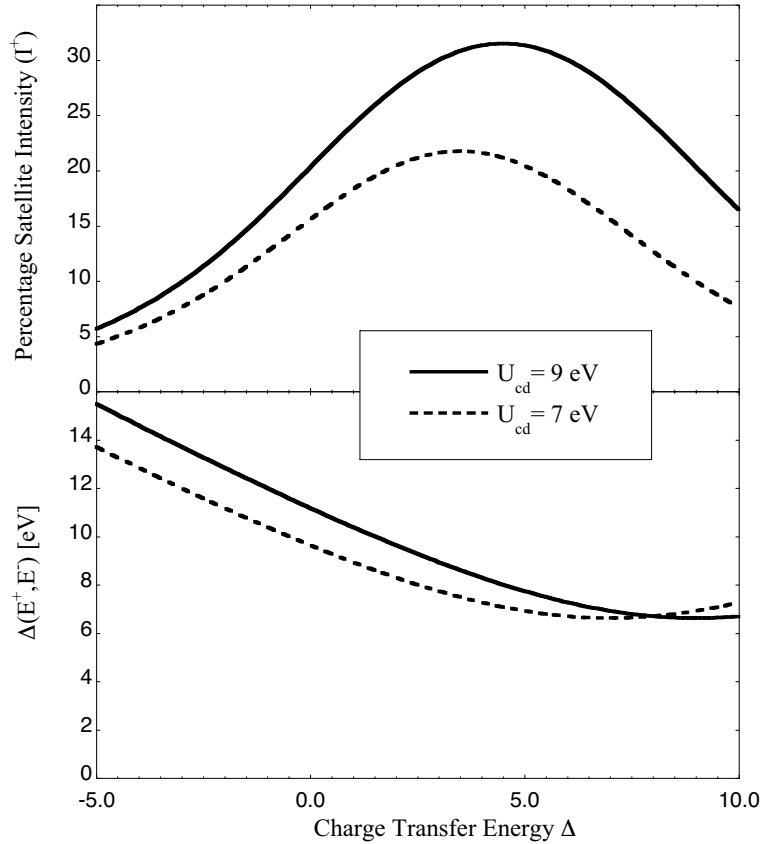


Figure 24: *Upper panel: Percentage of intensity in the final state anti-bonding combination (satellite peak) versus charge transfer energy for two different values of  $U_{cd}$  for an  $n=5$  system. The hopping terms were set to 1.0 eV and 2.0 eV for  $T_{2g}$  and  $E_g$  symmetry, respectively. Lower panel: Energy difference between bonding and anti-bonding combination.*

energies and some of the intensity is transferred to the anti-bonding combination at higher energies. This effect is stronger when the order of the two configurations changes between intermediate and final state as was explained before. The quintet states are considerably split and redistributed by hybridization. As a result, the  $K\beta_{1,3}$  shoulder will be less pronounced and the  $K\beta'$  peak will be broadened by ligand-to-metal charge transfer.

The different effects of the inclusion of the charge transfer configuration on the high-spin and low-spin components of the final states are nicely explained in reference [40] for Ni. We can transfer the arguments to Mn. The basic idea is that the additional ligand orbital opens up another decay channel for the quintets but not for the septet as shown in Figure 26: A  $3d^6$  configuration can form a quintet or a triplet (neglecting lower spin states). An overall septet can only be formed by one combination of  $3d$  spins,  $3p$  spin and ligand spin which is when all spins add up. Recalling the discussion of symmetry mixing we find that the spin flip can occur in the metal  $3d$  shell or in the ligand orbital. These are the lowest two configurations in Figure 26. We thus find that a  $3d^6$  triplet term can contribute to the quintet  $K\beta$  final states. The number of possible final states is therefore increased for the quintet but not for the septet final states when charge transfer is included.

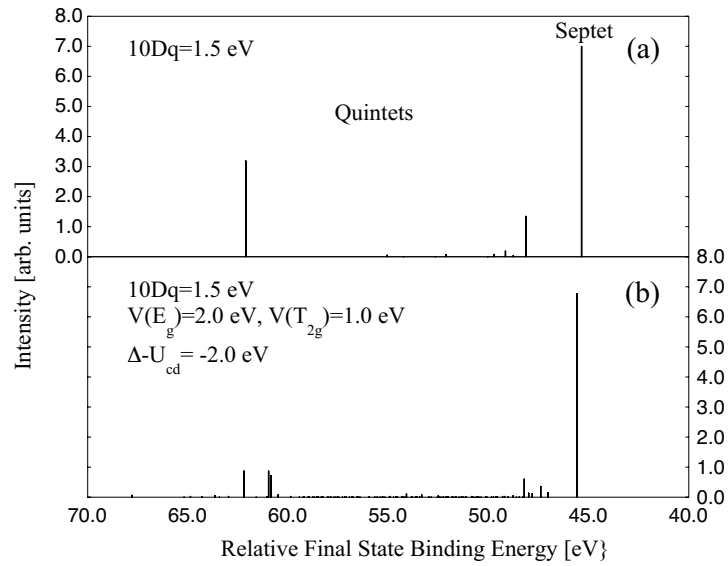


Figure 25:  $K\beta$  final states based on ligand field multiplet theory (a) without and (b) with ligand-to-metal charge transfer.

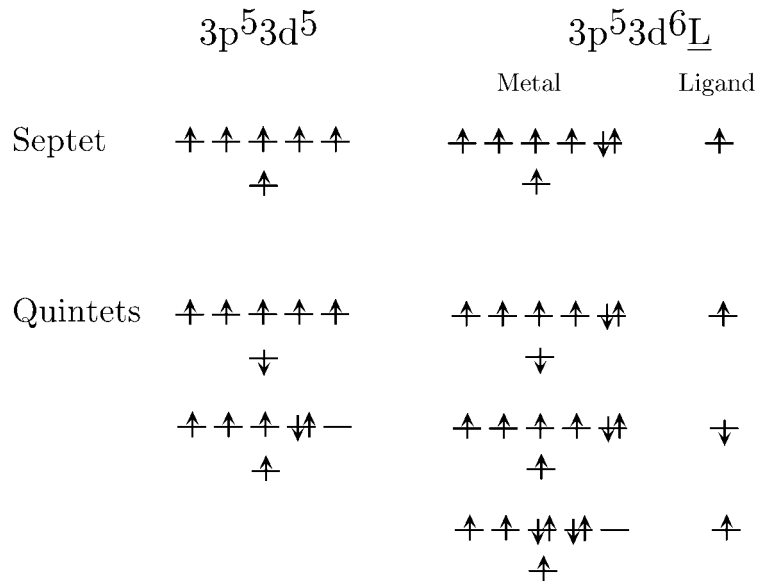


Figure 26: Possible  $K\beta$  final states in an  $n=5$  system including ligand-to-metal charge transfer. The metal  $3d$  shell is shown neglecting the ligand field splitting. Only the unpaired metal  $3p$  and ligand electrons are shown. The symmetry mixing for a  $3d^5$  configuration was discussed before. Charge transfer opens the possibility for metal  $3d^6$  triplet final states.

### 3.1.4 Limitations of Ligand Field Multiplet Theory

Ligand field multiplet theory yields very good results for core hole spectra that do not directly involve transitions to or from valence orbitals. The influence of the valence electrons on the spectra can be modeled by adjusting the empirical parameters or by scaling of the Slater integrals. Furthermore, in principle, as many configurations as necessary can be included in

the CI calculations to improve the results if sufficient computing power is available. As an example we consider a high-spin Fe(III) complex with a  $3d^5$  configuration in the ionic limit. For an ionic complex the net spin in the valence shell is close to  $S=5/2$  because only weak ligand to metal charge transfer should occur and the Fe valence electrons are mostly localized at the Fe center. The  $K\beta$  spectrum is expected to look very similar to atomic Fe. However, in a covalent molecular complex (e.g. a protein) the Fe  $3d$  electrons delocalize and ligand-to-metal charge transfer is expected to become stronger. Since the exchange integrals depend on the overlap of the interacting electronic wavefunctions the exchange splitting should be smaller for a covalent complex. In the calculations this can be simulated by scaling down the ( $3p, 3d$ ) Slater exchange integrals. The stronger ligand-to-metal charge transfer is explicitly included in the calculations by reducing the charge transfer energy  $\Delta$ . The net spin is then less than  $5/2$  depending on the admixture of  $3d^6$  in the bonding configuration and the exchange splitting further decreases.

However, when justifying different assumptions and the adjustment of the input parameters the inherent limitation of ligand field multiplet theory becomes evident: It is a semiempirical approach and there might be several, physically plausible but mutually exclusive ways to explain the experimental results even within the theory. Furthermore, even if ligand field theory can explain a spectral feature with an appropriate set of parameters, it is not clear whether the feature is due to effects not included in the theory after all. And finally, some features simply cannot be modeled by the theory at all. This limitation particularly becomes evident in absorption spectra because originally empty orbitals become occupied in the final state. As an example, the overall spectral structures in L-edge absorption spectra are well explained within ligand field theory because they are due to  $2p$  to  $3d$  excitations. However, a controversy exists concerning the interpretation of the satellite lines. Details are discussed in several references and shall not be pursued here [21, 42, 133, 141]. Ligand field multiplet theory fails to model transition metal K-edges except for the weak pre-edge structure that is, presumably, due to  $1s$ - $3d$  excitations. The ligand field theory does not include backscattering from first and higher coordination spheres, orbitals other than those with mainly  $3d$  character and, the way it is presented here, it is not a fully relativistic treatment of the problem.

The final states of the  $K\beta$  satellite transitions do not have a core hole in the final state and the spectra are no longer dominated by multiplet splittings but by the metal  $p$  projected density of states in the valence shell. Multiplet theory therefore is not a suitable tool to model  $K\beta$  satellite spectra. One appropriate theoretical approach to interpret the valence electron spectra of samples where band structure formation can be neglected is density functional theory.

## 3.2 Density Functional Theory

Time independent density functional theory models the ground state electron density  $\rho(\vec{r})$  or spin density  $\rho_\sigma(\vec{r})$  of a system [59, 7]. The first model to express the ground state energy as a functional of the electron density was introduced by Thomas and Fermi in 1927 [129, 53]. The computational effort compared to the Hartree-Fock calculations is considerably smaller because the model yields an integral equation for the electron density that can be solved directly. It does not attempt to model the N-electron ground state wavefunction and no SCF iteration is involved [36, 59]. The Thomas-Fermi model does not include electron exchange or correlation and therefore yields rather poor results [36]. Slater suggested a local

approximation to the exchange potential [119]. In his model, the exchange interaction at a point  $\vec{r}_0$  is calculated between the electron density of the system  $\rho(\vec{r}_0)$  and a homogeneous electron gas with a density  $\rho = \rho(\vec{r}_0)$ . The Slater model leads to the  $X_\alpha$  potential that replaces the non-local Hartree-Fock exchange [59]:

$$V_{X_\alpha}(\rho(\vec{r})) = -\frac{3e^2}{2\pi}\alpha[3\pi^2\rho(\vec{r})]^{1/3} \quad (45)$$

The parameter  $\alpha$  can be fitted to observable quantities [59]. The  $X_\alpha$  or Hartree-Fock-Slater method can be considered a hybrid between density functional theory and the Hartree-Fock approximation. Like the latter, it requires SCF iteration to obtain the N-electron ground state wavefunction but the non-local exchange in the Hartree-Fock picture is simplified by introducing the local exchange with a homogeneous electron density. It yields good results if the electron density  $\rho(\vec{r})$  varies slowly as a function of  $\vec{r}$  [59].

Currently, the density functional theory encountered in most applications is the one developed by Hohenberg, Kohn and Sham (for reviews see [77] and [59]). The following brief summary intends to emphasize the crucial aspects and to work out the differences to the Hartree-Fock method. No computational details are given because no calculations were performed by the author of this thesis. They can be found in the references given. The first Hohenberg-Kohn theorem states that all ground state electronic properties, and hence the ground state energy, are uniquely determined by the electron density and can be expressed as functionals of  $\rho(\vec{r})$ . The second theorem states that the ground state energy as a functional of  $\rho(\vec{r})$  is minimized by the true ground state density of the system [64], *i.e.* Kohn-Sham density functional theory is a variational method. The Hamiltonian describing the system without spin-orbit interaction is written as:

$$H = -\frac{1}{2} \sum_i \nabla_i^2 + \sum_i v(\vec{r}_i) + \frac{1}{2} \sum_{i \neq j} \frac{1}{r_{ij}} \quad (46)$$

Comparison with equation 13 shows that the second term includes the potential energy of the nuclear-electron attraction and the repulsion between pairs of nuclei. It is often referred to as ‘external potential’ and is uniquely defined by the electron density  $\rho(\vec{r})$ .

To obtain the electron density the ground state energy functional is defined as [77]:

$$E_{v(\vec{r})}[n(\vec{r})] \equiv \int v(\vec{r})\rho(\vec{r})d\vec{r} + F[\rho(\vec{r})] \quad (47)$$

and  $F[\rho(\vec{r})]$  is written as:

$$F[\rho(\vec{r})] = T_s[\rho(\vec{r})] + \frac{1}{2} \int \frac{\rho(\vec{r})\rho(\vec{r}')}{|\vec{r} - \vec{r}'|} d\vec{r}d\vec{r}' + E_{XC}[\rho(\vec{r})] \quad (48)$$

The first term is the kinetic energy of a fictitious, noninteracting system with density  $\rho(\vec{r})$ . Kohn-Sham density functional theory splits the electron-electron term into a ‘classical’ part which describes the electron-electron potential without electron correlation and the exchange correlation energy  $E_{XC}$  which, as well, contains the part of the kinetic energy that is not included in  $T_s$ . Since the ground state energy is a functional of  $\rho$ ,  $E_{XC}$  must be, too, because it contributes to the ground state energy. Their approach leads to a system of N equations:

$$h^{KS}\phi_j(\vec{r}) = \epsilon_j\phi_j(\vec{r}) \quad j = 1, \dots, N \quad (49)$$

with

$$h^{KS} = -\frac{1}{2}\nabla^2 + v(\vec{r}) + \int \frac{\rho(\vec{r}')}{|\vec{r} - \vec{r}'|} d\vec{r}' + v_{XC}(\vec{r}) \quad (50)$$

$$v_{XC}(\vec{r}) = \frac{\delta E_{XC}[\rho(\vec{r})]}{\delta \rho(\vec{r})} \quad (51)$$

Even though the equations resemble the Hartree-Fock equations the approach is fundamentally different. The Kohn-Sham orbitals  $\phi_j$  are not the one-electron wavefunctions of the system and the equations 49 therefore do not imply a one-electron picture. The functions  $\phi_j$  are not intended to have any physical significance apart from the fact that they combine to the electron density  $\rho$ :

$$\rho(\vec{r}) = \sum_{j=1}^N |\phi_j(\vec{r})|^2 \quad (52)$$

The theory so far is exact in the sense that we know that a unique exchange correlation energy  $E_{XC}$  as a functional of the electron density must exist. However, the form of the functional dependence of the exchange energy on the density is not known and therefore approximations have to be made. This is the only source of error in the Kohn-Sham density functional theory. A common approximation to the  $E_{XC}$  is that the electron moves in a homogeneous electron gas of constant density (local density approximation (LDA)):

$$E_{XC}^{LDA}[n(\vec{r})] = \int \epsilon_{XC}(n(\vec{r}))n(\vec{r})d\vec{r} \quad (53)$$

where  $\epsilon_{XC}$  is the exchange correlation energy per particle of a uniform interacting electron gas of density  $\rho$ . This quantity can be calculated exactly when the electron is assumed uncorrelated (independent-electron approximation) and we obtain a  $\rho^{1/3}$  dependence of the exchange potential as in the  $X_\alpha$  method:

$$v_x(\rho) = -\frac{e^2}{\pi}(3\pi^2\rho)^{\frac{1}{3}} \quad (54)$$

Comparison with equation 45 shows that the adjustable parameter in the  $X_\alpha$  model takes the value  $\alpha=2/3$ . The LDA approach works well for systems with electrons that behave like a Fermi gas. For molecules, other exchange correlation functionals (generalized gradient approximation GGA, B3-LYP) have been successfully applied [7, 112]. Considerable efforts are still being made in order to find more accurate expressions for the exchange correlation energy.

In order to solve the Kohn-Sham equations a basis set for the Kohn-Sham orbitals has to be chosen. The Kohn-Sham orbitals become the molecular orbitals of the complex and they can be written as linear combinations of atomic orbitals (LCAO), *i.e.* of all atoms in the complex. The atomic orbitals in turn can be expressed as linear combinations of Slater type or Gaussian functions. The coefficients of these functions are varied when the ground state energy functional is minimized [112]. The problem is solved iteratively in a self-consistent fashion. The exchange correlation energy does not change over the course of iterations and is the same for all  $\phi_j$ .

The formalism can be extended to the spin density (see *e.g.* [59]). One can distinguish between restricted and unrestricted calculations of the spin density. The former means that pairs of electrons share the same spatial component and only differ in the spin component of the spin-orbitals. The alternative is to assign a full spin-orbital to every electron, *i.e.* electrons are not paired in one spatial orbital anymore. This unrestricted method is sometimes used for open shell atoms such as *3d* transition metals to explain magnetic properties. The standard Kohn-Sham density functional theory does not include spin-orbit interaction.

Results obtained using the  $X_\alpha$  method and Kohn-Sham density functional theory will be used in Chapters 5.2 and 6.2, respectively. The results discussed in Chapter 6.2 are part of a collaboration with Jesper Bendix. He used the commercial program package Gaussian<sup>®</sup>. Details of the calculations are given when the results are discussed.

## 4 Double Excitation

So far the possibility of exciting two electrons simultaneously has not been addressed. In the two step picture that was used to explain fluorescence emission, the excitation of a second electron can either occur during the creation or during the decay of a  $1s$  vacancy. This is illustrated in Figure 27. The latter process can be either a pure electronic or a radiative Auger transition where a photon is emitted besides the excitation of an electron [1]. We are only interested in radiative Auger transitions (RAE). A theoretical treatment of multiply excited states is a challenge. We do not want to further complicate the theoretical interpretation of our fluorescence spectra and it is therefore desirable to experimentally separate doubly from singly excited final states. If this is not possible we would like to be able to estimate the fluorescence energy due to doubly excited states for the evaluation of the spectra. The purpose of this Chapter therefore is to elucidate some aspects of double excitation that are relevant in the context of this thesis. Experimental examples for KL double photoionization and KLL radiative Auger emission will be given. References where more detailed theoretical analyses of the double excitation processes were performed are cited.

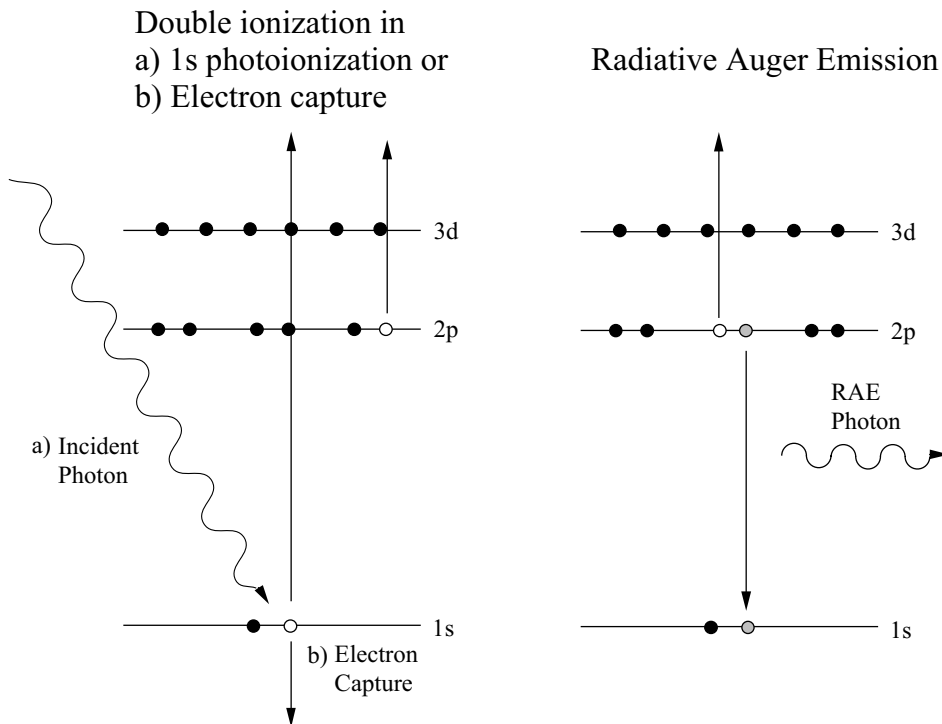


Figure 27: Possible mechanisms to reach doubly excited final states. On the left side the excitation of a second electron occurs during the creation of a  $1s$  vacancy. The two modes of excitation are shown. On the right, the excitation of a second electron occurs during the decay of the  $1s$  vacancy. The radiative Auger emission with a  $2p$  excitation is shown.

## 4.1 Multiple Excitations upon 1s Vacancy Creation

Any electronic transition in an atom causes a readjustment of the passive or spectator electrons, *i.e.* the electrons that are not directly involved in the transition, to the perturbed potential. A passive electron in an orbital  $\phi_{\mu}^i$  before the perturbation will relax into an orbital  $\phi_{\mu}^f$ . In an adiabatic transition we have  $\mu = \mu'$ , *i.e.* the final state orbital is described by the same set of quantum numbers. It is, nevertheless, a different orbital because it is part of the solution for the perturbed Hamiltonian. If the relaxation is non-adiabatic the electron will occupy an orbital with different quantum numbers ( $\mu \neq \mu'$ ). These transitions are referred to as shake-up or shake-off transitions. The relaxation will be adiabatic if  $t_0 \Delta E$  is much greater than  $\hbar$  where  $t_0$  is the time during which the potential changes and  $\Delta E$  is the shake-up or shake-off energy [130]. The case where  $t_0 \Delta E$  is much smaller than  $\hbar$  is the sudden approximation. Thomas introduced a model to describe the transition from adiabatic to sudden excitation of core electrons [130]. However, his approach does not explicitly include configuration interaction and is therefore not suitable to describe the threshold regime where the incident photon energy is tuned close to an edge energy.

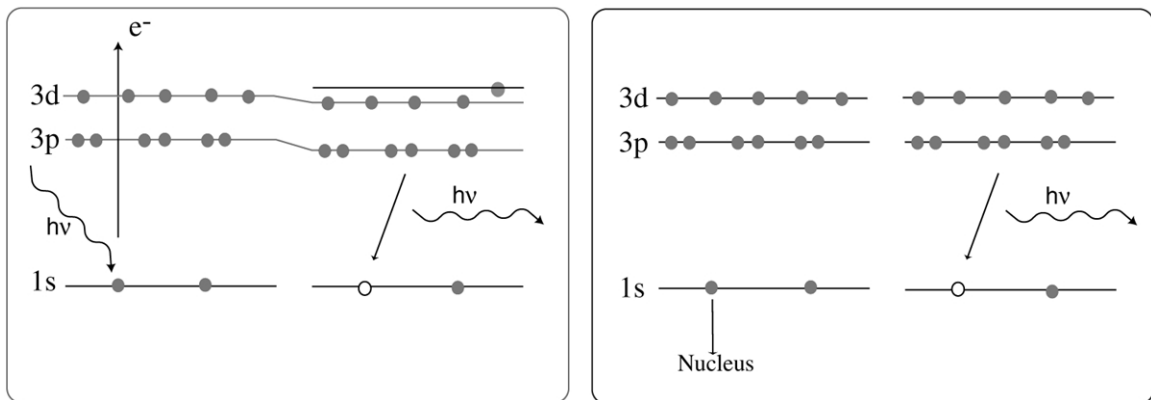


Figure 28: *Simplified illustration of relaxation process after photoionization (left) and after K capture decay (right). The 3d and 3p orbitals adjust to the new effective nuclear potential after photoionization. A non-adiabatic relaxation in the valence orbitals is shown with one electron occupying a higher orbital. No relaxation occurs after K capture because the 1s hole is compensated by the decrease in nuclear charge in terms of the effective potential experienced by the 3p and 3d electrons.*

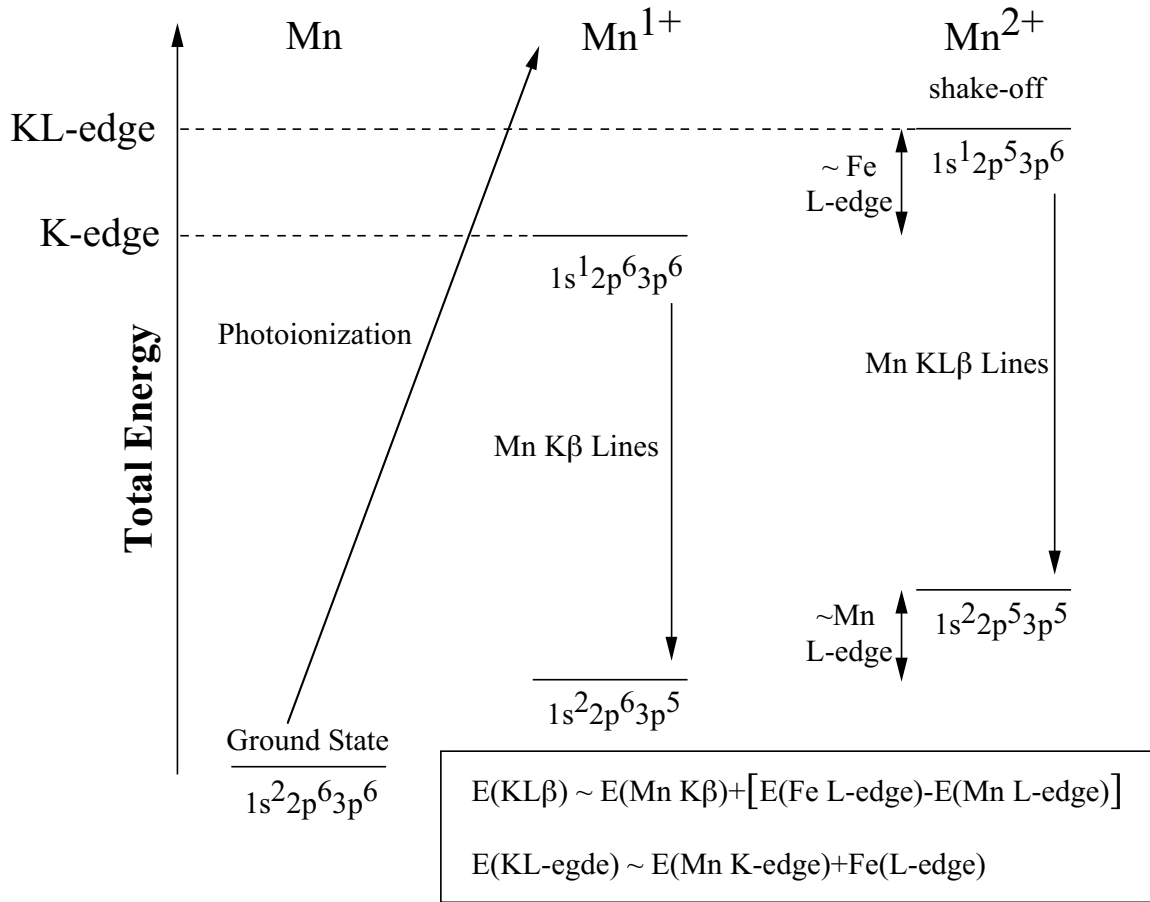
Shake probabilities have been calculated by several authors. Carlson and Nestor calculated the shake probabilities due to inner-vacancy production in Ne, Kr, Ar and Xe in the sudden approximation limit [33]. An alternative approach for the calculations was provided by Mukoyama *et al.* [99] who treated the change in central potential as a perturbation acting on the spectator electrons. In the context of this thesis it is important to determine whether the shake probabilities are different for the two modes of excitation. The change in effective potential experienced by the spectator electrons is very different in the case of K capture than for photoionization because in the former in addition to the vacancy production a proton in the nucleus is converted into a neutron. This is illustrated in Figure 28.  $P_{KK}$  and  $P_{KL}$  values for electron capture decay, *i.e.* the probabilities for double K or K and L vacancy production upon K electron capture in the nucleus, were measured and calculated by Campbell *et al.*

[31] as well as Chon and Law [34]. They found double excitation probabilities per single  $1s$  vacancy production on the order of  $10^{-4}$ . Mukoyama *et al.* calculated the probabilities for ionization of a second shell after K capture in V and Cr compounds and found values up to  $10^{-3}$  for valence electrons [98]. Still, the fluorescence intensities due to transitions from a doubly ionized  $1s$  intermediate state are too weak to measurably influence the  $K\alpha$  and  $K\beta$  spectra in the case of K capture as the mode of excitation.

The situation is different for  $1s$  photoionization because the electron photoexcitation causes a considerable perturbation of the electron shell. Mukoyama *et al.* calculated shake-off probabilities for valence electrons after photoionization in Cr and V of 1-10% [98]. The shake-off probability in inner-shell photoionization strongly depends on the incident photon energy and a theoretical explanation for this dependence on the incident photon energy is provided by the Thomas model [130]. The energy term scheme in Figure 29 shows the decay path for  $KL\beta$  emission in Mn. We can give a rough estimate for the lowest Mn KL-edge energy by using the simple  $Z+1$  model. The Fe  $L_{III}$ -edge is at 707 eV and the Mn K-edge at 6539 eV and we expect the lowest Mn KL edge at approximately 7246. To estimate the  $KL\beta$  fluorescence energy following Figure 29 we first have to determine the differences between the Mn- and Fe L-edges. These are 75.5 eV ( $L_I$ ), 70.0 eV ( $L_{II}$ ) and 68.1 eV ( $L_{III}$ ) [3]. The center of gravity of the  $K\beta$  main line multiplet is approximately 6485 eV and we therefore expect the  $KL\beta$  satellites at around 6553 to 6560 eV. This is of course a very crude approach that simplifies the screening as well as completely ignores multiplet splitting. Furthermore, it assumes that the  $KL\beta$  lines solely result from one doubly excited intermediate state. There is no convincing argument that this is indeed the case. The intermediate states can be spread over several eV and each populated intermediate state might contribute to the  $KL\beta$  satellite spectrum. However, we will see below that our rough estimate approximates the  $KL\beta$  fluorescence energy rather well.

Experimental results are shown in Figure 30 for different Mn oxides. Two spectra were taken for each compound, one well above the KL-edge at 10 keV and one below the KL-edge at 7 keV. Structure due to double ionization can be seen between 6540 and 6580 eV that means about 55 to 95 eV above the  $K\beta_{1,3}$  line in rough agreement with the prediction from the  $Z+1$  model. The large spread of  $KL\beta$  final states can be qualitatively understood within the multiplet model because now two holes instead of one couple to each other and to the valence electrons resulting in a large number of possible final states. Figure 31 shows the peak intensity ratio  $KL\beta/K\beta_{1,3}$  versus incoming photon energy in  $MnO_2$ . The energy bandwidth of the Si(1,1,1) double monochromator was between 2 and 3 eV. A constant background due to the tail of the  $K\beta_{2,5}$  line was subtracted. The onset of the  $KL\beta$  intensity is at approximately 7210 eV slightly below the value estimated using the  $Z+1$  model. A slow rise over several keV as predicted by the Thomas model can be seen and even at 10 keV the curve has not reached a plateau. The curve does not show any prominent resonances. These results are in agreement with studies by Deutsch *et al.* on Cu [47, 56].

The spectra shown in Figures 30 and 31 were taken on concentrated samples. This was necessary to obtain sufficient fluorescence intensity in the  $K\beta$  satellite region. Since the spectral features lie in the photon energy range of the steep rise in K-edge absorption the relative intensities are strongly influenced by self-absorption. The evolution of the curve shown in Figure 31 is still approximately correct because the self-absorption does not change with the incoming photon energy. The curve is furthermore affected by the change in relative absorption over the range of the incident photon energy (saturation effect [60]).

Figure 29: Term scheme for  $K\beta$  and  $KL\beta$  emission in Mn

The goal of the measurements was to separate double from single photoionizations and I therefore did not attempt any correction for self-absorption and saturation or an assignment of the spectral features. The  $K\beta$  satellite lines shown in the following Chapters of this thesis were taken with incident energies below the KL edge but above the KM edge (except for the spectra shown in Chapter 6.2). In this case, the probability for KL double excitation is negligible for photoionization as well as K capture. When comparing the two modes of excitation in the  $K\beta$  satellite region we can therefore rule out different probabilities for KL excitations. The  $Z+1$  model tells us that the spectral features due to double photoionization can be expected to appear at higher energies than the corresponding fluorescence emission from single photoionization. We therefore expect  $KM\beta$  lines with inner-shell M holes on the high energy sides of the  $K\beta$  main lines. A study of  $KM\beta$  lines in Ar is given in reference [45]. They found most of the  $KM_{II,III}\beta$  lines at higher fluorescence energies than the  $K\beta$  line. However, valence shell shake transitions in  $3d$  metals might result in additional lines on the low energy side of the  $K\beta$  main lines. This point will be addressed again in Chapter 5.1. The incident energy was not tuned below the KM edge because then we have to worry about post collision effects (PCI) since the kinetic energy of the outgoing electron is small and the electron might strongly interact with the remaining ion [65].

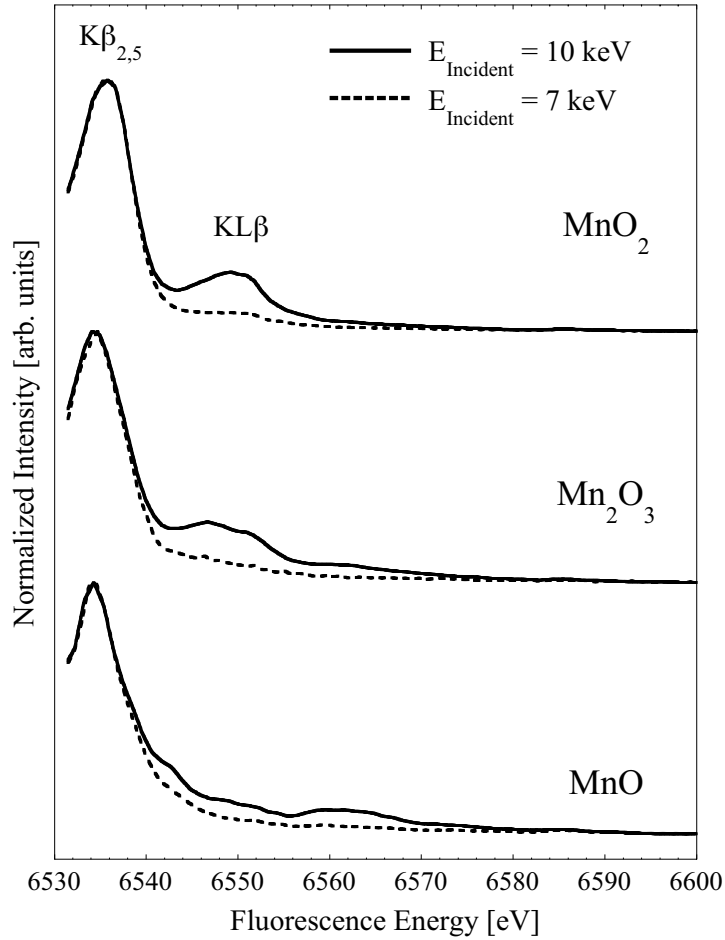


Figure 30:  $K\beta$  satellite region excited well above (solid line) and below (dashed line) the  $KL$ -edge for  $MnO$ ,  $Mn_2O_3$  and  $MnO_2$

## 4.2 Radiative Auger Emission

The fluorescence energy of radiative Auger emission is lower than the corresponding K emission by the energy it takes to elevate a second electron into an empty orbital or the continuum [57]. This is illustrated in the term scheme of Figure 32. The transitions are usually written as  $KS_T S_E$  where  $S_T$  denotes the shell from where the transition to the K shell occurs and  $S_E$  is the shell from where an electron is excited. As an example we consider KLL emission in Ni. The binding energy of a  $2p$  electron that is excited into the continuum in a RAE process will be greater than the Ni  $L_{III}$  edge (852.7 eV) because another  $2p$  electron decays into a  $1s$  orbital and the nuclear charge will be screened less. Slater gives a factor of 0.35 for the contribution of the nuclear screening between  $2p$  electrons [118]. The energy difference between the Ni  $L_{III}$  edge and the Cu  $L_{III}$  edge (932.7) is 80 eV. For a rough estimate of the KLL edge we can therefore calculate: 7478 eV (Ni  $K\alpha_1$ ) - (853 eV (Ni  $L_{III}$ ) + 0.35 \* 80 eV) = 6597 eV.

Figure 32 shows the KLL edges in Ni metal and  $K_2NiF_6$ . The spectra were taken on beamline X-25 at the National Synchrotron Light Source (NSLS). We used the Si(4,4,0) Bragg reflection for the analyzer crystals and the instrumental energy bandwidth of the spectrometer

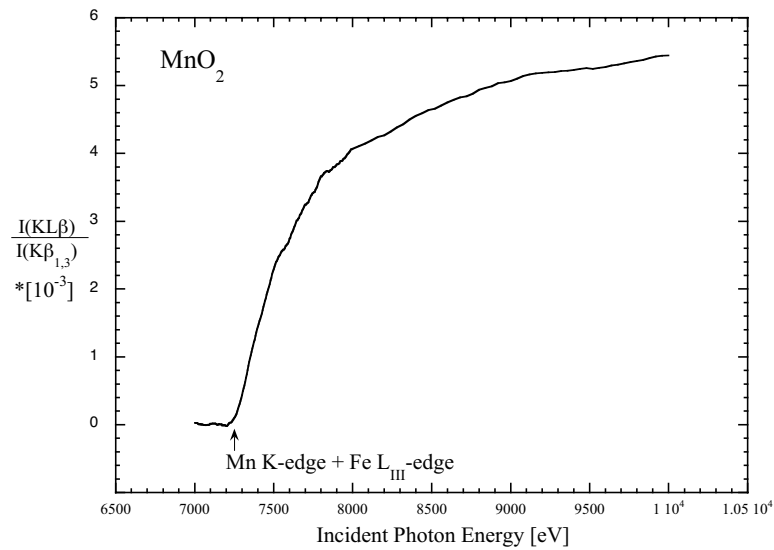


Figure 31: Peak intensity ratio between  $KL\beta$  line and  $K\beta_{1,3}$  line in  $MnO_2$  versus incident photon energy. A constant background was subtracted from the spectrum. A slow rise over several keV can be seen.

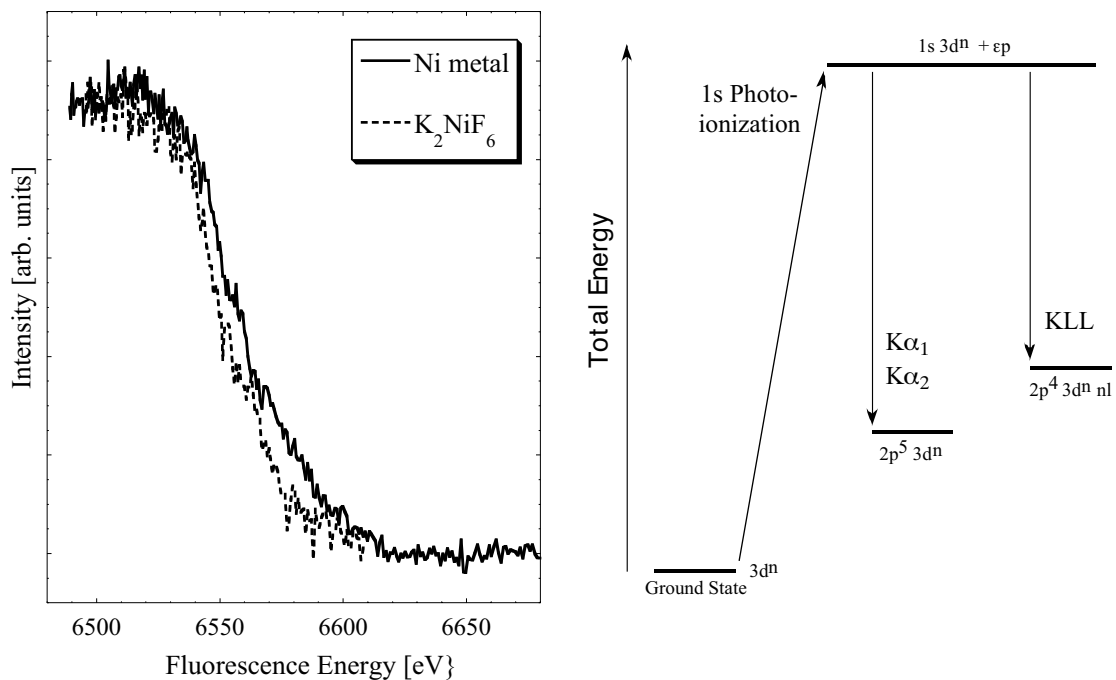


Figure 32: Right panel: Term scheme of KLL radiative Auger emission in a 3d metal. The case where the  $1s$  intermediate state is reached via photoionization is shown; left panel: KLL edge in Ni metal and  $K_2NiF_6$ . The KLL edges differ between the metallic Ni and Ni(IV) in an ionic compound, i.e. they show a chemical dependence.

was about 2 eV. The shake probability is related to the overlap integral between the emitting and the receiving orbital and is largest for monopole shake transitions [57]. The KLL-edge therefore resembles the K-edge and not the L-edge because it probes the p-density of unoccupied states. The onset of the structure in Figure 32 is at approximately 6600 eV and the crude estimate outlined above works surprisingly well. In a high resolution fluorescence experiment one can therefore easily separate the  $K\alpha$  or  $K\beta$  emission from the corresponding RAE ( $KLS_E$  and  $KMS_E$ ) that have an additional hole in a  $3p$  or lower orbital because the energy difference is at least that of the binding energy of a  $3p$  electron (for a study in Co and Ni see [122]).

We do not expect any differences in RAE probabilities between K capture and photoionization if we treat the fluorescence emission as a two step process because RAE occurs in the second step that is independent of the mode of excitation. The intensity of KMM lines relative to  $K\beta$  emission was measured to be less than 5% for transition metals in reference [32] in accordance with calculations by Scofield [117]. However, they do not distinguish between inner-shell M electrons ( $3s, 3p$ ) and valence electrons. To my knowledge neither experimental data nor absolute theoretical estimates are available for valence shell shake-up and shake-off processes accompanying the  $2p$  or  $3p$  to  $1s$  transitions in  $3d$  metal compounds. The possibility of RAE structures with valence electron shake-off and shake-up has to be kept in mind when analyzing the low energy side of the  $K\alpha$  and  $K\beta$  lines.

Finally, I would like to point to other groups that are concerned with the study of double photoionization. Deutsch *et al.* performed calculations for  $KK\alpha$  lines and found that quantum electrodynamics have to be invoked in order to correctly calculate the transition energies [46]. Kawai *et al.* use RAE to record absorption like spectra that show EXAFS oscillations (EXEFS) [73]. Double photoionizations are important in conventional EXAFS spectroscopy. The KL edge superimposes on the EXAFS oscillations and complicates the analysis. Evidence for KL edges was found in third period elements [55]. KL edges in absorption spectra of  $3d$  transition metal compounds are a topic of discussion (see [76] and references therein). KM edges influence the absorption near edge structure (XANES) and reduce the absorption cross section as expected from a one-electron picture [19]. In trace element studies (*e.g.* proton induced x-ray emission (PIXE)) an accurate knowledge of the  $K\alpha/K\beta$  ratio is crucial in order to discriminate the weak signals and thus all branching ratios have to be taken into account [69].

## 5 Influence of the Core Hole on K Fluorescence Emission

### 5.1 $K\beta$ Lines

This Chapter follows up on the theory established in the Chapter 3. It contains, however, experimental results and is therefore separate from the theoretical part of this thesis. Both Chapters together form the basis for a correct theoretical treatment of the  $K\beta$  emission. First, experimental spectra for the  $K\beta$  main lines in MnO after photoionization and in  $^{55}\text{Fe}_2\text{O}_3$  after K capture are discussed that motivated the theoretical investigation. A theoretical model to explain the experimental results will be presented. It was developed in collaboration with Frank de Groot.

#### 5.1.1 Experimental Observation

The experimental  $K\beta$  spectra of MnO after x-ray excitation and  $\alpha$ - $^{55}\text{Fe}_2\text{O}_3$  (hematite) following K capture are compared in Figure 33. The energy range of the  $3p$  to  $1s$  transitions is shown with the sharp  $K\beta_{1,3}$  peak at higher fluorescence energies and a broad  $K\beta'$  structure at lower fluorescence energies. The spectral intensities have been normalized to each other in the maximum of the  $K\beta_{1,3}$  peak. The energy scale is the measured fluorescence energy and the spectra were not shifted in energy with respect to each other. A constant background was subtracted from the K capture spectrum but not from the photoionization spectrum because of the very good signal to background ratio in the latter case.

It was discussed in Chapter 2 that the instrumental broadenings are identical for the two spectra and it was mentioned that the error for the relative energy calibration is  $\pm 0.07$  eV. A direct comparison is therefore possible. The two spectra roughly coincide on the low energy side of the  $K\beta'$  structure. The  $K\beta'$  peak is slightly weaker and shifted to lower energies for  $^{55}\text{Fe}_2\text{O}_3$ , and the MnO photoionization spectrum shows considerably more intensity between  $K\beta'$  and  $K\beta_{1,3}$ . The  $K\beta_{1,3}$  peak appears sharper for K capture and shifted to higher fluorescence energies. Furthermore, the MnO photoionization spectrum shows more intensity in the high energy tail of the  $K\beta_{1,3}$  line.

Similar studies have been done before. Schnopper *et al.* compared high resolution  $K\beta$  spectra from a metallic 1 Ci  $^{55}\text{Fe}$  source with PI spectra of metallic Mn [114, 115]. He discussed the probability of producing states of multiple excitation and ionization by readjustment after PI but within the experimental error he did not observe any differences in the spectra. Borchert *et al.* studied the x-ray emission in Au and Ho after K capture and after PI and they observed relative shifts of the emission energies [24, 25]. Dem'yanchuk *et al.* repeated the experiment on metallic  $^{55}\text{Fe}$  and reported a 0.6 eV shift of the K capture  $K\beta_{1,3}$  line relative to the x-ray excited line [44]. Recent results in an improved experimental set up using a 5 mCi metallic  $^{55}\text{Fe}$  source showed in accordance with Schnopper that the  $K\beta$  main lines for both excitation modes occur at the same energy within the experimental error [16]. Furthermore, in the latter study the  $K\beta$  main line for metallic  $^{55}\text{Fe}$  after KC was found to be narrower than for metallic Mn after PI. In the following a theoretical explanation for this narrowing in insulators is proposed but similar arguments can be applied to metals.

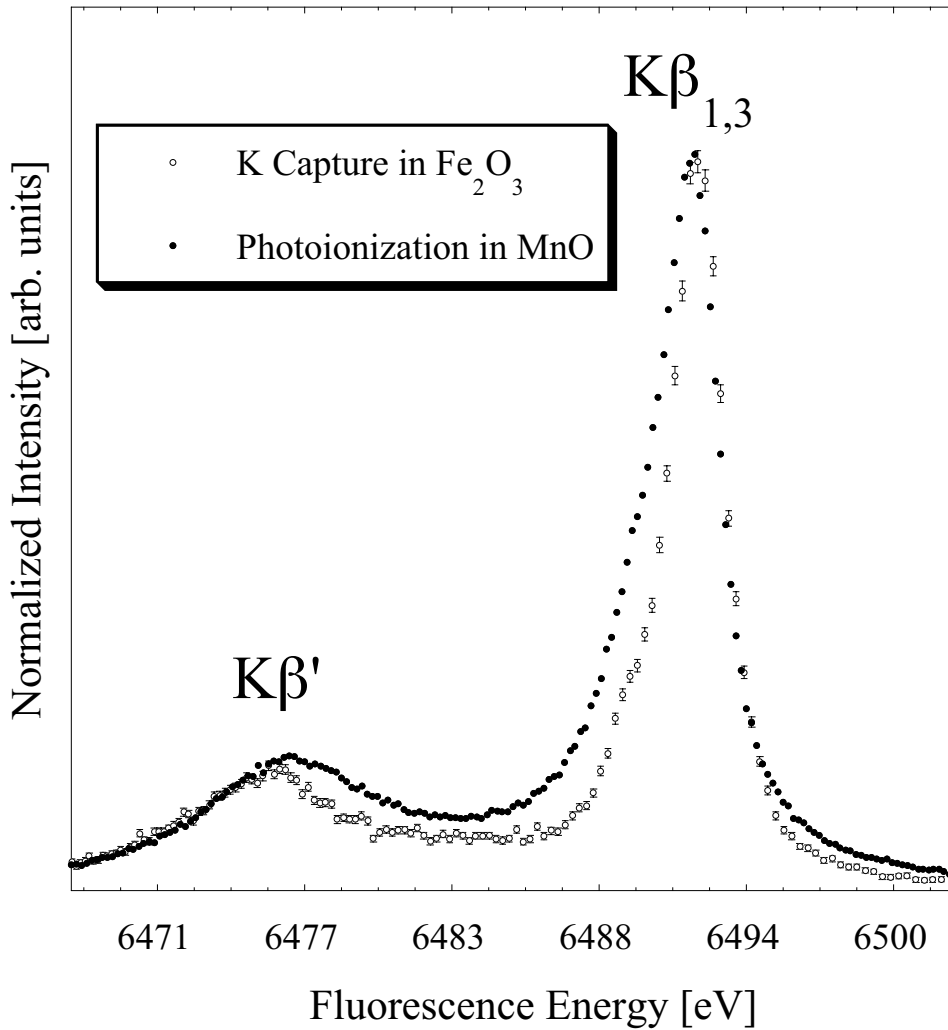


Figure 33: *Experimental  $K\beta$  spectra for MnO and  $^{55}\text{Fe}_2\text{O}_3$ . The instrumental broadening is  $\approx 0.8$  eV. The spectra are normalized to each other in the  $K\beta_{1,3}$  peak. The energy scale is the measured fluorescence energy and the spectra were not shifted in energy with respect to each other.*

The good results using the ligand field multiplet theory to model the  $K\beta$  emission in solids encouraged us to attempt to explain the observed differences between the two spectra within this theoretical framework. Fe in  $\text{Fe}_2\text{O}_3$  has the formal oxidation state (III) and Mn has (II) in MnO. The atomic configurations are  $3d^6 4s^2$  for Fe and  $3d^5 4s^2$  for Mn. The ligand field calculations start with the ion as was shown before. Both compounds are rather ionic and one can therefore assume a  $3d^5$  valence shell configuration for both ions. Since the Fe nucleus is converted into a Mn nucleus in the K capture process, we obtain exactly the same ionic Slater and spin-orbit parameters for Mn in MnO and Fe in  $\text{Fe}_2\text{O}_3$  in our theoretical model. A handle to alter the calculated spectra and account for the experimentally observed differences would be the scaling of the Slater integrals. However, considerably different scaling parameters are hard to justify given the very similar structures of the two compounds (the metal-oxygen bondlengths are 2.22 Å in MnO and 2.12 Å in  $\text{Fe}_2\text{O}_3$  [125]) and we realize that we cannot explain the observed differences in the  $K\beta$  spectra in a one-configuration atomic model.

Both metal ions are enclosed in an octahedral ligand environment [140]. Here the differences begin because different ligand field splittings are present in the two compounds. For MnO one finds  $10Dq=0.8$  eV [42] and for  $Fe_2O_3$   $10Dq=1.45$  eV [85] as derived from  $2p$  absorption spectra. However, we have seen before that the ligand field splitting hardly affects the  $K\beta$  spectrum in an  $n=5$  high-spin system and we can still not explain the observed differences in the  $K\beta$  spectra. In the final state of the K capture decay we obtain a Mn impurity with a  $3p$  hole in an  $Fe_2O_3$  lattice. It is not clear what  $10Dq$  value to use in this case. I therefore use in the ligand field calculations  $10Dq=1.0$  eV for MnO after photoionization and  $Fe_2O_3$  after K capture. This simplification will not affect conclusions given here.

The next step is to include two configurations in the form of charge transfer calculations. The charge transfer energies are  $\Delta=7$  eV for MnO and  $\Delta=3.5$  eV for  $Fe_2O_3$  [21]. If I use these two values in the calculations, the  $K\beta$  spectra will hardly differ because the admixture of the charge transfer configuration only slightly varies for the two values of  $\Delta$  (see Figure 23 in Chapter 3). So again, this cannot explain the observed differences. However, as was shown before, the separation of the two configurations depends on the core hole potential that acts on the valence electrons. This potential will not be the same for the two modes of excitation and we suspect that a dependence on the mode of excitation causes the differences in the spectra. We therefore have to investigate in what way the valence electrons react to the  $1s$  vacancy and, in case of K capture, a conversion of a proton into a neutron and what are the consequences on the  $K\beta$  spectra. The crucial idea is that the  $1s$  hole, *i.e.* a missing negative charge, is compensated by the decrease in nuclear charge in the K capture decay in terms of the effective potential experienced by the valence electrons. This is illustrated in Figure 34. With this assumption we see that the K capture case is rather simple because we can approximate the valence electron configuration to remain unperturbed after the  $1s$  vacancy creation. The photoionization process, however, requires a thorough investigation.

### 5.1.2 Relaxation after $1s$ Vacancy Creation

The Hamiltonian describing the system relaxes from  $H_0$  in the ground state to  $H_1$  in the  $1s$  intermediate state during the time  $t_0$  (see Chapter 4 and Figure 34). We observe approximately equal fluorescence energies after photoionization and K capture and we conclude that the relaxation of the electrons into the new orbitals, *i.e.* their adjustment to the new effective potential, is much faster than the lifetime of the  $1s$  vacancy. This is supported by the observation that the  $K\beta$  emission in metallic Mn and  $^{55}Fe$  is observed at identical fluorescence energies [116, 16]. The question is whether the electrons that occupy the  $3d$  orbitals follow this adjustment adiabatically, *i.e.* remain in their orbitals or whether configurations with higher energies are populated after the relaxation. I addressed the problem of double excitations in Chapter 4 and mentioned that little is known about valence shake-up and shake-off transition probabilities in  $3d$  metal compounds. The charge transfer scheme can be viewed as a valence electron monopole shake transition since the ligand orbital has the same irrep as the metal  $3d$  orbital. In our model, this monopole transition is driven by the sudden change in effective potential via the core-hole-d-electron potential  $U_{cd}$  in accordance with the theory introduced by Carlson and Nestor and further developed by others [33, 97]. It is, of course, here only treated empirically by changing the relative order of the configurations and thus ‘artificially’ occupying the higher (anti-bonding) configuration. Furthermore, the intensity of the shake transition is adjusted empirically by the hybridization parameters

### Mn Photoexcitation versus $^{55}\text{Fe}$ K-Capture

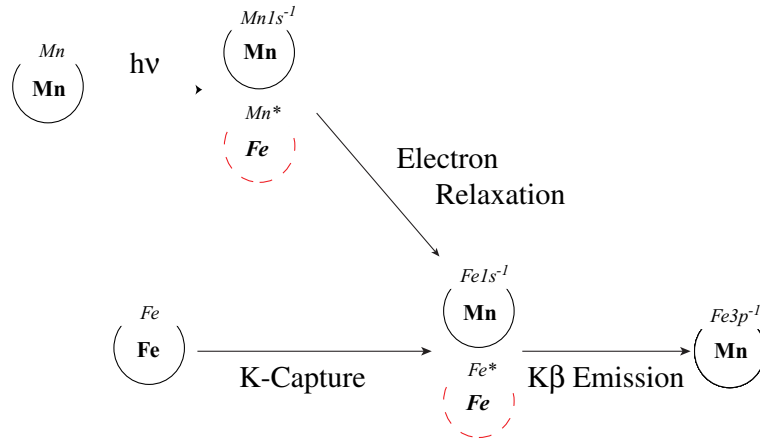


Figure 34: Comparison of photoionization in Mn and K capture in  $^{55}\text{Fe}$ . The **bold** element symbols inside the half circles represent the nuclei (Fe  $Z=26$ ; Mn  $Z=25$ ). The italic element symbols on the half circles represent the electronic configurations. In the dashed half circle I symbolically included the  $1s$  hole in the nuclear charge. The illustration therefore has to be understood with respect to the effective nuclear charge experienced by the valence electrons. An asterisk at the italic element symbol shows that the  $1s$  hole was included in the nuclear charge and the element symbol that represents the nucleus is printed bold italic. Immediately after the photoionization process we have a  $\text{Mn}^*$  configuration with a **Fe** nuclear charge. The electron shells therefore relax into a  $\text{Fe}^*$  configuration. No electronic valence shell relaxation occurs after K capture. In the diagram I assume that the relaxation is faster than the  $1s$  lifetime, i.e. the relaxation occurs before the  $\text{K}\beta$  emission.

and the charge transfer energy. In our model we include only one shake configuration due to limited computing power. Higher shake-ups will be lower in intensity because the shake probability scales with the wavefunction overlap and we expect the conclusions that we will draw not to be changed by more elaborate calculations.

In the photoionization experiment, the  $1s$  excited state will exhibit populated energy levels at energies higher than that of the lowest  $1s$  excited state. We therefore have to ask whether those higher lying  $1s$  excited states decay into the lowest  $1s$  state before the  $\text{K}\beta$  emission or whether they decay directly into a final state with a  $3p$  hole and thus contribute to the  $\text{K}\beta$  spectrum. In the following quantitative treatment of the problem I start with an investigation of the  $1s$  intermediate state.

#### 5.1.3 The $1s$ Intermediate State

$\text{K}\beta$  spectroscopy is a second order optical process and the question arises how to appropriately deal with the  $1s$  intermediate or fluorescence initial state. This state is reached in a photoexcitation experiment via a  $1s$  photoionization (XPS). I will treat this transition in the framework of the charge transfer model using two configurations. The anti-bonding combination obtains intensity if the ordering of the configurations changes as explained in

Chapter 3. This change is caused by the core-hole-d-electron Coulomb potential  $U_{1s3d}$ . The populated final states of the  $1s$  XPS are then spread over several eV. Figure 35 (a) shows the photoexcited  $1s$  intermediate states obtained in the charge transfer model. The charge transfer energy was set to  $\Delta=7$  eV for MnO which is the splitting of the two configurations in the ground state.  $U_{1s3d}$  was set to 9 eV and the splitting between the two configurations in the  $1s$  intermediate state is  $\Delta-U_{1s3d}=-2$  eV [21]. The ordering of the configurations is shown on the right of Figure 35 and in Figure 36. The complete set of the computational parameters is given in Table 5. The bonding and anti-bonding combination are split by 6.8 eV and the anti-bonding combination has 15% of the total intensity. Other states between the bonding and anti-bonding combination are weakly populated. They are symmetry mixed states that can be neglected for the present purpose because they are too weak to influence the  $K\beta$  spectrum. In the following I will refer to the two strong features as the low- and the high-lying  $1s$  intermediate state, respectively. It is interesting to note that Hansen calculated *ab initio* for Mn atoms that the  $3d^6(^5D)4s^6D$  term shifts below the  $3d^54s^2^6S$  term when a  $3p$  electron is removed [137]. This demonstrates the analogy between  $4s$  to  $3d$  shake processes in atoms and ligand-to-metal charge transfer in molecules and solids.

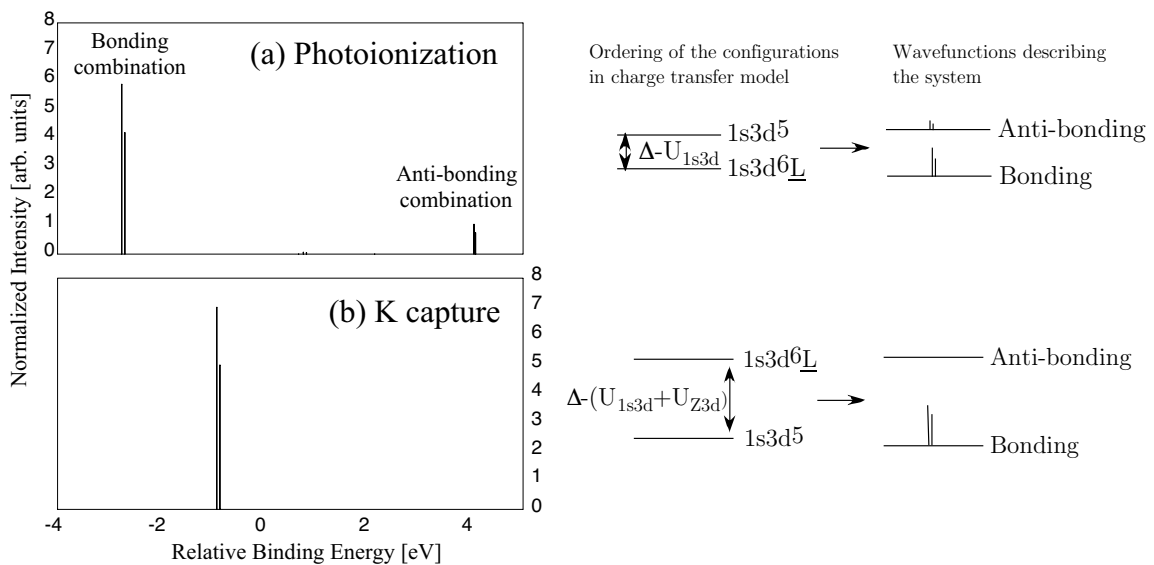


Figure 35: Calculated  $1s$  intermediate states for (a) photoionization in MnO and (b) K capture in  $Fe_2O_3$ . A  $1s$  XPS charge transfer calculation was performed for photoionization. The intermediate states after K capture are reached via annihilation of a  $1s$  electron by a proton. The ordering of the two configurations in the charge transfer model is shown on the right. The two configurations reorder in (a) due to the core hole effect while the ground state splitting is maintained in (b) if one assumes  $U_{1s3d}=-U_{Z3d}$ . The two configurations form the bonding and antibonding combinations that describe the electronic state of the system as explained in Chapter 3. Each populated combination is split by the  $(1s,3d)$  exchange interaction.

If we assume that the populated  $1s$  anti-bonding states in MnO after photoionization do not decay into the bonding states before the  $3p$  to  $1s$   $K\beta$  transition we can take the  $1s$  XPS final states as the  $K\beta$  fluorescence initial states. I will show below that comparison to the K capture data indicates that the populated anti-bonding states contribute to the  $K\beta$  spectrum of MnO after photoionization. But first we have to determine the  $1s$  intermediate

states that are reached after K capture. The correct Hamiltonian to describe the  $1s$  vacancy creation after K capture would be a nuclear  $\beta$ -decay like operator that mainly acts on the nucleus [80]. I neglect nuclear effects on the x-ray emission spectra (see Chapter 1.3). The effect of the K capture Hamiltonian on the electron shell is an annihilation of a  $1s$  electron. The same intermediate states are reached in a  $1s$  XPS neglecting interaction of the outgoing electron with the remaining ion. However, in the K capture process an additional term has to be added to the Hamiltonian that accounts for the change in nuclear charge. To simplify the problem one can use the same charge transfer Hamiltonian for K capture and XPS and reduce  $U_{cd}$  that acts on the  $3d$  electrons by the potential due to the additional nuclear charge. For a  $1s$  hole it is a good approximation to assume  $U_{1s3d} = -U_{Z3d}$  where  $U_{Z3d}$  denotes the change in potential experienced by the  $3d$  electrons caused by the decrease in atomic number. As a result the relative ordering of the two configurations  $|3d^5\rangle$  and  $|3d^6\bar{L}\rangle$  does not change and the anti-bonding combination is not populated. The  $K\beta$  fluorescence initial states after K capture are shown in Figure 35 (b).  $\Delta$  was set to 3.5 eV for  $\text{Fe}_2\text{O}_3$  [21]. Only the  $(1s, 3d)$  exchange split bonding combination is populated.

The ordering of the configurations in the charge transfer model is shown in Figure 36. The  $1s$  XPS mechanism was explained. The question remains how to deal with the change of the core hole from  $1s$  to  $3p$ . Taguchi *et al.* give a change of  $U_{cd}$  between the two core holes in Mn of 1 eV, *i.e.* in our case  $U_{3p3d} = 8$  eV [126]. The configurations are then split by  $\Delta - U_{3p3d} = -1$  eV in the final state of the photoionization experiment in MnO. Consequently one has to assume that in the K capture experiment the splitting between the two configurations changes, too, upon a  $3p$  to  $1s$  transition. While for photoionization the decrease in  $U_{cd}$  when going to a higher shell core hole seems established [42, 65], it is not clear for the K capture case how to deal with the change in core hole potential. The decrease in nuclear charge after K capture is better screened by a  $1s$  hole than by a  $3p$  hole in terms of the effective potential experienced by the  $3d$  electrons. While we approximated before  $|U_{1s3d}| = |U_{Z3d}|$  it now holds that  $|U_{3p3d}| < |U_{Z3d}|$ . This means that the  $3d$  electrons will adjust to a lower  $Z$ . The ground state charge transfer energy of MnO ( $Z=25$ ) is larger than that of  $\text{Fe}_2\text{O}_3$  ( $Z=26$ ), *i.e.* in this case lower  $Z$  corresponds to a larger charge transfer energy. These very rough, qualitative arguments suggest that the separation between the two configurations will increase for  $\text{Fe}_2\text{O}_3$  after K capture upon the  $3p$  to  $1s$  transition. However, I can only guess a value for  $U_{3p3d}$  after K capture and the inaccurate treatment of the change of the core-hole-d-electron potential  $U_{1s3d}$  to  $U_{3p3d}$  introduces an uncertainty in the theoretical results. I will use  $U_{1s3d} = U_{3p3d}$  and discuss the influence of the potential  $U_{3p3d}$  and other empirical parameters on the calculated spectra below.

#### 5.1.4 Final State Lifetime Broadening

Before comparing the theoretical results for the  $K\beta$  spectra with the experimental data the calculated stick spectra have to be convoluted with the lifetime and instrumental broadening. A  $K\beta$  spectrum is lifetime broadened by the  $1s$  intermediate state as well as the  $3p$  final state lifetime. The latter imposes considerable difficulties. The  $3p$  final states mainly decay non-radiatively via a Coster-Kronig (CK) or a super-Coster-Kronig decay (sCK) [127]. Calculations by several authors showed that the decay rates strongly depend on the multiplet term of the final state and they could successfully explain the suppression of the low-spin components in the  $3p$  XPS of atomic Cr and Mn [137] and in the  $K\beta$  spectra of Mn com-

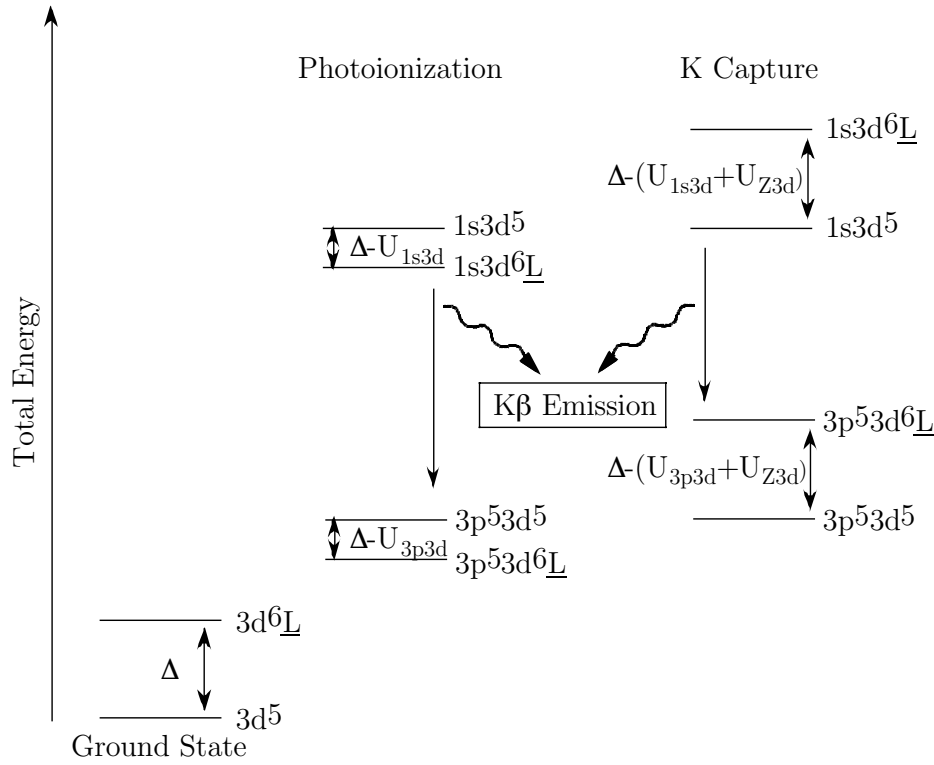


Figure 36: Ordering of the two configurations in the charge transfer model for the  $K\beta$  emission in an  $n=5$  system in the ground,  $1s$  intermediate and  $K\beta$  final states for photoionization and  $K$  capture. The scheme illustrates the inversion of the ordering after photoionization for the case  $U_{1s3d} > \Delta$ . For  $K$  capture  $U_{Z3d}$  is the potential due to the change in nuclear charge. If  $U_{Z3d} = -U_{1s3d}$  the ordering of the two configurations does not change in the  $1s$  intermediate state. In the  $K\beta$  final states  $U_{1s3d}$  is replaced by  $U_{3p3d}$ . The two configurations form the bonding and antibonding combinations that describe the electronic state of the system as explained in Chapter 3.

pounds [127]. For the latter, satisfactory agreement between theory and experiment was achieved for  $MnO$  and  $MnF_2$  by assuming a linear relation between the final state energy and the lifetime broadening of the final states. Hansen *et al.* obtained 0.13 eV and 2.5 eV FWHM including CI for the  $3p^53d^5(^6S)$   $^7P$  and  $^5P$  final states of atomic Mn, respectively [137]. They found a considerable decrease in the final state lifetime in CI calculations over single-configuration calculations for Mn atoms.

To account for the term dependent final state lifetime broadening I followed the procedure suggested by Taguchi *et al.* [127] and assumed a linear increase of the final state lifetime broadening towards lower fluorescence energies ( $FWHM \sim -0.2\omega$ ). I chose 0.4 eV as the starting value for this linear increase at the final state with highest fluorescence energy. The value is motivated by the value for atoms (0.13 eV) assuming shorter lifetime in the solid due to stronger CI. This is of course a gross simplification of the final state lifetime problem. The conclusions I will draw are not affected by this simplification. It is desirable for future theoretical works on  $K\beta$  spectroscopy to fully account for the term dependent lifetimes in the final states. The broadenings were applied to the stick spectra using a self-written routine

using the program package *Matlab*.

### 5.1.5 Calculated $K\beta$ Spectra

The calculated  $K\beta$  spectra are shown in Figure 37. The energy scale is shifted to coincide with the experimental fluorescence energies. Both theoretical spectra have the same center of mass energy. I chose as parameters for both calculations (K capture in  $\text{Fe}_2\text{O}_3$  and photoionization in  $\text{MnO}$ ):  $V(E_g)=2.0$  eV,  $V(T_{2g})=-1.0$  eV and  $10Dq=1.0$  eV. For photoionization I used  $U_{1s3d}=9$  eV and for K capture  $U_{1s3d}+U_{Z3d}=0$  eV.  $U_{3p3d}$  was set equal to  $U_{1s3d}$ . The influence of the empirical parameters on the spectra will be discussed below. The  $^{55}\text{Fe}_2\text{O}_3$  K capture spectrum was calculated using the one populated  $1s$  intermediate state (bonding combination) while for the  $\text{MnO}$  photoionization spectrum two  $K\beta$  spectra were calculated corresponding to the two strongly populated  $1s$  intermediate states, *i.e.* the bonding and anti-bonding combination. The final state lifetime broadening applied to the spectra is shown in Figure 37 (d). The spectra in Figure 37 were further convoluted with a 0.8 eV FWHM Gaussian to account for instrumental broadening.

Comparison of the  $K\beta$  spectra for K capture and photoionization resulting from the  $1s$  bonding combination shows that the low energy shoulder of the  $K\beta_{1,3}$  line is less pronounced after photoionization. It was shown in Chapter 3 that the quintet states are strongly effected by CI while the septet state hardly changes. The spectrum from the  $1s$  anti-bonding combination (Figure 37 (c)) has a  $K\beta_{1,3}$  and  $K\beta'$  structure, too, but the  $K\beta_{1,3}$  peak is split. If the  $1s$  anti-bonding combination in the intermediate state contributes to the  $K\beta$  spectrum we have to add the spectra shown in Figure 37 (b) and (c). This will mainly result in a broadening of the  $K\beta_{1,3}$  peak on the low energy side.

The splitting between  $K\beta_{1,3}$  and  $K\beta'$  is due to the ( $3p,3d$ ) exchange interaction as described in Chapter 3. The splitting appears reduced in the photoionization experiment compared to the K capture data. The magnitude of the splitting depends on the number of unpaired spins in the  $3d$  shell. The final states after photoionization have a stronger  $3d^6\bar{\underline{L}}$  admixture than the final states after K capture. This means that the net spin in the  $3d$  shell is reduced due to the core hole effect in photoionization and the splitting between  $K\beta_{1,3}$  and  $K\beta'$  is smaller in photoionization than after K capture. Besides this real reduction of the exchange splitting there is an apparent reduction of the splitting of the two peaks because of additional final states between the two peaks that are populated after photoionization (Figure 37).

Table 5 gives the values for the atomic Slater integrals used for the calculations together with the values set for the charge transfer energy  $\Delta$  and the core-hole-d-electron attraction  $U_{cd}$ . For the  $3p^5 3d^5$  ( $3p^5 3d^6\bar{\underline{L}}$ ) final state configuration the  $F_{dd}^2$ ,  $F_{dd}^4$  and  $F_{pd}^2$  direct and the  $G_{pd}^1$  and  $G_{pd}^3$  exchange integrals were calculated as well as the  $\zeta_{3p}$  spin-orbit coupling. The Coulomb integrals  $F_{pd}$  and  $G_{pd}$  were scaled down to 70% of their single configuration values in order to account for intra-atomic configuration interaction effects [36]. The scaling was set such that the  $K\beta_{1,3}$ - $K\beta'$  separation observed in the K capture experiment was approximately reproduced in the calculated spectrum. The same scaling was then used for the photoionization and the K capture calculations. For the calculation of the  $1s$  intermediate states, the  $1s3d^5\epsilon p$  and  $1s3d^6\bar{\underline{L}}\epsilon p$  channels were taken into account and no interaction of the continuum electron with the ionized atom was considered.

In order to quantify the experimental and theoretical results for the  $K\beta$  emission I reduced

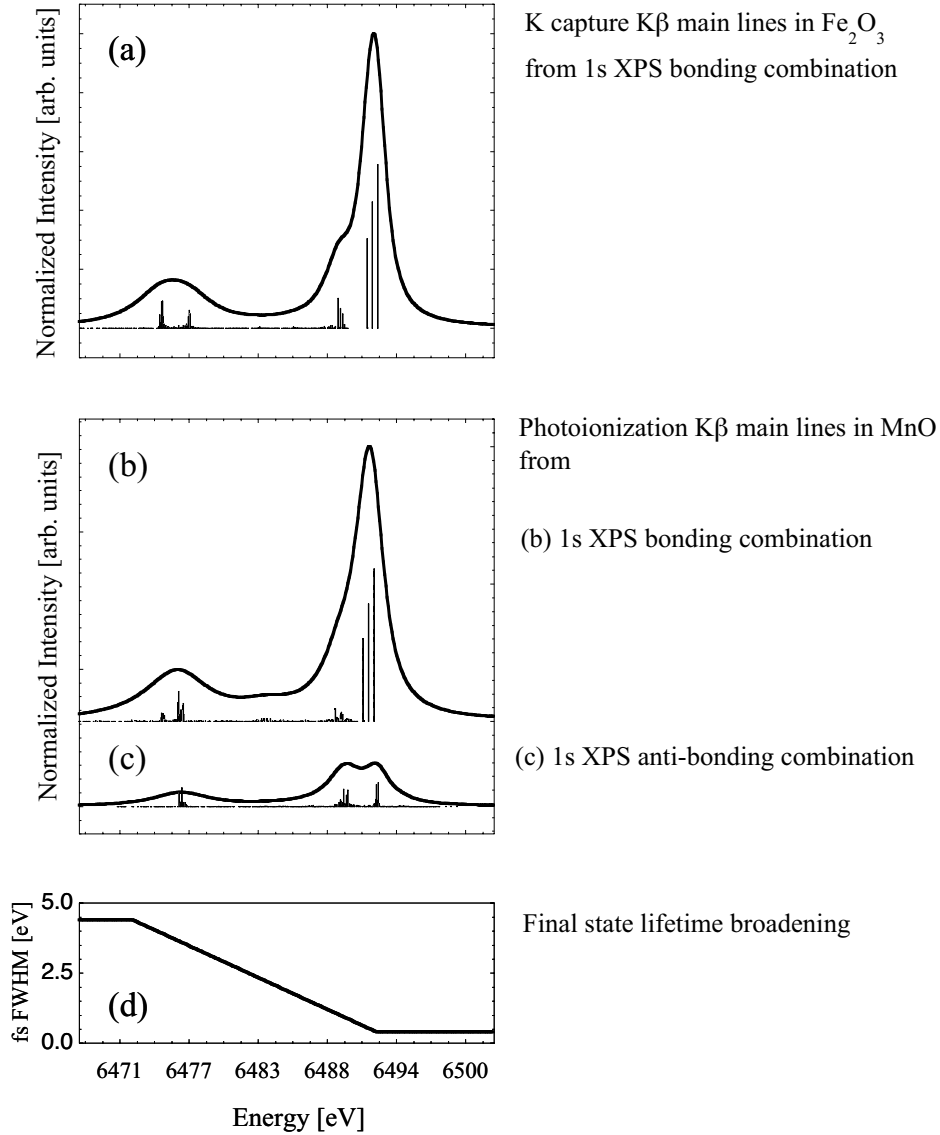


Figure 37: Calculated  $K\beta$  spectra for (a)  $K$  capture in  $^{55}Fe_2O_3$  and (b),(c) for  $MnO$  after photoionization. For the latter, part (b) shows the spectrum resulting from the low-lying  $1s$  intermediate state (bonding combination) while (c) shows the spectrum resulting from the high-lying  $1s$  intermediate state (anti-bonding combination). The final state (fs) lifetime broadening applied to the spectra is given in (d).

the spectra to their 1st ( $M_1$ ), 2nd ( $M_2$ ) and 3rd moments ( $M_3$ ) defined as

$$M_1 = \frac{\sum c_i e_i}{\sum c_i} \quad (55)$$

$$M_2 = \frac{\sum c_i (M_1 - e_i)^2}{\sum c_i} \quad (56)$$

$$M_3 = \frac{\sum c_i (M_1 - e_i)^3}{\sum c_i} \quad (57)$$

where  $c_i$  is the count rate at energy  $e_i$ . An energy range has to be picked for the moment

Table 5: Parameters used in the charge transfer calculations. For all configurations  $V(E_g)$  was set to 2.0.  $V(T_{2g})$  is half this value. For each state the separation of the two configurations ( $\Delta$  or  $\Delta-U_{c3d}$ ) is given in the third column. All configurational parameters are given in eV units.

Ground State	$3d^5$	$\Delta=7.0^a$ $\Delta=3.5^b$	$3d^6\underline{L}$
	$\zeta_d=0.04$ $F_{dd}^2=10.32$ $F_{dd}^4=6.41$		$\zeta_d=0.04$ $F_{dd}^2=9.07$ $F_{dd}^4=5.59$
Intermediate State	$1s3d^5$	$\Delta-U_{1s3d}=-2^a$ $\Delta=3.5^b$	$1s3d^6\underline{L}$
	$\zeta_d=0.06$ $F_{dd}^2=12.12$ $F_{dd}^4=7.58$ $G_{sd}^2=0.06$		$\zeta_d=0.05$ $F_{dd}^2=11.05$ $F_{dd}^4=6.87$ $G_{sd}^2=0.05$
Final State	$3p^53d^5$	$\Delta-U_{3p3d}=-2^a$ $\Delta=3.5^b$	$3p^53d^6\underline{L}$
	$\zeta_d=0.05$ $\zeta_p=0.80$ $F_{dd}^2=11.47$ $F_{dd}^4=7.18$ $F_{pd}^2=12.40$ $G_{pd}^1=15.40$ $G_{pd}^3=9.38$		$\zeta_d=0.04$ $\zeta_p=0.77$ $F_{dd}^2=10.43$ $F_{dd}^4=6.49$ $F_{pd}^2=11.64$ $G_{sd}^1=14.50$ $G_{sd}^3=8.75$

<sup>a</sup>photoionization in MnO

<sup>b</sup>K capture in Fe<sub>2</sub>O<sub>3</sub>

calculations. I chose the energies at 50% of the maximum  $K\beta_{1,3}$  intensity as the upper and lower limit for the energy range. This gives a rather small energy range in an effort to minimize the ambiguity resulting from the merely approximate treatment of the final state lifetime broadening. The stick spectra show that the main intensity of the peak comes from one final state term that is split by the  $3p$  spin-orbit interaction. The final state lifetime should hardly vary for the three components.

For the  $K\beta_{1,3}$  peak all three moments were calculated. For  $K\beta'$  only the first moment ( $M_1'$ ) was calculated using an energy range that includes intensities down to 70% of the  $K\beta'$  peak intensity. The first moment can be interpreted as the 'center of mass' while the second moment is related to the width and the third moment to the asymmetry of the spectral feature.

The results for the experimental as well as the theoretical spectra are summarized in Table 6. The energy scale for the theoretical spectra was shifted such that  $M_1$  for  $^{55}\text{Fe}_2\text{O}_3$  coincides with the experimental value. The other parameters in Table 6 are not effected by this shift. The first moment for  $K\beta'$  was used to determine the difference  $M_1-M_1'$  between  $K\beta_{1,3}$  and  $K\beta'$ . The statistical errors have been calculated for the experimental spectra and found to be negligible within the accuracy given in Table 6. Hence, only for  $M_1$  an error is given due to the uncertainty in the relative energy calibration of the spectrometer.

Table 6: *Experimental and calculated moments for MnO and  $^{55}\text{Fe}_2\text{O}_3$ . Four sets of parameters are given for MnO after photoionization. In (a) and (b) the same final state lifetime broadening as for  $^{55}\text{Fe}_2\text{O}_3$  after K capture was applied. Only the low-lying 1s intermediate state is included in (a) while in (b) both 1s intermediate states are included. In (c) and (d) a greater final state lifetime broadening was applied. In (c) only the low-lying 1s intermediate state is included while in (d) both 1s intermediate states are included. The error for  $M_1$  in MnO is due to the experimental uncertainty for the relative energy calibration. The errors for  $M_2$  and  $M_3$  are statistical errors and the error in  $M_1-M_1'$  is due to  $\Delta E_{R''}$  (see Chapter 2).*

	$M_1^a$ [eV]	$M_2$ [ $10^{-1}$ (eV) $^2$ ]	$M_3$ [ $10^{-1}$ (eV) $^3$ ]	$M_1-M_1'$ [eV]
<b>Experiment</b>				
$^{55}\text{Fe}_2\text{O}_3$	0.00	4.33 (2)	-0.13 (3)	16.50 (4)
MnO	-0.56(7)	8.69 (2)	-1.35 (4)	14.80 (4)
<b>Theory</b>				
$^{55}\text{Fe}_2\text{O}_3$	0.00 <sup>b</sup>	3.89	-0.11	16.34
MnO				
(a)	-0.31 <sup>b</sup>	4.23	-0.18	15.63
(b)	-0.37 <sup>b</sup>	5.42	-0.49	15.50
(c)	-0.40 <sup>b</sup>	6.56	-0.47	15.50
(d)	-0.51 <sup>b</sup>	8.72	-1.20	15.31

<sup>a</sup> -6492.80 eV

<sup>b</sup>Shifted such that  $M_1$  of theoretical  $^{55}\text{Fe}_2\text{O}_3$  spectrum coincides with experiment.

The experimental values in Table 6 confirm the results from a visual inspection of the spectra:  $M_1$  is shifted to lower energies for MnO after photoionization,  $M_2$  is about twice as large and  $M_3$  for MnO is about ten times as large as the corresponding values for  $^{55}\text{Fe}_2\text{O}_3$  after K capture. The difference  $M_1-M_1'$  is by 1.7 eV smaller for MnO.

The good agreement of the theoretical values for  $^{55}\text{Fe}_2\text{O}_3$  K capture for  $M_2$  and  $M_1-M_1'$  with the experiment is due to the adjustment of the parameters for the final state lifetime

broadening and the scaling of the Coulomb integrals. The asymmetry  $M_3$  is well reproduced in the theoretical spectrum.

Four different cases for the MnO photoionization calculations are considered. The parameters in (a) only include the lowest  $1s$  intermediate state. This case already reproduces the correct trend for all parameters.  $M_1$  is shifted to lower energies,  $K\beta_{1,3}$  and  $K\beta'$  move closer together ( $M_1-M_1'$ ) and the spectrum is broader and more asymmetric than for K capture. The parameters in (b) were obtained from the MnO  $K\beta$  spectrum that includes both strong  $1s$  intermediate states. The high-lying  $1s$  intermediate state broadens the spectrum on the low energy side resulting in a considerable increase for  $M_3$ . The agreement with experiment is better for all parameters. In (a) and (b) I assumed the same final state lifetime broadening for K capture and photoionization.

In order to investigate the influence of the final state lifetime broadening I determined the moments for a different broadening in MnO after photoionization. In Table 6 (c) and (d) I assumed 0.9 eV FWHM instead of 0.4 eV FWHM at high fluorescence energies and assumed the same linear increase of the broadening with decreasing fluorescence energy ( $-0.2\omega$  FWHM). A qualitative argument for the shorter final state lifetime can be given as follows: In a simplified one-electron LS coupling picture it can be argued that a sCK decay is forbidden for a septet final state because the spin of a single  $3d$  electron would have to flip to fill the  $3p$  vacancy (see Figure 16). In the charge-transfer picture this peak has a  $|3d^6\bar{L}\rangle$  admixture and a sCK decay no longer is forbidden. This suggests to assume a relation between the percentage of  $|3d^6\bar{L}\rangle$  admixture and the final state lifetime in the  $K\beta$  spectrum. The results for the moments including only the lowest  $1s$  intermediate state are shown in Table 6 (c). The agreement between experiment and theory is improved for all parameters compared to case (a) with equal final state lifetimes for K capture and photoionization.

At this point it is tempting to further increase the final state lifetime broadening in order to further improve the agreement with experiment. However, it is not possible to achieve good agreement for  $M_2$  and  $M_3$  simultaneously. A final state lifetime that would bring  $M_2$  of the theoretical spectrum to match with the experimental spectrum would result in a strong deviation between theory and experiment for  $M_3$ .

In Table 6 (d) the same lifetime broadening as in (c) was used but now the high-lying  $1s$  intermediate state was included for the calculation of the  $K\beta$  spectrum.  $M_1$ ,  $M_2$  and  $M_3$  are now very close to the experimental values while ( $M_1-M_1'$ ) is still off by 0.51 eV. This case gives the best agreement between theory and experiment for all four parameters.

The theoretical spectra corresponding to the four cases (a)-(d) are shown in Fig. 38. The different MnO photoionization simulations are compared to the same  $^{55}\text{Fe}_2\text{O}_3$  K capture simulation. The experimental results from Figure 33 are best reproduced for case (d). Finally, I compare in Figure 39 the experimental spectra with the best theoretical simulations. The agreement in the  $K\beta_{1,3}$  peak is very good except for a slight deviation in the low energy shoulder of the K capture spectrum. Towards lower energies ( $K\beta'$ ) the agreement is worse which is mainly due to the inaccurate treatment of the final state lifetime broadening.

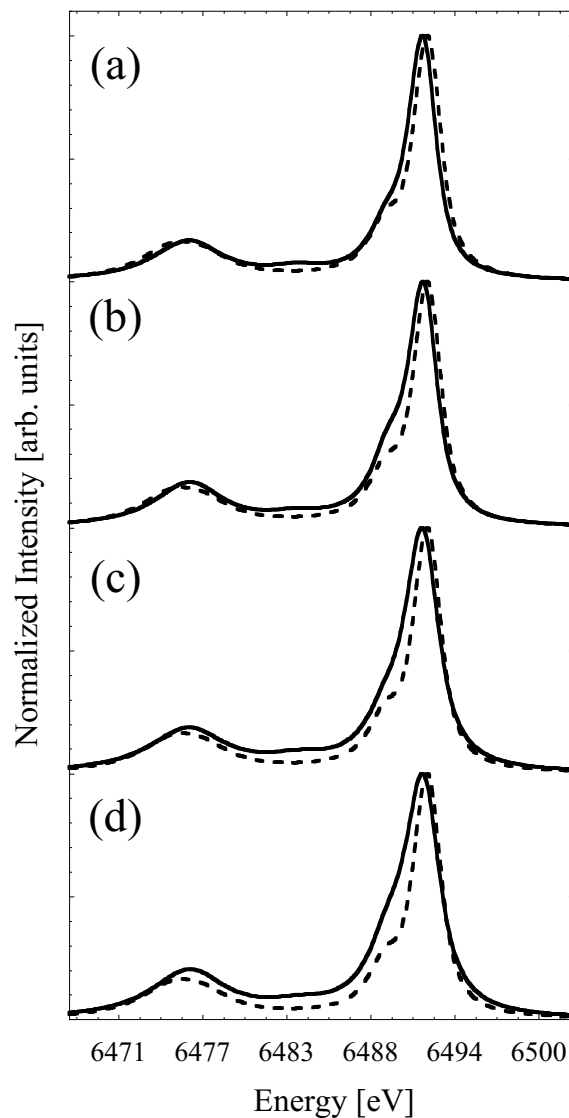


Figure 38: *Calculated  $K\beta$  spectra after photoionization in MnO (solid lines) and K capture in  $^{55}\text{Fe}_2\text{O}_3$  (dashed lines). The K capture spectra are the same in all four cases while four different MnO photoionization spectra are shown. In (a) and (b) the same final state lifetime broadening was applied. Only the low-lying  $1s$  intermediate state is included in (a) while in (b) both  $1s$  intermediate states are included. In (c) and (d) a greater final state lifetime broadening was applied. In (c) only the low-lying  $1s$  intermediate state is included while in (d) both  $1s$  intermediate states are included.*

### 5.1.6 Uncertainty Introduced by Empirical Parameters

The choice of empirical parameters in the calculations is not unique and the uncertainty has to be estimated. I performed calculations where I use (a)  $U_{1s3d}=U_{3p3d}$  and (b)  $U_{1s3d}=U_{3p3d}-1$  for K capture as well as photoionization. I find that the first moment of the  $K\beta_{1,3}$  peak shifts by 0.35 eV to lower energies for photoionization and by 0.14 eV for K capture for case (b). A change of the energy splitting of the two configurations influences the photoionization  $K\beta$  spectra more than for K capture because the K capture spectrum has a smaller admixture of

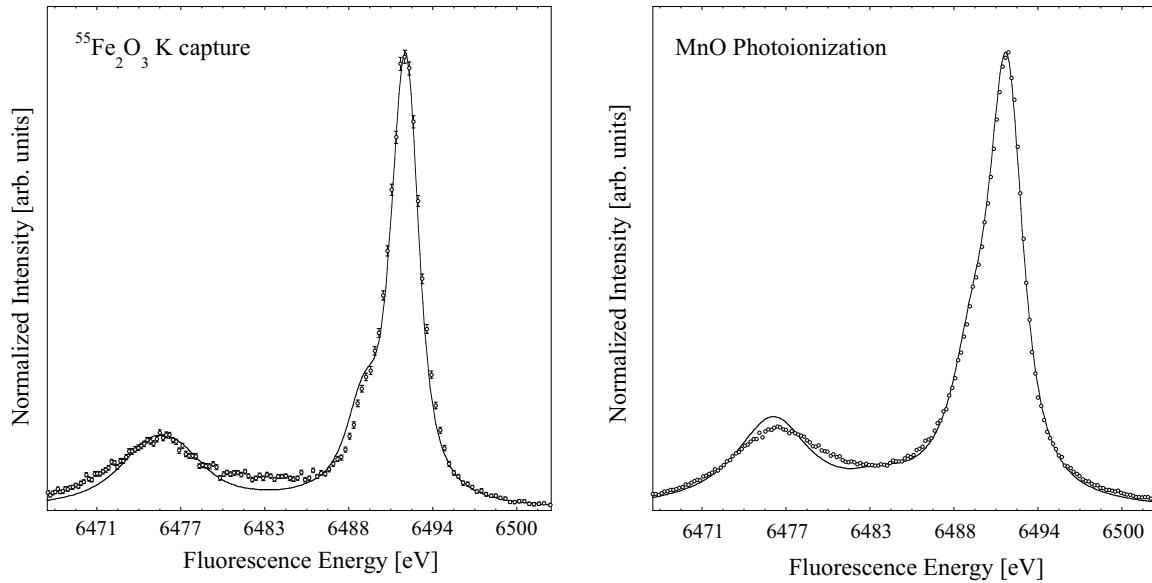


Figure 39: Comparison of experimental  $K\beta$  main lines with theoretical simulation for  $K$  capture in  $Fe_2O_3$  and photoionization in  $MnO$ . For the latter case (d) is shown that includes both  $1s$  intermediate states and an increased final state lifetime broadening compared to  $K$  capture.

the charge transfer configuration. I further find that the spectral shape expressed in terms of the second and third moment hardly changes for cases (a) and (b), neither for  $K$  capture nor for photoionization. Besides the core-hole-d-electron potential, I investigated the influence of the mixing terms and the ligand field splitting  $10Dq$  on the spectra. Assuming half and twice the values for  $V(E_g)$  and  $V(T_{2g})$  does not significantly influence the spectra and neither does the ligand field, as was already shown in Chapter 3. The strongest simplification is therefore the neglect of the change of the core hole potential between the intermediate and the final state. This will mainly influence the differences in calculated fluorescence energies for the two cases, *i.e.* the results for the first moment in Table 6.

### 5.1.7 Concluding Remarks

It can be concluded that both mechanisms, high-lying  $1s$  excited states as well as a change in the final state lifetime, have to be taken into account in order to explain the differences between  $K$  capture and photoionization. This conclusion is mainly based on the relative changes for the second and third moment between  $K$  capture and photoionization because they proved to be very stable for varying empirical parameters in the calculation. The first moment confirms the results. It is emphasized that the conclusions are based on trends between the spectra and not absolute values obtained in the calculations.

More accurate calculations to explain the differences between  $K$  capture and photoionization would include the intensities and fluorescence energies for states with higher shake-up as well as shake-off configurations. The measurements of  $KL\beta$  (L-shake-off) lines suggest that the fluorescence energies for shake-off transitions can be estimated using a simple  $Z+1$  model (see Chapter 4). This model yields higher fluorescence energies for the shake-off transitions

than for the  $K\beta$  lines. Thus, shake-off final states can be expected to appear on the high energy side of the  $K\beta_{1,3}$  peak. The experiment mainly shows a broadening on the low energy side which can be explained in the charge transfer picture that is equivalent to a monopole shake-up. The spectra show slightly higher intensity after photoionization in the high energy tail of the  $K\beta_{1,3}$  line which could be due to shake-off final states. However, the intensities are much weaker and the dominating effects are included in the charge transfer model. KMM Radiative Auger Lines would appear on the low energy side of the  $K\beta$  peaks. However, we do not expect different branching ratios for the KMM decay path between K capture and photoionization. Hence, even if KMM lines contribute to the spectra we do not expect to see any differences between the different modes of excitation.

## 5.2 $K\alpha$ Lines

### 5.2.1 Motivation: Chemical Dependence of $K\alpha_1$ Linewidth

A summary of analyses of  $K\alpha$  lines in transition metal compounds is given in Meisel's book [94]. It was found that the width of the  $K\alpha_1$  line is roughly proportional to the 'nominal' number of unpaired  $3d$  electrons, *i.e.* the number of unpaired  $3d$  electrons as derived from the formal oxidation state of the metal atom. This proportionality is usually explained within the framework of multiplet theory. Meisel gives the following derivation: First it is assumed that no orbital angular momentum is connected with the valence electrons. This point was addressed in Chapter 3. If one then couples the total angular momentum  $J=S$  in the  $3d$  shell with  $j$  of the  $2p$  hole to a total angular momentum  $J_{tot}=S+j$  one obtains for the energies of the coupled states [94]:

$$E(J_{tot}) \propto [J_{tot}(J_{tot} + 1) - S(S + 1) - j(j + 1)] \quad (58)$$

The  $K\alpha_1$  full width at half maximum (FWHM) will be related to the splitting between adjacent states which is proportional to  $J_{tot}$  (Landé interval rule [26]):

$$\Delta E(J_{tot}) = E(J_{tot}) - E(J_{tot} - 1) \propto J_{tot} = S + j \quad (59)$$

We have seen in Chapter 3 that for zero  $3d$  orbital angular momentum the  $K\alpha_1$  line is solely split by the  $(2p, 3d)$  exchange interaction and only the exchange integrals enter the proportionality factor because the averaged direct  $(2p, 3p)$  Coulomb interaction is zero. One can therefore write:

$$\Delta E_{K\alpha_1} \propto aS = a\frac{n}{2} \quad (60)$$

where  $n$  is the nominal number of unpaired  $3d$  electrons and

$$a = \frac{2}{15}G_{2p3d}^1 + \frac{3}{35}G_{2p3d}^3$$

is the exchange parameter for a pair of  $2p$  and  $3d$  electrons, *i.e.* the averaged  $(2p, 3d)$  exchange integral. The  $K\alpha_1$  linewidth is thus shown to be proportional to the Slater exchange integrals and the nominal number of unpaired  $3d$  electrons. Alternatively, some authors [74, 125] use Van Vleck's theorem for the energy terms of a  $l^n s$  configuration [135, 119]. The splitting between the terms  $J_{tot}=S+1/2$  and  $J_{tot}=S-1/2$  where  $S$  is the spin quantum number of the configuration  $l^n$  is given by

$$\Delta E_{ex} = \frac{2S + 1}{2l + 1} G^l(s, l) \quad (61)$$

where  $G^l(s, l)$  is the two-electron exchange integral. Equation 61 is equivalent to the Landé interval rule [135]. The equation is exact in the framework of multiplet theory and gives more insight into the problem than equation 58 that assumes jj-coupling which is a very crude approximation for the  $2p$  final states in a transition metal [141]. In order for equation 61 to be applicable to our problem the  $3d$  electrons have to couple to an electron without orbital angular momentum. This is clearly not the case for the  $K\alpha$  lines. Furthermore, Van Vleck neglects spin-orbit interaction in his model which we cannot for a  $2p$  core hole.

The experimental observations cited, *e.g.* in references [94] and [74], do not seem to have an exact theoretical basis within multiplet theory. The property of equation 61 that we are interested in is that the exchange splitting is proportional to  $S$  times the averaged ( $2p, 3d$ ) exchange integral which is also expressed in equation 60. I note that for a  $3d^5$   ${}^6S$  parent configuration with a  $p$  hole the  ${}^{5,7}P$  splitting is  $12/15G_{3p3d}^1 + 36/70G_{3p3d}^3 = 6a = (2S+1)a$  with  $S=5/2$  and  $a$  being the exchange parameter [119]. I therefore assume that for a system with zero valence angular momentum the exchange splitting is proportional to the valence spin  $S$  times the averaged exchange integral as expressed in equation 60. If the width of the  $K\alpha$  lines is dominated by the exchange interaction one can therefore expect to approximately see this proportionality in the full width at half maximum of the  $K\alpha$  lines. For the lack of a proper theoretical explanation in the literature we have to content with this intuitive approach. It is noted that symmetry mixing and configuration interaction have been neglected in the outlined considerations.

The simple relation 60 contains besides other approximations two important assumptions. First, the  $3d$  orbital angular momentum is assumed to be zero which can be justified by the aforementioned ‘quenching’ of the orbital angular momentum in  $3d$  transition metals. Even if the  $3d$  orbital angular momentum is larger than zero we might still observe a rough proportionality if the linewidth is dominated by the exchange interaction. However, no general statement can be made in this case. Second, the energy splitting resulting from the exchange interaction between the  $2p$  hole and the valence electrons is set proportional to  $a/2$ . This is a very crude approximation because it invokes a purely ionic picture. The exchange energy is due to the Coulomb energy that depends on the distance between the interacting electrons. It is therefore important to find out where the valence electrons in a compound actually are using, for example, density functional theory and, following that, how the net electron spin is distributed between the metal and its ligands.

Recently, the  $K\alpha$  emission in  $FeO$ ,  $Fe_2O_3$ ,  $K_3Fe(CN)_6$  and  $K_4Fe(CN)_6$  after photoionization was measured by Kawai *et al.* [74]. They analyzed the full width at half maximum (FWHM) of the  $K\alpha_1$  line and its dependence on the nominal number of unpaired  $3d$  electrons in the metal valence shell.  $Fe_2O_3$  is a high-spin  $Fe(III)$  compound and the nominal spin state is  $S=5/2$ .  $FeO$  contains high-spin  $Fe(II)$  and the nominal spin state is  $S=2$ .  $K_3Fe(CN)_6$  and  $K_4Fe(CN)_6$  contain low-spin  $Fe(III)$  and  $Fe(II)$  due to the strong ligand field exerted by the cyanide groups and the nominal spin states are  $S=1/2$  and  $S=0$ , respectively. Theoretically, this can be seen from the Tanabe-Sugano diagram [124] together with the calculated ligand field splitting  $10Dq$  of 5 eV that is given in reference [74]. Experimental evidence other than K fluorescence emission for a low-spin valence electron configuration in Fe cyanides is given by measurements of the magnetic susceptibility [54]. The point groups of the complexes can be best approximated in cubic symmetry. The ground state terms neglecting  $3d$  spin-orbit interaction are  ${}^5T_2$ ,  ${}^6A_1$ ,  ${}^2T_2$  and  ${}^1A_1$  for  $FeO$ ,  $Fe_2O_3$ ,  $K_3Fe(CN)_6$  and  $K_4Fe(CN)_6$ , respectively. The difference to the studies discussed in Meisel’s book is that Kawai *et al.* used covalent low-spin complexes as examples for  $S=0$  and  $S=1/2$  systems instead of ionic compounds with high metal oxidation states. The results by Kawai *et al.* are shown in Figure 40 where the measured  $K\alpha_1$  FWHM is plotted versus the nominal number of unpaired  $3d$  electrons. The FWHM hardly changes between  $FeO$  ( $n=4$ ) and  $Fe_2O_3$  ( $n=5$ ) and for both compounds the FWHM is smaller than an extrapolation using the FWHM of  $K_3Fe(CN)_6$  and  $K_4Fe(CN)_6$  would suggest. The proportionality predicted by equation 60 is not found.

Kawai *et al.* calculated the electron molecular orbitals in the ground state and in the  $1s$

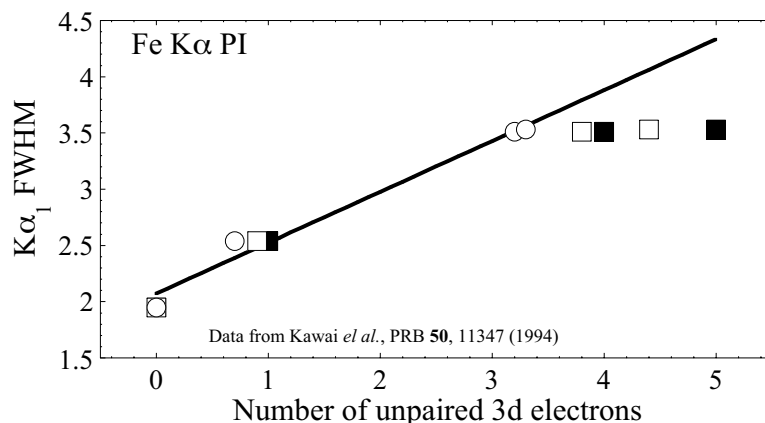


Figure 40: Measured  $K\alpha_1$  FWHM in Fe compounds after photoionization versus number of unpaired 3d electrons; (a) full boxes: nominal number of unpaired 3d electrons, (b) empty boxes: the effective ground state number of unpaired 3d electrons, (c) circles: the effective 1s excited state number of unpaired 3d electrons. All values were taken from reference [74]. The linear regression is shown for (c) which represents the best fit (see Table 7).

excited state of octahedral  $[MX_6]^q$  (M=metal, X=ligand, q=charge) model clusters using the spin-unrestricted discrete-variational (DV) Hartree-Fock-Slater ( $X\alpha$ ) molecular orbital method. By means of a Mulliken population analysis [100] they extracted the effective number of unpaired metal 3d electrons in the ground state and in the 1s excited state. It is noted that in order to describe the  $K\alpha$  emission the correct approach would be to calculate the effective number of unpaired 3d electrons in the final states with a 2p hole. However, the values hardly vary for calculations with a 1s and a 2p hole [72]. Kawai *et al.* obtain 0.0 for  $K_4Fe(CN)_6$  in both cases and 0.9 and 0.7 for  $K_3Fe(CN)_6$  in the ground state and in the excited state, respectively. For  $Fe_2O_3$  they calculate 4.4 in the ground state and 3.3 in presence of a 1s hole and for FeO they obtain 3.8 and 3.2, respectively. Thus, while the spin state of the covalent cyanides does not or barely change upon creation of a 1s vacancy a dramatic change occurs for the more ionic  $Fe_2O_3$  and FeO. Furthermore, the almost equal effective numbers of unpaired 3d electrons in the  $K\alpha$  final states of Fe and  $Fe_2O_3$  give rise to almost identical  $K\alpha$  spectra.

They conclude that multiplet splittings due to the exchange interaction cannot explain the  $K\alpha_1$  linewidth. Instead, ligand-to-metal charge transfer has to be included for a correct analysis. Kawai *et al.* state that the  $K\alpha_1$  linewidth does therefore not reflect the spin state of the metal atom in the compound. Even though the relation between  $K\alpha$  linewidth and exchange interaction is based on a crude model it is important to first correctly determine the ( $2p, 3d$ ) exchange interaction in a poly-nuclear complex before the proportionality given in equation 60 is abolished. In the following I therefore discuss the ( $2p, 3d$ ) exchange energy in a poly-nuclear complex and show that a proportional relation between  $K\alpha_1$  linewidth and metal spin state can be obtained if the same assumptions as in the free atom are made. Experimental evidence supporting this interpretation will be given.

### 5.2.2 ( $2p, 3d$ ) Exchange Interaction in a Poly-Nuclear System

In the following the problem of calculating the exchange interaction of the  $2p$  hole with the valence electrons in a poly-nuclear complex is addressed. The two spin orientations are denoted by  $\alpha$  and  $\beta$ , respectively. For a free atom/ion one can write:

$$\Delta E_{ex}^{2p3d} = \sum_{\mu,\nu} \langle 2p_{\nu}^{\alpha} 3d_{\mu}^{\alpha} | \frac{1}{r} | 3d_{\mu}^{\alpha} 2p_{\nu}^{\alpha} \rangle - \sum_{\mu,\nu} \langle 2p_{\nu}^{\beta} 3d_{\mu}^{\beta} | \frac{1}{r} | 3d_{\mu}^{\beta} 2p_{\nu}^{\beta} \rangle \quad (62)$$

*i.e.* the exchange integrals for all pairs of spin parallel  $2p$  and  $3d$  electrons is calculated and the difference is the exchange splitting between the configurations with  $\alpha$  or  $\beta$  orientation of the unpaired  $2p$  electron spin relative to the  $3d$  electrons. The indices  $\mu, \nu$  describe the magnetic quantum numbers. The inter-electron distance is  $r$  and the indices are dropped for simplicity. The exchange integrals can be evaluated by a multipole expansion of  $1/r$ . Averaging over all magnetic quantum numbers leads to the exchange parameter  $a$  as given above which describes the average ( $2p, 3d$ ) electron pair exchange energy [36]. I have assumed above that for a system with zero valence shell orbital angular momentum the ( $p, d$ ) exchange splitting is proportional to the averaged ( $p, d$ ) two-electron exchange integral times the number of ( $p, d$ ) electron pairs with parallel spins. There is one unpaired  $2p$  electron in a  $K\alpha$  final state and counting over all  $3d$  electrons one obtains:

$$\Delta E_{ex}^{2p3d} \propto |n_{3d^{\alpha}} a - n_{3d^{\beta}} a| \quad (63)$$

$$= \Delta n_{3d} a \quad (64)$$

$\Delta n_{3d}$  is the nominal number of unpaired  $3d$  electrons and corresponds to  $n$  in equation 60. If we now turn to a poly-nuclear complex we see that equation 63 suggests to replace  $n_{3d^{\alpha, \beta}}$  by the respective effective numbers  $n_{3d^{\alpha, \beta}}^{eff}$  as obtained in a density functional treatment with subsequent population analysis. We then obtain an expression for the ( $2p, 3d$ ) exchange energy splitting in a poly-nuclear complex:

$$\Delta E_{ex} \propto \Delta n_{3d}^{eff} a \quad (65)$$

I try to set this intuitive interpretation on a mathematical basis in appendix B. I kept this section separate from the main body of this thesis because the mathematical proof exhibits some gaps that I was not able to fill and I will point to these shortcomings in the appendix. However, it appears to me to be the correct overall approach to determine the exchange interaction in a poly-nuclear complex. Here, I note that the starting point of the mathematical treatment is to assume that a molecular orbital  $|i\rangle$  of the system can be written as linear combinations of atomic orbitals (LCAO)  $|a_m\rangle$ :  $|i\rangle = \sum_m c_m^i |a_m\rangle$ .

The exchange parameter  $a$  is constant if the same basis set of atomic orbitals to express the molecular orbitals for the series of metal compounds under investigation is used. If the basis set is changed one has to normalize to  $a$ . In most cases, however, the same basis set of atomic orbitals is used for one transition metal element [112].  $\Delta E_{ex}$  is then proportional to the effective number of unpaired  $3d$  electrons. In this picture, the rigid  $3d$  orbitals are filled or depleted depending on the chemical environment of the metal atom. Ligand and other metal orbitals ( $4s, 4p, \dots$ ) are neglected when calculating the exchange interaction of the  $2p$  hole. The computational effort is therefore shifted from evaluating all exchange integrals between the metal  $2p$  orbital and the one-electron molecular wavefunctions to calculating the effective number of unpaired  $3d$  electrons.

It is emphasized that in the interpretation implied in equation 65 the  $K\alpha_1$  linewidth is still determined by the exchange interaction like in the atomic multiplet model but the exchange interaction is calculated by taking the delocalization of the  $3d$  orbitals into account. This is important when  $K\alpha_1$  emission is used for chemical analysis. In this picture the  $K\alpha_1$  linewidth reflects the net electron spin located at the metal atom. Charge transfer changes the net spin and thus influences the linewidth via the exchange interaction.

Equivalent to adjusting the number of unpaired  $3d$  electrons would be to scale the atomic exchange integral. This is physically justified because more diffuse  $3d$  orbitals reduce the ( $2p, 3d$ ) overlap and thus the exchange integral. One can view the adjustment of the number of  $3d$  electrons as finding the scaling factor of the Slater exchange integrals. Consequently, one can apply the same procedure to all Slater integrals and find their scaling factors. We then have a combination of density functional theory and multiplet theory that complement each other.

In a third approach one can include several configurations in a ligand field multiplet calculation and thus account for the hybridization of the metal with the ligand orbitals. This influences the magnitude of the exchange interaction as well because a  $2p^5 3d^n$  configuration yields a different exchange integral in a Hartree-Fock SCF calculation than a  $2p^5 3d^{n+1}$  configuration.

However, as pointed out before, a fundamental difference between scaling the exchange integral or adjusting the number of unpaired  $3d$  electrons and including more configurations is that the latter can lead to additional final states in the calculations. We have seen for  $K\beta$  emission that including one charge transfer configuration results in a broadening of the  $K\beta_{1,3}$  line by adding more final states and it is necessary to study whether the same occurs for the  $K\alpha$  emission. I will therefore investigate the influence of configuration interaction on the  $K\alpha_1$  linewidth when I discuss multiplet calculations for the  $K\alpha$  emission.

### 5.2.3 Analysis of the $K\alpha_1$ Linewidth in $^{55}\text{Fe}$ and Mn Compounds

In order to test the model outlined above I first plot the results for the  $K\alpha_1$  FWHM by Kawai *et al.* versus the effective number of unpaired  $3d$  electrons. This is shown in Figure 40 for the ground and the  $1s$  excited state effective number of unpaired  $3d$  electrons. A linear regression was performed for all three cases, *i.e.* plots of the  $K\alpha_1$  FWHM versus (a) the nominal number of unpaired  $3d$  electrons as given by the formal oxidation and spin state of the metal atom, (b) the effective ground state number of unpaired  $3d$  electrons and (c) the effective  $1s$  excited state number of unpaired  $3d$  electrons. For (b) and (c) I used the values calculated by Kawai *et al.*. The standard errors  $S_r = \sqrt{\sum_{i=1}^n (y_i - a_0 - a_1 x_i)^2 / (n - 2)}$  for the three fits are shown in the first column of Table 7. The fit improves considerably for case (c). The linear regression for this case is shown in Figure 40.

This observation supports the interpretation suggested in equation 65. Kawai *et al.* do not say in their publication whether they used identical atomic basis sets for the population analysis and, hence, we do not know whether  $a$  is constant. It is, however, common practice to use identical basis sets if a comparison for different clusters with identical metal atoms is performed [112].

To further validate the model I measured the Mn  $K\alpha$  emission in MnO ( $n=5$ ),  $\text{Mn}_2\text{O}_3$  ( $n=4$ )

and  $\text{KMnO}_4$  ( $n=0$ ) after photoionization and in  $^{55}\text{Fe}_2\text{O}_3$ ,  $\text{K}_3^{55}\text{Fe}(\text{CN})_6$  and  $\text{K}_4^{55}\text{Fe}(\text{CN})_6$  after K capture. The experiment was performed using the  $\text{Ge}(3,3,3)$  Bragg reflection for the analyzer crystals and the Bragg angle was at about  $75^\circ$ . The total number of counts for the photoionization spectra is approximately 30000 counts/second and between 2000 counts/second ( $\text{K}_3^{55}\text{Fe}(\text{CN})_6$ ) and 2500 counts/second ( $^{55}\text{Fe}_2\text{O}_3$ ) for the K capture spectra. Different spectrometers were used in the two experiments. A position sensitive gas proportional counter was employed in the K capture experiment while a nitrogen cooled solid state (Ge) detector was employed in the photoionization experiment. The instrumental energy resolution in the K capture experiment was strongly influenced by the position resolution under  $75^\circ$  Bragg angle of the two-dimensional detector. The calculated instrumental resolution is 2.1 eV for the photoionization experiment. For the K capture experiment I estimate an instrumental broadening of 3.0 eV (see below). Thus, I cannot directly compare the two modes of excitation in this case like I did for the  $K\beta$  emission. However, I can compare the  $K\alpha$  spectra within each series of Mn and  $^{55}\text{Fe}$  compounds because the experimental conditions were identical for each series.

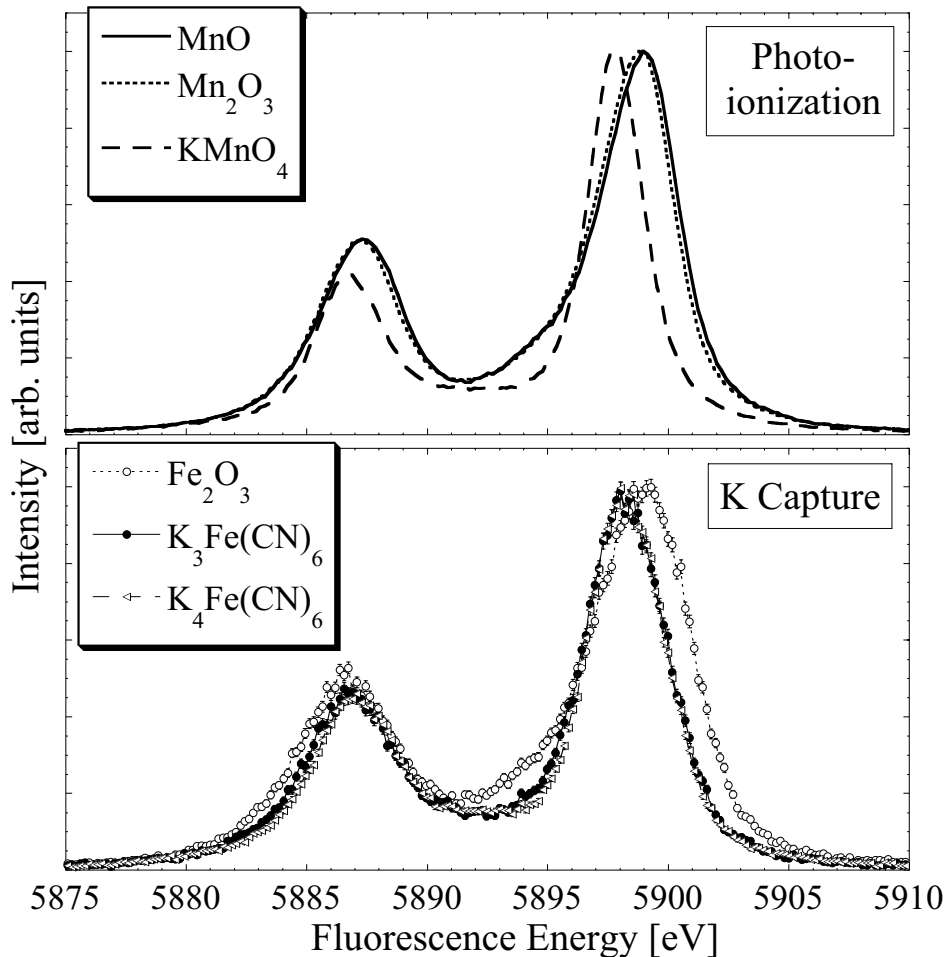


Figure 41:  $K\alpha$  lines in Fe compounds after K capture and in Mn compounds after photoionization

The  $K\alpha$  lines for the three  $^{55}\text{Fe}$  and the three Mn compounds are shown in Figure 41. I determined the FWHM for all  $K\alpha_1$  lines and plotted in Figure 42 the values versus the

number of unpaired  $3d$  electrons for the three cases (a), (b) and (c) as explained before. The effective number of unpaired  $3d$  electrons for the Mn compounds was obtained from reference [125] where the same theory was used as in the study by Kawai *et al.* For all three cases I performed a linear regression and determined the standard error. The results are shown in Table 7 and the linear regressions with the smallest standard error are shown in Figure 42. The analysis of the Mn  $K\alpha_1$  lines confirms the results found in the Fe  $K\alpha_1$  emission. The best linear fit is obtained for case (c) where the FWHM is plotted versus the  $1s$  excited state effective spin.

The  $1s$  core-hole-d-electron potential is compensated by the decrease in nuclear charge in the K capture experiment. The effective number of unpaired  $3d$  electrons in the  $K\alpha$  final states should therefore be approximately equal to the ground state number. We expect the best fit for case (b) where the  $K\alpha_1$  FWHM is plotted versus the ground state effective number of unpaired  $3d$  electrons. Table 7 shows that the best fit is obtained for (c) and the worst fit for (a). The trend is the same as for the Mn and Fe compounds after photoionization. The uncertainties for the standard errors as given in the Table do not allow to state in the K capture experiment which case (a,b or c) is the best representation of the valence electron configuration. I note that K capture decay leads to a Mn impurity in a FeX lattice which is not accounted for in the calculations. The standard errors for the K capture experiment in all three cases are much smaller than for the photoionization experiments and the  $K\alpha_1$  linewidth shows a very good agreement with the proportionality predicted by equation 65.

Figure 42 shows different slopes for the linear regressions for the Mn and the  $^{55}\text{Fe}$  compounds even though the exchange parameter should be identical for the two series following the arguments given in Chapter 5.1 because photoionization in Mn and K capture in  $^{55}\text{Fe}$  are compared. The slope, of course, depends on the set of values that is chosen for the number of unpaired  $3d$  electrons. These values in turn are calculated in references [74] and [125] using different atomic basis sets for Mn and Fe and, hence, the exchange parameters are not identical between the two series of compounds. This is simply due to different theoretical approaches in the ligand field multiplet model and in density functional theory. The exchange parameter is larger for Fe which is consistent with a greater slope. Using the Cowan code [36] I calculate for the exchange parameters for a  $2p^5 3d^5$  configuration in Mn and Fe 0.94 eV and 1.12 eV, respectively. The values will be different for the atomic basis sets used in the density functional calculations but Fe will still have a larger exchange parameter.

The error for the above analysis has to be discussed. The experimental error for the FWHM is small and the standard errors given in Table 7 are hardly effected by this error except for K capture as discussed before. The calculated effective numbers of unpaired  $3d$  electrons are given for FeO and Fe<sub>2</sub>O<sub>3</sub> in references [74] and [125]. They used the same theory to obtain the molecular orbitals and performed a Mulliken population analysis for each compound. However, the calculated values for the effective number of unpaired  $3d$  electrons differ up to 0.16 between the two references for the same compound. It has been suggested that a Mulliken population analysis yields unphysical results for compounds that have largely diffused orbitals [66]. I cannot judge how accurate the results given in the references are but I can estimate an error for the analysis from the deviations between the values given in the two references. Table 7 gives two standard errors for the linear regression in Fe compounds after photoionization where I used the values given in both references. The trend is the same for both sets. I therefore conclude that the  $K\alpha_1$  linewidth exhibits an approximate proportional dependence on the effective number of unpaired  $3d$  electrons.

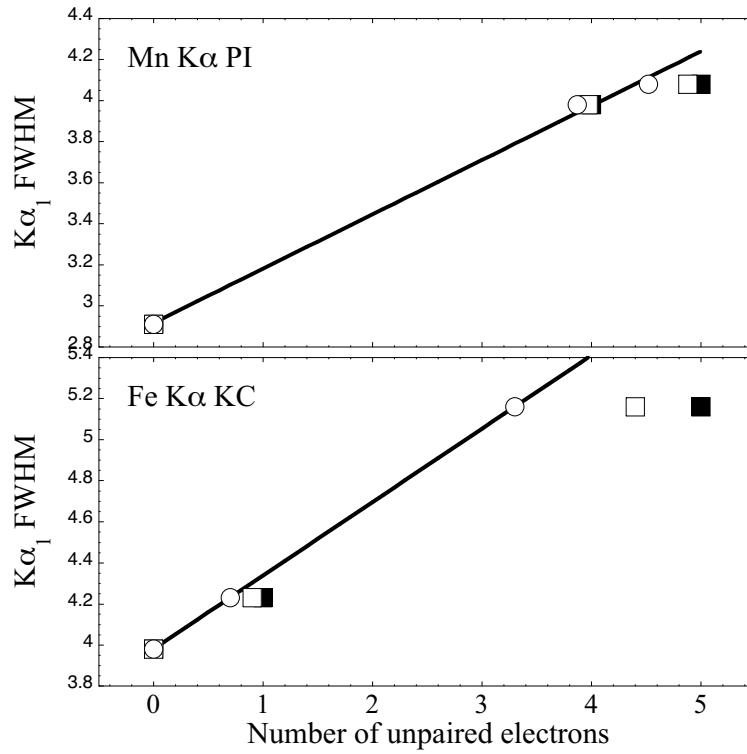


Figure 42: *Experimental FWHM of  $K\alpha_1$  lines in Mn and Fe compounds after K capture or photoionization versus number of unpaired 3d electrons; (a) full boxes: nominal number of unpaired 3d electrons, (b) empty boxes: the effective ground state number of unpaired 3d electrons, (c) circles: the effective 1s excited state number of unpaired 3d electrons. The linear regression is shown for case (c) which gives the best fit, i.e. the smallest standard error as given in Table 7. The uncertainties for the  $K\alpha_1$  FWHM is approximately the size of the symbols for K capture ( $\pm 0.05$  eV) and smaller for photoionization ( $\pm 0.02$  eV).*

### 5.2.4 Multiplet Calculations

I performed ligand field multiplet calculations for the  $K\alpha$  emission in a similar manner as described before for the  $K\beta$  emission. The 10Dq values were 1.45 eV for  $\text{Fe}_2\text{O}_3$  and 5.0 eV for the cyanides [74]. For the hybridization I used  $V(E_g)=2.0$  eV and  $V(T_{2g})=-1.0$  eV. For all three compounds the same center of mass final state energy was assumed.

I am interested in investigating two mechanisms in the calculations. One is the effect of varying admixture of  $|3d^n \underline{L}\rangle$  on the  $K\alpha_1$  linewidth. Second, I would like to find out whether inclusion of the decay from the anti-bonding  $1s$  intermediate state broadens the spectrum like it did in the case of the  $K\beta_{1,3}$  line. The admixture of the charge transfer configuration can be adjusted by changing the splitting between the two configurations. I used  $\Delta=3.5$  eV and  $\Delta=0.0$  eV for  $\text{K}_3\text{Fe}(\text{CN})_6$  and I treated the ionic  $\text{Fe}_2\text{O}_3$  using the same parameters that I used for the  $K\beta$  calculations. To simulate the K capture case I assumed the ordering of the two configurations to remain unchanged and the splitting between the two configurations was set equal to  $\Delta=3.5$  eV in the  $1s$  intermediate as well as in the  $K\alpha$  final state. For photoionization I used  $U_{1s3d}=U_{2p3d}=9$  eV and thus  $\Delta-U_{2p3d}=-5.5$  eV for the splitting of the two configurations in the intermediate and in the final state. Like in the  $K\beta$  calculations

Table 7: Standard error for linear regression of  $K\alpha_1$  FWHM versus number of unpaired  $3d$  electrons. The values for the effective number of unpaired  $3d$  electrons were taken from reference [74] except for (\*) where the calculated values were taken from reference [125]. The uncertainties for the values were obtained by assuming an error of  $\pm 0.02$  eV for the  $K\alpha_1$  FWHM for the photoionization experiment and  $\pm 0.05$  eV for the K capture experiment. The FWHM for the Fe photoionization spectra were taken from reference [74] where no error was given.

Number of unpaired electrons obtained from	Standard error [*10 <sup>-1</sup> ]		
	Fe PI	Mn PI	<sup>55</sup> Fe KC
(a) Formal Spin State	2.02	1.03 (2)	0.11 (6)
(b) DFT Calculated Ground State	1.67/1.78*	0.91* (2)	0.07 (6)
(c) DFT Calculated $1s$ Excited State	1.40/1.51*	0.52* (2)	0.00 (6)

I added the  $K\alpha$  emission from the bonding and the anti-bonding  $1s$  intermediate state weighed by their intensities after a  $1s$  photoionization. Kawai *et al.* argue that the core hole affects the valence electrons less in covalent cyanides due to the stronger screening of the ligand electrons and the effective number of  $3d$  electrons therefore does not change much between the ground and the  $1s$  excited state. I thus did not perform separate calculations for photoionization and K capture in the cyanides.

To simulate the ‘quenching’ of the orbital angular momentum I performed an additional calculation for  $K_3Fe(CN)_6$  where I set the direct ( $2p, 3d$ ) Coulomb integral  $F_{2p3d}^2$  to zero. This is not the most elegant way to simulate a zero orbital angular momentum because the average over the coefficients is zero for S symmetry in the  $3d$  shell and not the Slater integral (see Chapter 3). The  $F_{2p3d}^2$  Slater integral is important for symmetry mixing where the coefficients are not zero for  $L=0$ . However, the symmetry mixed states are rather weak and hardly influence the width of the  $K\alpha_1$  line.

The stick spectra were convoluted by a 1.5 eV Lorentzian to account for the  $1s$  and the  $2p$  lifetime broadenings [83]. I did not account for different final state lifetimes since it is not important in this context. I just mention here that, generally, the  $K\alpha_2$  final states have a shorter lifetime because of possible  $2p_{1/2}2p_{3/2}3d$  Coster-Kronig decays [43]. Furthermore, a 3.0 eV Gaussian convolution was applied to account for instrumental broadening. This value was set such that the FWHM of the  $K_4Fe(CN)_6$  spectrum coincides with the calculated spectrum for a  $3d^6$  low-spin configuration which does not show any exchange splitting. The theoretical  $K\alpha_1$  line has in this case only one final state and its width is determined by the applied Lorentzian and Gaussian broadening (see Figure 44). The Slater integrals were scaled down to 85% of their single configuration value. The spin-orbit values were not scaled.

Figure 43 shows three different  $K\alpha$  spectra for  $Fe_2O_3$ . It can be seen that changing the

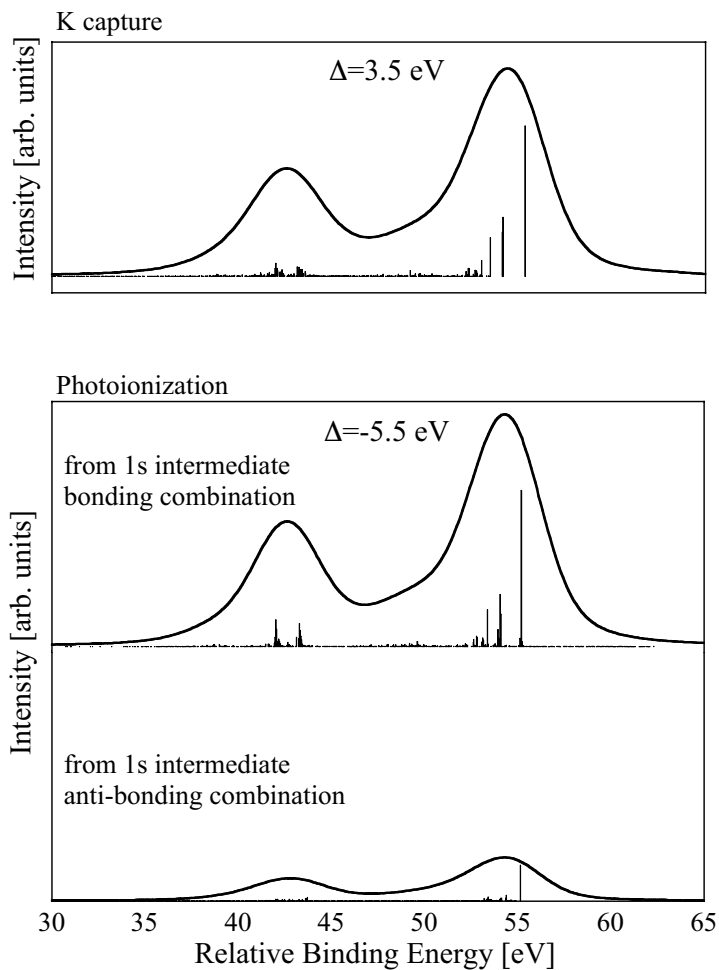


Figure 43: *Ligand field multiplet calculations including charge transfer for  $K\alpha$  lines in  $Fe_2O_3$  simulating K capture (top) and photoionization (two bottom spectra). The applied broadenings are 1.5 eV Lorentzian and 3.0 eV Gaussian.*

charge transfer energy hardly influences the spectra and only analysis of the  $K\alpha_1$  linewidth reveals the differences as will be shown below. The  $K\alpha$  emission from the anti-bonding combination has a similar overall structure as the spectrum from the bonding combination with a  $K\alpha_1$  and  $K\alpha_2$  peak. The  $K\alpha_1$  line shows just one strong final state that is shifted by only 0.059 eV to higher energies compared to the strongest  $K\alpha_1$  final state in the spectrum of the bonding spectrum. We can therefore expect that adding the spectra will actually result in a narrowing of the overall  $K\alpha_1$  linewidth.

The theoretical simulations of the  $K\alpha$  lines in the three compounds after K capture are shown in Figure 44. For the cyanides the calculations with  $\Delta=0.0$  eV are shown and for  $Fe_2O_3$  the case with  $\Delta=3.5$  eV and only the decay from the bonding  $1s$  intermediate state, *i.e.* the K capture case. The splitting between the final states that form the  $K\alpha_1$  line increases for  $Fe_2O_3$  compared to  $K_3Fe(CN)_6$ . The final states at lower binding energy have less intensity. In a simple picture this can be understood by the statistical weight of the final states: The final states with lower J values are less degenerate and they appear at lower binding energies. Additional states are populated due to symmetry mixing. The spectrum

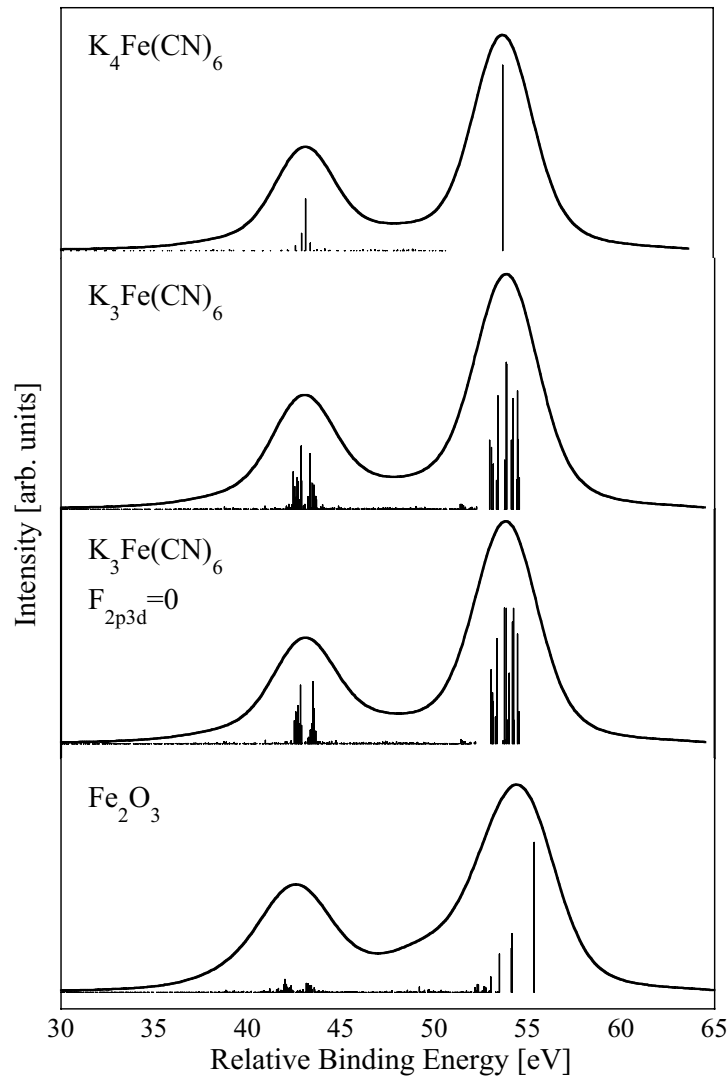


Figure 44:  $K\alpha$  emission in Fe compounds calculated using ligand field multiplet theory including one charge transfer configuration. The spectra that simulate the K capture case are shown, i.e.  $\Delta=3.5$  eV for  $\text{Fe}_2\text{O}_3$  and  $\Delta=0$  eV for the cyanides. The applied broadenings are 1.5 eV Lorentzian and 3.0 eV Gaussian.

of  $\text{K}_3\text{Fe}(\text{CN})_6$  without ( $2p,3d$ ) direct Coulomb interaction ( $F_{2p3d}=0$ ) shows slightly weaker symmetry mixed states between  $K\alpha_1$  and  $K\alpha_2$ . The intensities of the strong lines that form  $K\alpha_1$  slightly redistribute.

The FWHM of the experimental K capture data and the multiplet calculations are compared in Table 8. Three calculated values for  $\text{Fe}_2\text{O}_3$  are shown where I used: (a)  $\Delta=3.5$  eV, (b)  $\Delta=-5.5$  eV and only the  $1s$  bonding combination was included for the  $1s$  intermediate state, (c)  $\Delta=-5.5$  eV and bonding as well as anti-bonding combinations as  $1s$  intermediated states are included. The three values only slightly vary and are close to the experimental result. This shows that the calculations based on atomic multiplets yield good results for  $^{55}\text{Fe}_2\text{O}_3$ . The FWHM decreases when the charge transfer energy is reduced by  $U_{1s3d}$  because of a stronger admixture of a  $2p^53d^6\bar{L}$  configuration that has a smaller exchange splitting than a  $2p^53d^5$  configuration. This is in agreement with the results by Kawai *et al.* who observe a

smaller effective number of unpaired  $3d$  electrons in the final state than in the ground state.

Table 8: *Experimental and theoretical results for  $K\alpha_1$  FWHM in Fe compounds. The experimental results were obtained in a K capture experiment. The details of the multiplet calculations are given in the text. Three values are given for  $Fe_2O_3$ : (a)  $\Delta=3.5$  eV, (b)  $\Delta=-5.5$  eV bonding  $1s$  intermediate state, (c)  $\Delta=-5.5$  eV bonding and antibonding  $1s$  intermediate state. The three values for  $K_3Fe(CN)_6$  are for (i)  $\Delta=3.5$  eV, (ii)  $\Delta=0.0$  eV and (iii)  $\Delta=0.0$  eV,  $F_{2p3d}^2=0$ . The theoretical values for the Gaussian and Lorentzian broadenings were set to reproduce the FWHM in  $K_4Fe(CN)_6$ .*

	Experiment	Multiplet calculations		
$Fe_2O_3$	5.16 (5)	(a) 5.18	(b) 5.09	(c) 5.07
$K_3Fe(CN)_6$	4.23 (5)	(i) 4.36	(ii) 4.27	(iii) 4.23
$K_4Fe(CN)_6$	3.98 (5)	3.98		

The  $K\alpha_1$  FWHM in  $Fe_2O_3$  even slightly decreases when the  $K\alpha$  emission from the antibonding  $1s$  intermediate state is added (case (c) in Table 8). This behavior is opposite to the  $K\beta$  emission where we observed a broadening of the  $K\beta_{1,3}$  line. Thus, the additional  $K\alpha$  final states that can be reached when high-lying  $1s$  intermediate states are populated do not broaden the  $K\alpha_1$  line.

The three values shown in Table 8 for  $K_3Fe(CN)_6$  are for (i)  $\Delta=3.5$  eV (ii)  $\Delta=0.0$  eV and (iii)  $\Delta=0.0$  eV,  $F_{2p3d}^2=0$ . Reducing the charge transfer energy and thus increasing the  $3d^6\bar{L}$  low-spin admixture reduces the  $K\alpha_1$  FWHM as it was observed for  $Fe_2O_3$ . Case (iii) for  $K_3Fe(CN)_6$  simulates zero or fully ‘quenched’  $3d$  orbital angular momentum. The linewidth further decreases because of the lack of direct Coulomb splitting. All three values are very close to the experimental number.

The experimental values were taken in a K capture experiment. I expect the calculations closest to the K capture value for  $Fe_2O_3$  for case (a) where the order of the configurations was set to remain unchanged. For the covalent  $K_3Fe(CN)_6$  either case (ii) or case (iii) should reproduce the experimental values. Case (iii) is closer to the experimental value suggesting a fully quenched orbital angular momentum. However, the differences are too small to draw conclusions concerning the degree of quenching. Finally, I show in Figure 45 a comparison between the experimental and the calculated spectra that give the best agreement with the experiment for the  $K\alpha_1$  FWHM. For all three compounds the  $K\alpha_{1,2}$  splitting is too small in the calculations. At this point, I do not have an explanation for this. The error  $\Delta E_{R''}$  as discussed in Chapter 2 can explain an experimental error in the splitting. However, the error would be the same for all three spectra while the discrepancy in Figure 45 between the theoretical and experimental  $K\alpha_{1,2}$  splittings vary for the three compounds. Very good agreement is achieved in the  $K\alpha_1$  lineshape. I point out that in the calculations equal center

of mass energies were chosen for the three simulations. It is remarkable that with this assumption the relative  $K\alpha_1$  peak positions are rather well reproduced in the calculations even though the  $K\alpha_1$  line shifts by  $\approx 1$  eV (see Figure 41). This indicates that the shift is mainly caused by multiplet effects and not an absolute shift of the  $1s$  and  $2p$  orbital due to a change in the chemical environment. This point will be addressed again when the  $K\beta$  emission from the same compounds will be discussed in Chapter 7.

### 5.2.5 Concluding Remarks

It was found that the  $K\alpha_1$  linewidth roughly shows a proportional dependence on the effective number of unpaired  $3d$  electrons. This observation can be theoretically understood by assuming that the  $K\alpha_1$  line is broadened by the exchange interaction between the  $2p$  hole and the populated  $3d$  orbitals and it therefore reflects the net spin located at the metal atom. Results in K capture experiments support this interpretation and for the three compounds that were investigated a behavior closer to proportionality was found after K capture than for the same compounds measured after photoionization. The better agreement for K capture could be due to fewer double ionizations than after photoionization as discussed in Chapter 4. With respect to possible chemical analysis it is important to note that the  $K\alpha$  emission reveals information of the metal atom in the excited state and not the ground state.

To explain the proportional behavior one has to assume zero  $3d$  orbital angular momentum. In octahedral symmetry the orbital angular momentum is fully quenched for A and E symmetries but no general statement can be made for T symmetries [61]. All Mn and Fe compounds that were investigated, except for  $K_3Fe(CN)_6$ , should therefore have zero orbital angular momentum if one obtains the ground state symmetry from the Tanabe-Sugano diagram and if the compounds are strictly octahedral. Strong covalency contributes to the quenching [54]. The contribution from the direct Coulomb splitting will therefore be small in  $K_3Fe(CN)_6$ . Ligand field multiplet calculations including charge transfer reproduce the  $K\alpha$  spectra rather well except for the  $K\alpha_{1,2}$  splitting.

It is important to mention other mechanisms that shape the  $K\alpha_1$  peak. The asymmetry is due to unequal intensities in the final states because of, in the simplest atomic picture, different statistical weights in the final states and configuration interaction (see Figure 44). It is therefore possible that the line width changes due to a redistribution of intensity instead of a change in the exchange splitting because of, for example, a change in geometry of the complex. It is difficult to evaluate this effect because the intensities are subject to several different contributions. One therefore does not expect rigorous proportionality. However, the experimental results suggest that the linewidth is dominated by the exchange interaction.

## 5.3 $K\beta$ Satellite Emission

The perturbation of the valence electron configuration due to  $1s$  vacancy production can be studied directly by analyzing the  $K\beta$  satellite region after photoionization and K capture. Figure 46 shows the results for  $Fe_2O_3$ ,  $K_3Fe(CN)_6$  and  $K_4Fe(CN)_6$ . Unlike in the direct comparison of the two modes of excitation for the  $K\beta$  emission where I compared MnO and  $^{55}Fe_2O_3$ , *i.e.* two different compounds, I now compare spectra from the same compounds and shifted the fluorescence energies. The spectra were taken using a Ge(6,2,0) Bragg reflec-

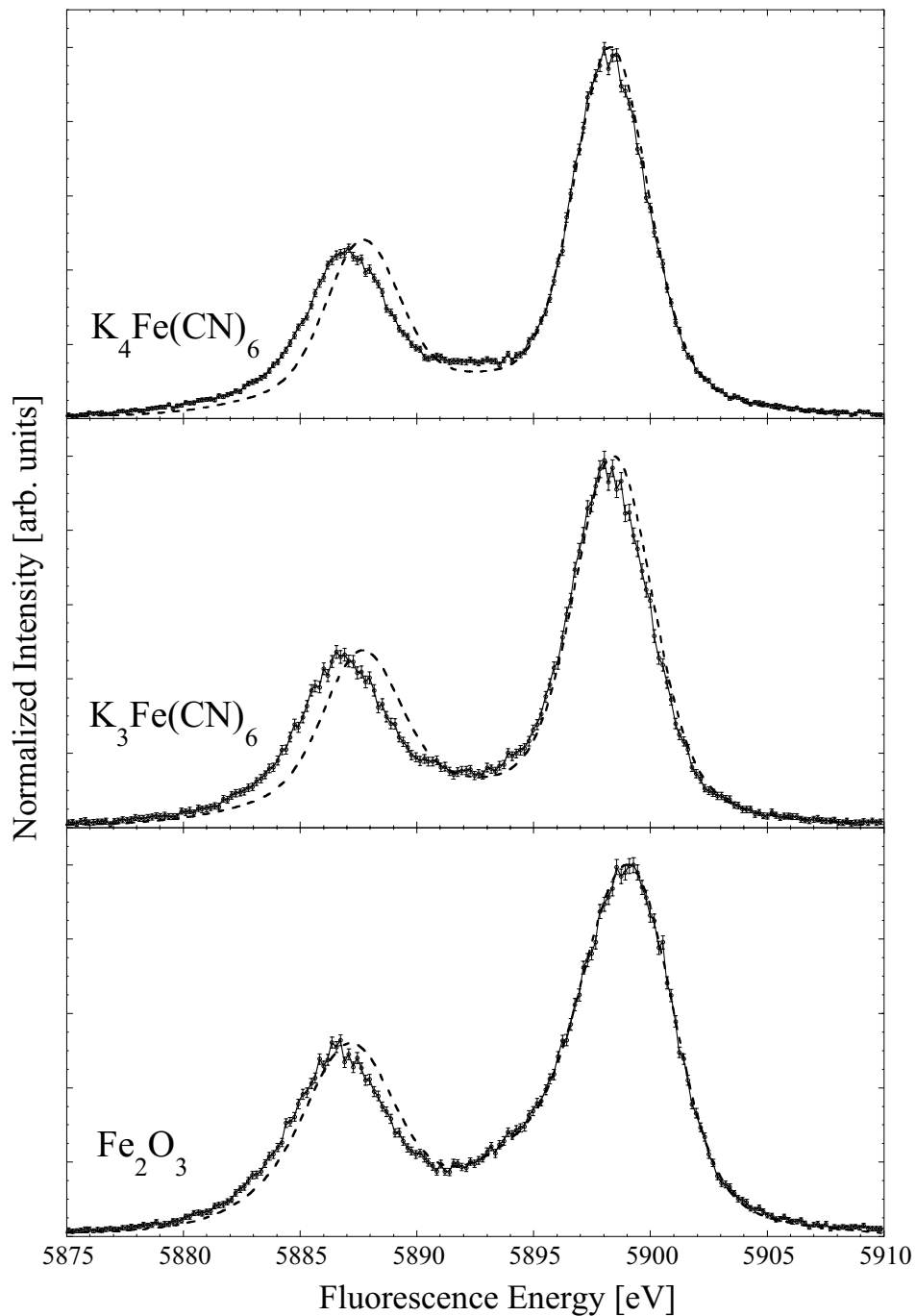


Figure 45: Comparison of experimental  $K\alpha$  lines recorded after  $K$  capture to ligand field multiplet calculations including charge transfer (dashed lines). The calculations that yield the best agreement with the experiment for the  $K\alpha_1$  FWHM as given in Table 8 are shown. For  $Fe_2O_3$   $\Delta=3.5$  eV and for the cyanides  $\Delta=0$  eV. The energy scale of the theoretical spectra was shifted such that the calculated and measured  $K\alpha_1$  lines coincide for  $Fe_2O_3$ .

tion for the photoionization experiment and a Si(4,4,0) Bragg reflection for the  $K$  capture experiments. The photoionization spectra were recorded at the BioCAT beamline at the APS where the incident beam was focused to 0.5 mm vertical and 1 mm horizontal size. The calculated instrumental energy broadenings are 1.8 eV for the  $K$  capture experiment and 1.4

eV for the photoionization experiment. The incident excitation energy was set to 7.80 keV above the Fe K-edge (7.11 keV) but below the estimated KL-edge at 7.89 keV. The tail of the  $K\beta_{1,3}$  peak was subtracted in all spectra.

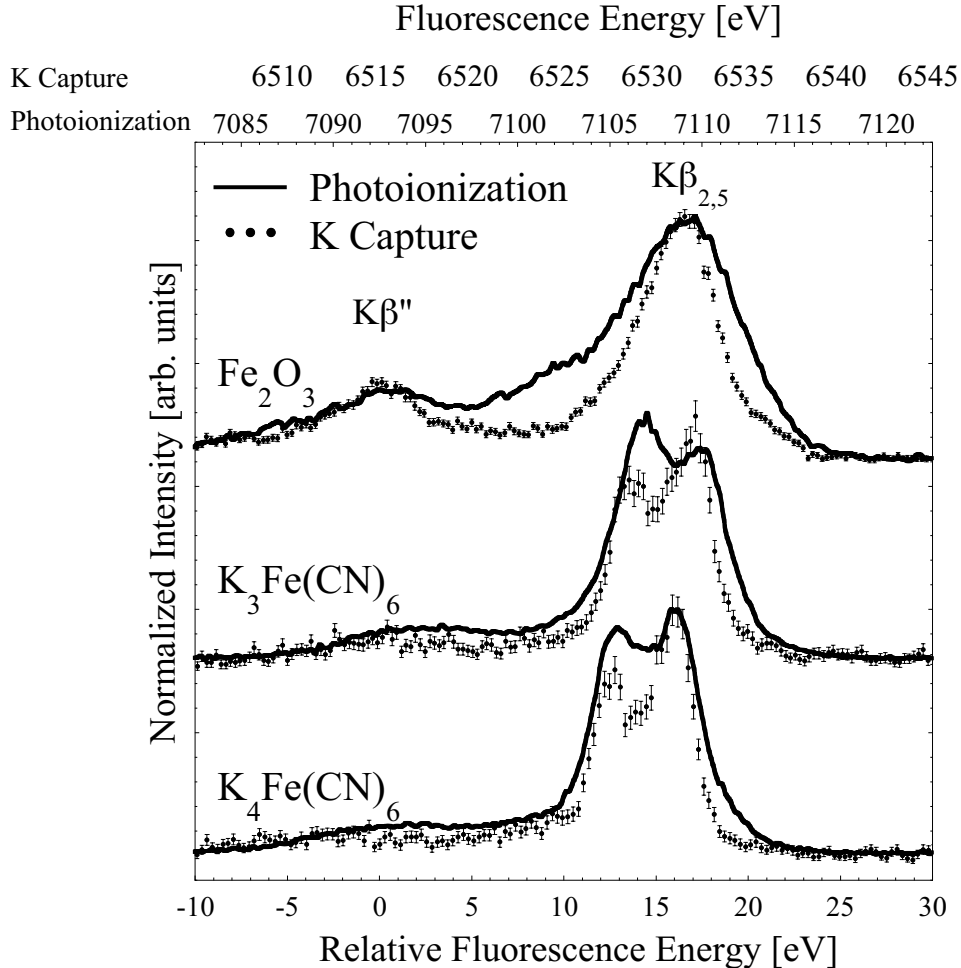


Figure 46:  $K\beta$  satellite emission in Fe compounds after K capture (KC) and photoionization (PI). The energy scales on top are the measured fluorescence energies for the photoionization and the K capture experiment. To facilitate direct comparison a common energy scale (relative fluorescence energy) is given in the bottom. The feature in  $Fe_2O_3$  at about 0 eV relative fluorescence intensity is the  $K\beta''$  or cross over peak. It was used to align the photoionization and K capture spectra relative to each other.

All spectral features recorded after photoionization are broader than in the data taken after K capture even though the instrumental energy bandwidth is smaller in the synchrotron experiment. Furthermore, the intensity ratios of the two bands in the  $K\beta_{2,5}$  structure of the cyanides change between the two modes of excitation. The broadening indicates that more final states are populated after photoionization. This supports the conclusions drawn in Chapter 5 that a non-adiabatic relaxation of the valence electrons occurs after  $1s$  photoionization. The valence orbitals do not (or hardly) relax after K electron capture because the effective potential experienced by the valence electrons does not change. However, the final states of the spectra after K capture have a Mn nucleus ( $Z=25$ ) instead of an Fe nucleus. The valence orbitals in case of K capture therefore have to adjust to a new effective potential

during the  $3d$  to  $1s$  decay. The valence electrons have to relax twice in the photoionization experiment, during the photoionization and during the  $3d$  to  $1s$  decay. The question is whether the shake probability is larger during the first relaxation, *i.e.* the  $1s$  photoionization, than the second, *i.e.* the  $3d$  to  $1s$  decay. The shake probability for the photoionization process was discussed in Chapter 4. The  $3d$  to  $1s$  transition can be viewed as the inverse of an absorption process. It has been argued that a resonant excitation into the valence shell is a process close to the adiabatic limit [19]. This can be understood in the charge transfer picture by assuming that the potential  $U_{dd}$  due to the additional electron in the  $3d$  shell is approximately equal to the core-hole-d-electron potential  $U_{cd}$  [42]. The separation of the two configurations in the final state of a  $1s$  to  $3d$  absorption process is  $\Delta - U_{cd} + U_{dd} \approx \Delta$ . Hence, the ordering of the two configurations does not change and the anti-bonding (shake) configuration is not populated.

It will be shown in the next chapter that comparison of the K capture  $K\beta$  satellite spectra with valence shell XPS data for  $\text{Fe}_2\text{O}_3$  indicates that the valence shell is only little perturbed in the K capture experiment. However, in the final state of the K capture decay a Mn impurity is embedded in an FeX (X=O,CN) lattice. This will result in a distortion of the lattice that might effect the valence orbitals. I just mention this here without further investigation. This point becomes important in case one wants to argue which mode of excitation yields results closer to the actual valence electron configuration in the ground state. The experimental spectra and the discussion that was presented so far suggest that the K capture experiment is the ‘cleaner’ approach with a less perturbed valence shell.

## 6 $K\beta$ Satellite Spectra

The  $K\beta$  satellite spectra of  $\text{Fe}_2\text{O}_3$  and  $[\text{Rh}(\text{en})_3][\text{Mn}(\text{N})(\text{CN})_5]\cdot\text{H}_2\text{O}$  are discussed in this Chapter. In both cases I use results obtained by other groups. I compare the  $K\beta$  satellite emission in  $\text{Fe}_2\text{O}_3$  to valence band XPS taken by Fujimori *et al.* [58] and calculations by de Groot and Nagel [41, 102]. Kohn-Sham density functional theory calculations were performed by Jesper Bendix for the complex  $[\text{Rh}(\text{en})_3][\text{Mn}(\text{N})(\text{CN})_5]\cdot\text{H}_2\text{O}$  [13]. Before I discuss the results I give a brief account of Fermi's Golden Rule in the dipole approximation as outlined in reference [19]. The transition probability between an initial state  $\psi_i^N$  and a final state  $\psi_f^N$  where both states are expressed by N-electron wave functions is given by:

$$W_{if} \propto \omega_{if}^3 |\langle \Psi_f^N | \hat{\epsilon} \vec{r}_i | \Psi_i^N \rangle|^2 \quad (66)$$

With  $\omega_{if}$  being the frequency for the energy difference between  $E_i$  and  $E_f$ . The energies  $E_{i,f}$  and the wavefunctions are determined for the fully relaxed states. In the sudden approximation one can factorize the N-electron wavefunctions as  $\Psi_i^N = \phi_i \psi_0^{N-1}$  and  $\Psi_f^N = \phi_f \psi_f^{N-1}$ . The one-electron wavefunctions  $\phi$  describe the orbitals that are directly involved in the transition, *i.e.* the dipole operator only acts on these orbitals. For the  $K\beta$  satellites the fluorescence initial state is the  $1s$  excited state  $1s3d^n$  and  $\phi_i$  identifies with the  $3d$  or, more general, valence orbital (VO) and  $\phi_f$  identifies with the  $1s$  wavefunction in the fully relaxed final state. In a one-electron, sudden approximation picture one can therefore estimate the intensities for a  $K\beta$  satellite spectrum by writing:

$$W_{if} \propto \omega_{if}^3 |\langle \psi_f^{N-1} | \psi_0^{N-1} \rangle|^2 |\langle \phi_f^{1s} | \hat{\epsilon} \vec{r} | \phi_i^{VO} \rangle|^2 \quad (67)$$

$$\sim \omega_{if}^3 |\langle \phi_f^{1s} | \vec{r} | \phi_i^{VO} \rangle|^2 \cos^2 \gamma = \omega_{if}^3 |\vec{r}_{if}|^2 \cos^2 \gamma \quad (68)$$

where  $\phi^{VO}$  describes a valence electron orbital as obtained in the  $1s$  excited state and  $\vec{\epsilon}$  is the polarization vector of the outgoing photon. The angle  $\gamma$  is defined between the vectors  $\hat{\epsilon}$  and  $\vec{r}$ . The term  $|\langle \psi_f^{N-1} | \psi_0^{N-1} \rangle|^2$  is a many-body overlap integral that is less than one [19]. It will be neglected in the following one-electron analyses.

### 6.1 $K\beta$ Satellite Spectra in $\text{Fe}_2\text{O}_3$

The valence shell electron configuration can be studied using photoelectron spectroscopy [65]. If the energy  $h\nu$  of the monochromatic incident beam is known, the binding energy  $E_B$  of a particular final state is given by  $E_B = h\nu - E_K$  where  $E_K$  is the measured kinetic energy of the outgoing electron. The valence shell XPS in  $\alpha\text{-Fe}_2\text{O}_3$  (hematite) was measured by several authors [58, 86].  $K\beta$  satellite lines and valence electron XPS have the same electronic final state configuration with one valence electron missing compared to the ground state. However, the  $K\beta$  satellite spectra show the valence shell 'filtered' by the dipole selection rules for a transition to the  $1s$  shell. The valence electrons occupy more or less delocalized molecular orbitals or electron bands. It is helpful to express these orbitals or bands in terms of atomic orbitals because then we can apply our knowledge from atomic physics in order to, for example, estimate transition probabilities. However, some ambiguity exists. The electrons in the oxygen  $2p$  band partly occupy Fe  $4p$  levels. This is a question of which reference system one chooses and since we are concerned with transitions to the Fe  $1s$  shell we eventually would like to express the electron density in terms of Fe atomic orbitals.

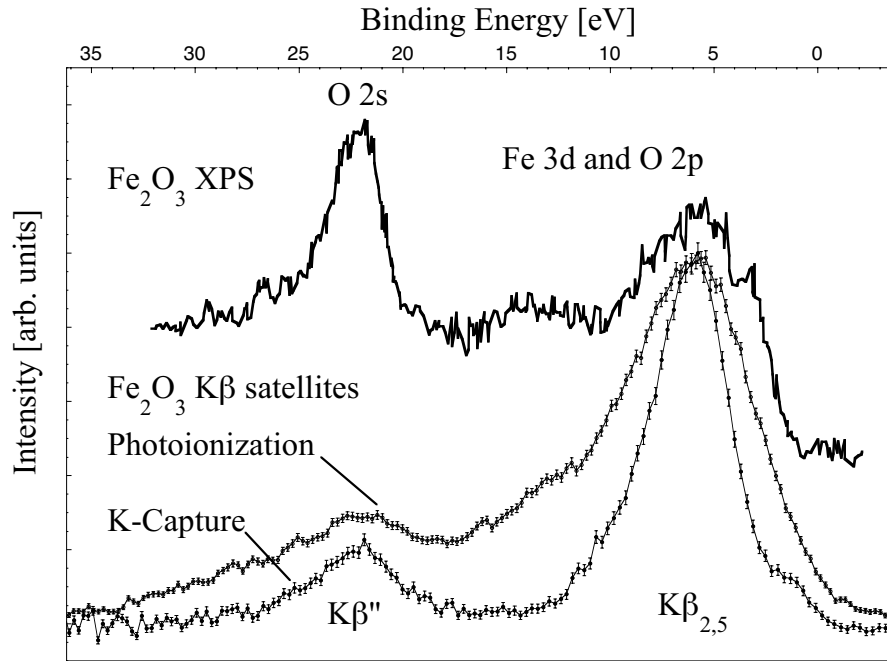


Figure 47: Comparison of valence-band XPS (from reference [58]) with  $K\beta$  satellite emission after  $K$  capture and photoionization where the tail of the  $K\beta_{1,3}$  line was subtracted. The spectra are aligned relative to each other in the oxygen  $2s$  peak and the binding energy scale is taken from the XPS spectrum.

Figure 47 shows the  $Fe_2O_3$  valence electron XPS recorded by Fujimori *et al.* at  $h\nu=1253.6$  eV photon energy well above the Fe L-edge [58] together with the  $K\beta$  satellite spectra recorded after  $K$  capture and photoionization. The energy scales of the spectra are aligned to each other in the maximum of the oxygen  $2s$  peak and the binding energy scale is shown as given in reference [58]. The XPS spectrum sits on a strong background which Fujimori calls ‘integral’ background. The rough assignment of the spectral features given in the Figure for the XPS experiment with the oxygen  $2s$  band at higher binding energies and Fe  $3d$  orbitals together with the oxygen  $2p$  band at lower binding energies seems well established and is not argued in the different publications. The  $K\beta''$  line is assigned to an oxygen  $2s$  to Fe  $1s$  transition and is therefore sometimes referred to as ‘cross-over peak’. This is elaborated in detail in reference [17] and the feature is therefore not discussed here. An assignment of the nitrogen  $2s$  to Mn  $1s$  cross-over peak in  $[Rh(en)_3][Mn(N)(CN)_5]\cdot H_2O$  is presented in the next Section. I just use this knowledge to align the energy scales of the  $K\beta$  spectra and the XPS spectrum in Figure 47. The  $K\beta_{2,5}$  feature shows one strong line while the XPS spectrum shows a strong (6 eV) and a weak (14 eV) structure where the strong XPS feature aligns with the  $K\beta_{2,5}$  peak at about 6 eV binding energy. We expect valence electrons that have orbital angular momentum  $p$ -character relative to the Fe center to dominate the  $K\beta$  satellite spectrum because of the dipole selection rules. The weak XPS feature at about 14 eV binding energy that does not show in the  $K\beta$  spectrum therefore has mainly Fe  $d$ -character while the strong line contains contributions from valence electrons with metal  $p$ -character.

So far a first qualitative interpretation of the  $K\beta$  satellite spectra. I included in Figure 47 the  $K\beta$  satellite spectrum recorded after photoionization. It can be seen that due to the broader structure after photoionization one could not have reached the same conclusions outlined

above from the comparison between valence XPS and  $K\beta$  emission after photoionization. There is intensity at about 14 eV binding energy in the photoionization  $K\beta$  spectrum and using the dipole selection rules one cannot make a statement concerning the orbital symmetry with respect to the Fe center of the molecular orbitals that give rise the weak XPS structure.

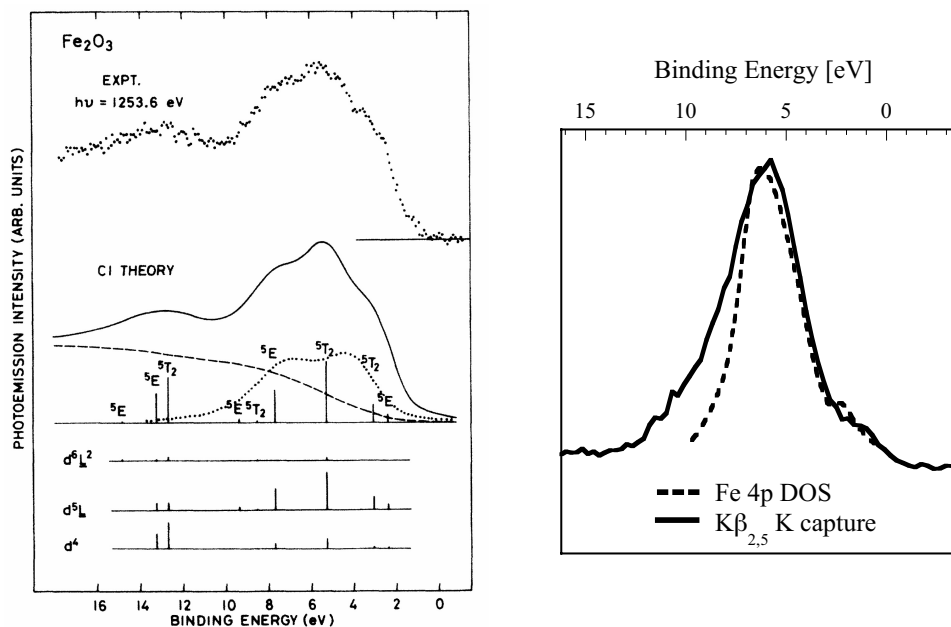


Figure 48: Analysis of the valence band in  $\text{Fe}_2\text{O}_3$ . The Figure on the left with a comparison of the experimental valence band XPS to configuration interaction (CI) calculations was taken from reference [58]. The dashed line shows an ‘integral’ background and the dotted line depicts the oxygen  $2p$  band. The CI calculations were performed on a  $[\text{FeO}_6]^{9-}$  cluster and the decomposition into configuration components for each final state line is shown in the bottom panel. For details on instrumental and lifetime broadening see reference [58]. The spectra on the right show the calculated Fe  $4p$  DOS taken from reference [102] (dashed line) together with the  $K\beta_{2,5}$  line recorded after K capture (solid line).

A theoretical analysis of the  $\text{Fe}_2\text{O}_3$  valence XPS in references [58, 86] invokes a ligand-to-metal charge transfer scheme. A summary and analysis of x-ray emission and absorption results is given by Dräger *et al.* [49]. The consensus is that configuration interaction is important for the interpretation of the spectra. The spectra and diagrams given in Figure 48 show the results from a charge transfer calculation that includes three configurations  $|3d^4\rangle$ ,  $|3d^5\bar{L}\rangle$  and  $|3d^6\bar{L}^2\rangle$  together with the XPS results. The Figure on the left is taken from reference [58]. Ligand field charge transfer calculations that yield similar results were carried out by de Groot *et al.* and are published in reference [41]. The weak structure at about 14 eV binding energy is assigned to mainly Fe  $3d^4$  final states while the Fe  $3d^5\bar{L}$  final states mainly contribute to the intensity of the strong XPS feature at around 6 eV. Fujimori *et al.* assign the oxygen  $2p$  band to the strong XPS feature. Multiple-scattering  $X\alpha$  calculations by Nagel show that the Fe  $4p$  density of states (DOS) partly lies below the Fermi energy and has a maximum around 6 eV binding energy. Part of the Fe  $4p$  DOS will therefore be populated. A comparison of the  $K\beta_{2,5}$  peak measured after K capture with the Fe  $4p$  density of occupied states is shown on the right in Figure 48. The experimental spectrum is not corrected for the instrumental broadening. However, as mentioned in Chapter 2 I measured the  $\text{Fe}_2\text{O}_3$   $K\beta$

satellite lines with two different instrumental broadenings (calculated  $\Delta E_{geo}=1.4$  eV and 2.0 eV). The spectra do not differ within the statistical error indicating that the instrumental broadening hardly influences the spectra. The  $K\beta_{2,5}$  line has a FWHM of  $\approx 4$  eV and is about 1 eV broader than the calculated Fe  $4p$  DOS. Both show a shoulder on the low binding energy side. The calculations do not include the fact that in K capture the final state reflects the valence band configuration of a Mn impurity in an  $\text{Fe}_2\text{O}_3$  lattice. This could explain the broader feature in the experiment. The  $X\alpha$  calculations predict that there is no Fe  $4p$  occupied density of states around 14 eV binding energy.

The assignment of the spectral features given in Figure 48 agrees with our crude estimate from the comparison of the XPS with the  $K\beta$  K capture spectra. The weak XPS feature at 14 eV binding energies has solely Fe  $3d$  character and therefore does not show in the  $K\beta$  satellite spectra. It seems that there is no significant structure arising from Fe  $3d$  orbitals but the intensity of the  $K\beta_{2,5}$  peak is due to the density of occupied Fe  $4p$  states. I thus find that the XPS experimental data and the theoretical investigations using ligand field charge transfer calculations as well as multiple scattering  $X\alpha$  cluster calculations are consistent with the  $K\beta$  K capture satellite spectra. The  $K\beta$  satellite spectra after photoionization show the  $K\beta''$  and the  $K\beta_{2,5}$  structures but the broadening of the spectra limits the conclusions that can be drawn from a comparison with XPS as well as the calculations. I conclude that K capture as a mode of excitation yields information closer to the actual ground state valence electron configuration than photoionization.

## 6.2 Angular Dependence of $K\beta$ Satellite Lines in $[\text{Mn}(\text{N})(\text{CN})_5]^{3-}$

The angular dependence of the  $K\beta$  satellite emission in an oriented single crystal of a Mn nitrido complex  $[\text{Rh}(\text{en})_3][\text{Mn}(\text{N})(\text{CN})_5]\cdot\text{H}_2\text{O}$  was investigated. I carried out the experiments together with Uwe Bergmann. Jesper Bendix performed Kohn-Sham density functional calculations on  $[\text{Mn}(\text{N})(\text{CN})_5]^{3-}$  and obtained LCAO that describe the molecular orbitals. I used his results for a further theoretical analysis and to simulate the experimental spectra. The single crystal was prepared at Caltech by the literature method [13]. As shown in Figure 49, the Mn atom is surrounded by five cyanide groups and one nitrogen (nitrido). The Mn-nitrido bond is oriented along the  $z$ -direction. The four cis cyanide groups and the Mn atom do not lie in a plane (the  $xy$ -plane) but the four cyanide groups are displaced by 0.19 Å away from the nitrido in negative  $z$ -direction. The crystallographic distances are shown in Table 9 [13]. The structure of the complex is best approximated by the point group  $C_{4v}$  and the molecular structure suggests a strong spatial orientation of the molecular orbitals. The short Mn-N bond length at 1.50 Å in  $z$ -direction results in a large overlap between the Mn  $1s$  and the nitrido orbitals and the nitrido contribution to  $K\beta$  emission is expected to be large.

The  $K\beta$  satellite emission after photoionization of the oriented single crystal was measured for two different orientations of the Mn-nitrido axis relative to the analyzer crystals. The analyzer crystal orientation is described by the normal on the crystal surface at the center of the crystals and denote the angle between this normal and the Mn-nitrido axis  $\alpha$ . For the spectrum with the Mn-nitrido axis close to  $0^\circ$  relative to the analyzer crystals we only used two analyzers and oriented the Mn-nitrido axis towards the two analyzers. The angle in this case was  $\alpha \approx 8^\circ$ . In order to realize the  $\alpha=90^\circ$  case we oriented the Mn-nitrido axis parallel to an imaginary line connecting the centers of the two crystal (see Figure 9 in Chapter 2).

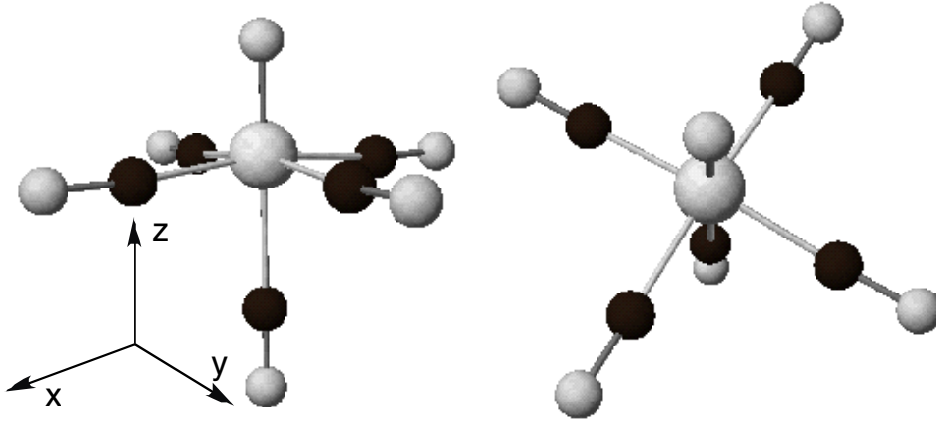


Figure 49: Structure of  $[Mn(N)(CN)_5]^{3-}$ . The dark balls are carbon atoms, the small grey balls are nitrogen and the larger grey ball is a Mn atoms. The nitrogen atom that is directly bond to the Mn is the nitrido at 1.50 Å bondlength. The Mn-nitrido direction is assigned to the z-axis and the plane parallel to the cyanide plane that includes the Mn atom is the xy-plane (at  $z=0$ ).

Table 9: Crystallographic distances in [Å] units for  $[Mn(N)(CN)_5]^{3-}$ .

Mn-N	Mn-C <sup>cis</sup>	Mn-C <sup>trans</sup>	C-N
1.50	1.99	2.24	1.15

One analyzer crystal covers a range of  $\Delta\alpha \approx 3^\circ$ . The total angular error bar is rather large ( $\approx \pm 10^\circ$ ) but as we will see below, the intensity dependence on the angle scales with  $\cos^2$  and as long as we are close to  $0^\circ$  and  $90^\circ$  the error in intensity due to the large error in angle is acceptable. The energy of the incident beam was tuned to 9.1 keV. This is above the Mn KL-edge (see Chapter 4) and we have to bear in mind that  $KL\beta$  lines might contribute to the spectra. At this high excitation energy (2.6 keV above Mn K-edge) the polarization of the incident beam will not affect the fluorescence emission. The experimental spectra are shown in Figure 50. The spectra were taken on beamline 10-2 at SSRL and the instrumental energy broadening was  $\approx 1.3$  eV (see Chapter 2).

The peak at 0 eV relative fluorescence energy is the  $K\beta''$  or ‘cross-over’ peak that we already encountered in  $Fe_2O_3$  in the previous Section. It is generally assigned to a ligand (oxygen, nitrogen or fluorine)  $2s$  to metal  $1s$  transition as discussed in detail in reference [17]. Its origin will be analyzed below using density functional theory results. The structures at

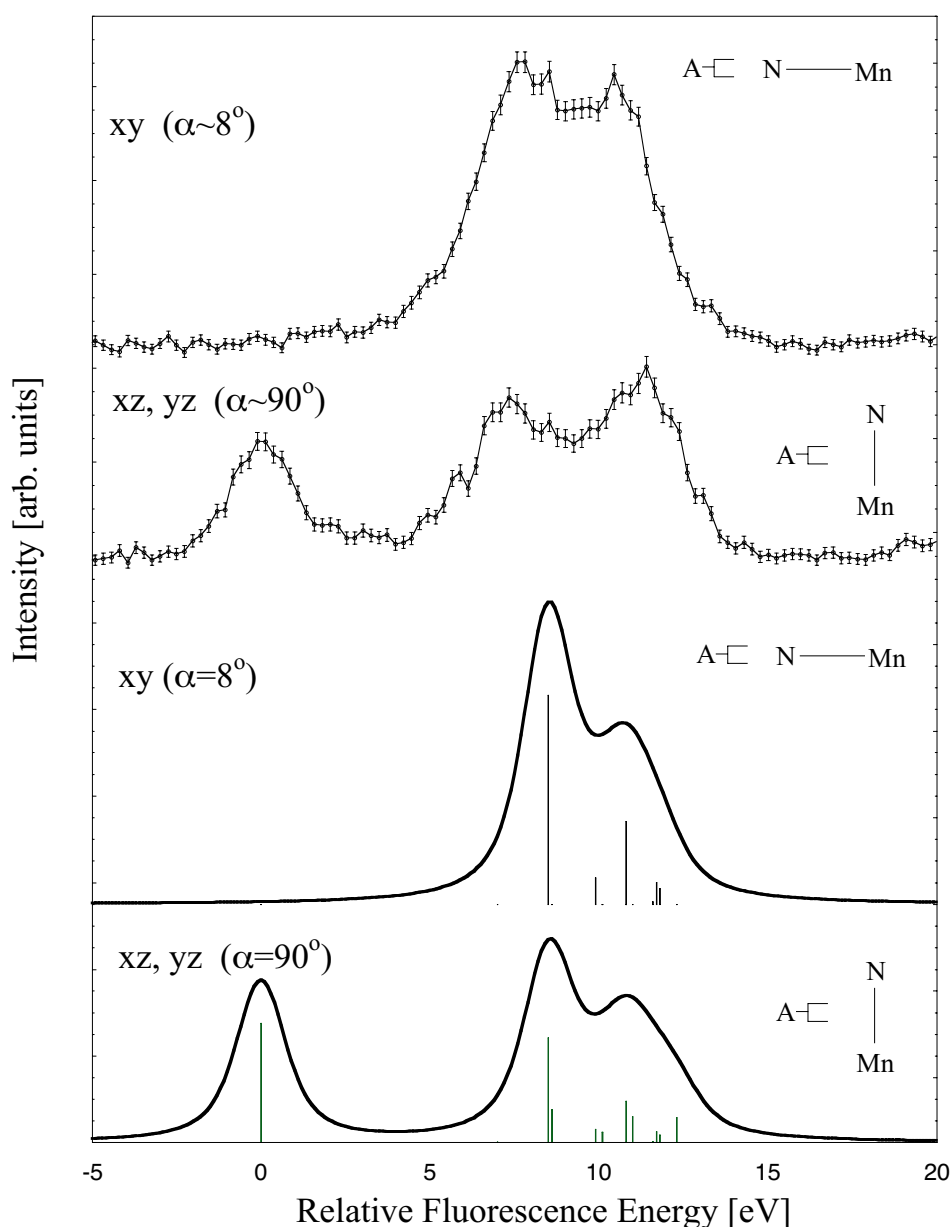


Figure 50:  $\text{Mn } K\beta$  satellite lines in  $[\text{Rh}(\text{en})_3][\text{Mn}(\text{N})(\text{CN})_5]\cdot\text{H}_2\text{O}$ . The top two spectra show the experimental results after photoionization for angles  $\alpha \approx 90^\circ$  and  $8^\circ$ . The tail of the  $K\beta_{1,3}$  peak was subtracted and the spectra are normalized to each other in the entire  $K\beta$  spectral area. The bottom two spectra show the corresponding calculations for the two angles. A 1.2 eV Lorentzian and 1.3 eV Gaussian broadening was applied to the stick spectra to account for the lifetime and instrumental broadening, respectively. The experimental and theoretical spectra are aligned in the cross-over peak. The insets on the right show the (simplified) respective orientation between the Mn-nitrido axis and the analyzer (A).

higher energies are the  $K\beta_{2,5}$  lines. The cross-over peak disappears at  $\alpha \approx 8^\circ$ . The  $K\beta_{2,5}$  feature shows two ‘bands’ separated by about 2.7 eV. The relative intensities of the two bands vary between the two angles: the band at higher energies gains in intensity relative to the band at lower energies for  $\alpha \approx 90^\circ$ .

In order to understand the angular dependence I further break down the integral given in equation 68:

$$W_{if} \sim \omega_{if}^3 |\vec{r}_{if}|^2 \cos^2 \gamma = \omega_{if}^3 (|x_{if}|^2 \cos^2 \gamma_x + |y_{if}|^2 \cos^2 \gamma_y + |z_{if}|^2 \cos^2 \gamma_z) \quad (69)$$

where the angles  $\gamma_{x,y,z}$  describe the angles between the unit vectors  $\hat{x}, \hat{y}, \hat{z}$  and the polarization vector of the outgoing photon. Because of the rotational symmetry  $C_4$  around the z-axis one obtains  $|x_{if}| = |y_{if}|$  and I denote the transition integral resulting from either x or y as dipole operator by  $|(x, y)_{if}|$ . In the notation given above  $\alpha = (90^\circ - \gamma_z)$  and it holds for the two extreme cases  $\alpha = 90^\circ$

$$W_{if} \sim \omega_{if}^3 (|(x, y)_{if}|^2 + |z_{if}|^2) \quad (70)$$

and  $\alpha = 0^\circ$ :

$$W_{if} \sim \omega_{if}^3 2|(x, y)_{if}|^2 \quad (71)$$

A qualitative analysis of the transition probabilities can now be attempted using symmetry arguments. There are five irreps in  $C_{4v}$  namely  $A_1, A_2, B_1, B_2$  and E. The coordinates (x,y,z) can be assigned to irreps and one finds that (x,y) transform as E and z transforms as  $A_1$  [7]. In order for a transition to be orbitally allowed the direct product  $\Gamma_i \times \Gamma_{xyz} \times \Gamma_f$  has to contain  $A_1$  [54]. The Mn  $1s$  orbital will hardly be affected by the crystal field and I assume the atomic S symmetry will branch to  $A_1$  in  $C_{4v}$  [29]. Determining the direct product using Tables, *e.g.* in reference [54], one finds that only the symmetries  $A_1$  and E of the valence electron orbitals yield non-zero transition integrals. For  $|z_{if}|$  one obtains  $A_1$  and for  $|(x, y)_{if}|$  one obtains E symmetry for the valence electron orbital with non-zero transition integrals.

We now turn to the experimental results again. The cross-over peak disappears when the Mn-nitrido axis points towards the analyzer crystals, *i.e.*  $\cos \gamma_z = 90$  ( $\alpha = 0^\circ$ ) and we only have contributions from  $|(x, y)_{if}|$  as expressed in equation 71. This in turn means that the spectra do not show any transitions resulting from valence orbitals with  $A_1$  symmetry because the transition integrals for the transitions with (x,y) as dipole operator and  $A_1$  as the symmetry in the valence orbital are zero. The spectrum taken at  $\alpha \approx 8^\circ$  mostly shows transitions from valence orbitals with E symmetry except for a small  $A_1$  contribution due to the fact that  $\alpha$  is not exactly zero. It can thus be concluded that the valence orbital that can be assigned to the cross-over peak has  $A_1$  symmetry. The spectrum taken at  $\alpha \approx 90^\circ$  shows equal contributions from E and  $A_1$  symmetry.

It is desirable to validate this interpretation using a theoretical model. Jesper Bendix determined the occupied molecular orbitals in the framework of Kohn-Sham density functional theory [13]. Equation 68 shows that I have to use the valence orbitals in the  $1s$  excited state in order to calculate the transition matrix elements. In the calculations the  $1s$  hole was simulated by an additional nuclear charge (Z+1 model). Furthermore, I need to insert the Mn  $1s$  orbital of the fully relaxed final state. However, at the time when this thesis was written I did not have access to results of a final state calculation and I therefore used the Mn  $1s$  orbital of the excited state. I only compare relative intensities and the error introduced by using the wrong Mn  $1s$  orbital is probably obscured by more dramatic simplifications (see below). The Kohn-Sham density functional calculations were performed using the LDA exchange correlation functional. A population analysis was performed using the Mulliken model [100]. Table 10 lists the symmetries, relative energies and LCAO of the calculated occupied molecular orbitals in the energy range of the  $K\beta$  satellites. I point out that the Mulliken population analysis yields a negative Mn  $4p$  contribution for orbital #6 (7E). Table

10 has two main sources of errors. First, as noted before, the method proposed by Mulliken has been criticized for giving unphysical results, particularly for systems with strong electron delocalization [112]. The error occurs when the coefficients for the atomic orbitals in the LCAO of the molecular orbital are determined by means of a Mulliken population analysis. The molecular orbitals as obtained in the density functional calculations are still correctly expressed in the LCAO. One can view the LCAO description of a molecular orbital as a linear expansion and one aims to use terms in the linear expansion that are close to physical atomic orbitals. A second source of error arises from the fact that the molecular orbitals are described by a finite set of functions. I expect the population analysis to be the main contribution to the error in Table 10. Bearing the limitations of the Mulliken method in mind I will nevertheless analyze the contributions from the different atoms to the  $K\beta$  satellite spectrum.

The atomic orbitals are written as linear combinations of Slater type orbitals of the form:

$$\phi_{Slater} = Nr^{(n-1-l)}e^{-r\zeta} \quad (72)$$

with the principal quantum number  $n$  and the orbital quantum number  $l$ . The parameters  $\zeta$  are adjusted to model the atomic orbitals best. The coefficients  $N$  are the results of the variational procedure in the Kohn-Sham model. I used the program *Mathematica* to numerically calculate the  $\langle \phi_f^{Mn_{1s}} | \vec{r} | \phi_i^{AO} \rangle$  transition integrals for each atomic orbital  $\phi_i^{AO}$ . The results are shown in Table 11. The Mn  $4p$  orbital yields the strongest contribution but it is only a factor 2.7 larger than the integrals for the  $N^{nitrido}$   $2s$  and  $2p_{(x,y)}$  orbitals. Other strong contributions arise from the carbons that directly bind to the Mn. Combining the results from Table 11 with the relative contributions to the orbital  $13A_1$  (Table 10) that is assigned to the cross-over peak shows that 91.2% of the cross over peak intensity comes from a  $N^{nitrido}$   $2s$  orbital while the Mn  $3p$  and Mn  $4p$  orbitals only account for 3.1% and 4.7%, respectively. This result shows that the main intensity of the cross-peak indeed arises from a ligand  $2s$  orbital. I do not expect this result to be flawed by the shortcomings of the Mulliken population analysis. Note that the Mn atom and the  $C^{cis}$  and  $N^{cis}$  atoms are not in a plane giving small but finite values for the cis-ligands  $2s$  and  $2p_{(x,y)}$  orbitals in  $\langle \phi_f^{Mn_{1s}} | z | \phi_i^{AO} \rangle$  and for the cis-ligand  $2p_z$  orbital in  $\langle \phi_f^{Mn_{1s}} | (x, y) | \phi_i^{AO} \rangle$ .

I used equation 69 together with Tables 10 and 11 to calculate the transition integrals for the molecular orbitals and obtained the spectra shown in Figure 50. I applied a Lorentzian broadening of 1.2 eV and a Gaussian broadening of 1.3 eV. Our theoretical spectra do not include any configuration interaction. We have seen for the  $K\beta$  spectra that in particular symmetry mixing can strongly influence the relative intensities and energy positions of the final states. Furthermore, it is likely that shake-up and shake-off final states are populated, too, as I have already discussed in context with the comparison between K capture and photoionization. However, this crude approach to calculate the  $K\beta$  satellite spectrum already reproduces some spectral features. First I note that the orbital assigned to the cross over peak indeed has  $A_1$  symmetry in the calculations. A study of the cross over peak intensity dependence on the angle  $\alpha$  can be found in reference [14]. The calculations approximately yield the experimentally observed energy splitting between the cross over peak and the  $K\beta_{2,5}$  feature. They furthermore reproduce the two  $K\beta_{2,5}$  bands. Even though the relative intensity ratio of the two  $K\beta_{2,5}$  bands is not well reproduced in the theoretical spectrum, the calculations seem to give the correct trend: The structure at  $\approx 8.5$  eV becomes weaker relative to the structure at  $\approx 11.5$  eV when changing from  $xy$ - to  $(xz,yz)$ -orientation. The reason for this is that the strongest contribution at 8.5 eV to the  $xy$ -spectrum (orbital # 5

Table 10: *Symmetries, transition energies and LCAO for molecular orbitals above  $K\beta''$  ( $13A_1$ ). The calculated relative intensities for  $\alpha=90^\circ$  and  $\alpha=0^\circ$  are given. The energies are given in eV relative to the  $13A_1$  orbital.*

#	MO	Energy	Relative Intensity $\alpha=90^\circ$	Relative Intensity $\alpha=0^\circ$
1	$13A_1$	0.0	0.56	0
			86% $N^{nitrido}(2s) + 2.14\% N^{nitrido}(2p_z) + 0.57\% N^{cis}(2s) + 0.48\% Mn(3p_z) + 1.64\% Mn(4p_z) + 1.67\% C^{cis}(2p_x)$	
2	$14A_1$	7.0	0.00	0
			36% $C^{cis}(2s) + 29\% C^{cis}(2p_{x,y}) + 11\% Mn(4s) + 9\% N^{cis}(2s) + 0.21\% Mn(4p_z)$	
3	$4B_1$	8.5	0	0
			32% $Mn(3d_{x^2-y^2}) + 30\% C^{cis}(2s) + 14\% C^{cis}(2p_{x,y}) + 13\% N^{cis}(2s)$	
4	$15A_1$	8.6	0.15	0
			20% $Mn(3d_{z^2}) + 26\% C^{trans}(2s) + 14\% N^{trans}(2s) + 13\% N^{trans}(2p_z) + 9\% C^{trans}(2p_z) + 6.14\% Mn(4p_z)$	
5	$6E$	8.5	0.50	1.00
			34% $C^{cis}(2s) + 15.58\% Mn(4p_{x,y}) + 16\% C^{cis}(2p_{x,y}) + 16\% N^{cis}(2s) + 12\% N^{cis}(2p_{x,y})$	
6	$7E$	9.9	0.06	0.13
			44% $Mn(3d_{z,x,yz}) + 32\% N(2p_{x,y}) - 0.11\% Mn(4p_{x,y})$	
7	$16A_1$	10.1	0.05	0
			34% $N(2p_z) + 20\% N^{trans}(2p_z) + 12\% N^{trans}(2s) + 13\% Mn(3d_{z^2}) + 0.60\% Mn(4p_z)$	
8	$1B_2$	10.5	0	0
			46% $C^{cis}(2p_{x,y}) + 18\% Mn(3d_{xy}) + 37\% N^{cis}(2p_{x,y})$	
9	$17A_1$	10.8	0.00	0
			38% $N^{cis}(2p_{x,y}) + 13\% N^{cis}(2s) + 12\% N^{nitrido}(2p_z) + 0.01\% Mn(4p_z)$	
10	$5B_1$	10.7	0	0
			44% $N^{cis}(2p_{x,y}) + 17\% N^{cis}(2s) + 19\% Mn(3d_{x^2-y^2}) + 10\% C^{cis}(2p_{x,y})$	
11	$8E$	10.8	0.19	0.39
			48% $N^{cis}(2p_{x,y}) + 10\% N^{cis}(2s) + 19\% C^{cis}(2p_{x,y}) + 6.90\% Mn(4p_{x,y})$	
12	$18A_1$	11.0	0.12	0
			42% $N^{cis}(2p_z) + 35\% C^{cis}(2p_z) + 10\% N^{trans}(2p_z) + 2.92\% Mn(4p_z)$	
13	$9E$	11.6	0.01	0.01
			33% $N^{cis}(2p_z) + 19\% C^{cis}(2p_z) + 14\% N^{cis}(2p_{x,y}) + 0.02\% Mn(4p_{x,y})$	
14	$1A_2$	11.5	0	0
			64% $N^{cis}(2p_{x,y}) + 33\% C^{cis}(2p_{x,y})$	
15	$10E$	11.7	0.06	0.11
			33% $N^{cis}(2p_{x,y}) + 11\% C^{cis}(2p_{x,y}) + 17\% N^{cis}(2p_z) + 2.26\% Mn(4p_{x,y})$	
16	$11E$	11.8	0.04	0.07
			23% $N^{trans}(2p_{x,y}) + 11\% C^{trans}(2p_{x,y}) + 28\% N^{cis}(2p_{x,y}) + 0.44\% Mn(4p_{x,y})$	
17	$19A_1$	12.3	0.12	0
			20% $N^{cis}(2p_z) + 15\% C^{trans}(2p_z) + 15\% C^{trans}(2s) + 14\% N^{trans}(2p_z) + 14\% N(2p_z) + 2.96\% Mn(4p_z)$	
18	$2B_2$	13.6	0	0
			73% $Mn(3d_{xy}) + 23\% N^{cis}(2p_{x,y})$	

Table 11: Relative magnitudes of transition integrals  $\langle \phi_f^{Mn_{1s}} | \vec{r} | \phi_i^{AO} \rangle$  for  $z$  and  $(x,y)$  as dipole operators.  $\phi_i^{AO}$  denotes an atomic orbital in the 1s excited state.

	$\phi_i^{AO}$	$\mathbf{z}$	$(\mathbf{x},\mathbf{y})$
$\text{C}^{cis}$	2s	2.7	28.2
	$2p_{(x,y)}$	4.4	19.6
	$2p_z$	25.7	4.4
$\text{N}^{cis}$	2s	0.8	12.2
	$2p_{(x,y)}$	1.5	17.8
	$2p_z$	6.7	1.5
$\text{C}^{trans}$	2s	25.9	0
	$2p_{(x,y)}$	0	21.0
	$2p_z$	22.2	0
$\text{N}^{trans}$	2s	9.4	0
	$2p_{(x,y)}$	0	5.1
	$2p_z$	15.3	0
$\text{N}^{nitrido}$	2s	36.6	0
	$2p_{(x,y)}$	0	36.6
	$2p_z$	16.3	0
Mn	$4p_{(x,y,z)}$	100.0	
Mn	$3p_{(x,y,z)}$	228.4	

(6E), see Table 10) arises from the Mn  $4p_{(x,y)}$  orbitals. The Mn  $4p_x$  and  $4p_y$  intensities add when looking at the xy-plane ( $\alpha = 0^\circ$ ). Either orbital contributes to the spectrum when going to xz- or yz-direction and the intensity of this contribution is halved compared to the xy-direction.

I conclude that density functional calculations help to qualitatively understand the  $K\beta$  satellite emission using the dipole approximation and symmetry arguments. The spectra are dominated by transitions from valence orbitals that have orbital angular momentum  $p$  character relative to the metal center. I attempted a quantitative interpretation in a simple one-electron, sudden approximation approach and obtained a rough agreement between theory and experiment. The energy splittings are rather well reproduced. However, to calculate the correct relative intensities a more elaborate theoretical approach including configuration interaction is necessary. I note that a comparison to K capture experimental spectra probably would yield better agreement with a theory that does not include shake transitions. However, only few laboratories are equipped to carry out radiochemistry and I could not obtain the  $[\text{Rh}(\text{en})_3][\text{Mn}(\text{N})(\text{CN})_5] \cdot \text{H}_2\text{O}$  crystal spiked with  $^{54}\text{Mn}$ . Finally, I point to a study by Dräger *et al.* who investigated polarized spectra from single crystalline  $\text{Na}_2\text{Fe}(\text{NO})(\text{CN})_5 \cdot \text{H}_2\text{O}$  [48]. The structure of this nitroprusside complex is very similar to our Mn nitrido sample and most of the arguments used here apply to the nitroprusside, as well.

## 7 Chemical Dependence of $K\beta$ Emission

In the following I summarize  $K\beta$  spectra from Mn, Fe and Ni compounds as well as metalloproteins containing Fe, namely myoglobin. The purpose of this Chapter is to give an overview over  $K\beta$  spectra and to illustrate the usefulness of  $K\beta$  spectroscopy for chemical analysis. I will try to derive simple relations between the formal oxidation state of the metal atom and a change in spectral features. For a more detailed analysis the calculated effective number of unpaired  $3d$  electrons can be used. However, since this number is not always available I use the formal oxidation state and I will give examples where the limits of this approximation are reached. For experimental details see Chapter 2.

### 7.1 $K\beta$ Main Lines in $^{54}\text{Mn}$ Compounds after K Capture

I start with  $K\beta$  spectra taken in  $^{54}\text{Mn}$  compounds and compare them to one- and two-configuration ligand field multiplet calculations. The total number of counts in the  $K\beta_{1,3}$  peak for the spectra shown in Figure 51 are  $\approx 900$ ,  $\approx 630$  and  $\approx 450$  for  $^{54}\text{MnO}$ ,  $^{54}\text{Mn}_2\text{O}_3$  and  $^{54}\text{MnO}_2$ , respectively. A constant background was subtracted from the spectra. The three experimental spectra shown in Figure 51 exhibit a chemical dependence of the  $K\beta$  main lines. The  $K\beta'$  structure becomes weaker for higher oxidation states. All three  $K\beta_{1,3}$  peaks show a negative asymmetry which is caused by a shoulder on the low energy side. The  $K\beta_{1,3}$  line in  $^{54}\text{Mn}_2\text{O}_3$  appears broader than for the other Mn compounds. Furthermore, the low energy shoulder in  $^{54}\text{MnO}_2$  stretches to lower fluorescence energies compared to  $^{54}\text{MnO}$  and  $^{54}\text{Mn}_2\text{O}_3$ .

In a theoretical analysis it is desirable to include as few empirical parameters as possible. I therefore first carried out single configuration ligand field multiplet calculations for Cr  $3d^5$ ,  $3d^4$  and  $3d^3$  ions in an octahedral environment and I then investigated the influence of charge transfer configuration interaction. Including one configuration I assume ground state symmetries  $^6A_1$ ,  $^5E$  and  $^4A_2$  for  $^{54}\text{MnO}$ ,  $^{54}\text{Mn}_2\text{O}_3$  and  $^{54}\text{MnO}_2$ , respectively, neglecting spin-orbit coupling. While for  $^{54}\text{MnO}$  and  $^{54}\text{MnO}_2$  octahedral symmetry is a good approximation I have to take possible influences of a Jahn-Teller distortion in  $^{54}\text{Mn}_2\text{O}_3$  into account [54, 140]. I therefore performed additional calculations for Cr  $3d^4$  in a reduced ( $D_{4h}$ ) symmetry in order to simulate the splitting of the  $d_{x^2-y^2}$  and  $d_{z^2}$  orbitals. A value of  $D_s=0.36$  eV is suggested in reference [108] and I adopted this value together with  $10Dq=1.0$  eV to investigate the effect of reduced symmetry on the  $K\beta$  main lines. Four hopping terms exist in  $D_{4h}$  symmetry to express the metal-ligand hybridization. I used  $V(B_1)=3.0$  eV,  $V(A_1)=1.73$  eV,  $V(B_2)=-1.5$  eV and  $V(E)=-1.03$  eV. These values simulated transition metal L-edge spectra satisfactorily [39]. In all calculations, the  $(3p,3d)$  Slater parameters were scaled down to 70% and the  $(3d,3d)$  Slater parameters to 80% (see Chapter 5.1).

I investigated the dependence of the spectra on the ligand field splitting  $10Dq$  in  $O_h$  symmetry within physical limits for a high spin configuration ( $10Dq=1.0$  to  $3.0$  eV) and found that it can be neglected in view of the statistical error in the experimental spectra. I therefore used  $10Dq=1.0$  eV for all three  $O_h$  calculations. Furthermore, the center of gravity of the final state configuration is identical for all calculated spectra. The energy scale of the theoretical spectra is shifted such that the first moment for the experimental  $^{54}\text{MnO}$  spectrum coincides with the ligand field calculations for the Cr  $3d^5$  ion. The Cr K level natural width is 1.08

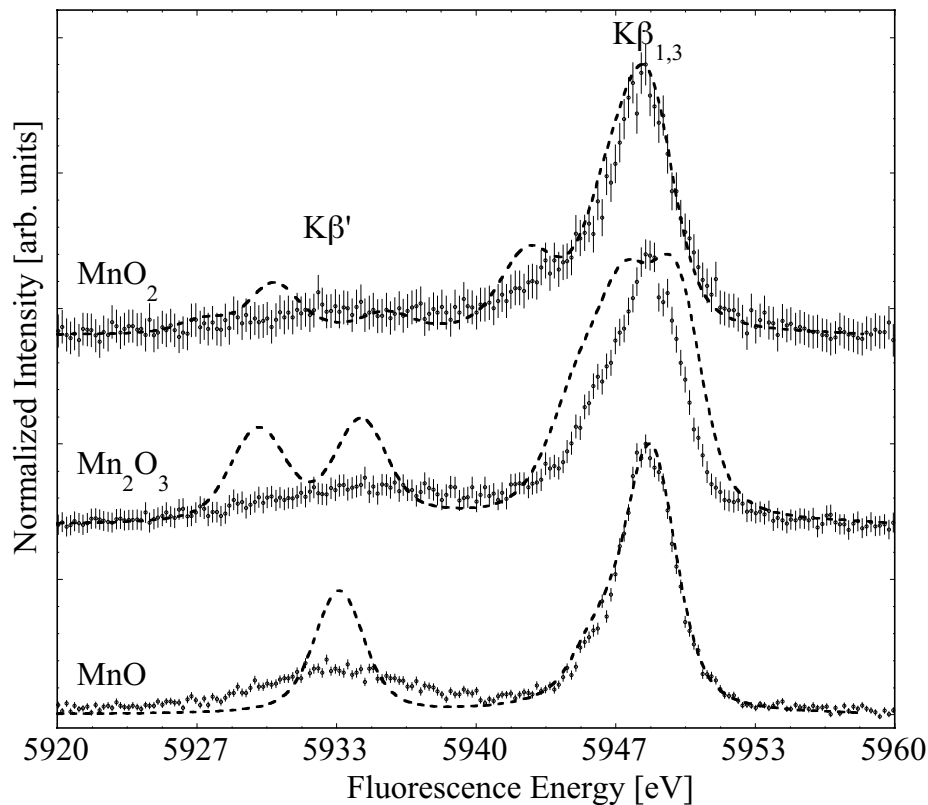


Figure 51:  $K\beta$  main lines in  $^{54}\text{Mn}$  compounds measured after  $K$  capture. The experimental spectra are compared to one-configuration ligand field multiplet calculations (dashed lines). For  $^{54}\text{Mn}_2\text{O}_3$  the calculations in  $D_{4h}$  symmetry with  $10Dq=1.0$  eV and  $Ds=0.36$  eV are shown. The  $^{54}\text{MnO}$  and  $^{54}\text{MnO}_2$  simulations were obtained in  $O_h$  symmetry with  $10Dq=1.0$  eV. The theoretical spectra are broadened by a 1.3 eV Lorentzian and a 2.0 eV Gaussian

eV [83] and I used a slightly higher value (1.3 eV) for the Lorentzian broadening to account for the final state lifetime. I applied a constant lifetime broadening, *i.e.* I did not consider a term dependent final state lifetime. I chose this approach because there is, to my knowledge, no theoretical treatment in the literature of the final state lifetime in Mn(III) and Mn(IV) compounds unlike for Mn(II) as discussed in Chapter 5. For a comparison of theoretical spectra it is important to use the same level of theory and I therefore used a constant lifetime broadening for all theoretical spectra. The spectra were furthermore convoluted by a 2.0 eV Gaussian to account for instrumental broadening. The instrumental broadening was set such that the width of the experimental  $^{54}\text{MnO}$   $K\beta_{1,3}$  peak was approximately reproduced in the calculations.

Three different simulations for the  $^{54}\text{Mn}_2\text{O}_3$  ( $\text{Cr } 3d^4$ ) spectrum are shown in Figure 52 for atomic ( $\text{SO}_3$ ), octahedral ( $O_h$ ,  $10Dq=1.0$  eV) and Jahn-Teller distorted (tetragonal,  $D_{4h}$ ,  $10Dq=1.0$  eV,  $Ds=0.36$  eV) point group symmetry. E symmetry in  $O_h$  can branch into  $A_1$  and  $B_1$  in  $D_{4h}$  [54] and the calculations yield  $A_1$  for the ground state symmetry of  $^{54}\text{Mn}_2\text{O}_3$ . The results of the calculations are very sensitive to the  $10Dq$  and  $Ds$  values in  $D_{4h}$  unlike the  $O_h$  calculations that are very stable with respect to  $10Dq$ . It is difficult to validate the calculations by comparison with the experimental results because of poor statistics in the  $K$  capture data and the neglect of term dependent final state lifetime broadening in

the calculations. However, a striking difference between the  $O_h$  and  $D_{4h}$  spectra is that the asymmetry of the  $K\beta_{1,3}$  peak changes from positive to negative. Since a negative asymmetry is in accordance with the experimental observation I conclude that it is necessary to describe  $^{54}\text{Mn}_2\text{O}_3$  in  $D_{4h}$  symmetry and I use the bottom spectrum of Figure 52 as the simulation for  $^{54}\text{Mn}_2\text{O}_3$ . I note that a photoionization experiment would, of course, yield better statistics but then the influence of the change of the effective nuclear potential has to be evaluated. I have argued before that the valence electron configuration in a K capture experiment is closer to the actual ground configuration. A discussion of the photoexcited  $\text{Mn}_2\text{O}_3$  is given in reference [108].

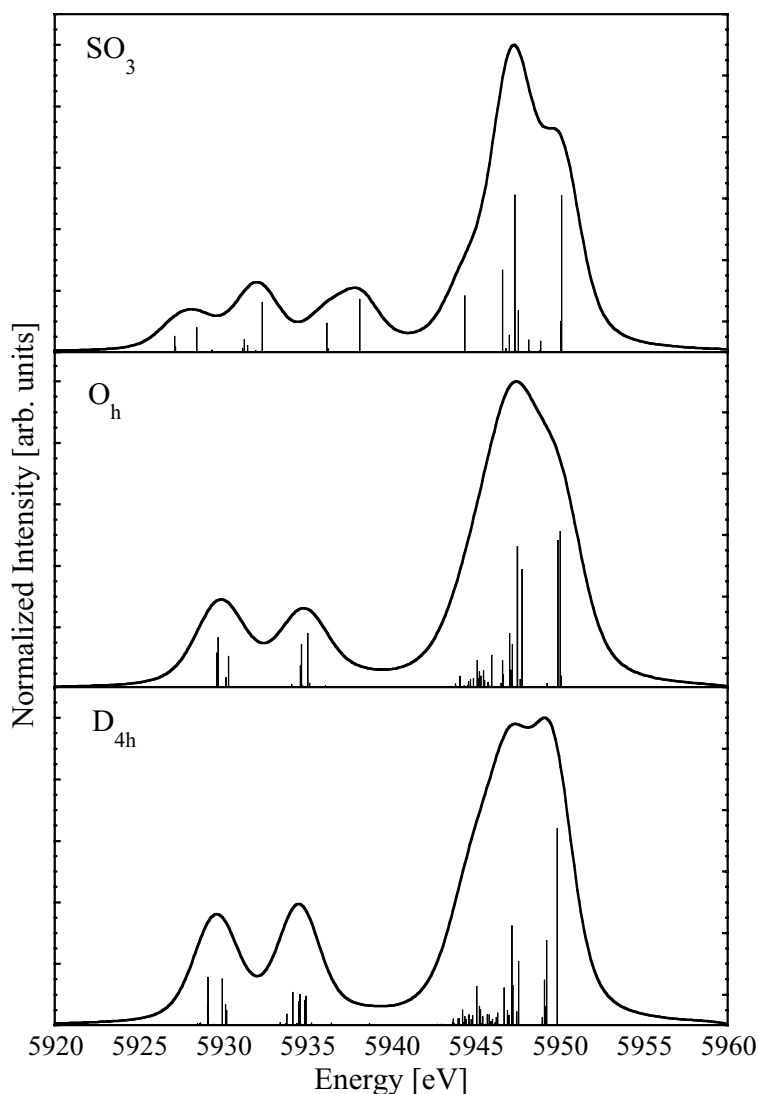


Figure 52: *Single configuration ligand field multiplet calculations for  $\text{Cr } 3d^4$  in three different symmetries. The energy scale was shifted to coincide with the experiment. The ligand field splitting in  $O_h$  is  $10Dq=1.0$  eV and in  $D_{4h}$  the values are  $10Dq=1.0$  eV and  $Ds=0.36$  eV. The applied broadenings are a 1.3 eV Lorentzian and a 2.0 eV Gaussian. No term dependent final state lifetime broadening was included.*

The theoretical simulations using one configuration for the three Mn compounds are compared to the experimental results in Figure 51. The MnO spectrum was discussed in detail

in Chapter 5. Except for the  $K\beta_{1,3}$  peak in  $^{54}\text{MnO}$  the agreement is rather poor. However, a close look reveals some similarities between the calculations and the experimental results. The uncertainty for the ligand field parameters  $10Dq$  and  $Ds$  for the  $^{54}\text{Mn}_2\text{O}_3$  simulation gives a large range of different theoretical  $K\beta$  spectra that I cannot discuss here. However, all  $^{54}\text{Mn}_2\text{O}_3$  simulation in  $D_{4h}$  symmetry yield negative asymmetry for the  $K\beta_{1,3}$  peak. Besides the asymmetry, the calculated  $3d^4$  configuration ( $^{54}\text{Mn}_2\text{O}_3$ ) shows a broader  $K\beta_{1,3}$  peak than for the other compounds in agreement with the experiment. The simulation for  $^{54}\text{MnO}_2$  shows structure on the low energy side of the  $K\beta_{1,3}$  peak at about 5942.5 eV fluorescence energy. This structure approximately coincides with a pronounced low energy tail of the  $K\beta_{1,3}$  peak in the experimental spectrum. From these observations it can be concluded that the ligand field multiplet model appears to be the correct approach to model the experimental spectra.

In an effort to improve the agreement with the experiment in the calculations I carried out two-configuration ligand field multiplet calculations. I chose as charge transfer energies  $\Delta=7.0$  eV for  $^{54}\text{MnO}$  and  $\Delta=3.0$  eV for  $^{54}\text{Mn}_2\text{O}_3$  and  $^{54}\text{MnO}_2$  in the  $1s$  intermediate and final state [21] (see Chapter 5.1). The hopping terms were set to  $V(E_g)=2.0$  eV and  $V(T_{2g})=-1.0$  eV. The results are compared to the experimental spectra in Figure 53. For  $^{54}\text{Mn}_2\text{O}_3$  and  $^{54}\text{MnO}_2$  the overall agreement with the experiment is improved. The low energy shoulder of the  $^{54}\text{MnO}$   $K\beta_{1,3}$  peak is less pronounced in the charge transfer calculations in agreement with the experiment. However, it seems that  $^{54}\text{Mn}_2\text{O}_3$  still is not adequately described by the theory. I ascribe this to an inaccurate description of the Jahn-Teller distortion in the theoretical model. Other discrepancies between theory and experiment arise from the inadequate final state lifetime treatment.

In order to quantify the chemical dependence I use a moment analysis as performed before in Chapter 5. Recent studies in references [136, 95] use the first moment of the  $K\beta_{1,3}$  peak in Mn compounds to investigate the Mn oxidation state. This assumption is primarily based on empirical observations. For a theoretical explanation I use the following approach: As a working hypothesis I first propose that upon Mn oxidation or reduction the change of the center of gravity of the entire  $K\beta$  multiplet can be neglected with respect to the observed shift in the  $K\beta_{1,3}$  line. This implies that the total energies of  $1s$  and  $3p$  orbitals shift by the same amount when the number of valence electrons is changed and I thus neglect the difference in screening of the nuclear charge by a valence electron. In an ionic picture this is a gross simplification because of the strong ( $3p,3d$ ) overlap. However, in a compound the metal atom is not ionized and the electrons in hybridized orbitals will still contribute to the screening. Second, I assume that the valence electrons influence the  $K\beta_{1,3}$  fluorescence energy primarily *via* the ( $3p,3d$ ) exchange interaction. Since the  $K\beta'$  and  $K\beta_{1,3}$  features are predominantly split by the exchange interaction, the  $K\beta_{1,3}$  peak shifts to lower fluorescence energies for a smaller effective number of unpaired  $3d$  electrons because the exchange splitting is reduced and the center of gravity remains constant. I acknowledge that this is a very simple approach to a complex problem. However, with respect to complex molecular structures as they are encountered in proteins it is desirable to obtain a simple handle on the interpretation. I therefore try to find a correlation between the formal oxidation state and  $K\beta_{1,3}$  first moment. A more sophisticated approach would include results from density functional calculations for the effective number of unpaired valence electrons as described in Chapter 5. In the following moment analysis of the spectra I will include the theoretical results from the charge transfer calculations.

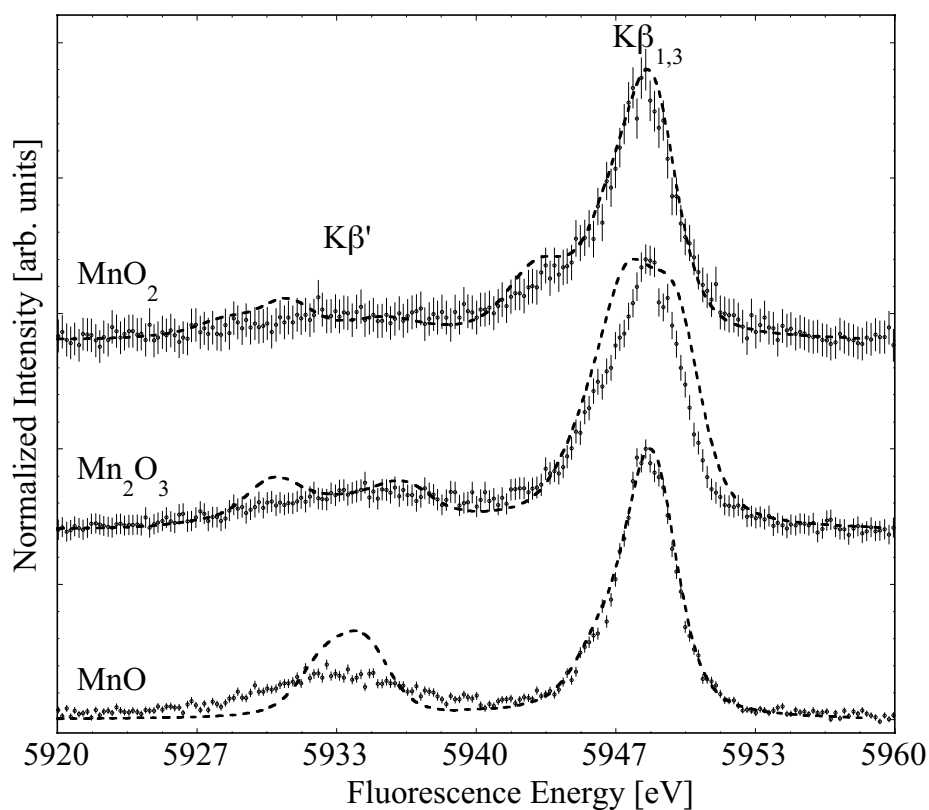


Figure 53: Charge transfer configuration interaction calculations for  $^{54}\text{Mn}$  compounds (dashed lines) compared to experimental spectra. The same ligand field parameters as in Figures 52 and 51 are used. The charge transfer energies are  $\Delta=7.0$  eV for  $^{54}\text{MnO}$  and  $\Delta=3.0$  eV for  $^{54}\text{Mn}_2\text{O}_3$  and  $^{54}\text{MnO}_2$ . For  $^{54}\text{Mn}_2\text{O}_3$  the  $D_{4h}$  calculations are shown.

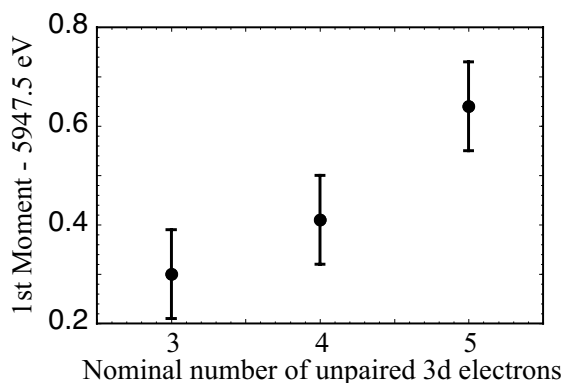


Figure 54: Experimental first moments of  $K\beta_{1,3}$  peak in Mn compounds. The nominal number of unpaired 3d electrons is derived from the formal oxidation state. The error of  $\pm 0.09$  eV is due to the uncertainty in the relative energy calibration.

Following the arguments given above I calculate the first moments of the  $K\beta_{1,3}$  experimental peak using data points down to 50% of the peak intensity. Since the experimental spectra show rather poor statistics, the selection of the energy range for the moment analysis is connected with a rather large error. The results with the errors are shown in Figure 54.

Table 12: Results of  $K\beta_{1,3}$  moment analysis for experimental and calculated spectra of Mn compounds. The theoretical values of the charge transfer calculations are shown. The symmetries that were used in the theoretical simulations are given. The energy scale of the calculated spectra was shifted such that the  $K\beta_{1,3}$  first moments coincide for  $^{54}\text{MnO}$ .

	Experiment				Theory		
	$M_1$ [-5948.14 eV]	$M_2$ [(eV) <sup>2</sup> ]	$M_3$ [(eV) <sup>3</sup> ]		$M_1$ [eV]	$M_2$ [(eV) <sup>2</sup> ]	$M_3$ [(eV) <sup>3</sup> ]
$^{54}\text{MnO}$	0.00	0.69 (1)	-0.01 (1)	$O_h$	0.00	0.77	-0.05
$^{54}\text{Mn}_2\text{O}_3$	-0.23 (9)	1.49 (1)	-0.23 (4)	$D_{4h}$	0.04	1.93	-0.10
$^{54}\text{MnO}_2$	-0.34 (9)	1.10 (1)	-0.09 (3)	$O_h$	-0.30	1.08	-0.12

We observe that the  $K\beta_{1,3}$  first moment shifts to lower fluorescence energies with a smaller number of unpaired  $3d$  electrons confirming the crude model. All three moments are listed in Table 12 for the experimental and theoretical values. Rather good agreement in  $M_2$  and  $M_3$  is achieved for  $^{54}\text{MnO}$  and  $^{54}\text{MnO}_2$ . The negative asymmetry for  $^{54}\text{Mn}_2\text{O}_3$  is reproduced in the  $D_{4h}$  calculations. However, the magnitudes of the values for  $M_2$  and  $M_3$  are too large in the theoretical simulation for  $^{54}\text{Mn}_2\text{O}_3$ . Furthermore, the first moment  $M_1$  does not follow the trend observed in the experiment. I therefore conclude that the  $K\beta$  emission in octahedral complexes can be described rather well in the ligand field charge transfer model. Additional empirical parameters are necessary in lower symmetries and the calculated  $K\beta$  spectra considerably change depending on the choice of parameters. Here, more extensive calculations of the ligand field parameters, the hopping terms and the final state lifetimes are necessary to remove some of the ambiguity in the calculated spectra and to achieve better agreement between theory and experiment.

## 7.2 $K\beta$ Main Lines in $^{55}\text{Fe}$ Compounds after K Capture

Figure 55 shows the  $K\beta$  main lines in  $^{55}\text{Fe}_2\text{O}_3$ ,  $\text{K}_3^{55}\text{Fe}(\text{CN})_6$  and  $\text{K}_4^{55}\text{Fe}(\text{CN})_6$  recorded after K capture. The experimental details are given in Chapters 5.1 and 2. The total number of counts in the  $K\beta_{1,3}$  peaks of all three spectra is  $\approx 5000$ . I performed ligand field multiplet calculations including charge transfer using the same empirical parameters as I used for the  $K\alpha$  calculations presented in Chapter 5.2: For  $\text{Fe}_2\text{O}_3$  I set  $\Delta=3.5$  eV and  $10Dq=1.45$  eV, for both cyanides I used  $\Delta=0.0$  eV and  $10Dq=5.0$  eV which yields a low spin configuration. I set  $U_{1s3d}=U_{3p3d}=0$  in all calculations. The hopping terms in  $O_h$  symmetry were set to  $V(E_g)=2.0$  eV and  $V(T_{2g})=-1.0$  eV. In all calculations, the  $(3p,3d)$  Slater parameters were scaled down to 70% and the  $(3d,3d)$  Slater parameters to 80%. Since  $\text{K}_3\text{Fe}(\text{CN})_6$  might exhibit a Jahn-Teller distortion [68], I performed additional calculations for this complex in  $D_{4h}$  symmetry with  $Ds=0.4$  eV and  $10Dq=1.0$  eV and  $V(B_1)=3.0$  eV,  $V(A_1)=1.73$  eV,

$V(B_2)=-1.5$  eV and  $V(E)=-1.03$  eV. The center of gravity of the final state configuration was set equal for all calculations and shifted such that the first moment for the  $Fe_2O_3$  simulation coincides with the experimental value. No term dependent final state lifetime broadening was considered. The theoretical spectra are broadened by a 1.5 eV Lorentzian and a 1.0 eV Gaussian.

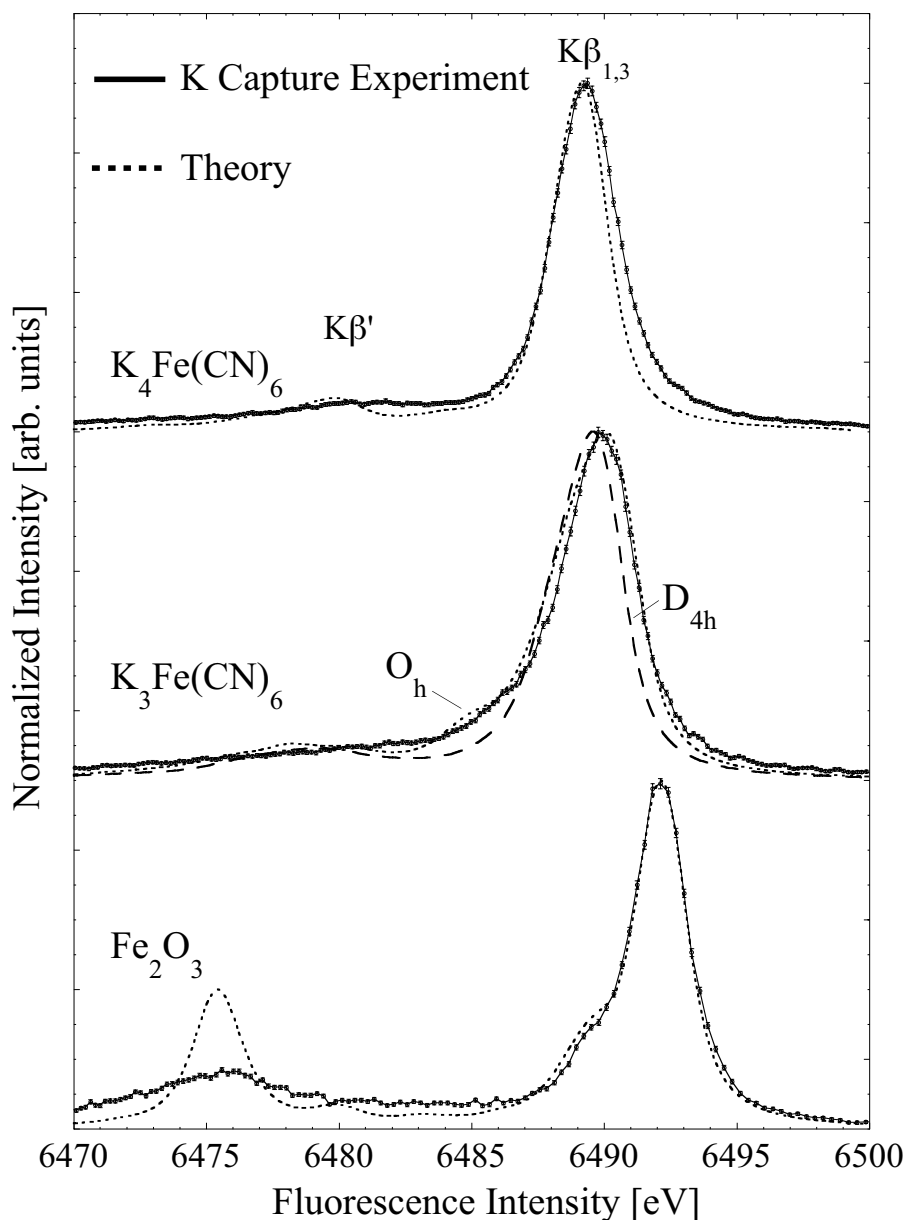


Figure 55:  $K\beta$  main lines in Fe compounds measured after K capture. The experimental spectra (solid lines) are compared to ligand field multiplet calculations including ligand-to-metal charge transfer (dashed lines). The sets of empirical parameters are given in the text. Two calculations to simulate  $K_3Fe(CN)_6$  in  $O_h$  and  $D_{4h}$  symmetry were carried out. Calculations for  $Fe_2O_3$  and  $K_4Fe(CN)_6$  were performed in  $O_h$  symmetry. The theoretical spectra are broadened by a 1.5 eV Lorentzian and a 1.0 eV Gaussian.

Figure 55 shows rather good agreement between theory and experiment. The  $Fe_2O_3$  spectrum was discussed in detail in Chapter 5.1. Between the two calculations for  $K_3Fe(CN)_6$ ,  $O_h$

symmetry seems to simulate the experimental spectrum better than  $D_{4h}$ . The calculated  $K\beta_{1,3}$  peak in  $\text{K}_4\text{Fe}(\text{CN})_6$  is narrower than the experimental peak. At this point, I do not have an explanation for that.

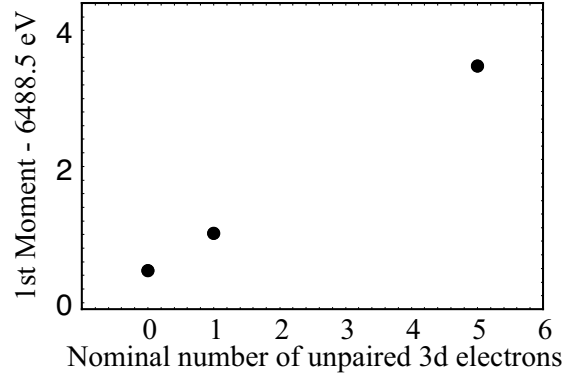


Figure 56: *Experimental first moments of  $K\beta_{1,3}$  peak in Fe compounds. The nominal number of unpaired 3d electrons is derived from the formal oxidation and spin state. The uncertainties arising from the error in relative energy calibration ( $\pm 0.04$  eV) are approximately the size of the markers used in the figure.*

To validate the proposed relation between  $K\beta_{1,3}$  first moment and number of unpaired 3d electrons  $M_1$  is plotted in Figure 56 versus the nominal number of unpaired 3d electrons. The same trend as already found for the Mn compounds is observed. Table 13 lists all moments for the experimental and theoretical spectra. For all three compounds the theoretical values show the same trends as the experimental spectra.  $M_1$  shifts to lower energies with a smaller number of unpaired 3d electrons, the magnitudes of  $M_2$  and  $M_3$  are largest for  $\text{K}_3\text{Fe}(\text{CN})_6$  and all three compounds exhibit negative asymmetry in the  $K\beta_{1,3}$  peak.

Table 13: *Results of  $K\beta_{1,3}$  moment analysis for experimental and calculated Fe compounds. The energy scale of the calculated spectra was shifted such that the  $K\beta_{1,3}$  first moments coincide for  $\text{Fe}_2\text{O}_3$ . The symmetries are given for the theoretical simulations. The error in  $M_1$  is due to the uncertainty in the relative energy calibration. All other errors are statistical errors.*

	Experiment				Theory		
	$M_1$ [-6492.08 eV]	$M_2$ [ $10^{-1}$ (eV) <sup>2</sup> ]	$M_3$ [ $10^{-1}$ (eV) <sup>3</sup> ]		$M_1$ [eV]	$M_2$ [ $10^{-1}$ (eV) <sup>2</sup> ]	$M_3$ [ $10^{-1}$ (eV) <sup>3</sup> ]
$\text{Fe}_2\text{O}_3$	0.00	4.33 (2)	-0.13 (3)	$O_h$	0.00	4.14	-0.10
$\text{K}_3\text{Fe}(\text{CN})_6$	-2.32 (4)	7.80 (2)	-0.45 (3)	$O_h$	-2.46	10.16	-1.09
$\text{K}_4\text{Fe}(\text{CN})_6$	-2.79 (4)	5.95 (2)	-0.02 (2)	$O_h$	-3.01	4.32	-0.11

It is important to note that the relative shifts in the first moment of the investigated Fe compounds as well as of  $^{54}\text{MnO}$  and  $^{54}\text{MnO}_2$  are well reproduced in the calculations. We recall that the center of gravity energy of the entire multiplets were set to equal values in the calculations. This supports the assumption that the shift of the  $K\beta_{1,3}$  line is mainly caused by multiplet effects, in particular, the ( $3p,3d$ ) exchange interaction, and that the change in absolute energies of the  $1s$  and  $3d$  orbitals is far less important.

### 7.3 $K\beta$ Lines in Ni Compounds and Fe Proteins

All spectra in the following were recorded after photoionization. The protein data were obtained at the APS and the spectra were taken at a temperature of  $\approx 50\text{K}$  to reduce radiation damage. The Ni data were recorded at the National Synchrotron Light Source (NSLS).

#### 7.3.1 Heme Center in Myoglobin

Delocalization of the  $3d$  electrons will result in weaker ( $3p,3d$ ) interaction. Furthermore, ligand-to-metal charge transfer can alter the net spin located at the metal atom and the actual spin state of the metal atom will differ from the value that is derived from the formal oxidation state. As an example for a molecular complex I show  $K\beta$  spectra of Fe in myoglobin that I recorded at the APS together with Uwe Bergmann. The samples were prepared by the group of Prof. Ann Walker at Tucson University. The structure of myoglobin is shown in Figure 57. The  $\text{O}_2$  ligand can be replaced by other ligands resulting in different spin and oxidation states of the Fe. I investigated samples with  $\text{H}_2\text{O}$  (as isolated), N (imidazole) and CO as ligands instead of the  $\text{O}_2$ . Dithionite reduces the Fe to a lower oxidation state.

The  $K\beta$  main lines are shown in Figure 58. The samples are well characterized by other techniques. Measurements of the magnetic moments of the molecular complex indicate  $S=5/2$  for the protein as isolated,  $S=1/2$  for the imidazole ligand and  $S=0$  for the dithionite reduced sample with CO as the Fe ligand [138]. Imidazole and CO as ligand therefore yield low spin Fe configurations. I argued before, that a lower net spin located at the metal atom results in a shift of the  $K\beta_{1,3}$  first moment to lower energies. Figure 58 already indicates the expected shift between the spectra. A first moment analysis of the  $K\beta_{1,3}$  peak yields 7058.80 eV for the as isolated protein, 7058.58 eV for the imidazole ligand and 7058.37 for the dithionite treated protein with a CO ligand confirming the proposed relation between spin state and first moment.

However, a comparison between ionic  $\text{Fe}_2\text{O}_3$  and the as isolated protein in Figure 59 shows that even though in both complexes the Fe ion is high-spin with a formal oxidation state of (III) the spectra are very different. The effective number of unpaired  $3d$  electrons located at the Fe is expected to be considerably smaller in the molecular complex due to electron delocalization. The  $K\beta_{1,3}$  peak in myoglobin as isolated is shifted to lower energies and the  $K\beta'$  structure is less pronounced. This is the general trend we observe in the  $K\beta$  main lines when the net spin in the metal valence shell decreases.

I conclude that the results of the  $K\beta$  main line analysis in myoglobin as an example for a molecular system with strong electron delocalization are consistent with the multiplet interpretation of the  $K\beta$  emission. The first moments show the expected shifts and the

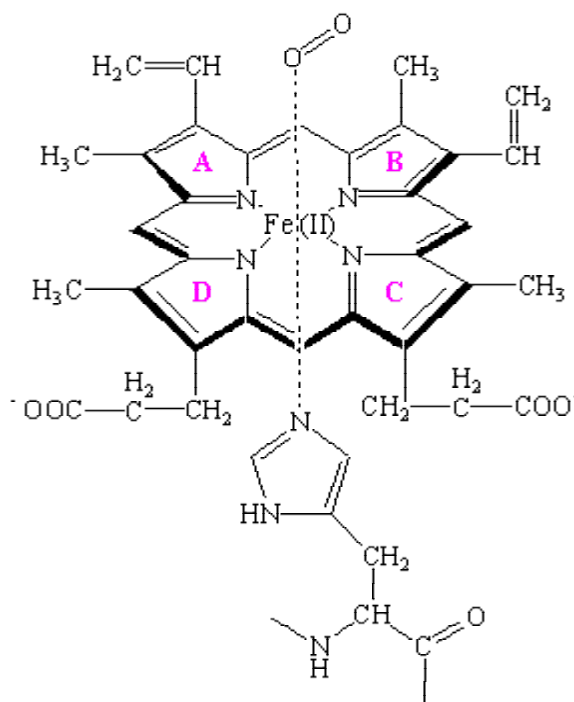


Figure 57: Molecular structure of myoglobin with a porphyrin ring bound to the Fe. The  $O_2$  ligand of Fe is replaced by  $H_2O$ , N (imidazole) or CO in the samples that were investigated.

overall  $K\beta$  main line structure is in agreement with the multiplet interpretation. Finally, I show the  $K\beta$  satellite lines in the same myoglobin samples in Figure 60. The spectra were normalized to each other with respect to the entire  $K\beta$  spectral area. I did not attempt any interpretation of the spectra and simply state that a chemical dependence can be observed. A detailed analysis could be performed in the framework of density functional theory as performed in Chapter 6.

### 7.3.2 Ni Compounds

Ni complexes are often referred to as a systems with strong electron correlation [143, 59]. In the charge transfer model this is accounted for by including three configurations, *i.e.* two ligand-to-metal charge transfer configurations. This is discussed in detail in references [42] and [133]. Because of the strong configuration interaction the relation between formal oxidation state and net spin located at the Ni becomes less accurate than for ionic compounds with weak electron correlation. As an example,  $K\beta$  main lines in Mn and Ni compounds are compared in Figure 61. The Ni spectra were taken at NSLS and the Mn spectra at SSRL. I carried out the experiments together with Uwe Bergmann. In all compounds, the metal (Mn or Ni) nearest neighbors are fluorine atoms which should yield a rather ionic bond due to the strong electronegativity of fluorine. The insets show the  $K\beta_{1,3}$  first moments versus the nominal number of unpaired  $3d$  electrons. The differences are much smaller for the Ni than for the Mn compounds. Theoretical interpretations of the Ni  $K\beta$  spectra are given in references [40] and [75]. The  $3p$  XPS in atomic Ni and in  $NiCl_2$  are discussed in references

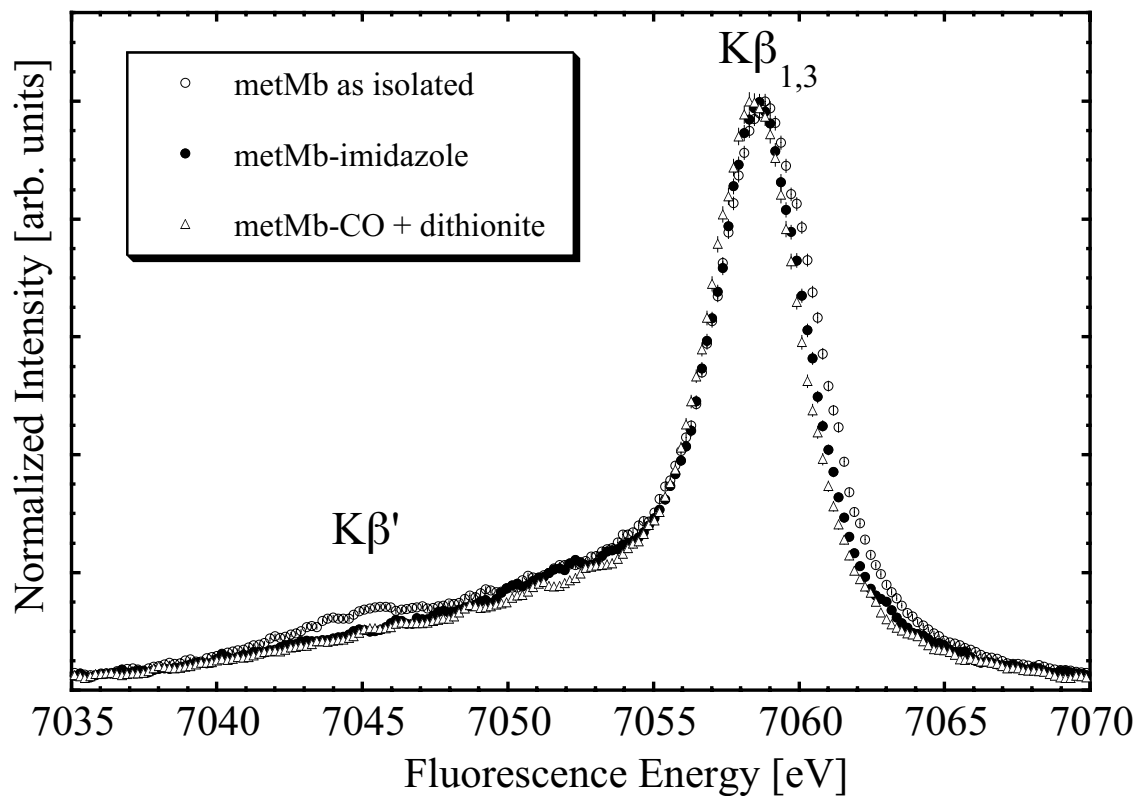


Figure 58:  $K\beta$  main lines in myoglobin with different ligands. The nominal Fe spin states are  $S=5/2$  (as isolated),  $S=1/2$  (imidazole) and  $S=0$  (CO + dithionite).

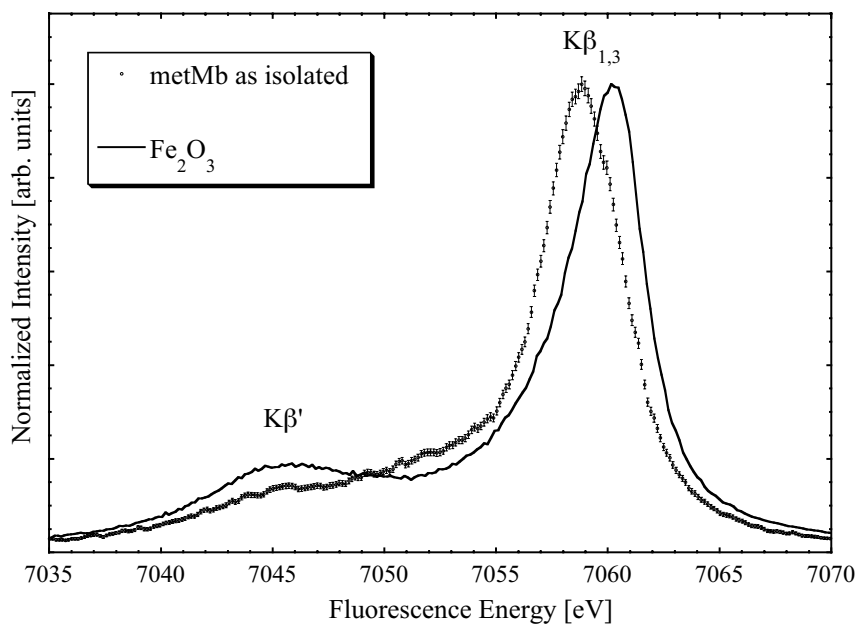


Figure 59: Comparison of the  $K\beta$  main lines in  $Fe_2O_3$  and myoglobin as isolated. In both complexes Fe has a formal spin state of  $S=5/2$ .

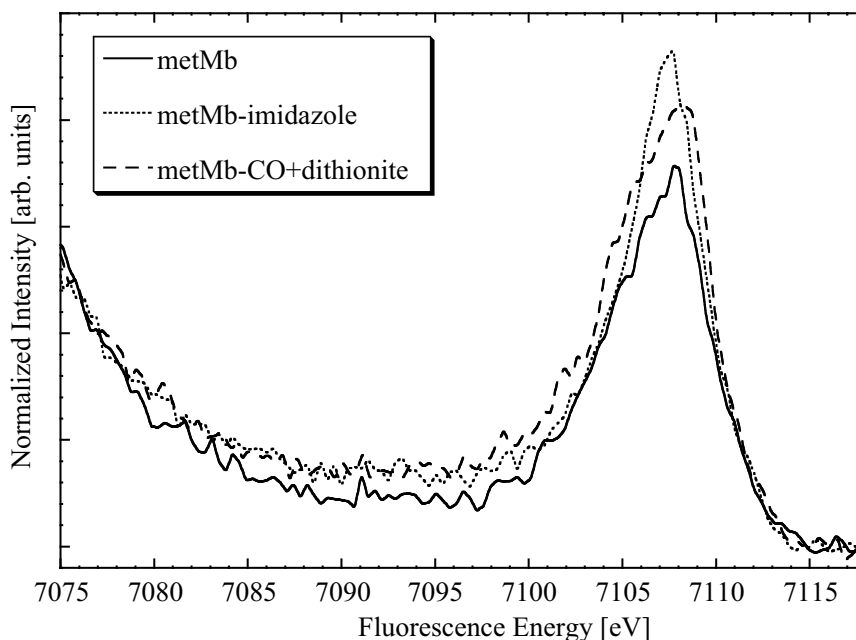


Figure 60:  $K\beta$  satellite lines in myoglobin samples. The spectra are normalized to each other in the entire  $K\beta$  spectral area. The spectra are not further interpreted except for the statement that a chemical dependence can be observed. No statistical error bars are shown for clarity in the graph. An error can be derived from the scattering of the data.

[131] and [104], respectively.

The charge transfer energies  $\Delta$  for different Ni compounds were determined by van der Laan *et al.* [134] and Lenglet *et al.* [88] in L-edge absorption spectra combined with a theoretical analysis based on the ligand field multiplet approach including charge transfer.  $\Delta$  separates the  $3d^8$  and the  $3d^9\bar{L}$  configurations in Ni(II) high-spin compounds. Since the spin located at the Ni is  $S=1$  for  $3d^8$  and  $S=1/2$  for  $3d^9\bar{L}$  we expect smaller ( $3p, 3d$ ) exchange splitting with stronger  $3d^9\bar{L}$  admixture, *i.e.* with smaller  $\Delta$ . We observed for Mn and Fe compounds that the  $K\beta_{1,3}$  first moment shifts to lower energies with a smaller effective number of unpaired  $3d$  electrons, *i.e.* a smaller net spin located at the metal atom. Following these arguments we expect that the Ni  $K\beta_{1,3}$  first moment shifts to lower energies with decreasing charge transfer energy. I compare the  $K\beta$  main lines for different Ni(II) compounds in Figure 62 and plot the  $K\beta_{1,3}$  first moments versus the charge transfer energies as given in reference [134].

The Ni experimental results confirm the proposed relation between  $K\beta_{1,3}$  first moment and effective number of unpaired  $3d$  electrons. Summarizing the  $K\beta$  main line results I state that the ligand field model including ligand to metal charge transfer is a valid approach to explain the  $K\beta$  main line emission in Mn, Fe and Ni compounds and proteins. The  $K\beta_{1,3}$  first moment reflects the spin state of the metal atom in the complex.

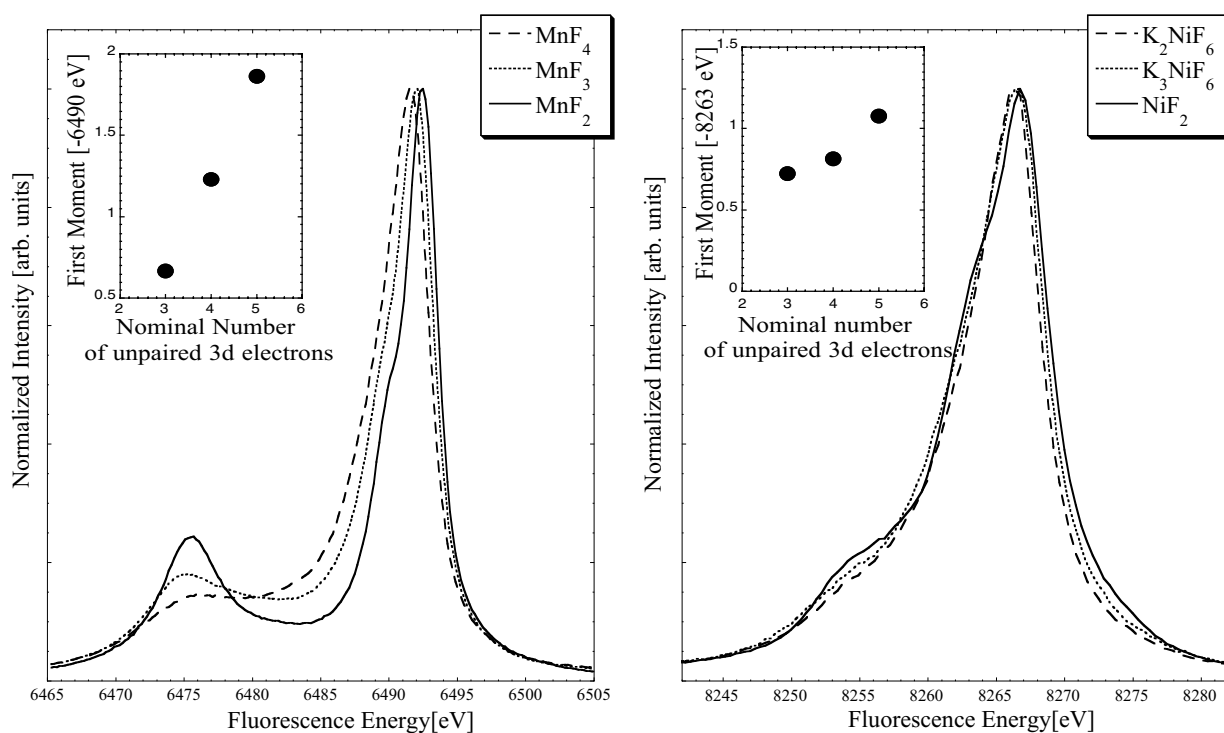


Figure 61: Comparison of  $K\beta$  main lines in Mn and Ni compounds for different formal oxidation states. The insets show the  $K\beta_{1,3}$  first moments versus the nominal number of unpaired 3d electrons.

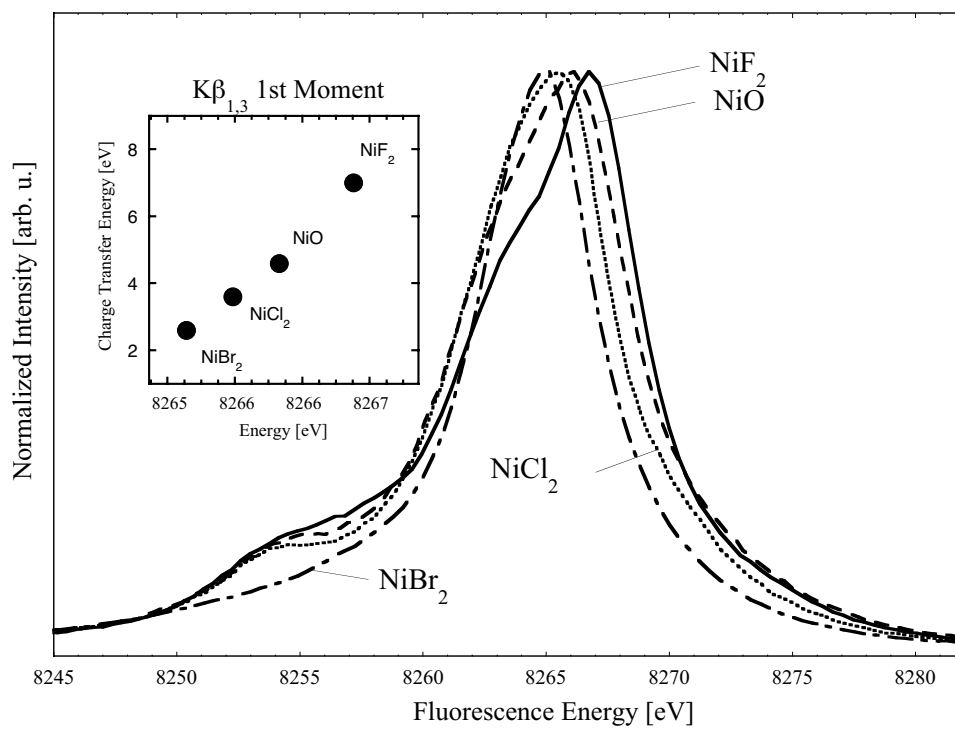


Figure 62:  $K\beta_{1,3}$  main lines in Ni compounds with varying charge transfer energy  $\Delta$ . The inset shows the  $K\beta_{1,3}$  first moment versus the charge transfer energy  $\Delta$ . The values for  $\Delta$  were obtained from reference [134].

## 8 Summary and Outlook

The K fluorescence emission in Mn, Fe and Ni compounds as well as the Fe containing metalloprotein myoglobin was investigated in this thesis. A multi-crystal spectrometer was built as part of the experimental work and its spectral and focal properties were discussed. The influence of the chemical environment was analyzed. The dependence on the mode of excitation was demonstrated and interpreted within ligand field multiplet theory including configuration interaction on the basis of ligand-to-metal charge transfer. Multiple excitations in the intermediate and final states were addressed and the similarity between shake transitions and ligand-to-metal charge transfer was pointed out. Results from density functional calculations were used to analyze the valence to  $1s$  transitions in a Mn-nitrido complex and in  $\text{Fe}_2\text{O}_3$ . The results can be summarized as follows:

- Ligand field multiplet theory can explain the  $K\alpha$  and the  $K\beta$  main line spectral features. Extending the model by including configuration interaction on the basis of ligand-to-metal charge transfer improves the agreement between theory and experiment.
- The perturbation of the valence shell due to core hole creation can be studied by comparing spectra where the  $1s$  vacancy was created either by photoionization or by radioactive electron capture decay from the K shell. The valence electrons relax non-adiabatically after photoionization. The resulting shake configurations influence the K fluorescence emission.
- K fluorescence spectra recorded after K capture decay show considerably less perturbation of the valence shell and therefore provide information about a valence electron configuration that approximately corresponds to the ground state configuration.
- The  $K\alpha_1$  full width at half maximum and the  $K\beta_{1,3}$  first moment in the compounds and proteins studied in this work show a dependence on the metal valence shell net spin. This can be understood in the framework of multiplet theory by assuming that the dependence is caused by the exchange interaction between the spin-unpaired core electron and the net spin in the valence shell. The  $K\alpha_1$  full width at half maximum shows an approximately proportional dependence on the effective number of spin-unpaired  $3d$  electrons. K fluorescence emission can therefore be used for chemical analysis. It is, however, important to bear in mind that the core hole excited state is probed.
- The relative energy shifts in the  $K\alpha$  and  $K\beta$  peaks between different compounds are rather well reproduced in the multiplet calculations assuming equal center of gravity energies. The chemical dependence is therefore not caused by a change in the difference of binding energies between the  $1s$  and the  $2p$  or  $3p$  orbital but by multiplet effects.
- Density functional calculations are a valuable approach to interpret the  $K\beta$  satellite spectral features. The spectra are dominated by dipole transitions. A rough quantitative agreement between theory and experiment could be achieved within a one-electron, sudden approximation picture for a molecular Mn-nitrido complex.

Interesting future studies for the comparison of the two modes of excitations would be on systems that show a strong change upon creation of a core hole. It is desirable to complete the series of Fe compounds measured after K capture with spectra of  $\text{FeO}$  since  $\text{Fe}_2\text{O}_3$  and  $\text{FeO}$  yield almost identical  $K\alpha$  spectra after photoionization. The spectra should differ in the K capture experiment if the ground state valence shell configuration is approximately

preserved after K capture. Some systems change their spin state (*e.g.* high-spin to low-spin in  $\text{Co}_2\text{O}_3$ ,  $\text{SrCoO}_3$  and  $\text{LaNiO}_3$  [125]) upon creation of a core hole using photoionization. It would be interesting to study whether the spin state is preserved after K capture.

In general, K capture studies, particularly the  $K\beta$  satellite emission, are desirable on any system in which one wishes to investigate the ground state valence electron configuration. However, experimental difficulties limit this technique because not many laboratories are equipped for radiochemistry. Furthermore, suitable K capture isotopes are not available for every element. There are, however, many interesting questions regarding complexes containing Mn and Fe. The group of Prof. Stephen Cramer is currently starting a new project using  $^{49}\text{V}$ .

Concerning synchrotron work using hard x-rays it is interesting to perform studies in the realm of  $1s$  resonant excitations. Few studies using  $1s2p$  resonant inelastic x-ray scattering can be found in the literature where a  $1s$  electron is excited resonantly into one of the lowest unoccupied molecular orbitals and the subsequent  $2p$  to  $1s$  radiative decay is recorded using a crystal analyzer spectrometer. The perturbation of the valence shell is expected to be reduced compared to photoionization because a resonant excitation is closer to the adiabatic limit. The  $1s2p$  two-dimensional resonant landscape can be interpreted in terms of final states with either a  $1s$  or a  $2p$  hole giving complementary information about the valence shell configuration.

## A Two-Dimensional Gas Proportional Counter

The two-dimensional gas proportional counter can be used in connection with a Canberra multi-parameter unit ND-9900 in order to generate (x,y) lists of the count rates. This is explained in reference [139]. Additionally to the information given in this reference we want to point out, that jumper W6 in the ADCs has to be adjusted when operated with the ND-9900 unit. Unfortunately, with this set up the acquired count rate on the ADCs is only read into the Alpha-computer when a certain buffer limit is reached. This is unacceptable for a low count rate experiment. Since we did not succeed in changing the set up such that every single count is written onto the computer hard drive, we left the multi-parameter unit out and acquired one dimensional data files.

### Setup 2D Gas Proportional Detector

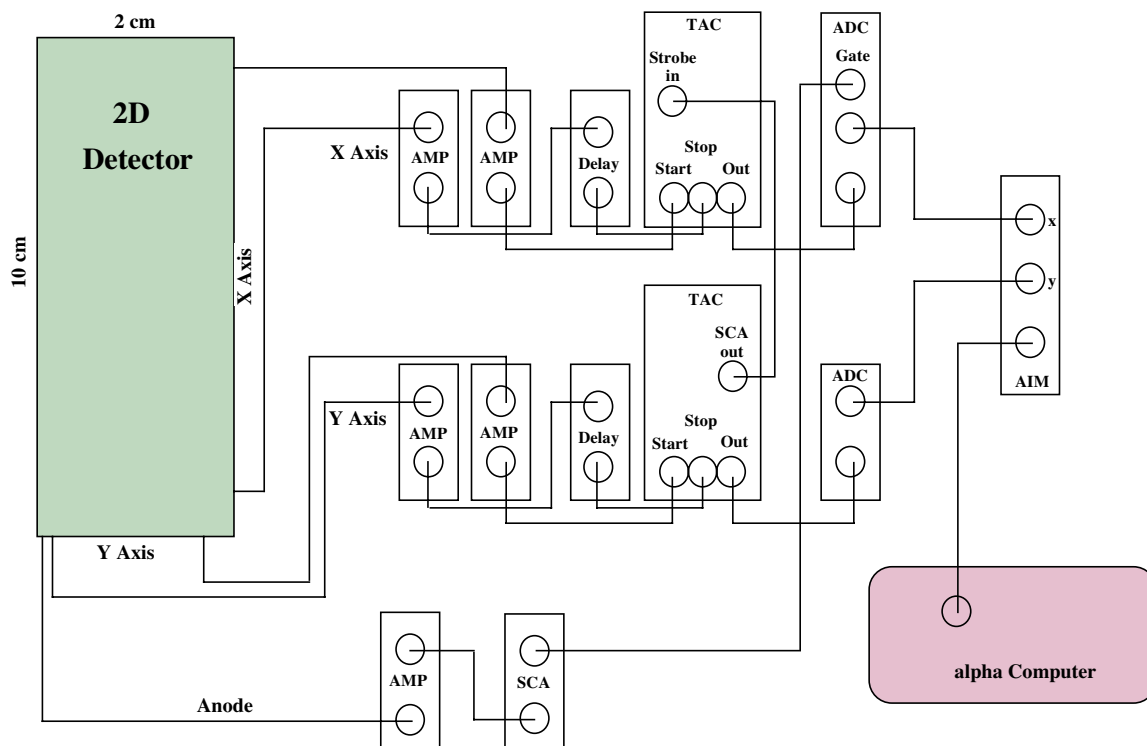


Figure 63: *Diagram for operation of two-dimensional position sensitive gas proportional counter. Only the x-direction is recorded and the y-signal is used to gate the x-TAC. A y-range can be picked by setting the time SCA on the y-TAC.*

The set up is shown in figure 63. The ADC signal is directly fed into the AIM module (adjust W6!). If we read out the X and Y signals separately we obtain the integrated spectra in the respective direction. The Y-signal is used to gate the X-TAC. The time SCA on the Y-TAC is used to select a range in Y-direction. The Y-signal can be acquired simultaneously if information about the horizontal focus on the detector is desired. Furthermore the anode signal can be used to gate the X-ADC to take advantage of the anode energy resolution. The shaping amplifier should be set to  $2.0 \mu\text{s}$  and the bipolar signal should be fed into the

SCA in order to achieve the coincidence requirements between the X-TAC and the anode SCA pulses that go into the X-ADC.

## B (2p,3d) Exchange Interaction in a Poly-Nuclear System

The same procedure as used in chapter 5.2 for an atomic system can be applied to a poly-nuclear system. We assume that the Hamiltonian of the poly-nuclear system was evaluated within any theoretical framework (*e.g.* density functional theory) and we obtained one-electron molecular spin-orbitals. If the calculations are spin-unrestricted we obtain two sets of orbitals with spin orientation  $\alpha$  and  $\beta$ , respectively. Each molecular orbital is normalized to one and its population is either one or zero. The molecular orbitals can be written as linear combinations of atomic orbitals (LCAO):

$$\begin{aligned} |i^\alpha\rangle &= \sum_m c_m^{i^\alpha} |a_m^\alpha\rangle \\ |j^\alpha\rangle &= \sum_m c_m^{j^\alpha} |a_m^\alpha\rangle \end{aligned}$$

where  $|a_m^\alpha\rangle$  are the normalized atomic orbitals of all atoms in the system weighed by the real coefficients  $c_m$ . The index  $m$  contains all quantum numbers except for the spin. We further assume that the LCAO is symmetry adapted, *i.e.* only orbitals with the same symmetry in the point group of the molecular complex form a molecular orbital. The exchange energy for an electron pair that occupies the orbitals  $|i^\alpha\rangle$  and  $|j^\alpha\rangle$  is given by the exchange integral  $\langle i^\alpha j^\alpha | \frac{1}{r} | j^\alpha i^\alpha \rangle$ . For one pair of molecular orbitals we then obtain:

$$\langle i^\alpha j^\alpha | \frac{1}{r} | j^\alpha i^\alpha \rangle = \sum_{m_l, m_l'} \sum_{m_r, m_r'} c_{m_l}^{i^\alpha} c_{m_l'}^{j^\alpha} c_{m_r}^{j^\alpha} c_{m_r'}^{i^\alpha} \langle a_{m_l}^\alpha a_{m_l'}^\alpha | \frac{1}{r} | a_{m_r}^\alpha a_{m_r'}^\alpha \rangle \quad (73)$$

We are interested in the exchange interaction of the  $2p$  hole. The metal atom inner-shell orbitals will be almost pure atomic orbitals and we can approximate the coefficients  $c_m$  to be one, *i.e.*  $|i\rangle_{inner-shell} = 1 \cdot |a\rangle_{inner-shell}$ . We then obtain for a  $2p$  electron with spin orientation  $\alpha$  that exchange interacts with an electron in a molecular orbital  $|j\rangle$ :

$$\begin{aligned} \langle 2p_\nu^\alpha j^\alpha | \frac{1}{r} | j^\alpha 2p_\nu^\alpha \rangle &= \sum_{m_l} \sum_{m_r} c_{m_l}^{j^\alpha} c_{m_r}^{j^\alpha} \langle 2p_\nu^\alpha a_{m_l}^\alpha | \frac{1}{r} | a_{m_r}^\alpha 2p_\nu^\alpha \rangle \quad (74) \\ &= \sum_m (c_m^{j^\alpha})^2 \langle 2p_\nu^\alpha a_m^\alpha | \frac{1}{r} | a_m^\alpha 2p_\nu^\alpha \rangle + \sum_{m_l \neq m_r} c_{m_l}^{j^\alpha} c_{m_r}^{j^\alpha} \langle 2p_\nu^\alpha a_{m_l}^\alpha | \frac{1}{r} | a_{m_r}^\alpha 2p_\nu^\alpha \rangle \quad (75) \end{aligned}$$

The greek index  $\nu$  describes the magnetic quantum number. In the second step the quadratic terms of the sum were separated. Now we have to evaluate the atomic integrals in equation 75. The integral will be very small for ligand atomic orbitals because their overlap with the metal  $2p$  orbital is small and we therefore only consider the metal orbitals for  $|a_m\rangle$ . In order for the orbital to contribute to the exchange energy it has to be populated with an effective net spin. Orbitals higher than  $4p$  are usually not populated [112] and orbitals lower than  $3d$  do not show an effective net spin, *i.e.* the electron spins are paired. One can perform the evaluation of the integrals by means of a multipole expansion of  $1/r$  again. The quadratic terms lead to the atomic  $(2p, a_m)$  exchange integrals weighed by the square of their coefficients  $c_m^j$  in the LCAO description of the molecular orbital  $|j\rangle$ . For this quadratic term we will only consider the metal  $3d$  orbitals and neglect the exchange contribution from

the metal  $4s$  and  $4p$  orbitals. This can be justified because the spins in the latter orbitals are usually paired with ligand electrons [54]. However, for a detailed analysis one has to include these orbitals, as well.

A treatment of the non-quadratic part in equation 75 can be found in the book by Cowan [36]. Even though three different atomic orbitals are included in the integral it is still part of a two-electron interaction. The non-quadratic part arises because the valence electron is spread over several atomic orbitals. By evaluating the coefficients  $c^k(l_i m_{l_i}, l_j m_{l_j})$  (not to confuse with the coefficients in the LCAO) one can see that only the term  $\langle 2p_\nu 4s | \frac{1}{r} | 3d_{z^2}(m_l=0) 2p_\nu \rangle$  is non-zero. Many compounds have octahedral or tetrahedral symmetry and we can eliminate the non-quadratic part using symmetry arguments. All  $3d$  orbitals have different symmetries ( $E_g$  or  $T_{2g}$ ) than the  $4s$  orbital ( $A_{1g}$ ) and they cannot both appear in a symmetry adapted LCAO. That means that either one of the coefficients  $c_{m_l, r}^j$  is zero. In the following we will consider this case.

We see that the exchange integral between the  $2p$  hole and a molecular orbital  $|j\rangle$  is:

$$\langle 2p_\nu^\alpha j^\alpha | \frac{1}{r} | j^\alpha 2p_\nu^\alpha \rangle \approx \sum_{\mu} (c_{3d_\mu}^j)^2 \langle 2p_\nu^\alpha 3d_\mu^\alpha | \frac{1}{r} | 3d_\mu^\alpha 2p_\nu^\alpha \rangle \quad (76)$$

The sum over  $m$  in equation 75 turns into the sum over all  $3d$  magnetic quantum numbers  $\mu$ . The sum over  $\mu$  is not really necessary because only one  $\mu$  appears in the same LCAO. However, we can keep the sum because the coefficients  $c_{3d_\mu}^j$  ensure that only populated orbitals appear as non-zero terms in the sum. We now sum over all molecular orbitals  $|j^\alpha\rangle$  and over all  $2p$  orbitals, *i.e.* the  $2p$  magnetic quantum numbers, and obtain for the exchange energy for one spin direction:

$$E_{ex}^{2p^\alpha 3d^\alpha} = \sum_{\mu, \nu} \sum_j (c_{3d_\mu}^j)^2 \langle 2p_\nu^\alpha 3d_\mu^\alpha | \frac{1}{r} | 3d_\mu^\alpha 2p_\nu^\alpha \rangle \quad (77)$$

$$= \sum_{\mu, \nu} [\langle 2p_\nu^\alpha 3d_\mu^\alpha | \frac{1}{r} | 3d_\mu^\alpha 2p_\nu^\alpha \rangle \sum_j (c_{3d_\mu}^j)^2] \quad (78)$$

Here the first obstacle occurs. The sum over  $j$  can be performed first but not the sum over the magnetic quantum numbers. I therefore obtain a coefficient  $(c_{3d_\mu}^j)^2$  connected with every integral in the sum over the magnetic quantum numbers and I cannot average the atomic exchange integrals to the exchange parameter  $a$ . One could replace the coefficients  $(c_{3d_\mu}^j)^2$  by their mean value  $(\bar{c}_{3d^\alpha})^2$  and thus eliminate the index  $\mu$ . Then the averaging can be done and one obtains:

$$E_{ex}^{2p^\alpha 3d^\alpha} \approx a(\bar{c}_{3d^\alpha})^2 \quad (79)$$

This equation might be exact but I did not succeed in proving it. We now take the difference between  $\alpha$  and  $\beta$  spin orientation again:

$$\Delta E_{ex}^{2p^{3d}} \propto |(\bar{c}_{3d^\alpha})^2 - (\bar{c}_{3d^\beta})^2| a \quad (80)$$

We now want to relate this expression to results of a population analysis. In a Mulliken population analysis the population of an atomic orbital  $a_m$  is given by [100]

$$n_{a_m} = \sum_j N^j [(c_m^j)^2 + \sum_{n \neq m} c_m^j c_n^j S_{m,n}] \quad (81)$$

$$S_{m,n} = \langle a_m | a_n \rangle \quad (82)$$

where the sum over  $j$  extends over all molecular orbitals and the sum over  $n$  extends over all atomic orbitals that appear in the LCAO of the molecular orbital  $|j\rangle$ .  $N^j$  is the number of electrons in the molecular orbital  $|j\rangle$ . It is one in spin-unrestricted calculations and we then have to add an index to denote the spin of the orbital. The integral  $S_{m,n}$  is the overlap population. The overlap of the metal  $3d$  orbital with the ligand atomic orbitals can be considerable. However, the overlap contribution to the total population  $n_{am}$  might be zero. We could then directly relate the sum over  $j$  in equation 78 to the population  $n_{3d_\mu^\alpha}$ . Within the metal the only contribution to the overlap population can arise from higher  $d$  orbitals because of the normalization properties of the spherical harmonics. However,  $4d$  and higher orbitals will hardly be populated, *i.e.* the coefficients  $c_m^i$  will be small. Table 14 shows the metal and ligand orbitals classified by their symmetries [107]. Appropriate linear combinations of ligand orbitals can form orbitals with the same symmetry as the metal orbitals. Both coefficients  $c_m^i$  and  $c_n^i$  in equation 81 have to be non-zero simultaneously for the overlap population to contribute to the total population of the atomic orbital  $|a_m\rangle$  and thus we only have to sum over those orbitals that belong to the same symmetry, *i.e.* can be part of the LCAO for one molecular orbital  $|i\rangle$ . All six ligands are identical and have identical atomic orbitals in octahedral symmetry. Further investigation of the overlap population was not carried out in this work.

Table 14: *Linear combination of ligand atomic orbitals classified by their symmetries together with the metal orbitals for octahedral complexes [107]. The ligands 1 to 4 are in the  $xy$ -plane while 5 and 6 lie on the  $z$ -axis. Ligand  $\sigma$  orbitals can be either  $2s$  or  $2p$  orbitals and are denoted  $\phi$ .*

	Metal	Ligand $\sigma$	Ligand $\pi$
$E_{2g}$	$3d_{z^2}$ $3d_{x^2-y^2}$	$\frac{1}{2\sqrt{3}}(2\phi_5 + 2\phi_6 - \phi_1 - \phi_2 - \phi_3 - \phi_4)$ $\frac{1}{2}(\phi_1 + \phi_2 - \phi_3 - \phi_4)$	
$T_{2g}$	$3d_{xy}$ $3d_{xz}$ $3d_{yz}$		$\frac{1}{2}(2p_{y_1} - 2p_{y_2} + 2p_{y_3} - 2p_{y_4})$ $\frac{1}{2}(2p_{z_1} - 2p_{z_2} + 2p_{z_5} - 2p_{z_6})$ $\frac{1}{2}(2p_{z_3} - 2p_{z_4} + 2p_{y_5} - 2p_{y_6})$

If one can neglect the overlap population, we can give the number of spin  $\alpha$  and spin  $\beta$  metal  $3d$  electrons and calculate the difference:

$$n_{eff} = \left| \sum_j \sum_\mu (c_{3d_\mu^\alpha}^j)^2 - \sum_j \sum_\mu (c_{3d_\mu^\beta}^j)^2 \right| \quad (83)$$

$$= \left| (\bar{c}_{3d^\alpha})^2 - (\bar{c}_{3d^\beta})^2 \right| \quad (84)$$

which is the effective number of unpaired  $3d$  electrons. In the last step I performed the same averaging as I did before between equations 78 and 79. Comparison with equation 80 shows that the  $(2p,3d)$  exchange interaction in a poly-nuclear system is proportional to  $n_{eff}$ . Note

that in the ionic limit of the poly-nuclear complex instead of a covalent poly-nuclear system we would obtain  $c_{3d}^i = 1$  or  $0$  because all orbitals are pure atomic, and  $n_{eff}$  becomes the nominal number of unpaired  $3d$  electrons  $n$ .

We finally I obtain an expression for the  $(2p, 3d)$  exchange energy splitting in a poly-nuclear complex:

$$\Delta E_{ex}^{2p3d} \propto n_{eff} a \quad (85)$$

## References

- [1] T. Aberg. *Phys. Rev. A, Gen. Phys. (USA)*, 4:1735–40, 1971.
- [2] B. K. Agarwal. *X-ray spectroscopy : an introduction*. Springer series in optical sciences ; v. 15. Springer-Verlag, 2nd edition, 1991.
- [3] Center for X-Ray Optics and ALS. *X-Ray Data Booklet*. Lawrence Berkeley National Laboratory, 2nd edition, 2001.
- [4] A. L. Ankudinov, A. Nesvishskii, and J. J. Rehr. Theory and Computation for Synchrotron Radiation Spectroscopy Frascati,, pages 105–9, 2000.
- [5] N. W. Ashcroft and N. D. Mermin. *Solid state physics*. Holt Rinehart and Winston, 1976.
- [6] P. W. Atkins, M. S. Child, and C. S. G. Phillips. *Tables for group theory*. Oxford U.P., 1970.
- [7] P. W. Atkins and R. S. Friedman. *Molecular quantum mechanics*. Oxford University Press, 3rd ed edition, 1997.
- [8] P Bagus, 2000. Personal Communication.
- [9] P. S. Bagus, R. Broer, W. A. De Jong, W. C. Nieuwpoort, F. Parmigiani, and L. Sangaletti. *Phys. Rev. Lett. (USA)*, 84:2259–62, 2000.
- [10] Carl Johan Ballhausen. *Introduction to ligand field theory*. McGraw-Hill series in advanced chemistry. McGraw-Hill, 1962.
- [11] B. W. Batterman and H. Cole. *Rev. Mod. Phys.*, 36:681–717, 1964.
- [12] J Becquerel. *Z. Physik*, 58:205, 1929.
- [13] J. Bendix, R. J. Deeth, T. Weyhermuller, E. Bill, and K. Wieghardt. *Inorg Chem*, 39:930–938, 2000.
- [14] U. Bergmann, J. Bendix, P. Glatzel, H. B. Gray, and S. P. Cramer. *J. Phys. Chem.*, in press, 2001.
- [15] U. Bergmann and S. P. Cramer. In *Proc. SPIE - Int. Soc. Opt. Eng. (USA)*, Crystal and Multilayer Optics, pages 198–209, 1998.
- [16] U. Bergmann, P. Glatzel, F. deGroot, and S. P. Cramer. *J. Am. Chem. Soc.*, 121:4926–4927, 1999.
- [17] U. Bergmann, C. R. Horne, T. J. Collins, J. M. Workman, and S. P. Cramer. *Chem. Phys. Lett.*, 302:119–24, 1999.
- [18] H Bethe. *Ann. Phys.*, 3:133–208, 1929.
- [19] A. Bianconi, J. Garcia, M. Benfatto, A. Marcelli, C. R. Natoli, and M. F. Ruiz-Lopez. *Phys. Rev. B, Condens. Matter (USA)*, 43:6885–92, 1991.

- [20] M. A. Blokhin. *X-ray spectroscopy*. International monographs on advanced mathematics and physics. Hindustan Pub. Corp., 1962.
- [21] A. E. Bocquet, T. Mizokawa, T. Saitoh, H. Namatame, and A. Fujimori. *Phys. Rev. B*, 46:3771–84, 1992.
- [22] R. A. Boie, J. Fischer, Y. Inagaki, F. C. Merritt, V. Radeka, L. C. Rogers, and D. M. Xi. In *Nucl. Instrum. Methods Phys. Res. (Netherlands)*, Proceedings of the International Conference on X-Ray Detectors for Synchrotron Radiation, pages 93–115, 1982.
- [23] G. L. Borchert, P. G. Hansen, B. Johnson, H. L. Ravn, O. W. B. Schult, and P. Tidemand-Petersson. *Phys. Lett. A*, 63A:15–18, 1977.
- [24] G. L. Borchert, P. G. Hansen, B. Jonson, I. Lindgren, H. L. Ravn, O. W. B. Schult, and P. Tidemand-Petersson. *Phys. Lett. A*, 66A:374–6, 1978.
- [25] G. L. Borchert, P. G. Hansen, B. Jonson, I. Lindgren, H. L. Ravn, O. W. B. Schult, and P. Tidemand-Petersson. *Phys. Lett. A*, 65A:297–300, 1978.
- [26] B. H. Bransden and C. J. Joachain. *Physics of atoms and molecules*. Longman, 1983.
- [27] I. D. Brown, A. Dabkowski, and A. McCleary. *Acta Crystallogr B-Struct Sci*, 53:750–761, 1997.
- [28] G. B. Bunker, T. Irving, E. Black, K. Zhang, R. Fischetti, S. Wang, and S. Stepanov. In *AIP Conf. Proc. (USA)*, Synchrotron Radiation Instrumentation. Tenth US National Conference, page 16, 1997.
- [29] Philip H. Butler. *Point group symmetry applications : methods and tables*. Plenum Press, 1981.
- [30] W. A. Caliebe, C. C. Kao, J. B. Hastings, M. Taguchi, A. Kotani, T. Uozumi, and F. M. F. de Groot. *Phys. Rev. B*, 58:13452–8, 1998.
- [31] J. L. Campbell, J. A. Maxwell, and W. J. Teesdale. *Phys. Rev. C, Nucl. Phys. (USA)*, 43:1656–63, 1991.
- [32] J. L. Campbell, A. Perujo, W. J. Teesdale, and B. M. Millman. *Phys. Rev. A, Gen. Phys. (USA)*, 33:2410–7, 1986.
- [33] T. A. Carlson and Jr. Nestor, C. W. *Phys. Rev. A, Gen. Phys. (USA)*, 8:2887–94, 1973.
- [34] M. C. Chon and J. Law. *Phys. Rev. A, At. Mol. Opt. Phys. (USA)*, 50:1372–6, 1994.
- [35] Claude Cohen-Tannoudji, Bernard Diu, and Franck Laló. *Quantum mechanics*. Wiley, 1977.
- [36] R. D. Cowan. *The Theory of Atomic Structure and Spectra*. University of California Press, 1981.
- [37] S. P. Cramer, H. Wang, C. Bryant, M. Legros, C. Horne, D. Patel, C. Ralston, and X. Wang. *Spectroscopic Methods in Bioinorganic Chemistry*, pages 154–178. American Chemical Society, 1998.

- [38] Crismatec. <http://www.crisimatec.com>. Technical report, 2001.
- [39] F. M. F. de Groot, 2001. Personal Communication.
- [40] F. M. F. de Groot, A. Fontaine, C. C. Kao, and M. Krisch. *J. Phys.*, 6:6875–84, 1994.
- [41] F. M. F. de Groot, J. C. Fuggle, B. T. Thole, and G. A. Sawatzky. *Phys. Rev. B, Condens. Matter (USA)*, 42:5459–68, 1990.
- [42] F.M.F. de Groot. *J. Electron Spectrosc. Relat. Phenom.*, 676:529–622, 1994.
- [43] F. M. F. deGroot, M.-A. Arrio, P. Saintavit, C. Cartier, and C. T. Chen. *Solid State Commun.*, 92:991–995, 1994.
- [44] A. V. Dem'yanchuk, A. Z. Zhmudskiy, V. F. Surzhko, and V. I. Shiyanovskiy. *Fiz. Metal. Metalloved.*, 43:1307–1308, 1977.
- [45] R. D. Deslattes, R. E. LaVilla, P. L. Cowan, and A. Henins. *Phys. Rev. A, Gen. Phys. (USA)*, 27:923–33, 1983.
- [46] M. Deutsch, 2001. Personal Communication.
- [47] R. Diamant, S. Huotari, K. Hamalainen, C. C. Kao, and M. Deutsch. *Phys. Rev. Lett. (USA)*, 84:3278–81, 2000.
- [48] G. Drager and O. Brummer. *Phys. Status Solidi B (East Germany)*, 124:11–28, 1984.
- [49] G. Drager, W. Czolbe, and J. A. Leiro. *Phys. Rev. B*, 45:8283–7, 1992.
- [50] H. Ebert, L. Baumgarten, C. M. Schneider, and J. Kirschner. *Phys. Rev. B, Condens. Matter (USA)*, 44:4466–9, 1991.
- [51] ESRF-APS. Xop-x-ray oriented programs v2.0. Technical report, ESRF-APS, 2000.
- [52] H. Feist, M. Feldt, C. Gerth, M. Martins, P. Sladeczek, and P. Zimmermann. *Phys. Rev. A, At. Mol. Opt. Phys. (USA)*, 53:760–5, 1996.
- [53] E Fermi. *Atti accad. Lincei*, 6:602, 1927.
- [54] B. N. Figgis. *Introduction to ligand fields*. Interscience Publishers, 1967.
- [55] A. Filipponi, T. A. Tyson, K. O. Hodgson, and S. Mobilio. *Phys. Rev. A, At. Mol. Opt. Phys. (USA)*, 48:1328–38, 1993.
- [56] M. Fritsch, C. C. Kao, K. Hamalainen, O. Gang, E. Forster, and M. Deutsch. *Phys. Rev. A, At. Mol. Opt. Phys. (USA)*, 57:1686–97, 1998.
- [57] T. Fujikawa and J. Kawai. *J. Phys. Soc. Jpn. (Japan)*, 68:4032–6, 1999.
- [58] A. Fujimori, M. Saeki, N. Kimizuka, M. Taniguchi, and S. Suga. *Phys. Rev. B, Condens. Matter*, 34:7318–28, 1986.
- [59] Peter Fulde. *Electron correlations in molecules and solids*. Springer series in solid-state sciences ; 100. Springer-Verlag, 3rd enl. edition, 1995.

- [60] J. Goulon, C. Goulon-Ginet, R. Cortes, and J. M. Dubois. *J. Phys.*, 43:539–548, 1982.
- [61] John Stanley Griffith. *The theory of transition-metal ions*. University Press, 1964.
- [62] K. Hamalainen, C. C. Kao, J. B. Hastings, D. P. Siddons, L. E. Berman, V. Stojanoff, and S. P. Cramer. *Phys. Rev. B, Condens. Matter (USA)*, 46:14274–7, 1992.
- [63] B. Hermsmeier, C. S. Fadley, M. O. Krause, J. Jimenez-Mier, P. Gerard, and S. T. Manson. *Phys. Rev. Lett. (USA)*, 61:2592–5, 1988.
- [64] P. Hohenberg and W. Kohn. *Phys. Rev. B*, 136:864, 1964.
- [65] Stefan Hüfner. *Photoelectron spectroscopy : principles and applications*. Springer series in solid-state sciences ; 82. Springer, 2nd edition, 1996.
- [66] Chang Hyunju, J. F. Harrison, T. A. Kaplan, and S. D. Mahanti. *Phys. Rev. B, Condens. Matter (USA)*, 49:15753–8, 1994.
- [67] Canberra Industries Inc. Ge detectors user’s manual. Technical report, 1995.
- [68] Z. Iqbal. *J. Phys. C, Solid State Phys. (UK)*, 10:3533–43, 1977.
- [69] K. Ishii and S. Morita. *Nucl. Instrum. Methods Phys. Res. B, Beam Interact. Mater. At. (Netherlands)*, B34:209–16, 1988.
- [70] R. W. James. *Solid State Physics*, 15:53, 1963.
- [71] H.H. Johann. *Z. Physik*, 69:185, 1931.
- [72] J. Kawai, 2001. Personal Communication.
- [73] J. Kawai and K. Hayashi. In *J. Electron Spectrosc. Relat. Phenom. (Netherlands)*, Todai Symposium 1997 and Sixth ISSP International Symposium on Frontiers in Synchrotron Radiation Spectroscopy, pages 243–5, 1998.
- [74] J. Kawai, C. Suzuki, H. Adachi, T. Konishi, and Y. Gohshi. *Phys. Rev. B, Condens. Matter*, 50:11347–54, 1994.
- [75] J. Kawai, M. Takami, and C. Satoko. *Phys. Rev. Lett.*, 65:2193–6, 1990.
- [76] A. Kodre, M. Hribar, I. Arcon, D. Glavic-Cindro, M. Stuhec, R. Frahm, and W. Drube. *Phys. Rev. A, At. Mol. Opt. Phys. (USA)*, 45:4682–7, 1992.
- [77] W. Kohn, A. D. Becke, and R. G. Parr. *J Phys Chem*, 100:12974–12980, 1996.
- [78] W. Kohn and L. J. Sham. *Phys. Rev.*, 140:A1133, 1965.
- [79] D. C. Koningsberger and Roelof Prins. *X-ray absorption : principles, applications, techniques of EXAFS, SEXAFS, and XANES*. Chemical analysis ; v. 92. Wiley, 1988.
- [80] E. J. Konopinski. *The Theory of Beta Radioactivity*. The International Series of Monographs in Physics. Oxford University Press, 1966.
- [81] A. Kotani. *J. Electron Spectrosc. Relat. Phenom. (Netherlands)*, 100:75–104, 1999.

- [82] M. O. Krause. *J. Phys. Chem. Ref. Data (USA)*, 8:307–27, 1979.
- [83] M. O. Krause and J. H. Oliver. *J. Phys. Chem. Ref. Data*, 8:329–38, 1979.
- [84] M. Krisch. *Spektrale und fokale Eigenschaften von gebogenen Bragg-Kristallen*. PhD thesis, Universität Dortmund, 1993.
- [85] P. Kuiper, B. G. Searle, P. Rudolf, L. H. Tjeng, and C. T. Chen. *Phys. Rev. Lett.*, 70:1549–52, 1993.
- [86] R. J. Lad and V. E. Henrich. *Phys. Rev. B*, 39:13478–85, 1989.
- [87] K. Läger. *Über den Einfluss der Bindungsart und der Kristallstruktur auf das K-Röntgenemissionsspektrum von Aluminium und Silizium*. PhD thesis, Ludwig-Maximilians-Universität, 1968.
- [88] M. Lenglet and F. Hochu. *Mater. Res. Bull. (USA)*, 32:863–72, 1997.
- [89] D. R. Lide, editor. *Handbook of Chemistry and Physics*. CRC Press, 77 edition, 1996–1997.
- [90] David R. Lide. *CRC handbook of chemistry and physics : a ready-reference book of chemical and physical data*. CRC Press, 73rd (1992-93 ) edition, 1992.
- [91] T. Mallah, S. Thiebaut, M. Verdaguer, and P. Veillet. *Science (USA)*, 262:1554–7, 1993.
- [92] M. Martins, 2001. Personal Communication.
- [93] L. F. Mattheiss. *Phys. Rev. B, Solid State*, 5:290–306, 1972.
- [94] A. Meisel, G. Leonhardt, and R. Szargan. *X-Ray Spectra and Chemical Binding*, volume 37 of *Chemical Physics*. Springer-Verlag, 1989.
- [95] J. Messinger, J. H. Robblee, U. Bergmann, C. Fernandez, P. Glatzel, H. Visser, R. M. Cinco, K. L. McFarlane, E. Bellacchio, S. A. Pizarro, S. P. Cramer, K. Sauer, M. P. Klein, and V. K. Yachandra. *J. Amer. Chem. Soc.*, 123:7804–7820, 2001.
- [96] A. S. Michalowski. *Acta Oncol*, 33:139–157, 1994.
- [97] T. Mukoyama, Y. Ito, and K. Taniguchi. *X-Ray Spectrom.*, 28:491–6, 1999.
- [98] T. Mukoyama and K. Taniguchi. *Adv. Quantum Chem.*, 37:139, 2000.
- [99] T. Mukoyama and M. Uda. *Phys. Rev. A*, 61:030501/1–4, 2000.
- [100] R. S. Mulliken. *J. Chem. Phys.*, 23:1833, 1955.
- [101] E. B. Myers, D. C. Ralph, J. A. Katine, R. N. Louie, and R. A. Buhrman. *Science (USA)*, 285:867–70, 1999.
- [102] S. Nagel. *J. Phys. Chem. Solids (UK)*, 46:905–19, 1985.
- [103] K. Okada and A. Kotani. *J. Phys. Soc. Jpn.*, 61:4619–37, 1992.

- [104] K. Okada, A. Kotani, H. Ogasawara, Y. Seino, and B. T. Thole. *Phys. Rev. B*, 47:6203–6, 1993.
- [105] Center for X-Ray Optics. X-ray interaction with matter. Technical report, LBNL, 2001.
- [106] J. Orenstein and A. J. Millis. *Science (USA)*, 288:468–74, 2000.
- [107] Leslie E. Orgel. *An introduction to transition-metal chemistry: ligand-field theory*. Methuen; Wiley, 2nd edition, 1966.
- [108] G. Peng, F. M. F. Degroot, K. Hamalainen, J. A. Moore, X. Wang, M. M. Grush, J. B. Hastings, D. P. Siddons, W. H. Armstrong, O. C. Mullins, and S. P. Cramer. *J. Am. Chem. Soc.*, 116:2914–2920, 1994.
- [109] A. P. Ramirez. *J. Phys., Condens. Matter. (UK)*, 9:8171–99, 1997.
- [110] J. Rehr, 2001. Personal Communication.
- [111] James F. Riordan and Bert L. Vallee. *Metallobiochemistry*. Methods in enzymology v. 227. Academic Press, 1993.
- [112] J. Rodriguez, 2001. Personal Communication.
- [113] D. E. Sayers, E. A. Stern, and F. W. Lytle. *Phys. Rev. Lett. (USA)*, 27:1204–7, 1971.
- [114] H. W. Schnopper. *Phys. Rev.*, 131:2558–2560, 1963.
- [115] H. W. Schnopper. *Phys. Rev.*, 154:118–123, 1967.
- [116] H. W. Schnopper and L. G. Parratt. *Röntgenspektren und Chemische Bindung*, pages 314–324. Leipzig University Press, 1966.
- [117] J. H. Scofield. *Phys. Rev.*, 179:9, 1969.
- [118] J. C. Slater. *Phys. Rev.*, 36:57 – 64, 1930.
- [119] John Clarke Slater. *Quantum theory of atomic structure*. International series in pure and applied physics. McGraw-Hill, 1960.
- [120] G. C. Smith and B. Yu. In *IEEE Trans. Nucl. Sci. (USA)*, 1994 Nuclear Science Symposium and Medical Imaging Conference, NSS/MIC, pages 541–7, 1995.
- [121] G. C. Smith, B. Yu, J. Fischer, V. Radeka, and J. A. Harder. In *Nucl. Instrum. Methods Phys. Res. A, Accel. Spectrom. Detect. Assoc. Equip. (Netherlands)*, Sixth International Wire Chamber Conference, pages 78–85, 1992.
- [122] S. N. Soni. *Phys. Lett. A (Netherlands)*, 209:57–60, 1995.
- [123] SSRL. <http://www-ssrl.slac.stanford.edu/bart/bl10-2doc.html>. Technical report, 2001.
- [124] Satoru Sugano, Yukito Tanabe, and Hiroshi Kamimura. *Multiplets of transition-metal ions in crystals*. Pure and applied physics v. 33. Academic Press, 1970.

- [125] C. Suzuki, J. Kawai, H. Adachi, and T. Mukoyama. *Chem. Phys. (Netherlands)*, 247:453–70, 1999.
- [126] M. Taguchi, J. C. Parlebas, T. Uozumi, A. Kotani, and C. C. Kao. *Phys. Rev. B*, 61:2553–60, 2000.
- [127] M. Taguchi, T. Uozumi, and A. Kotani. *J. Phys. Soc. Jpn.*, 66:247–56, 1997.
- [128] B. T. Thole, G. van der Laan, and P. H. Butler. *Chem. Phys. Lett.*, 149:295, 1988.
- [129] L H Thomas. *Proc. Cambridge Phil. Soc.*, 23:542, 1927.
- [130] T. D. Thomas. *Phys. Rev. Lett. (USA)*, 52:417–20, 1984.
- [131] K. Tiedtke, Ch Gerth, B. Kanngiesser, B. Obst, P. Zimmermann, M. Martins, and A. Tutay. *Phys. Rev. A, At. Mol. Opt. Phys. (USA)*, 60:3008–12, 1999.
- [132] K. Tsutsumi. *J. Phys. Soc. Jpn*, 14:1696, 1959.
- [133] G. van der Laan, J. Zaanen, G. A. Sawatzky, R. Karnatak, and J. M. Esteve. *Solid State Commun.*, 56:673–6, 1985.
- [134] G. van der Laan, J. Zaanen, G. A. Sawatzky, R. Karnatak, and J. M. Esteve. *Phys. Rev. B*, 33:4253–63, 1986.
- [135] J. W. Van Vleck. *Phys. Rev.*, 45:405, 1934.
- [136] H. Visser, E. Anxolabehere-Mallart, U. Bergmann, P. Glatzel, J. H. Robblee, S. P. Cramer, J. J. Girerd, K. Sauer, M. P. Klein, and V. K. Yachandra. *J. Amer. Chem. Soc.*, 123:7031–7039, 2001.
- [137] A. von dem Borne, R. L. Johnson, B. Sonntag, M. Talkenberg, A. Verweyen, P. Wernet, J. Schulz, K. Tiedtke, C. Gerth, B. Obst, P. Zimmermann, and J. E. Hansen. *Phys. Rev. A, At. Mol. Opt. Phys. (USA)*, 62:052703/1–12, 2000.
- [138] Ann Walker, 2000. Personal Communication.
- [139] X. Wang. *High Resolution X-Ray Fluorescence Spectroscopy-A New Technique for Site- and Spin-Selectivity*. PhD thesis, University of California, 1996.
- [140] A. F. Wells. *Structural inorganic chemistry*. Oxford science publications. Clarendon Press ; Oxford University Press, 5th edition, 1990.
- [141] Ph Wernet, B. Sonntag, M. Martins, P. Glatzel, B. Obst, and P. Zimmermann. *Phys. Rev. A, At. Mol. Opt. Phys. (USA)*, 63:050702/1–4, 2001.
- [142] C. S. Wu and S. A. Moszkowski. *Beta Decay*, volume 16 of *Interscience Monographs and Texts in Physics and Astronomy*. Interscience Publisheres, 1966.
- [143] J. Zaanen, C. Westra, and G. A. Sawatzky. *Phys. Rev. B*, 33:8060–73, 1986.
- [144] William H. Zachariasen. *Theory of X-ray diffraction in crystals*. Dover Publications, 1967.

# Acknowledgement

I thank Prof. Bernd Sonntag who helped me in a difficult situation. His intensive study of my work, his broad knowledge and his dedication considerably contributed to this thesis.

I thank Prof. Stephen Cramer for his creative ideas, his support and for his consideration when I needed the time to write this thesis.

I thank Uwe Bergmann for building a beautiful spectrometer and for his help during the experiments. And I thank him for many passionate and fruitful discussions.

I thank Frank de Groot for his enormous patience when he explained the multiplet program to me, for answering numerous questions and for helping me to keep my model compounds straight.

I thank Stephan Friedrich for his invaluable efforts to find me a job and my way in Berkeley. I thank Tobias Funk for his Matlab knowledge. I thank both of them for putting up with me.

I thank Lilian Jaquament, Robert Jones, Artur Braun, Jorge Rodriguez, Hongxin Wang, Daulat Patil, Weiwei Gu and Ping-Chang Lin for creating a friendly atmosphere in the group.

I thank Philippe Wernet for reading chapters of this thesis and his advice.

I thank Christopher Gerth and Joachim Schulz for building a bridge to Hamburg.

I furthermore thank

the beamline staff at SSRL, NSLS and APS for their help.

Ted Hillyer, Sue Christoffersen and Mike for their support in Davis.

the PSII people on campus for being a synchrotron family.

I thank

all my friends

my father

and

my mother